Hydroelastic Stability and Wave Propagation in Fluid-Filled Channels

A thesis submitted to the School of Mathematics of the University of East Anglia in partial fulfilment of the requirements for the degree of Doctor of Philosophy

Neil Peter Deacon

August 2014

Abstract

In this thesis analytical and numerical methods are used to investigate the stability and propagation of waves in various fluid-filled elastic-walled channels. In Chapter 2 a linear temporal stability analysis is performed for various channel wall configurations, the results of which are compared to determine how different physical effects contribute to the stability. In Chapter 3 a linear spatial stability analysis is performed for flow between linear plates, this is a limiting case of the wall configuration in Chapter 2. Roots of the dispersion relation are found and their stability and direction of propagation determined.

Chapters 4 and 5 focus on the propagation of nonlinear waves on liquid sheets between thin infinite elastic plates. Both linear and nonlinear models are used for the elastic plates. One-dimensional time-dependent equations are derived based on a long-wavelength approximation. Symmetric and antisymmetric travelling waves are found with the linear plate model and symmetric travelling waves are found for the fully-nonlinear case. Numerical simulations are employed to study the evolution in time of initial disturbances and to compare the different models used. Nonlinear effects are found to decrease the travelling wave speed compared with linear models. At sufficiently large amplitude of initial disturbances, higher order temporal oscillations induced by nonlinearity can lead to thickness of the liquid sheet approaching zero. Finally, in Chapter 6, an extension of the model from Chapters 4 and 5 is considered, the elasticities of the two channel walls are allowed to differ. The effect of this difference is determined through a mix of techniques and the limiting case of one wall having no elasticity is discussed.

Acknowledgements

I would like to thank my supervisors, Dr. Emilian Părău, Dr. Richard Purvis and Dr. Robert Whittaker, for their endless patience and guidance throughout my time as a post-graduate.

I wish to thank my parents, who encouraged my interest in Mathematics from a young age, without your love and support over the years I would not have made it this far. To my friends, especially Mark and Chris, thank you for being a way to escape from work when necessary.

Finally, my heartfelt thanks to Amy. Through all of my studies you have loved me, believed in me, supported me and helped me more than you know.

Contents

List of tables

List of figures

CHAPTER ONE

INTRODUCTION

1.1 Background

Interactions between fluids and elastic boundaries occur frequently in both natural and mechanical environments (Korobkin *et al.*, 2011). Such problems are mathematically challenging, due to the coupling between the moving fluid and the deformable boundary. In this thesis, we examine several variations of these coupled systems involving the flow of inviscid fluid in a two-dimensional channel between two thin elastic plates. This type of system can also be used as a simplified model of flow in an elastic-walled pipe, with reduced dimensionality.

These flows arise in the pulmonary and arterial networks (Grotberg, 1994; Walsh, 1995), where the airways and blood vessels can be modelled as an elastic channel or pipe. In addition to bending effect and wall tension, the models often include a system of springs on the outside of the interface to capture the effects of the surrounding tissue. Such a system also arises in flat-plate-type fuel assemblies used in the cooling systems of nuclear reactors (Kim & Davis, 1995). These types of nuclear reactors consist of stacks of flat plates of fuel, between which coolant flows to ensure the temperature does not reach a dangerous level. More recently, the use of instabilities in these systems as an energy-harvesting device (Tang & Païdoussis, 2009) has been proposed. In this, a plate

Figure 1.1: An illustration of the two possible modes, antisymmetric (left) and symmetric (right). The dashed lines represent the centreline.

subjected to flow either side produces an instability for large enough flow velocity, the movement of the plate is then used to disrupt the magnetic field of special plates either side of the channel generating an electric current.

In all the systems we will consider both in the literature review and the main body of the thesis, two distinct modes of fluid-boundary interface shape are possible, the first is for the two interfaces to be perfectly in phase with each other, this is referred to as the antisymmetric mode, the second is for the two interfaces to be in antiphase, this is known as the symmetric mode. A sketch of the two modes can be seen in Figure 1.1.

A large proportion of the study of fluid flow between elastic plates (or in a pipe) is focused on stability analysis, which can be split into two distinct varieties: temporal stability analysis and spatial stability analysis. Temporal stability analysis considers the behaviour in time of a spatial perturbation, usually in the form of an initial condition, while spatial stability analysis considers the behaviour in space of a periodic in time perturbation at a fixed point. Instabilities in a stability analysis with a spatial component can be classified as either convective or absolute. Convective instabilities are characterised by the long time response at the driver tending to zero so that the perturbation is swept away from the source. Absolute instabilities result in the long time response at the driver tending to infinity as the perturbation grows quicker than it moves away from the source leading to the whole domain being affected.

In this introduction we will present a review of relevant literature, looking first at coupled fluid-elastic systems that are most closely related to the systems we plan to study in this thesis. These consist of both pipes (Walsh, 1995) and channels (de Langre, 2002). While we consider systems in this thesis that involve fluid flowing between elastic walls, it has been shown that the equations for axial flow on the outside of an elastic channel

are the same (Triantafyllou, 1992). The only difference between the two types of flow is in the definition of the added mass term of the equations which refers to the mass of the structure for the beam in axial flow, but is the mass of the fluid conveyed by the pipe.

Walsh (1995) used shell theory to examine pipes with three different kinds of inviscid plug flow: internal, annular and planar. The internal flow was axisymmetric in a fully flexible pipe; the annular flow was axisymmetric, between a flexible inner shell and a rigid outer one; and the planar flow considered flow between a rigid plane and a flexible one. In all cases the flexible boundary had a spring term to represent the stiffness of surrounding tissue (Grotberg, 1994; Gaver *et al.*, 1996; Heil & Hazel, 2011). If both axial and normal displacements of the wall are considered in a coupled mode then unstable long-wave flutter can occur, but in the absence of the coupling the pipe will be stable. This long-wave instability was more pronounced at higher wall-to-fluid mass ratios as this increased the effect of the coupling term.

The stability of a fluid-filled pipe on an elastic foundation has been considered by de Langre & Ouvrard (1999), but only for the antisymmetric mode. The pipe wall is modelled as a linear elastic plate, with axial tension and a spring foundation, while the fluid is modelled as internal plug flow. They showed that the case when the bending stiffness dominates over the tension and spring foundation can be considered as a long-wavelength approximation of the more general dispersion relation derived by Walsh (1995). In this case there is a critical mass ratio parameter $\beta_c = 8/9$ below which the instabilities are absolute, while above the instabilities are convective. The ratio of flexural rigidity and tension is found to be important with absolute instability more likely when flexural rigidity dominates but convective instability is more prevalent when tension dominates.

The analysis of de Langre & Ouvrard (1999) was extended to the symmetric mode for the same system in the absence of the elastic foundation by de Langre (2000). The point of transition between convective and absolute instability was found numerically for systems dominated by flexural rigidity or axial tension, and in the limit of a thin film (channel thickness tending to zero), the transition was found in closed form.

These works were combined by de Langre (2002) in a paper determining the transition velocity at which flows become absolutely unstable for a variety of geometries in terms of a second physical parameter that depended on the problem. For channel flow, both antisymmetric and symmetric modes were considered, with the second physical parameter the nondimensional channel width, for flows both between two plates and two membranes. The plates were modelled with bending stiffness and wall inertia, the membranes were modelled with tension and wall inertia while the fluid was modelled with plug flow. Flows over a single flat plate or membrane were also considered, with the large channel width limit being shown to reduce to the flat plate model. A key feature of de Langre & Ouvrard (1999), de Langre (2000) and de Langre (2002) is that they do not seek the individual roots for the dispersion relation, but admit that this is still necessary to classify which side of the transition velocity absolute instability occurs.

The propagation of two-dimensional hydroelastic waves on sheets of fluid bounded by nonlinear elastic plates was studied by Blyth *et al.* (2011). The walls of the channel were modelled as a nonlinear plate in the absence of wall inertia, while the fluid motion is governed by Laplace's equation. Sample solutions were found for a static fluid, which decouples the two plates, with the insistence of one wave in a unit length. Nonlinear travelling waves in the presence of moving fluid were found for both the antisymmetric and symmetric modes, and bifurcation branches were found for the symmetric mode.

In the large-channel-width limit, the behaviour of the two channel walls decouples and uniform flow over a single elastic plate is recovered. This is also a widely studied problem, Brazier-Smith & Scott (1984) performed a stability analysis of the dispersion relation, working numerically to determine the critical fluid velocities and frequencies that divided different regions of behaviour. The same problem was approached analytically by Crighton & Oswell (1991) who used asymptotic analysis to determine the same thresholds in closed form, while the nonlinear stability was considered by Peake (2001).

All the papers discussed above consider infinite length domains, as will be studied in this thesis. While not of direct relevance it is worthwhile to note that for flow between two finite length plates, we still obtain both a symmetric and an antisymmetric mode (e.g.

Michelin & Llewellyn Smith, 2009; Schouveiler & Eloy, 2009).

In the absence of elastic walls, we recover the classical problem of plane liquid sheets (or liquid jets), in which we can see similar behaviour to the systems we are interested in. The reduction of order in the boundary conditions results in systems that are slightly easier to work with but which result in suprisingly similar behaviour to elastic channels and pipes. The primary difference between the fluid–elastic and the fluid systems is that in the latter case, pinch off can occur and result in droplet formation (Eggers & Dupont, 1994; Mehring & Sirignano, 1999), for which there is no direct equivalent in the fluid-elastic systems.

A temporal stability analysis of the antisymmetric mode of a plane liquid sheet was performed by Squire (1953), stating that a temporal stability analysis of the symmetric mode revealed it to be unstable but less so than the antisymmetric mode. Li (1993) demonstrated that Squire's assertion that the antisymmetric mode is more unstable than the symmetric mode only held for Weber numbers above a critical value dependent on the ratio of the fluid and gas densities. For very large Weber numbers, the maximum growth rates of the two modes become comparable and are thus equally important.

Keller *et al.* (1973) performed a spatial stability analysis of a semi-infinite jet. The dispersion relation was derived and then solved asymptotically under the assumptions of both high and low jet velocity. For high jet velocity, two unstable modes were found. However one was found to be of extremely long wavelength and so was discarded as it is unlikely to be observed in short jets as used experimentally. The second unstable mode was shown to have the same growth rate as the temporal growth rate in Squire (1953) explaining the good agreement between prior results and experiments. The dispersion relation was also solved numerically for representative values of the frequency and jet velocity and contours of the unstable mode were then plotted. From the contours the growth rate, frequency and wavelength of disturbances can be calculated for different parameter values.

As well as extending the work of Squire (1953), Li (1993) also performed a spatial stability analysis of the semi-infinite plane liquid sheet, under the assumption of a high

velocity in the liquid, so as to ensure only convective instabilities are present, and for small gas to liquid density ratios. Roots of the dispersion relation were sought by calculating asymptotic solutions and then classified according to the prevalent technique in the analysis of spatial stability roots (see Briggs, 1964; Bers, 1983, and Chapter 3). For both the antisymmetric and symmetric mode one unstable root was found that travelled downstream (as the semi-infinite nature of the sheet prohibited upstream travelling waves). A direct correlation between the density ratio and the spatial growth rate was found, which, when the ratio was zero resulted in a stable sheet. For inviscid flows, the asymptotic solutions were shown to be indistinguishable from the numerical solution to the dispersion relation.

Wave propagation in nonlinear planar liquid sheets in a vacuum leading to distortion and break up was studied in Mehring & Sirignano (1999). A nonlinear system of equations was derived in terms of the flow velocities and the sheet thickness and centreline. Travelling wave solutions were found for a linear system based on the undisturbed axial velocity and sheet thickness, with the other two parameters being zero in the undisturbed state. These solutions were then used as initial conditions to investigate the temporal evolution of travelling waves on the sheet, with the effect of the nonlinear curvature being a particular focus. They found a decrease in velocity of the waves in the nonlinear system in comparison to the linear travelling waves and also at larger amplitude disturbances the introduction of a higher order temporal oscillation in the symmetric mode. Nonlinear effects were found to enable sheet disintegration despite the inherent stability.

1.2 Thesis Outline

The thesis can be considered as having two distinct parts, in the first we consider the hydroelastic stability of linear systems, while in the second we consider wave propagation in stable nonlinear systems.

We begin in Chapter 2 by considering the linear temporal stability of a uniform plug flow through a flexible channel. For the dynamic condition specifying the behaviour of

the fluid–wall interface we consider the impact of a variety of physical effects including bending stiffness, inertia, axial tension and springs attached to the wall. We show the existence of two modes, an antisymmetric mode and a symmetric mode. For various permutations of the parameters, we determine range of wavenumbers for which the system is either stable or unstable, when appropriate we derive conditions that guarantee stability of the systems and when they are unstable we determine both the most unstable wavenumber and the corresponding maximum growth rate.

In Chapter 3 we perform another linear stability analysis on the linear plate model from Chapter 2 but this time from a spatial perspective. This has an increased difficulty in comparison to the temporal analysis so the concept of the Briggs–Bers technique is introduced to help determine the stability of roots to the dispersion relation. Beginning by neglecting as many terms as possible from the dispersion relation, the positions of the roots are tracked as physical effects are reintroduced to the system increasing the complexity. At the same time, the propagation direction and stability of the roots is analysed to give a picture of the behaviour of the system. Results are then compared to de Langre (2002).

In Chapter 4, our focus shifts from determining the stability of linear systems to wave propagation in nonlinear systems where stability is assumed by extending the work of Mehring & Sirignano (1999) for a fluid sheet. The dynamic condition at the fluid-wall interface is governed by the same nonlinear plate equation used in Blyth *et al.* (2011), and we follow their lead in considering the wall to be inertia free. The governing equations are derived according to the method set out by Mehring & Sirignano (1999) to give a nonlinear-fluid–nonlinear-plate model. We also consider two simplified models derived from this: a nonlinear-fluid–linear-plate and a linear-fluid–linear-plate model. Travelling wave solutions are sought to all three models, analytically where possible but also through the use of numerical computations. Asymptotic analysis is also used to help validate the numerical solution for the nonlinear-fluid–linear-plate model as the channel thickness tends to zero.

In Chapter 5, we build on the work in Chapter 4, by deriving a numerical scheme to

determine the temporal evolution of travelling wave solutions to the linear-fluid–linear-plate model in the two nonlinear models. The scheme is validated checking the error when the scheme is given travelling wave solutions to the two nonlinear models as initial conditions. Results are then found for both the antisymmetric and symmetric modes with a focus on the effects of the nonlinear terms in both the fluid and the curvature upon the profiles of the channel walls. We observe that despite the absence of a destabilising physical effect it is still possible for the thickness of the channel to approach zero over time.

As a natural extension to the model used in Chapters 4 and 5, in Chapter 6 we increase the complexity of the system by allowing the elasticities of the two channel walls to differ. The requisite changes are made to both the model and the numerical scheme to include a nondimensional ratio of bending stiffnesses, D. Travelling-wave solutions are found in the linear-fluid–linear-plate model. These are then used as initial conditions to determine their propagation through time in the nonlinear-fluid–nonlinear-plate model as we seek to determine the effect of the ratio. We discuss the equivalence of the $D = 1/n$ and $D = n$ systems for $n \in \mathbb{R}_+$ and the breakdown of this equivalence at $D = 0$ and as $D \to \infty$.

This thesis seeks to introduce new results in the study of flows between elastic walled channels, predominantly by extending previous studies for liquid sheets with a free surface. In our temporal stability analysis we show that elastic walled channels can exhibit previously unconsidered instabilities, while our spatial analysis highlights which roots of the dispersion relation correspond to different types of propagating waves. For channels with nonlinear curvature included in the walls we will demonstrate the existence of a new type of travelling wave, as well as show that nonlinear effects can result in channel closure in a stable channel. Finally, the system we consider in Chapter 6 has not been considered previously, so we present some preliminary results as a starting point for future research.

CHAPTER TWO

TEMPORAL STABILITY ANALYSIS OF FLOW IN AN ELASTIC CHANNEL

2.1 Introduction

In this chapter we will examine the temporal stability of flow in an infinitely long elastic channel subjected to a spatial perturbation as an initial condition. A set of linear equations will be derived that couples the fluid flow with the response of the elastic walls to describe the behaviour of the physical system. A linear stability analysis will be performed to derive the dispersion relation by considering the response to small perturbations around an undisturbed state consisting of steady solutions to the system. The dispersion relation will be examined in various limiting cases to determine the effect the various physical parameters have on the stability of the system, before combining this understanding to examine the full dispersion relation.

The coupling in the system will consist of a balance in the dynamic boundary condition between the pressure and the physical effects in the wall. These physical effects will consist of a bending stiffness, inertia, axial tension and spring response which are commonly found in the literature (e.g. Walsh, 1995; de Langre, 2002). The bending stiffness and inertia combine to give the terms found in a linear plate equation, a commonly

used model for channel walls. The addition of axial tension and spring response are motivated by a biological application of systems of this type, specifically flow in blood vessels (Walsh, 1995) and in airways (e.g. Heil & Hazel, 2011), in which the spring response can be considered the effect of surrounding tissue on the channel. The channel walls considered in this chapter are restricted to move only in the transverse direction of the channel, an assumption justified in the case of blood vessels but not in airways (Walsh, 1995).

2.2 Problem Formulation

We consider an infinite channel containing an incompressible, inviscid Newtonian fluid of density ρ. The channel is centered on the $\tilde{x}$-axis and bounded at $\tilde{y} = \tilde{h}_{\pm}(\tilde{x}, \tilde{t})$ by elastic walls. The fluid has a velocity $\tilde{\mathbf{u}} = (\tilde{u}(\tilde{x}, \tilde{y}, \tilde{t}), \tilde{v}(\tilde{x}, \tilde{y}, \tilde{t}), 0)$, and pressure $\tilde{p}(\tilde{x}, \tilde{y}, \tilde{t})$ (see Figure 2.1). The governing equations for the fluid are Euler's equations (e.g. Acheson, 1990)

$$\frac{\partial \tilde{\mathbf{u}}}{\partial \tilde{t}} + (\tilde{\mathbf{u}} \cdot \tilde{\nabla})\tilde{\mathbf{u}} = -\frac{1}{\rho}\tilde{\nabla}\tilde{p}, \tag{2.2.1}$$

$$\tilde{\nabla} \cdot \tilde{\mathbf{u}} = 0, \tag{2.2.2}$$

in the range $-\infty < \tilde{x} < \infty$, $\tilde{h}_- < \tilde{y} < \tilde{h}_+$. On $\tilde{y} = \tilde{h}_{\pm}(\tilde{x}, \tilde{t})$ we have the kinematic condition

$$\frac{\mathrm{D}}{\mathrm{D}\tilde{t}}\left(\tilde{h}_{\pm} - \tilde{y}\right) = 0, \tag{2.2.3}$$

where $\mathrm{D}/\mathrm{D}\tilde{t}$ is the material derivative. We can write (2.2.3) as

$$\tilde{v} = \tilde{u}\frac{\partial \tilde{h}_{\pm}}{\partial \tilde{x}} + \frac{\partial \tilde{h}_{\pm}}{\partial \tilde{t}}. \tag{2.2.4}$$

On $\tilde{y} = \tilde{h}_{\pm}(\tilde{x}, \tilde{t})$, we also use the dynamic condition

$$\tilde{p} - p_a = \pm D\frac{\partial^4 \tilde{h}_{\pm}}{\partial \tilde{x}^4} \pm \rho_b h_b \frac{\partial^2 \tilde{h}_{\pm}}{\partial \tilde{t}^2} \mp T\frac{\partial^2 \tilde{h}_{\pm}}{\partial \tilde{x}^2} \pm m\left(\tilde{h}_{\pm} \mp H_0\right). \tag{2.2.5}$$

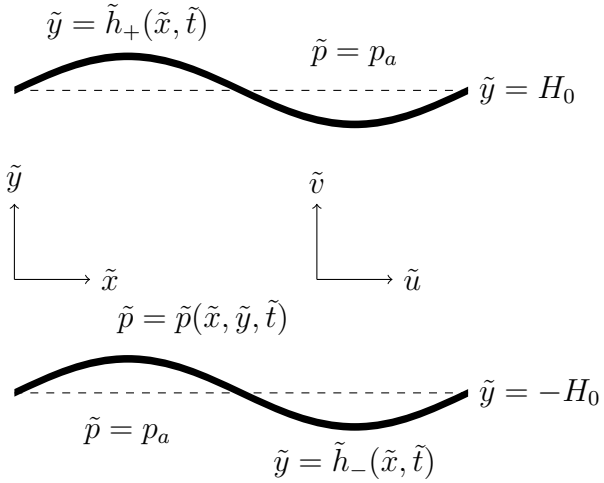

Figure 2.1: Dimensional problem setup.

The first two terms on the right hand side constitute a linear plate model in which D is the bending stiffness, and ρ_b and h_b are, respectively, the density and thickness of the beam. The first of the two terms represents bending stiffness in the beam and the second term represents inertia in the beam. At small amplitudes, such as the initial disturbances that will be applied, this allows us to capture the correct behaviour while keeping the algebra relatively simple. The third term represents a longitudinal or axial tension applied to the plate, with T a surface tension. The fourth term represents a restoring force proportional to the displacement, with m a spring constant per unit area.

Working in a static frame of reference, we have a basic flow, pressure and boundary position that satisfies (2.2.1), (2.2.2), (2.2.4), (2.2.5) and is steady and independent of $\tilde{x}$. This is given by

$$\tilde{\mathbf{u}}^* = (U, 0, 0), \qquad \tilde{p}^* = p_a, \qquad \tilde{h}^*_\pm = \pm H_0, \tag{2.2.6}$$

where stars denote the base state of the system variables. The assumption of the flow being unidirectional with a constant profile is called plug flow. It is a common choice in the literature (e.g. de Langre & Ouvrard, 1999; Peake & Sorokin, 2001; de Langre, 2002) for its simplicity to work with as it does not introduce any boundary layers while maintaining the key features of any results. The effect of alternate base velocity profile was investigated for thin liquid sheets by Rao & Ramamurthi (2009), where it was found that for linear or parabolic profiles with their maximum at the centreline of the liquid

sheet, the effect was to both reduce the maximum growth rate as well as the range of wavenumbers for which instabilities arose. It is thought a similar behaviour will occur in this problem, suggesting that the use of plug flow serves to find an upper bound on both growth rate and wavenumber ranges of instabilities.

Taking the characteristic velocity of the system as U, and the characteristic length as H_0, a characteristic time is then given by H_0/U. We non-dimensionalise the system as follows

$$(\tilde{x},\tilde{y}) = H_0(x,y), \quad \tilde{h}_\pm = H_0 h_\pm, \quad (\tilde{u},\tilde{v}) = U(u,v), \quad \tilde{t} = \frac{H_0}{U}t, \quad \tilde{p} = p_a + Pp, \tag{2.2.7}$$

where P is an unknown scale for pressure which is to be determined. Substituting into (2.2.1) and rearranging we obtain

$$\frac{\partial \mathbf{u}}{\partial t} + (\mathbf{u}\cdot\nabla)\mathbf{u} = \frac{-P}{\rho U^2}\nabla p, \tag{2.2.8}$$

which suggests a suitable pressure scaling is $P = \rho U^2$ as it removes any dimensional parameters from (2.2.8). Rescaling (2.2.2), and (2.2.4) shows they remain invariant, but when we rescale (2.2.5) we obtain

$$p = \pm\alpha\frac{\partial^4 h_\pm}{\partial x^4} \pm \beta\frac{\partial^2 h_\pm}{\partial t^2} \mp \tau\frac{\partial^2 h_\pm}{\partial x^2} \pm \gamma\left(h_\pm \mp 1\right), \tag{2.2.9}$$

where

$$\alpha = \frac{D}{\rho U^2 H_0^3}, \quad \beta = \frac{\rho_b h_b}{\rho H_0}, \quad \tau = \frac{T}{\rho U^2 H_0}, \quad \gamma = \frac{mH_0}{\rho U^2} \tag{2.2.10}$$

are all dimensionless parameters that are ratios of a physical effect to the inertial forces in the fluid. Specifically, α is the ratio of bending forces, β is the ratio of mass per unit length of the plate, τ is the ratio of tension applied to the plate and γ is the ratio of spring

tension per unit length. The governing equations are now

$$\frac{\partial \mathbf{u}}{\partial t} + (\mathbf{u} \cdot \nabla)\mathbf{u} = -\nabla p, \tag{2.2.11}$$

$$\nabla \cdot \mathbf{u} = 0, \tag{2.2.12}$$

in the range $-\infty < x < \infty, h_-(x,y,t) < y < h_+(x,y,t)$. This is subject to the kinematic boundary condition

$$v = u\frac{\partial h_\pm}{\partial x} + \frac{\partial h_\pm}{\partial t}, \tag{2.2.13}$$

and the dynamic boundary condition given by (2.2.9) on $y = h_\pm$. The basic flow (2.2.6) becomes

$$\mathbf{u}^* = (1,0,0), \qquad p^* = 0, \qquad h_\pm^* = \pm 1. \tag{2.2.14}$$

2.3 Linear Stability Analysis

We disturb the basic flow and the walls with small perturbations, $\mathbf{u}'$, p' and $\eta'_\pm$

$$\mathbf{u} = \mathbf{u}^* + \mathbf{u}' = (1 + u', v'), \tag{2.3.1}$$

$$p = p^* + p' = p', \tag{2.3.2}$$

$$y = h_\pm^* + h'_\pm = \pm 1 + \eta'_\pm. \tag{2.3.3}$$

We linearise (2.2.11) – (2.2.13) and (2.2.9) by neglecting terms quadratic in perturbed quantities, to obtain

$$\frac{\partial \mathbf{u}'}{\partial t} + (\mathbf{u}^* \cdot \nabla)\,\mathbf{u}' = -\nabla p', \tag{2.3.4}$$

$$\nabla \cdot \mathbf{u}' = 0, \tag{2.3.5}$$

with boundary conditions

$$v' = \frac{\partial \eta'_{\pm}}{\partial x} + \frac{\partial \eta'_{\pm}}{\partial t} \qquad \text{on } y = \pm 1, \tag{2.3.6}$$

$$p' = \pm \left(\alpha \frac{\partial^4 \eta'_{\pm}}{\partial x^4} + \beta \frac{\partial^2 \eta'_{\pm}}{\partial t^2} - \tau \frac{\partial^2 \eta'_{\pm}}{\partial x^2} + \gamma \eta'_{\pm} \right) \qquad \text{on } y = \pm 1. \tag{2.3.7}$$

In order to analyse the stability we restrict ourselves to perturbations of the form

$$\mathbf{u}' = e^{st} e^{ikx} \hat{\mathbf{u}}(y), \tag{2.3.8}$$

$$p' = e^{st} e^{ikx} \hat{p}(y), \tag{2.3.9}$$

$$\eta'_{\pm} = e^{st} e^{ikx} \hat{\eta}_{\pm}, \tag{2.3.10}$$

where $k \in \mathbb{R}$ and $k > 0$ is known, $s \in \mathbb{C}$ is to be found and it is understood we are taking the real part in (2.3.8)–(2.3.10). Since this is a linear problem, any general perturbation can be considered as a superposition of the above equations. Looking at the form of (2.3.8)–(2.3.10) we can see that the perturbations consist of a spatial oscillatory term given by the e^{ikx}, but an unknown contribution arises from s as it is to be determined. Since $s \in \mathbb{C}$ we can write $s = s_R + is_I$ and the temporal component becomes $e^{s_R t} \left(\cos\left(s_I t\right) + i \sin\left(s_I t\right) \right)$. That is to say, the imaginary part of s provides a temporal oscillation while the real part tells us whether or not the perturbation grows or decays in time. If $\mathrm{Re}\left(s\right) > 0$, then as t increases, $e^{s_R t}$ will grow and the perturbation will give rise to instabilities, while if $\mathrm{Re}\left(s\right) < 0$, then the perturbations will decay and be stable. Finally, if $\mathrm{Re}\left(s\right) = 0$ the perturbations will persist, neither growing nor decaying. This is referred to as being neutrally stable.

We now substitute (2.3.8)–(2.3.10) into the governing equations and boundary conditions (2.3.4)–(2.3.7). The momentum equation (2.3.4) can be split up into its x and y components, noting that $\left(\mathbf{u}^* \cdot \nabla\right) \equiv \frac{\partial}{\partial x}$,

$$(s + ik)\hat{u} = -ik\hat{p}, \tag{2.3.11}$$

$$(s + ik)\hat{v} = -\frac{\partial \hat{p}}{\partial y}. \tag{2.3.12}$$

The continuity equation (2.3.5) gives us

$$ik\hat{u} + \frac{\partial \hat{v}}{\partial y} = 0. \tag{2.3.13}$$

The kinematic condition (2.3.6) and the dynamic condition (2.3.7) can each be split up into two equations. On $y = 1$ they are

$$\hat{v} = (s + ik)\hat{\eta}_+, \tag{2.3.14}$$

$$\hat{p} = \left(\alpha k^4 + \beta s^2 + \tau k^2 + \gamma\right)\hat{\eta}_+, \tag{2.3.15}$$

respectively, while on $y = -1$ we have

$$\hat{v} = (s + ik)\hat{\eta}_-, \tag{2.3.16}$$

$$\hat{p} = -\left(\alpha k^4 + \beta s^2 + \tau k^2 + \gamma\right)\hat{\eta}_-. \tag{2.3.17}$$

We substitute (2.3.11) and (2.3.12) into (2.3.13) and rearrange to get

$$\frac{\partial^2 \hat{p}}{\partial y^2} - k^2\hat{p} = 0, \tag{2.3.18}$$

which has solutions of the form

$$\hat{p} = A\cosh(ky) + B\sinh(ky), \tag{2.3.19}$$

where A and B are arbitrary constants. Substitution of $\hat{p}$ into (2.3.11) and (2.3.12) finds $\hat{u}$ and $\hat{v}$ respectively

$$\hat{u} = -\frac{ik}{(s + ik)}\left(A\cosh(ky) + B\sinh(ky)\right), \tag{2.3.20}$$

$$\hat{v} = -\frac{k}{(s + ik)}\left(A\sinh(ky) + B\cosh(ky)\right). \tag{2.3.21}$$

which can in turn be substituted into the kinematic boundary condition (2.3.14) and

(2.3.16) to generate $\hat{\eta}_+$ and $\hat{\eta}_-$

$$\hat{\eta}_+ = -\frac{k}{(s+ik)^2}\left(A\sinh(k) + B\cosh(k)\right), \tag{2.3.22}$$

$$\hat{\eta}_- = \frac{k}{(s+ik)^2}\left(A\sinh(k) - B\cosh(k)\right). \tag{2.3.23}$$

Finally, we need to satisfy the dynamic boundary conditions (2.3.15) and (2.3.17). Substitution of $\hat{p}$ and $\hat{\eta}_+$ into (2.3.15) and $\hat{p}$ and $\hat{\eta}_-$ into (2.3.17) respectively yield, after some rearrangement,

$$\left(\alpha k^4 + \beta s^2 + \tau k^2 + \gamma\right)\left(-\frac{k}{(s+ik)^2}\right) = \frac{A\cosh(k) + B\sinh(k)}{A\sinh(k) + B\cosh(k)}, \tag{2.3.24}$$

$$\left(\alpha k^4 + \beta s^2 + \tau k^2 + \gamma\right)\left(-\frac{k}{(s+ik)^2}\right) = \frac{A\cosh(k) - B\sinh(k)}{A\sinh(k) - B\cosh(k)}. \tag{2.3.25}$$

Clearly the left hand side of both (2.3.24) and (2.3.25) are identical and so we can write

$$\frac{A\cosh(k) + B\sinh(k)}{A\sinh(k) + B\cosh(k)} = \frac{A\cosh(k) - B\sinh(k)}{A\sinh(k) - B\cosh(k)}, \tag{2.3.26}$$

which after multiplying up, rearranging and making use of identities gives us

$$AB = 0, \tag{2.3.27}$$

so we must have either $A = 0$ or $B = 0$. These values of A and B correspond to two distinct modes, symmetric and antisymmetric. The symmetric mode is characterised by the upper and lower interfaces being perfectly out of phase, $\eta_+ = -\eta_-$, while the antisymmetric mode is characterised by the interfaces being in phase, $\eta_+ = \eta_-$. This is illustrated in Figure 1.1. We consider these modes separately.

2.3.1 Antisymmetric Mode

If we set $A = 0$ as a result of (2.3.27), then (2.3.19)–(2.3.23) become

$$\hat{p} = B\sinh(ky), \tag{2.3.28}$$

$$\hat{u} = -\frac{ik}{s+ik}B\sinh(ky), \tag{2.3.29}$$

$$\hat{v} = -\frac{k}{s+ik}B\cosh(ky), \tag{2.3.30}$$

$$\hat{\eta}_+ = -\frac{k}{(s+ik)^2}B\cosh(k), \tag{2.3.31}$$

$$\hat{\eta}_- = -\frac{k}{(s+ik)^2}B\cosh(k). \tag{2.3.32}$$

It is clear that $\hat{\eta}_+ = \hat{\eta}_-$ and so the upper and lower interfaces are in phase, and therefore $A = 0$ generates the antisymmetric mode. To seek a stability criterion we set $A = 0$ in (2.3.24), which is quadratic in s. Completing the square then gives a dispersion relation between the complex growth rate, s, and the wavenumber, k,

$$\left(s + \frac{ik}{1+\beta k\coth(k)}\right)^2 = f_a(k;\alpha,\beta,\gamma,\tau), \tag{2.3.33}$$

where

$$f_a(k;\alpha,\beta,\gamma,\tau) = \frac{(\beta k^3 - \alpha k^5 - \tau k^3 - \gamma k)\tanh(k) - (\alpha\beta k^6 + \beta\tau k^4 + \beta\gamma k^2)}{(\beta k + \tanh(k))^2}. \tag{2.3.34}$$

Rearranging leads to

$$s = -\frac{ik}{1+\beta k\coth(k)} \pm \sqrt{f_a(k;\alpha,\beta,\gamma,\tau)}. \tag{2.3.35}$$

In order for perturbations to be neutrally stable, $\sqrt{f_a}$ must be purely imaginary else s will have a root with $\mathrm{Re}\,(s) > 0$ leading to instabilities. If $\sqrt{f_a}$ is imaginary then $\mathrm{Re}\,(s) = 0$ so we have neutrally stable perturbations. Our condition for stability is thus, $f_a \leq 0$, or

from (2.3.35),

$$\frac{(\beta k^3 - \alpha k^5 - \tau k^3 - \gamma k)\tanh(k) - (\alpha\beta k^6 + \tau\beta k^4 + \beta\gamma k^2)}{(\beta k + \tanh(k))^2} \leq 0. \tag{2.3.36}$$

This inequality has not been considered before. We will analyse (2.3.36) after deriving the equivalent stability condition for the symmetric mode.

2.3.2 Symmetric Mode

If we set $B = 0$ in (2.3.19)–(2.3.23) then we find

$$\hat{p} = A\cosh(ky), \tag{2.3.37}$$

$$\hat{u} = -\frac{ik}{s+ik}A\cosh(ky), \tag{2.3.38}$$

$$\hat{v} = -\frac{k}{s+ik}A\sinh(ky), \tag{2.3.39}$$

$$\hat{\eta}_+ = -\frac{k}{(s+ik)^2}A\sinh(k), \tag{2.3.40}$$

$$\hat{\eta}_- = \frac{k}{(s+ik)^2}A\sinh(k). \tag{2.3.41}$$

Equations (2.3.40) and (2.3.41) determine that $\hat{\eta}_+ = -\hat{\eta}_-$ and the two interfaces are perfectly out of phase. The same method used to derive the stability criteria for the antisymmetric mode is used again here, so we omit the working. The dispersion relation between s and k for the symmetric mode is

$$\left(s + \frac{ik}{1+\beta k\tanh(k)}\right)^2 = f_s(k;\alpha,\beta,\gamma,\tau), \tag{2.3.42}$$

where

$$f_s(k;\alpha,\beta,\gamma,\tau) = \frac{(\beta k^3 - \alpha k^5 - \tau k^3 - \gamma k)\coth(k) - (\alpha\beta k^6 + \beta\tau k^4 + \beta\gamma k^2)}{(\beta k + \coth(k))^2}. \tag{2.3.43}$$

The requirement of $\mathrm{Re}(s) \leq 0$ for stability still holds, this time for f_s, so rearrangement of (2.3.42) gives a stability criteria of $f_s \leq 0$, or

$$\frac{(\beta k^3 - \alpha k^5 - \tau k^3 - \gamma k)\coth(k) - (\alpha\beta k^6 + \beta\tau k^4 + \beta\gamma k^2)}{(\beta k + \coth(k))^2} \leq 0. \tag{2.3.44}$$

The dispersion relation (2.3.42) and stability condition (2.3.44) will be analysed further in the following sections.

2.4 Stability in limiting cases

The stability conditions (2.3.36) and (2.3.44) both contain one variable, k, and four parameters, α, β, τ, and γ. This makes it difficult to analyse directly and determine whether the system is always stable or if instabilities arise. We will first consider limiting cases where we set various combinations of the parameters to be zero. Our aim being to determine which physical features are crucial to the stability of the flow.

2.4.1 Wall-inertia free system

Firstly we consider the case where the wall inertia is negligible. This corresponds to $\beta \to 0$ and (2.3.36) and (2.3.44) then become

$$-\frac{(\alpha k^5 + \tau k^3 + \gamma k)}{\tanh(k)} \leq 0, \tag{2.4.1}$$

$$-\left(\alpha k^5 + \tau k^3 + \gamma k\right)\tanh(k) \leq 0 \tag{2.4.2}$$

respectively for the antisymmetric and symmetric modes. Since $\alpha, \tau, \gamma, k > 0$ both conditions will be automatically satisfied. So the system is always stable in the absence of wall inertia. The other effects are all stabilising, and hence wall inertia is required to obtain instabilities. Therefore, in all other cases, we have $\beta \neq 0$ so as to allow the possibility of instabilities.

2.4.2 Wall-inertia only system

Alternatively if we consider wall inertia to be dominant, we have $\alpha = \tau = \gamma = 0$, and the stability conditions can be written as

$$\frac{\beta k^3 \tanh(k)}{(\beta k + \tanh(k))^2} \leq 0, \tag{2.4.3}$$

$$\frac{\beta k^3 \coth(k)}{(\beta k + \coth(k))^2} \leq 0 \tag{2.4.4}$$

for the antisymmetric and symmetric modes respectively. For a single interface this model can be considered as a sheet of broken ice. Since $\beta, k > 0$ neither stability condition can be satisfied and so the system is unstable to all perturbations. The growth rate is increasing with the wavenumber. Thus, when we consider the full system with all parameters, it can exhibit both stable and unstable behaviour.

2.4.3 Wall inertia and bending stiffness (Linear plate model)

Including only wall inertia and bending stiffness, neglecting tension and restoring force, we set $\tau = \gamma = 0$, which returns us to the linear plate model as our dynamic boundary condition. Here we see different behaviour in the antisymmetric and symmetric modes and so consider each in turn.

Antisymmetric Mode

If $\tau = \gamma = 0$ then the antisymmetric dispersion relation (2.3.33) becomes

$$\left(s + \frac{ik}{1 + \beta k \coth(k)}\right)^2 = \frac{(\beta k^3 - \alpha k^5)\tanh(k) - \alpha\beta k^6}{(\beta k + \tanh(k))^2}. \tag{2.4.5}$$

For consistency we check the dispersion relation in the limit as $\rho \to 0$, with the other parameters fixed, we have $\alpha \to \infty$, $\beta \to \infty$ and α/β fixed. Then (2.4.5) reduces to $s^2 = -\alpha k^4/\beta$ the dispersion relation for a linear plate in the absence of any fluid (Brazier-Smith & Scott, 1984).

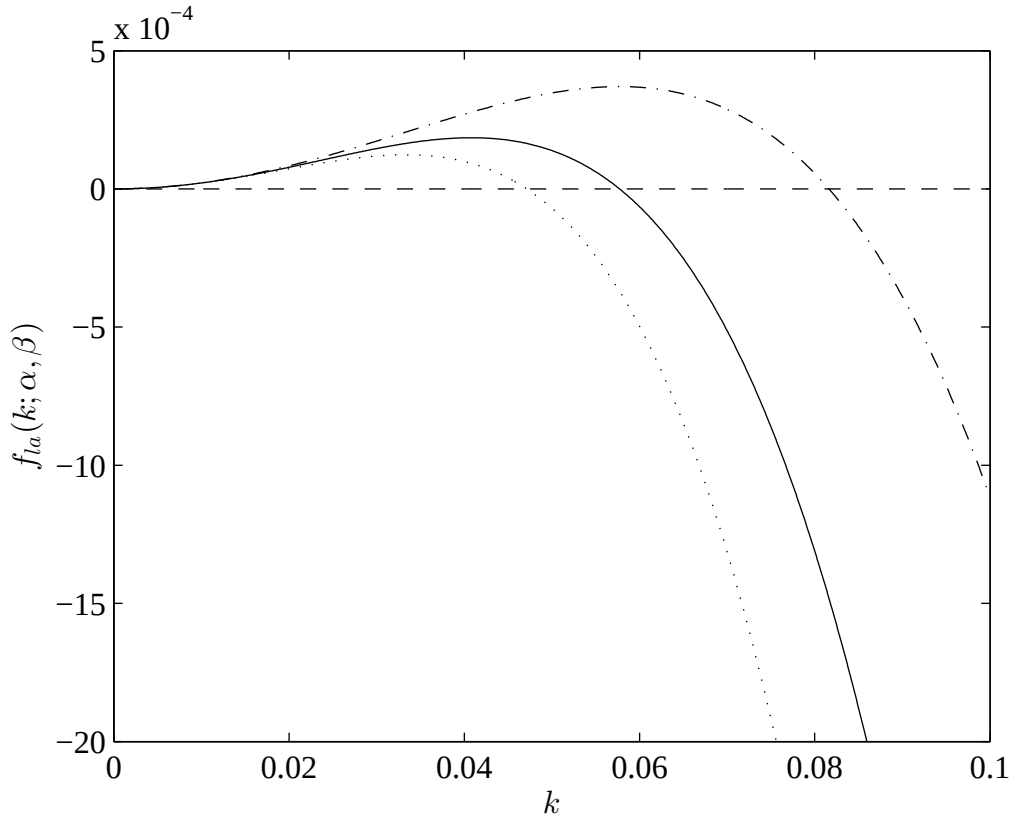

Figure 2.2: A plot of $f_{la}\,(k;\alpha,\beta)$ from (2.4.6) for $\beta = 0.5$ and $\alpha = 50$ (dashed-dot line), $\alpha = 100$ (solid line) and $\alpha = 150$ (dotted line). The dashed line represents the k axis, where the curve lies below it the perturbations are stable while above the dashed line they are unstable.

Our stability condition for the antisymmetric mode of the linear plate model then becomes, from (2.4.5),

$$\frac{(\beta k^3 - \alpha k^5)\tanh(k) - \alpha\beta k^6}{(\beta k + \tanh(k))^2} \leq 0, \tag{2.4.6}$$

and we denote the left hand side as $f_{la}\,(k;\alpha,\beta)$. We illustrate the range of values of k for which the perturbations are unstable for a given pair of values for the parameters α and β by plotting $f_{la}(k;\alpha,\beta)$ in Figure 2.2.

The values used in Figure 2.2 exhibit the generic behaviour of $f_{la}(k;\alpha,\beta)$, more formally, examination of f_{la} shows that $f_{la}(0;\alpha,\beta) = 0$, while in the limit $k \to \infty$, $f_{la} \to -\infty$. Near $k = 0$, $f'_{la}(k;\alpha,\beta) \sim 2\beta k/(\beta+1)^2 > 0$ so there must be a turning point in $k > 0$. Observation of the curves for a selection of values of α and β suggests there will only be one turning point and it is therefore a maximum.

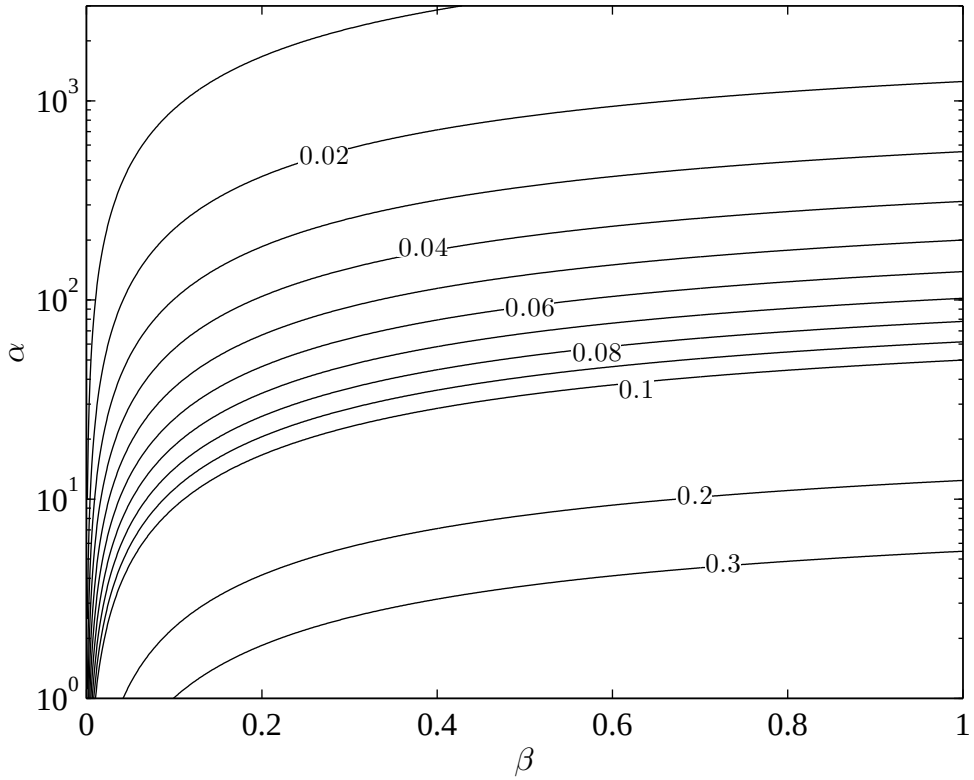

Figure 2.3: Contours of k_{la}^c for which $f_{la}\left(k_{la}^c;\alpha,\beta\right)=0$, for values of the parameters α and β. The contours serve as the stability boundary in α-β space, below the modes are unstable while on or above above the contours the modes are stable.

This translates to a region of instability for small k up to a critical value of k, denoted k_{la}^c, above which the system is stable. Physically, this means the system is unstable to long wavelength perturbations but stable to short wavelength perturbations.

Having confirmed that the antisymmetric mode contains a range of k values for which it is unstable, it is desirable to determine how k_{la}^c varies with α and β. This is done in Figure 2.3, which gives contours of the critical stability value of k_{la}^c where the system transitions from unstable to stable. For all the contours, the unstable region is below and to the right of the boundary, which itself is stable. We can see that the unstable region becomes much larger, very rapidly as β increases from small values suggesting that inertia is the main driver for any instabilities. This agrees well with the prior observation that in the absence of inertia the system is stable for all positive values of α, τ and γ.

If the perturbations are unstable then their growth rate is given by $\mathrm{Re}(s)=\sqrt{f_{la}}$, and the maximum possible growth rate will occur at the maximum of $f_{la}\left(k;\alpha,\beta\right)$. This is the

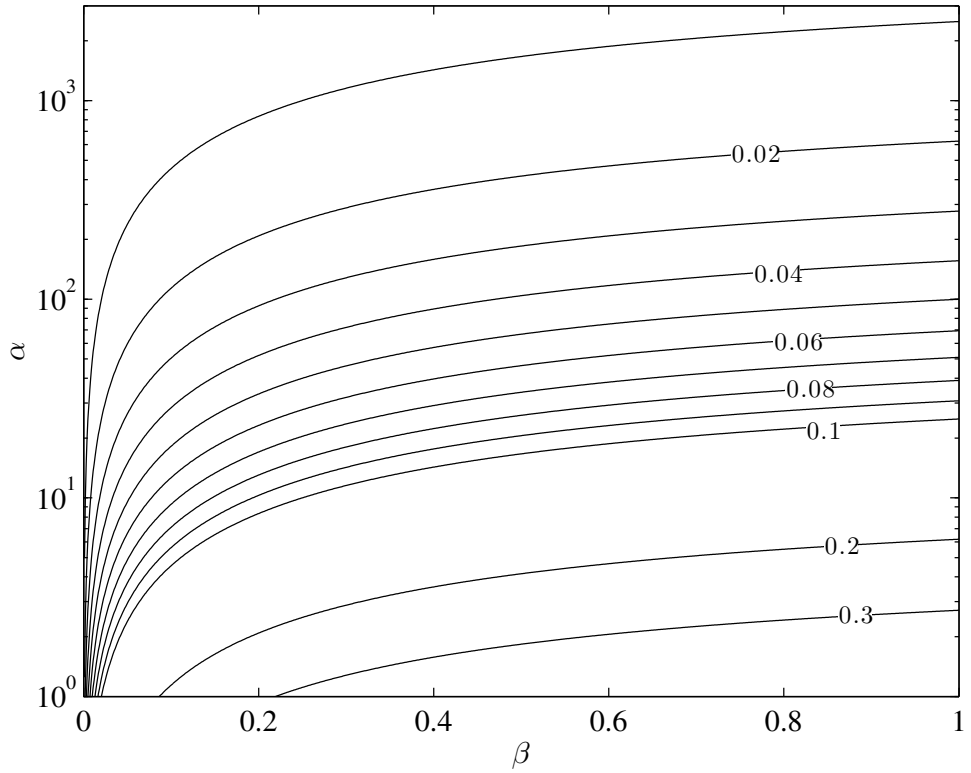

Figure 2.4: A contour plot of solutions to (2.4.7), the contours are constant values of k_{la}^*, the value of k that maximises the growth rate.

point at which

$$\frac{\partial f_{la}}{\partial k} = 0. \tag{2.4.7}$$

Physically we have $\alpha \geq 0$, $\beta \geq 0$ and have assumed $k > 0$. We would normally need to specify a condition on the second derivative of f_{la} with respect to k to classify the point as a maximum but, as previously stated, examination of f_{la} suggests that there is only one turning point in $k \geq 0$ and that it must be a maximum (as illustrated in Figure 2.2). We denote the solutions of (2.4.7) as k_{la}^*. These are illustrated in a contour plot (see Figure 2.4), the contours were found by rearranging (2.4.7) to the form $\alpha = g(k_{la}^*, \beta)$. We can clearly see that the shapes of the contours are qualitatively the same as in figure 2.3 but for a given pair of α and β, the value of k on the contour that passes through the point is lower than in 2.3, this can be explained by k_{la}^* lying between $k = 0$ and $k = k_{la}^c$ (for example see Figure 2.2).

The corresponding maximum growth rates are shown in Figure 2.5, with lines of fixed

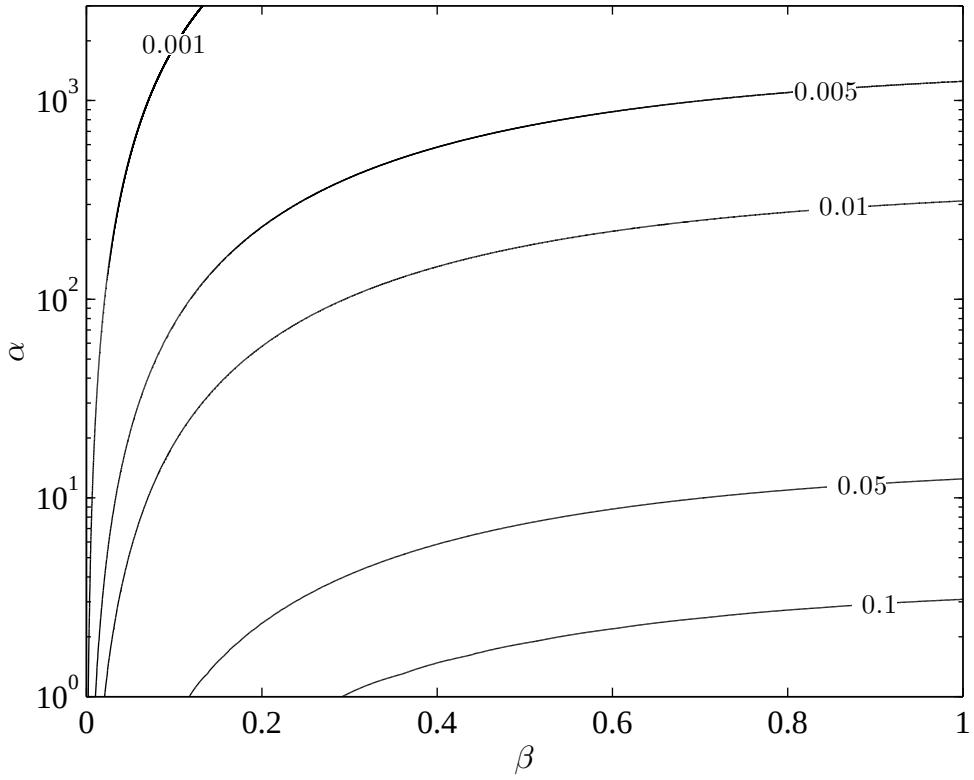

Figure 2.5: Contours of the maximum growth rate, given by $\sqrt{f_{la}\left(k_{la}^{*};\alpha,\beta\right)}$, the contours are constant growth rates.

$\sqrt{f_{la}\left(k_{la}^{*};\alpha,\beta\right)}$. The growth rates are always small for the parameter ranges, suggesting that any instabilities present are slowly growing on the timescale H_0/U. This means the linear analysis, in which we have assumed the size of the disturbances to be small, is valid for a long time before nonlinear effects take hold and a new approach must be chosen.

Symmetric Mode

For the linear plate model the symmetric mode dispersion relation, given by (2.3.42) becomes

$$\left(s+\frac{ik}{1+\beta k\tanh(k)}\right)^2=\frac{\left(\beta k^3-\alpha k^5\right)\coth(k)-\alpha\beta k^6}{\left(\beta k+\coth(k)\right)^2}. \tag{2.4.8}$$

Performing the same check on the dispersion relation as we did for the antisymmetric mode, that is $\rho\to 0$ keeping α/β fixed, we again return the dispersion relation for a linear plate in the absence of fluid (Brazier-Smith & Scott, 1984).

The stability condition can then be written, from (2.4.8),

$$\frac{(\beta k^3 - \alpha k^5)\coth(k) - \alpha\beta k^6}{(\beta k + \coth(k))^2} \leq 0, \tag{2.4.9}$$

where the left hand side is denoted $f_{ls}(k;\alpha,\beta)$. We verify that (2.4.9) is not always satisfied in Figure 2.6 by showing that unstable perturbations exist for the same values of α and β used for the antisymmetric mode in Figure 2.2.

Figure 2.6 illustrates the general behaviour of $f_{ls}(k;\alpha,\beta)$. We have $f_{ls}(0;\alpha,\beta) = 0$, while in the limit $k \to \infty$, $f_{ls} \to -\infty$. Near $k = 0$, the gradient of f_{ls} can be expressed in a series expansion at leading order as $f'_{ls}(k;\alpha,\beta) \sim 4\beta k^3 > 0$, so there will be a turning point in the range $k > 0$ that we are interested in. Observation suggests this will be both the only turning point and it will be a maximum.

Similarly to the antisymmetric mode it is possible to find a single value of k^c_{ls} such that $f_{ls}(k^c_{ls};\alpha,\beta) = 0$. The system is unstable for $0 < k < k^c_{ls}$ and stable for $k^c_{ls} \leq k$. So we again have a system that is unstable to long wavelength perturbations but stable to short wavelength perturbations.

As before we use a contour plot to illustrate how the critical stability point varies with α and β with lines of constant k^c_{ls} (see Figure 2.7). While the general shape of the contours is similar to that of Figure 2.3, the unstable regions, lying below and to the right of the contours, are larger. This suggests that the unstable region for the symmetric mode is greater than for the antisymmetric mode. We also see, as in the antisymmetric case, the instabilities are driven by the inertia parameter.

For small values of k we can approximate solutions to $f_{ls}(k^c_{ls};\alpha,\beta) = 0$. We can see in Figure 2.7 that the critical values k^c_{ls} of k are small. For $k \ll 1$, the equations for the critical stability point, from (2.4.9), can be written

$$\beta - \alpha k^2 - \alpha\beta k^4 = 0. \tag{2.4.10}$$

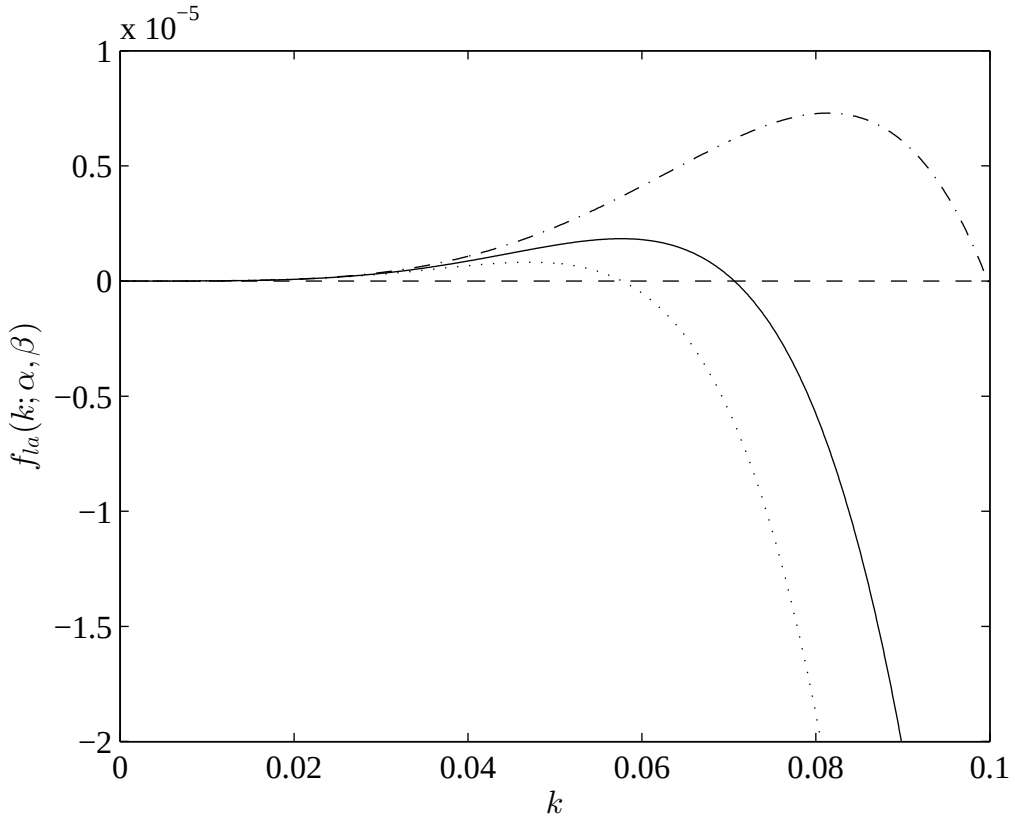

Figure 2.6: A plot of $f_{ls}\,(k;\alpha,\beta)$ for $\beta = 0.5$ and $\alpha = 50$ (dashed-dot line), $\alpha = 100$ (solid line) and $\alpha = 150$ (dotted line). The dashed line represents the k axis, where the curve lies below it the perturbations are stable while above the dashed line they are unstable.

Since $k \ll 1$, the last term on the left hand side can be ignored and we obtain an approximate expression for k_{ls}^c

$$k_{ls}^c \approx \sqrt{\frac{\beta}{\alpha}}. \tag{2.4.11}$$

These approximate solutions are also plotted in Figure 2.7 using dashed-dot lines, it turns out that this approximate solution is excellent for values of k_{ls}^c up to $k_{ls}^c \approx 0.2$, but even above this value the approximation remains reasonable for the values investigated.

The maximum growth rate of an instability in the symmetric mode occurs at a turning point of the function f_{ls} with α, β, $k \geq 0$. That is, at points such that

$$\frac{\partial f_{ls}}{\partial k} = 0, \tag{2.4.12}$$

the solutions to which we denote k_{ls}^*. These are illustrated in Figure 2.8, where again, with the turning point lying between $k = 0$ and $k = k_{ls}^c$, the value of k_{ls}^* of a contour

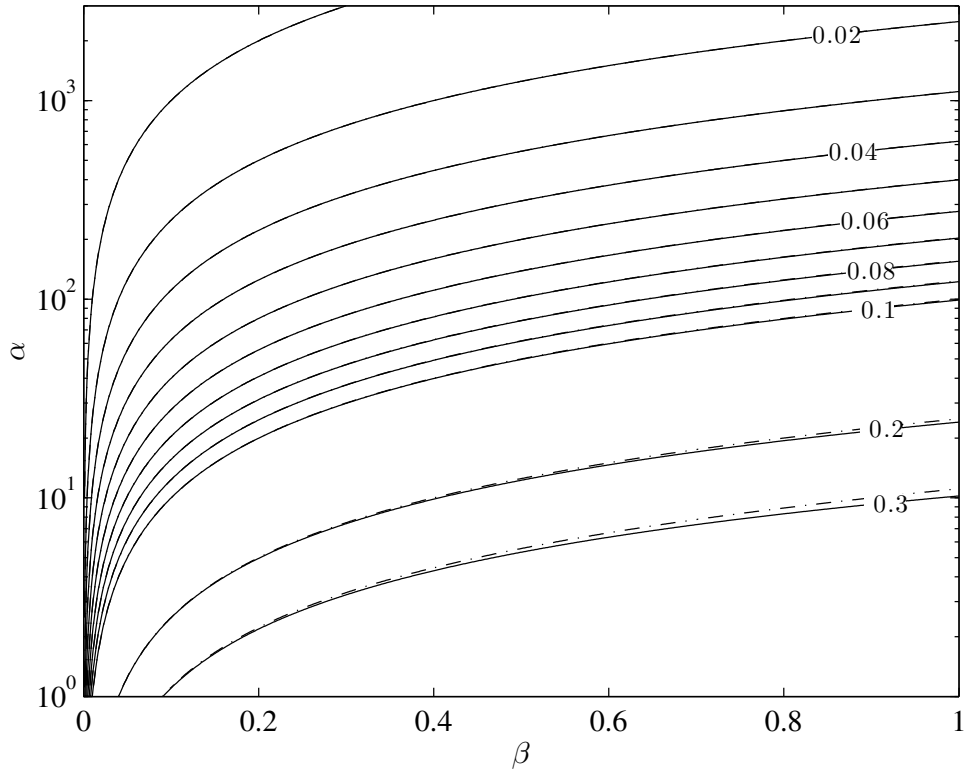

Figure 2.7: Contours of k_{ls}^c for which $f_{ls}\left(k_{ls}^c;\alpha,\beta\right)=0$, for values of the parameters α and β (solid lines). The contours serve as the stability boundary, below the modes are unstable while on or above the contours the modes are stable. Approximations of the contours, given by (2.4.11) are also shown (dashed-dot lines).

passing through a point corresponding to a given α and β is lower than its equivalent in Figure 2.7.

The value of the maximum growth rate is plotted in Figure 2.9, it can clearly be seen that the maximum growth rate of the symmetric mode is orders of magnitude smaller than that of the antisymmetric mode, for given values of α and β. Therefore, we can say that although the symmetric mode is unstable for a larger range of k values than the antisymmetric mode, the growth rates associated with the antisymmetric mode are much greater than the growth rates in the symmetric mode.

2.4.4 Wall inertia and tension (Membrane model)

Neglecting both the bending stiffness and the linear restoring force in the full model derived above in §2.3 changes the limiting case being studied to that of uniform plug flow

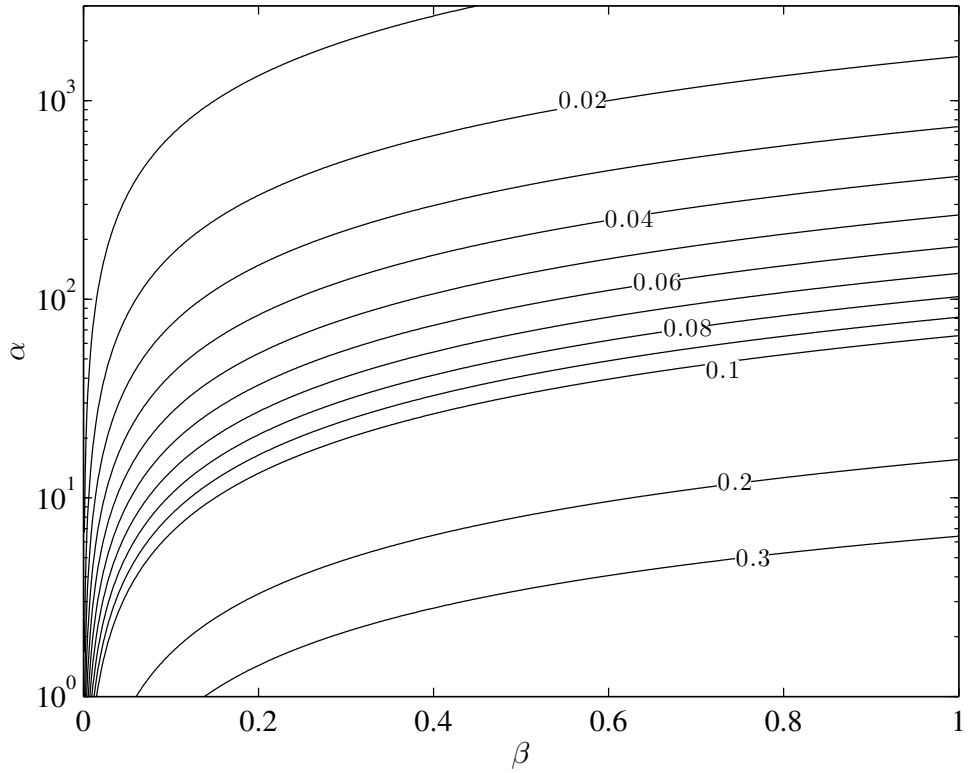

Figure 2.8: A contour plot of solutions to (2.4.12), the contours are constant values of k^*_{ls}, the value of k that maximises the growth rate of instabilities

between two membranes.

Antisymmetric Mode

If we set $\alpha = \gamma = 0$ in (2.3.33), we obtain the dispersion relation for the antisymmetric mode of uniform plug flow between two membranes

$$\left(s + \frac{ik}{1 + \beta k \coth(k)}\right)^2 = -\frac{(\tau - \beta)\, k^3 \tanh(k) + \beta\tau k^4}{(\beta k + \tanh(k))^2}, \tag{2.4.13}$$

which is equivalent to the dispersion relation derived by de Langre (2002). This gives a stability condition of

$$\frac{(\beta - \tau)\, k^3 \tanh(k) - \beta\tau k^4}{(\beta k + \tanh(k))^2} \leq 0. \tag{2.4.14}$$

We denote the left hand side of (2.4.14) as $f_{ma}(k; \beta, \tau)$. Clearly if $\beta \leq \tau$ then the stability condition is automatically satisfied, since $\beta, \tau, k > 0$. This constitutes a sufficient

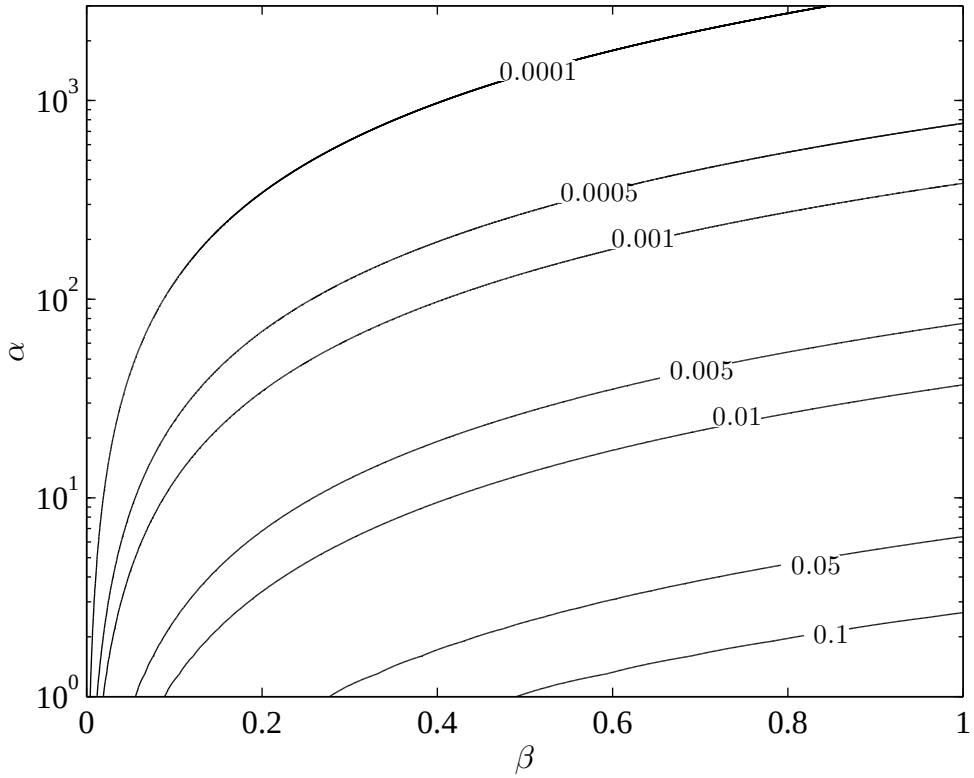

Figure 2.9: Contours of the maximum growth rate, given by $\sqrt{f_{ls}\left(k_{ls}^{*};\alpha,\beta\right)}$, the contours are constant growth rates.

condition on the stability but it turns out this can be refined further.

We rearrange the stability condition into the form

$$\frac{\beta}{1+\beta k\coth(k)} \leq \tau. \tag{2.4.15}$$

The change from the region where there is potential instability to guaranteed stability therefore occurs at

$$\frac{\beta}{1+\beta k\coth(k)} = \tau. \tag{2.4.16}$$

At $k = 0$, we have $\tau = \beta/(1+\beta)$, and the left hand side of (2.4.16), for a fixed β, is a decreasing function for $k > 0$. Our threshold for guaranteed stability for any k is therefore

$$\tau_{ma}^{c} = \frac{\beta}{1+\beta}. \tag{2.4.17}$$

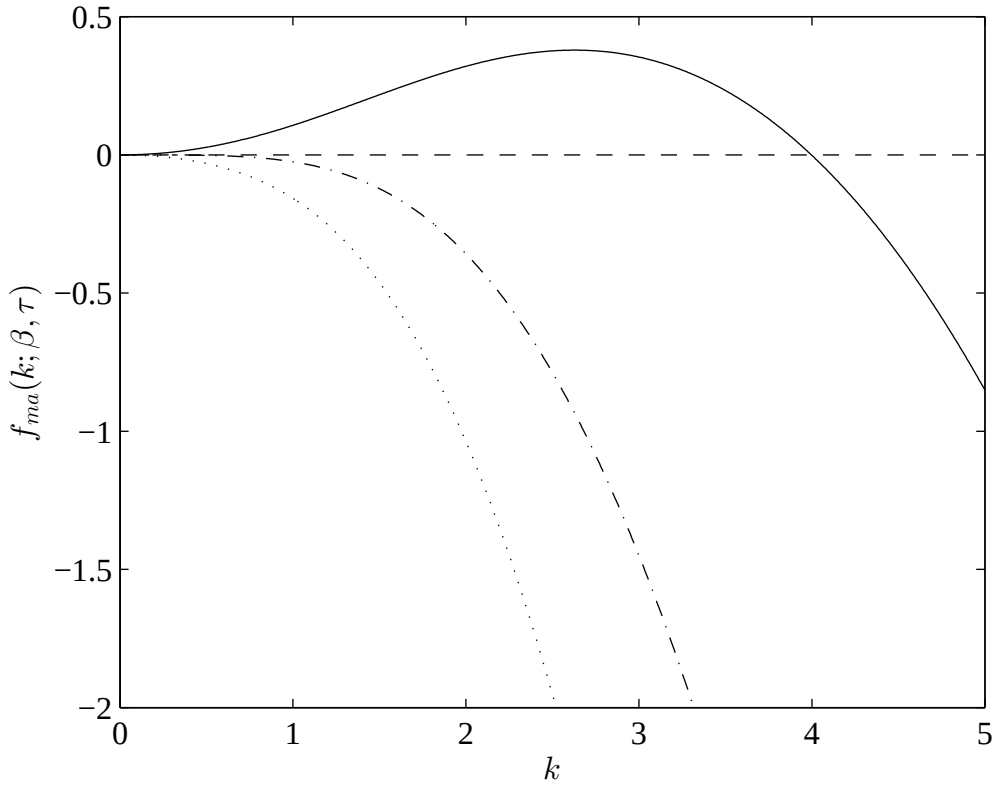

Figure 2.10: A plot of $f_{ma}(k;\beta,\tau)$ from (2.4.14) for $\beta = 0.5$ and $\tau = 1/6$ (solid line), $\tau = \tau^c_{ma} = 1/3$ (dashed-dot line) and $\tau = 1/2$ (dotted line). The dashed line represents the k axis, above this line the perturbations are unstable, while below the line they are stable.

If $\tau \geq \tau^c_{ma}(\beta)$ then the system is stable for all k, however if $\tau < \tau^c_{ma}(\beta)$ then there exists a range of k for which the system is unstable.

Figure 2.10 shows $f_{ma}(k;\alpha,\beta)$ for three pairs of values of β and τ. Examination of the function and its derivative tell us that $f_{ma}(0;\alpha,\beta) = 0$, we also see $f_{ma} \to -\infty$ as $k \to \infty$. Near $k = 0$ the derivative behaves like $f'_{ma}(k;\alpha,\beta) \sim -2k(\beta(\tau-1)+\tau)/(\beta+1)^2$, which is positive for $\tau < \tau^c_{ma}$. So for $\tau < \tau^c_{ma}$, f_{ma} is increasing at $k = 0$ and then decreasing for k large so we must have a maximum in the range $k > 0$ and observation of the function suggests that it will be the only turning point.

Therefore we have a region of instability for long wavelength perturbations and stability for short wavelength perturbations. This is similar to the linear plate model examined in the previous section.

The variation in the position of the critical stability point, denoted k^c_{ma}, at which $f_{ma}(k^c_{ma};\beta,\tau) = 0$ is illustrated in Figure 2.11. We observe that no instabilities are

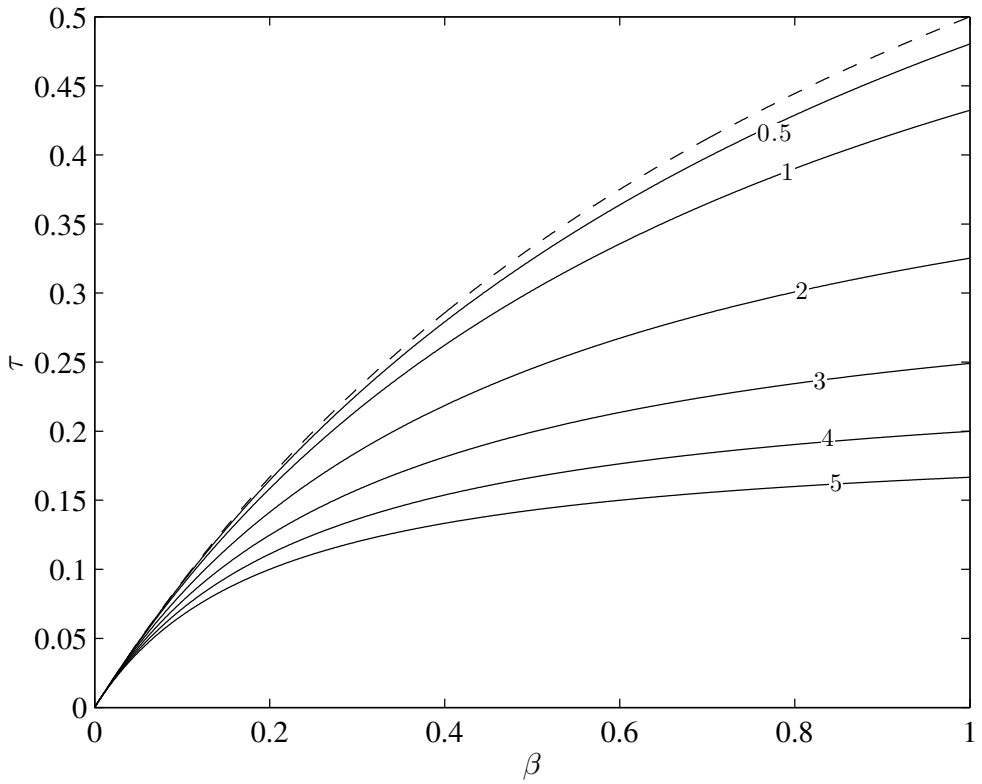

Figure 2.11: Contours of k^c_{ma} for which $f_{ma}(k^c_{ma};\beta,\tau)=0$, for values of the parameters β and τ. The contours serve as the stability boundary, below the modes are unstable while on or above the contours the modes are stable. The dashed line $k^c_{ma}=0$ is also the boundary of the global stability condition, $\tau \geq \tau^c_{ma}(\beta)$ as given by (2.4.17).

present for $\tau \geq \tau^c_{ma}(\beta)$ as predicted by (2.4.17). The values of k^c_{ma} along the contours are much greater for this model of a membrane than they were for the linear plate model, this can be put down to the inertial terms being the same order of k to the tension terms, while the bending terms in the linear plate model were a factor of k^2 different to the inertial terms.

Where the tension is small enough in relation to the inertia to allow for the presence of instability, we seek the k value of the maximum growth rate of any instabilities, which we will denote k^*_{ma}. Based on our assumption that there is only one maximum in $k>0$, this means solving

$$\frac{\partial f_{ma}}{\partial k}=0, \tag{2.4.18}$$

which can be done in the same way as for the linear plate model, by solving (2.4.18) for τ as a function of β and k_{ma}, as shown in Figure 2.12. The large region of no solutions is

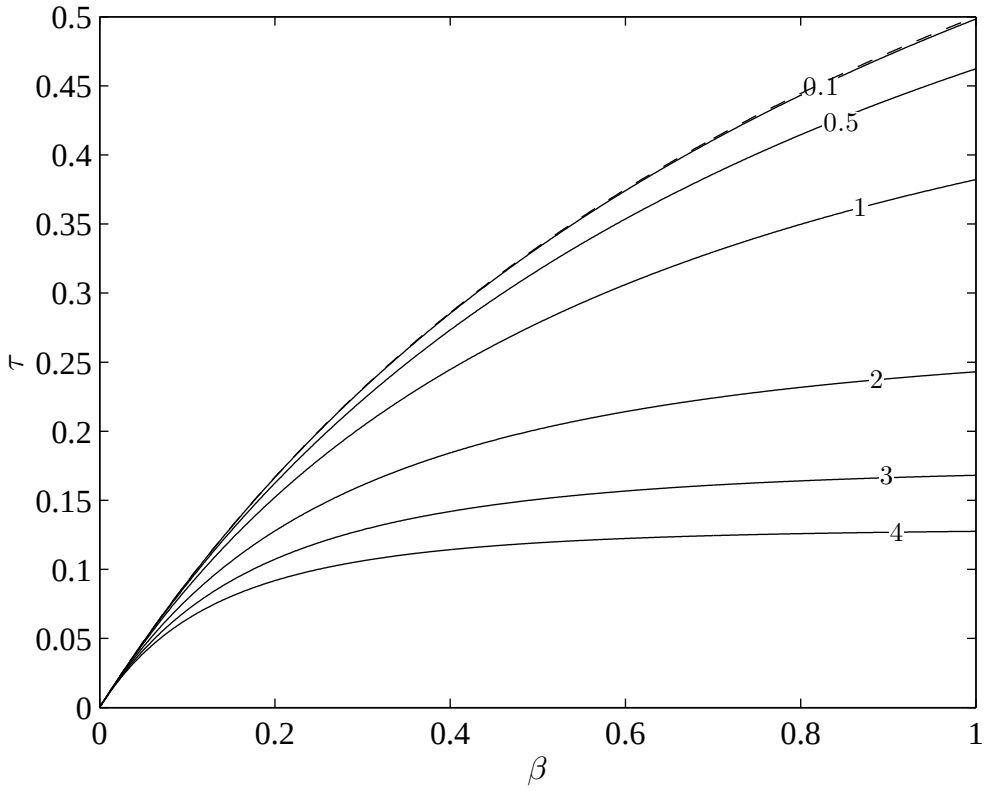

Figure 2.12: A contour plot of solutions to (2.4.18), the contours are constant values of k^*_{ma}, the wavenumber that maximises the growth rate of instabilities. The dashed line $k^*_{ma} = 0$ corresponds to zero growth rate.

present in the upper left quadrant due to the condition for stability that is independent of k given by (2.4.17). We see that the position of the maximum growth rate for a given τ and β is lower than the position of the critical stability point, as expected from the example given in Figure 2.10.

The value of the maximum growth rate is given by $\sqrt{f_{ma}(k^*_{ma}; \beta, \tau)}$, this is shown in 2.13. The maximum growth rate is generally much larger than in the case of the linear plate model, which can be attributed to the similarity in the order of the terms as explained for the position of the critical stability point.

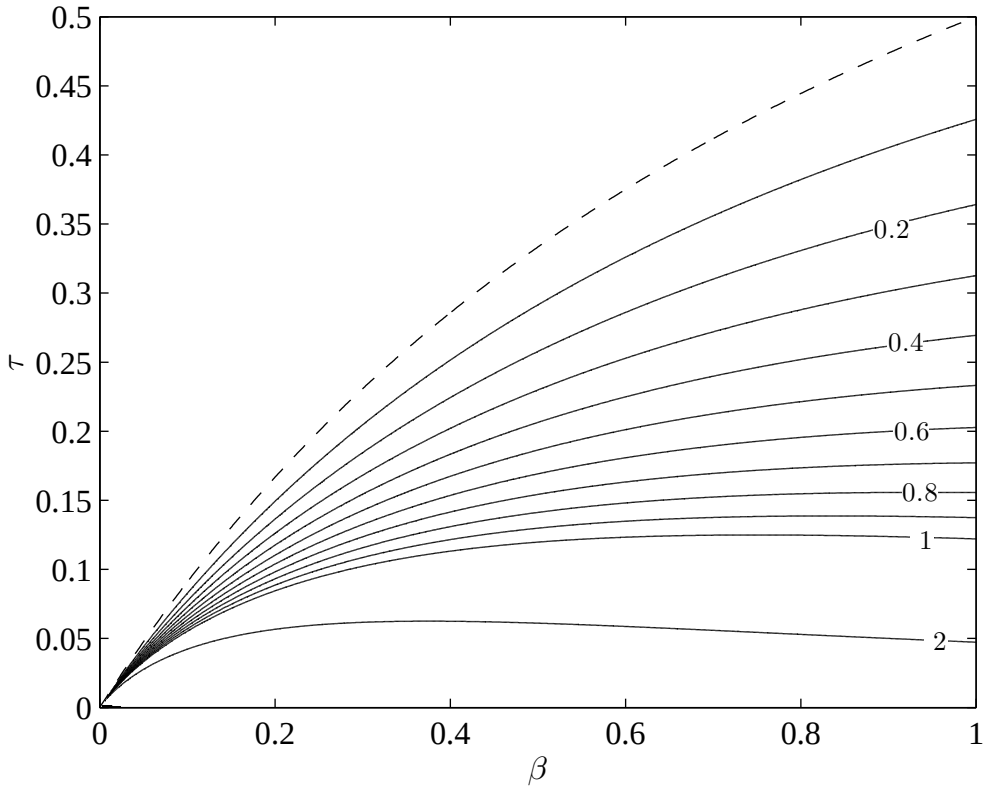

Figure 2.13: Contours of the maximum growth rate given by $\sqrt{f_{ma}(k^*_{ma};\beta,\tau)}$, the contours are constant growth rates. The dashed line $\sqrt{f_{ma}(k^*_{ma};\beta,\tau)} = 0$ marks the global stability boundary.

Symmetric Mode

For the symmetric dispersion relation (2.3.42), setting $\alpha = \gamma = 0$ gives

$$\left(s + \frac{ik}{1+\beta k\tanh(k)}\right)^2 = -\frac{(\tau-\beta)\,k^3\coth(k) + \beta\tau k^4}{(\beta k + \coth(k))^2}, \tag{2.4.19}$$

which is the dispersion relation for the symmetric mode of uniform plug flow between two membranes (de Langre, 2002) and the stability condition can be written

$$\frac{(\beta-\tau)\,k^3\coth(k) - \beta\tau k^4}{(\beta k + \coth(k))^2} \leq 0. \tag{2.4.20}$$

The left hand side of (2.4.20) is denoted as $f_{ms}(k;\beta,\tau)$. As in the antisymmetric mode we have the simple condition that if $\beta \leq \tau$ stability is guaranteed. So we first seek a

possible refinement of this condition. Rearranging (2.4.20) we find

$$\frac{\beta}{1+\beta k\tanh(k)} \leq \tau, \tag{2.4.21}$$

which at $k = 0$ gives the condition $\beta \leq \tau$. The left hand side of (2.4.21) is a decreasing function of k for fixed β and $k > 0$. Therefore its maximum must lie at $k = 0$ and so the critical value of τ, denoted τ^c_{ms} is given by

$$\tau^c_{ms} = \beta. \tag{2.4.22}$$

As $k \to \infty$, $\tau \sim 1/k$, so for all $\tau > \tau^c_{ms}(\beta)$ the system is stable for any perturbation of any wavenumber k, while for $\tau < \tau^c_{ms}(\beta)$ there will be a range of values of k for which perturbations will be unstable.

We now assume that $\tau < \beta$ so that it is now possible for instabilities to arise, which is shown by plotting $f_{ms}(k;\beta,\tau)$, for given pairs of values of β and τ, in Figure 2.14.

At $k = 0$, $f_{ms}(0;\beta,\tau) = 0$ and $f'_{ms}(k;\beta,\tau) \sim 4k^3(\beta-\tau)$ which is positive for $\tau < \beta$ as was assumed. As $k \to \infty$, $f_{ms} \to -\infty$, so combined with the behaviour at $k = 0$, this implies that there is at least one turning point in the region $k > 0$ and observation suggests it is the only one and a maximum. Thus, for $\tau < \beta$, the symmetric mode that results from uniform plug flow between two membranes is unstable to long wavelength perturbations but stable to short wavelength perturbations.

This analysis is extended to a wider range of values for β and τ in Figure 2.15, where contours of the critical stability point at which $f_{ms} = 0$, denoted k^c_{ms} are plotted. As predicted there are no instabilities present in the region $\tau \geq \beta$. The values of k^c_{ms} along the contours are the same order of magnitude as those for the antisymmetric but occur at higher values of τ. This suggests that for a given pair of parameter values there is a larger region of instability in the symmetric mode compared to the antisymmetric mode.

As we did for the linear plate model, it is possible to obtain approximate solutions to the location of the critical stability point. For values of k large enough that we can take $\coth(k) \approx 1$ (this requires only $k \approx 2$ or higher), the equation to solve to find k^c_{ms} can be

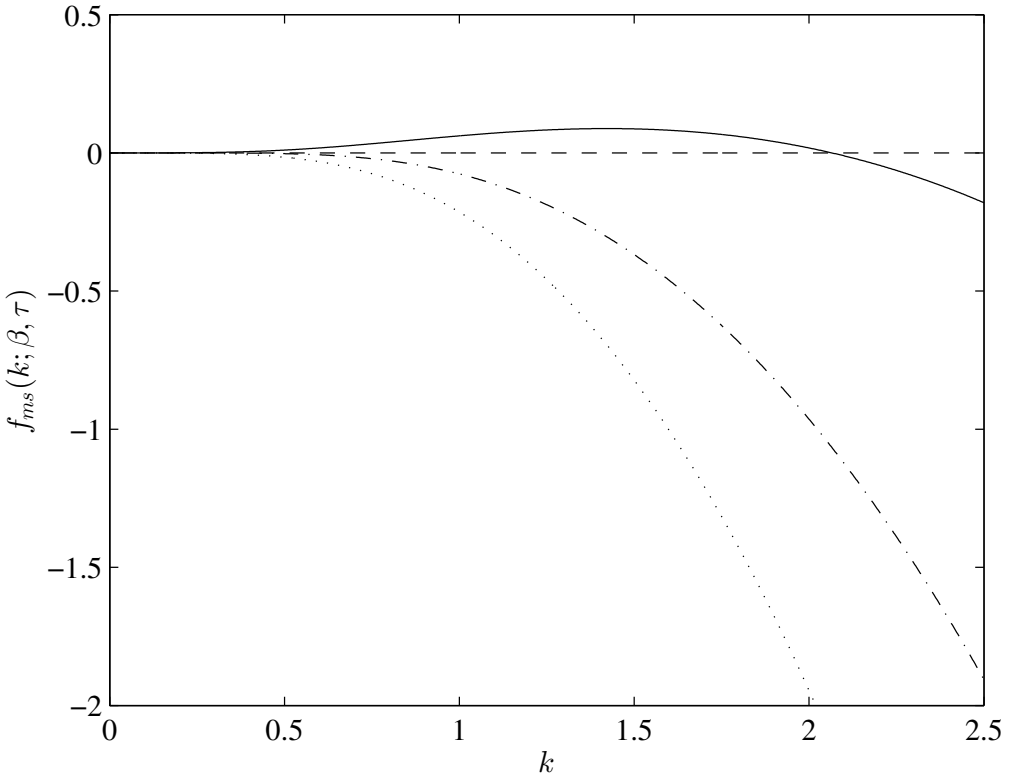

Figure 2.14: A plot of $f_{ms}(k;\beta,\tau)$ from (2.4.20) for $\beta = 0.5$ and $\tau = 1/4$ (solid line), $\tau = \tau^c_{ms} = 1/2$ (dashed-dot line) and $\tau = 3/4$ (dotted line). The dashed line represents the k axis, above this line the perturbations are unstable, while below the line they are stable.

written, from (2.4.19)

$$(\beta - \tau)k^3 - \beta\tau k^4 = 0, \tag{2.4.23}$$

and so we achieve approximate solutions of

$$k^c_{ms} \approx \frac{\beta - \tau}{\beta\tau}. \tag{2.4.24}$$

These approximate solutions are plotted using dashed-dot lines in Figure 2.15, the solutions are very good for $k^c_{ms} = 2$ or higher, but for values of k below this are found to significantly underestimate the size of τ needed.

To find the maximum growth rate when $\tau < \beta$, we are required to solve

$$\frac{\partial f_{ms}}{\partial k} = 0, \tag{2.4.25}$$

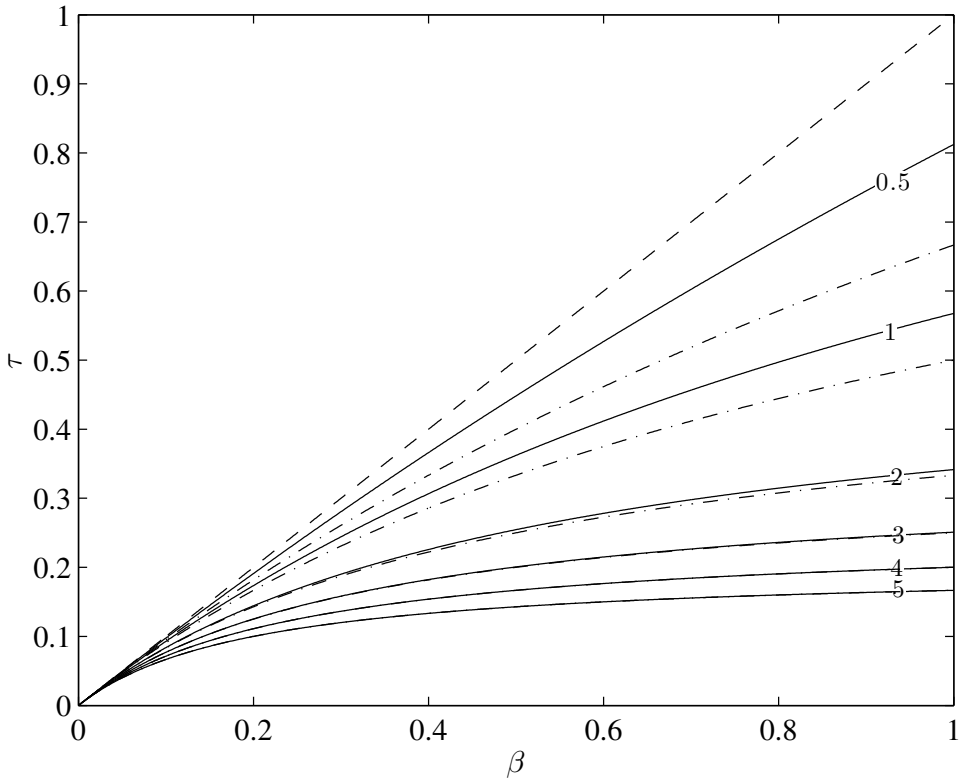

Figure 2.15: Contours of k_{ms}^c for which $f_{ms}(k_{ms}^c;\beta,\tau)=0$, for values of the parameters β and τ (solid lines). The contours serve as the stability boundary, below the modes are unstable while on or above the contours the modes are stable. The dashed line $k_{ms}^c=0$ is also the boundary of the global stability condition, $\tau \geq \tau_{ms}^c(\beta)$ as given by (2.4.22). Approximations of the contours, given by (2.4.24) are also shown (dashed-dot lines).

the solutions to which will be denoted k_{ms}^*. This is easy to solve for τ as a function of β and k and the results are shown in Figure 2.16. We have no solutions in the upper left triangle of the plot as assumed, while the solutions that do exist lie between $k=0$ and $k=k_{ms}^c$ as expected.

With the position of the maximum growth rate calculated, it is then simple to calculate the maximum growth rate itself. It is given by $\sqrt{f_{ms}(k_{ms}^*;\beta,\tau)}$ and is illustrated in Figure 2.17. The value of the contours are of similar size to those in the antisymmetric mode, and again much larger than the maximum growth rates of the linear plate model for the same reasons as discussed previously for the antisymmetric mode.

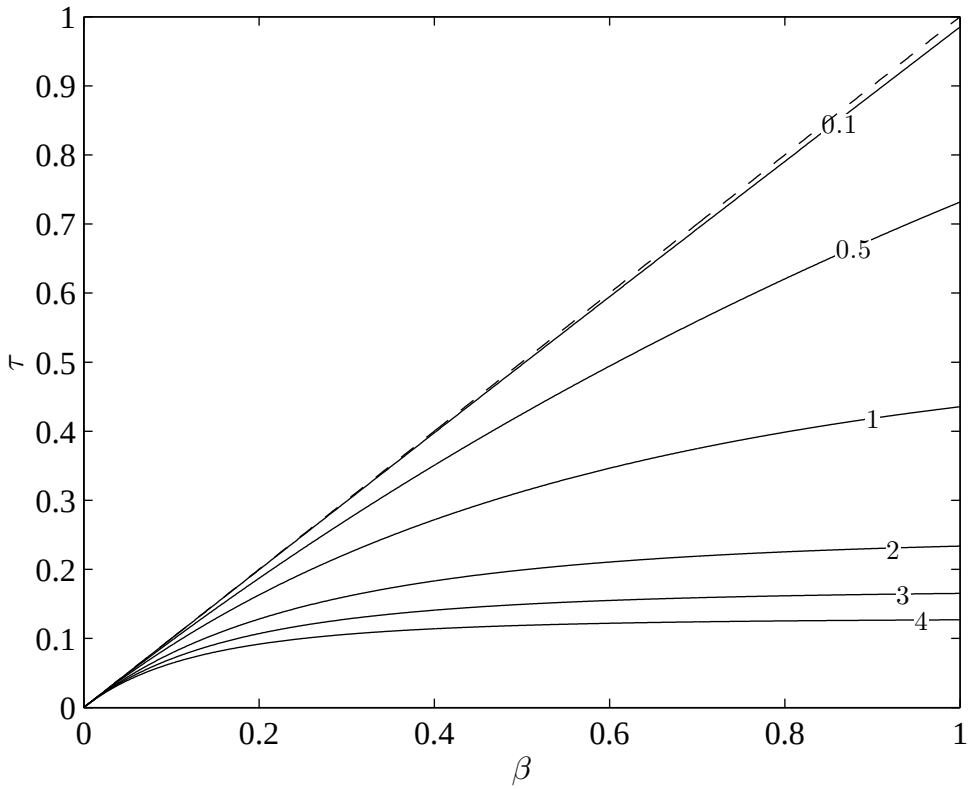

Figure 2.16: A contour plot of solutions to (2.4.25), the contours are constant values of k^*_{ms}, the wavenumber that maximises the growth rate of instabilities. The dashed line $k^*_{ms} = 0$ corresponds to zero growth rate.

2.4.5 Wall inertia and linear springs (Elastic solid model)

If we ignore the effects of the bending stiffness and the tension, the model simplifies to uniform flow between two elastic solids.

Antisymmetric Mode

Under the assumption of no bending stiffness or tension, that is $\alpha = \tau = 0$, then the antisymmetric dispersion relation (2.3.33) becomes

$$\left(s + \frac{ik}{1 + \beta k \coth(k)}\right)^2 = -\frac{(\gamma k - \beta k^3)\tanh(k) + \beta\gamma k^2}{(\beta k + \tanh(k))^2}, \tag{2.4.26}$$

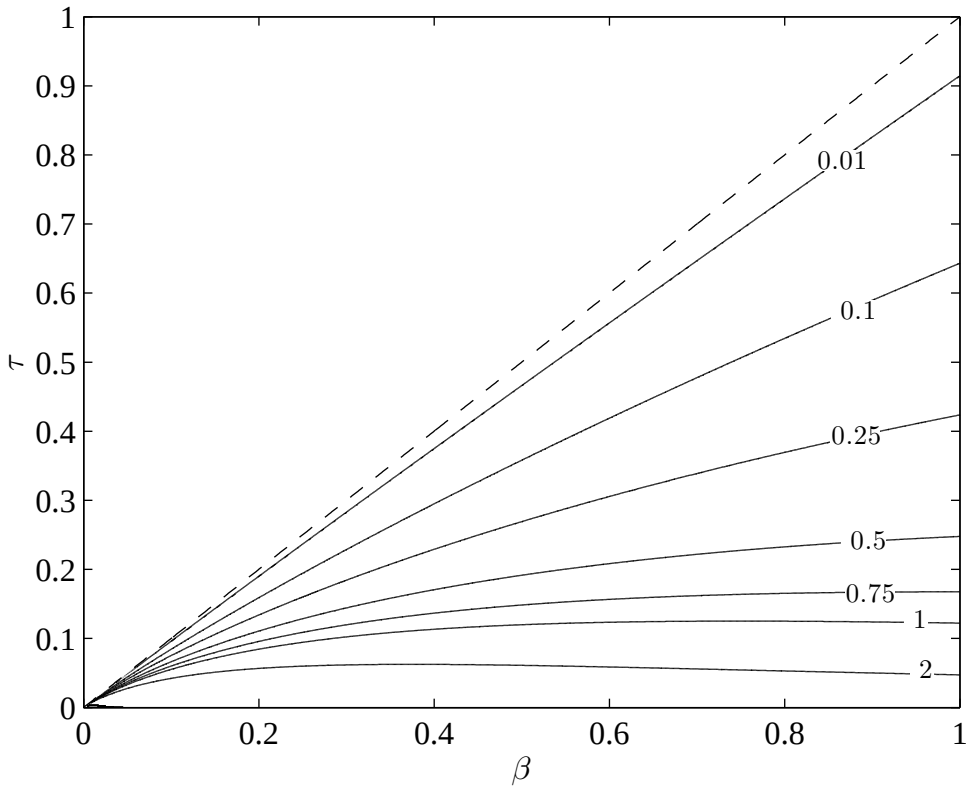

Figure 2.17: Contours of the maximum growth rate given by $\sqrt{f_{ms}(k^*_{ms};\beta,\tau)}$, the contours are constant growth rates. The dashed line $\sqrt{f_{ms}(k^*_{ms};\beta,\tau)} = 0$ marks the global stability boundary.

and so the stability condition can be written as

$$\frac{(\beta k^3 - \gamma k)\tanh(k) - \beta\gamma k^2}{(\beta k + \tanh(k))^2} \leq 0. \tag{2.4.27}$$

We denote the left hand side of (2.4.27) as $f_{ea}(k;\beta,\gamma)$ and illustrate that instabilities can exist for a pair of parameter values in Figure 2.18. We see that the behaviour of the function differs in comparison to the linear plate model (Figure 2.2) and the membrane model (Figure 2.10). In this case the flow is stable for long wavelength perturbations but unstable to short wavelength perturbations.

This is reinforced by examination of $f_{ea}(k;\beta,\gamma)$. At $k = 0$, $f_{ea}(0;\beta,\gamma) = -\gamma/(1+\beta)$, which is negative for any $\beta > 0$ and $\gamma > 0$. As $k \to \infty$, $f_{ea} \to \infty$, so there is a point in the range $k > 0$ where the perturbations change from stable to unstable.

We look first for the critical stability point, denoted k^c_{ea} such that $f_{ea}(k^c_{ea};\beta,\gamma) = 0$, for varying β and γ. This is shown in Figure 2.19 for contours of k^c_{ea}. As the values of

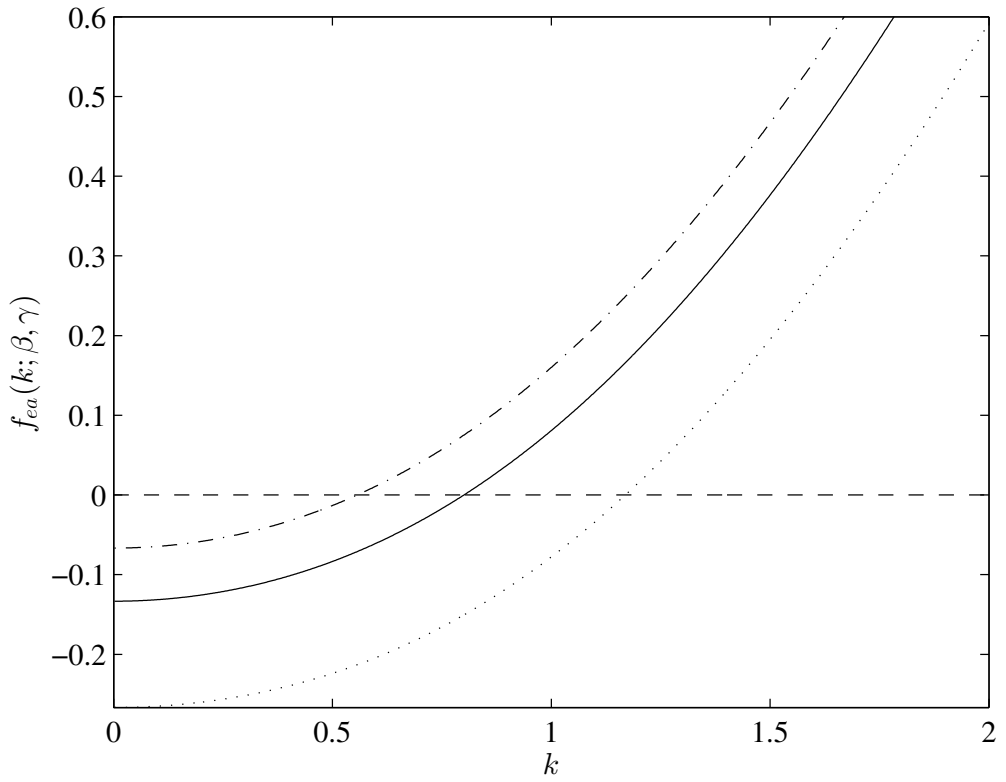

Figure 2.18: A plot of $f_{ea}(k;\beta,\gamma)$ from (2.4.27) for $\beta = 0.5$ and $\gamma = 0.1$ (dashed-dot line), $\gamma = 0.2$ (solid line) and $\gamma = 0.4$ (dotted line). The dashed line represents the k axis, above this line the perturbations are unstable, while below the line they are stable.

k^c_{ea} increases, the contours lie further from $\gamma = 0$, while for the other models as k^c_{la} or k^c_{ma} increases, the contours lay closer to $\alpha = 0$ or $\tau = 0$.

For the linear plate and membrane models we were able to seek the maximum growth rate by looking for the turning point of the stability condition, however in this instance the concept of a maximum growth rate no longer holds, since as previously noted, when $k \to \infty$, $f_{ea} \to \infty$. This suggests that the problem is ill-posed as arbitrarily short wavelength disturbances grow arbitrarily quickly, to counteract this, another physical effect (such as bending stiffness or axial tension) would need to be included in the analysis.

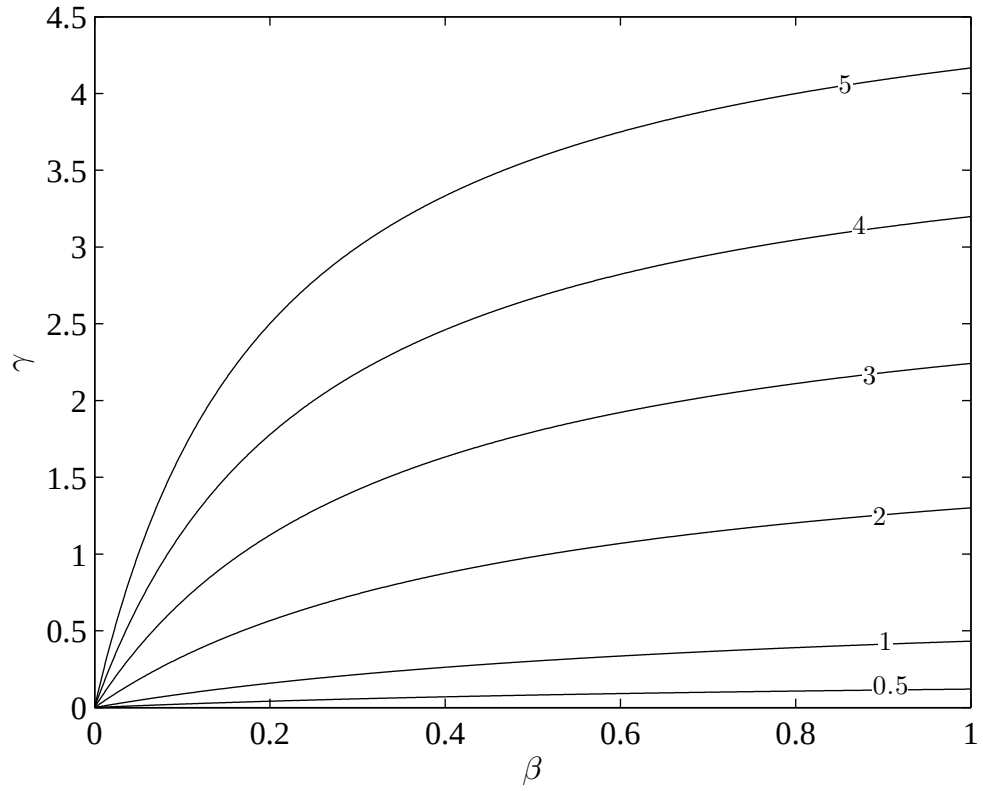

Figure 2.19: Contours of k_{ea}^c for which $f_{ea}(k_{ea}^c; \beta, \gamma) = 0$, for values of the parameters β and γ. The contours serve as the stability boundary, below the modes are unstable while on or above the contours the modes are stable.

Symmetric Mode

The dispersion relation for the symmetric mode in the absence of bending stiffness and tension, from (2.3.42), is

$$\left(s + \frac{ik}{1 + \beta k \tanh(k)}\right)^2 = -\frac{(\gamma k - \beta k^3)\coth(k) + \beta\gamma k^2}{(\beta k + \coth(k))^2}, \tag{2.4.28}$$

and the stability condition is therefore

$$\frac{(\beta k^3 - \gamma k)\coth(k) - \beta\gamma k^2}{(\beta k + \coth(k))^2} \leq 0. \tag{2.4.29}$$

The left hand side is denoted $f_{es}(k; \beta, \gamma)$ and the existence of instabilities in the model is illustrated in Figure 2.20. The qualitative behaviour of f_{es} is much the same as f_{ea}, there is a region of stability for long wavelength perturbations before becoming unstable as the

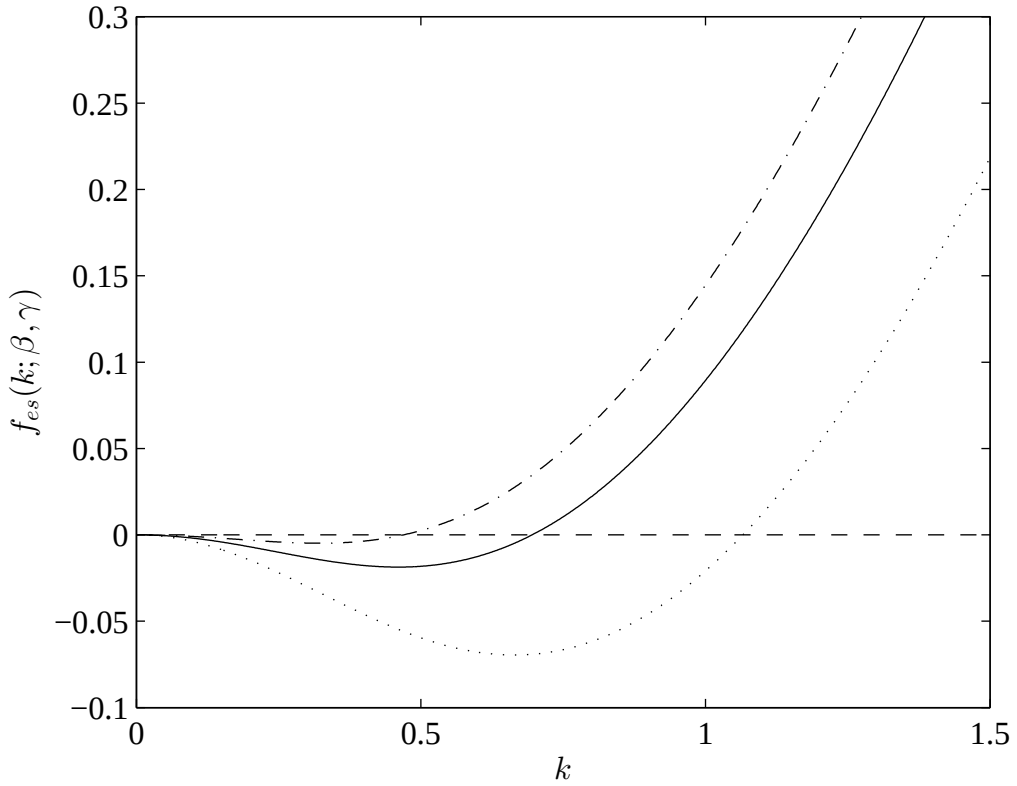

Figure 2.20: A plot of $f_{es}(k;\beta,\gamma)$ from (2.4.27) for $\beta = 0.5$ and $\gamma = 0.1$ (dashed-dot line), $\gamma = 0.2$ (solid line) and $\gamma = 0.4$ (dotted line). The dashed line represents the k axis, above this line the perturbations are unstable, while below the line they are stable.

wavelength of perturbations decreases.

Examination of f_{es} reveals that $f_{es}(0;\beta,\gamma) = 0$ and near $k = 0$, $f'_{es} \sim -2\gamma k$ which is negative for all $\gamma > 0$ in the range $k > 0$ that we are examining. Thus, the function is decreasing initially, but since $f_{es} \to \infty$ as $k \to \infty$ there must be a turning point in $k > 0$ before passing through the critical stability point k^c_{es} such that $f_{es}(k^c_{es};\beta,\gamma) = 0$.

The behaviour of this critical stability point is illustrated in Figure 2.21 with contours of constant k^c_{es} as β and γ vary. Again the unstable region lies below and to the right of the contours, for the same reasons as for the antisymmetric mode.

As previously, approximate values of the critical stability contours can be found if we assume k is large enough that $\coth(k) \approx 1$. In this case, the equation governing the location of the critical stability point can be written

$$\beta k^2 - \beta\gamma k - \gamma = 0. \tag{2.4.30}$$

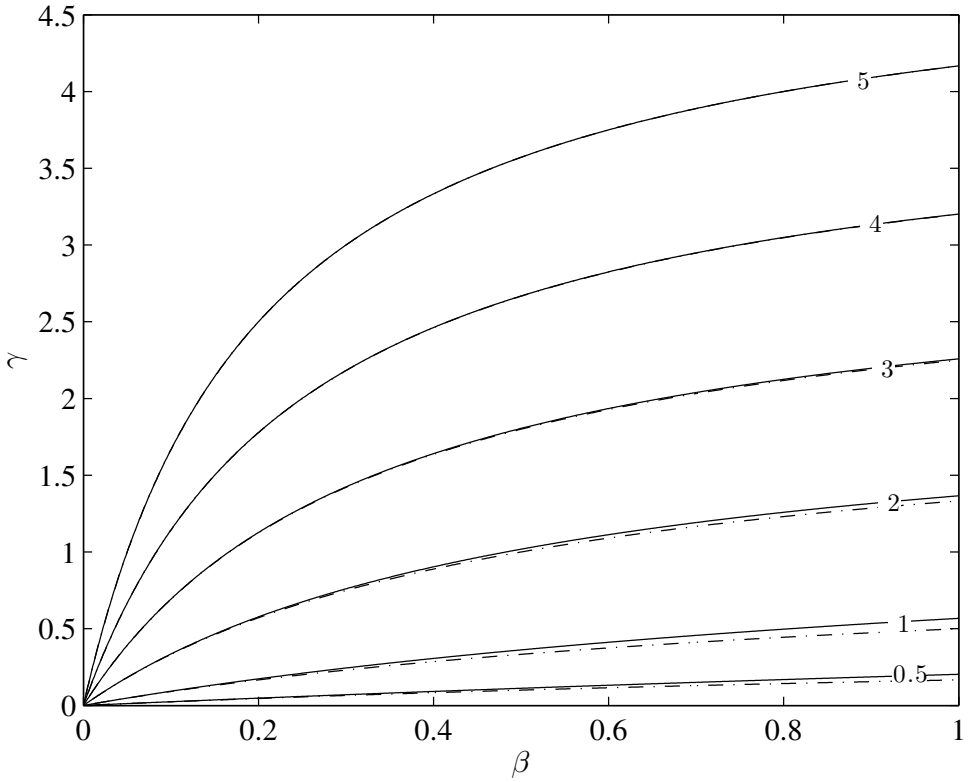

Figure 2.21: Contours of k_{es}^c for which $f_{es}(k_{es}^c; \beta, \gamma) = 0$, for value of the parameters β and γ (solid lines). The contours serve as the stability boundary, below the modes are unstable while on or above the contours the modes are stable. Approximations of the contours, given by (2.4.31) are also shown (dashed-dot lines).

This is a quadratic solution in k with solution

$$k_{es}^c \approx \frac{\gamma + \sqrt{\gamma^2 + 4\gamma/\beta}}{2}, \tag{2.4.31}$$

where the positive root has been taken since k is assumed to be positive.

The approximate solutions are included using dashed-dot lines in Figure 2.21, as before for values of $k_{es}^c \geq 2$ the approximate solutions are very accurate. Some accuracy is lost for $k_{es}^c < 2$ but the approximate solutions remain more accurate for the elastic solid system than they were for the membrane system.

There is no meaning to the concept of the maximum growth rate for the symmetric mode, in the same way as for the antisymmetric mode, since $f_{es} \to \infty$ as $k \to \infty$, suggesting the problem is ill-posed.

2.4.6 Three or more parameters

We now attempt to extend our analysis to the cases where only one of α, β or γ are negligible, to help our understanding of the behaviour of the full system. Further progress can be made by considering the stability conditions in an alternate form. For the antisymmetric mode, we rewrite (2.3.36) as

$$\frac{\beta \tanh(k)}{\beta k + \tanh(k)} \leq \alpha k^2 + \tau + \frac{\gamma}{k^2}, \tag{2.4.32}$$

while for the symmetric mode, (2.3.44) is rewritten as

$$\frac{\beta \coth(k)}{\beta k + \coth(k)} \leq \alpha k^2 + \tau + \frac{\gamma}{k^2}. \tag{2.4.33}$$

For the limiting cases to be examined using this alternate form of the stability condition, the left hand side of each of (2.4.32) and (2.4.33) remain unchanged. We determine the asymptotic behaviour of the left hand side of these equations now to avoid repetition.

In the antisymmetric mode, the behaviour of the left hand side of (2.4.32) as $k \to 0$, is given by

$$\frac{\beta \tanh(k)}{\beta k + \tanh(k)} \sim \frac{\beta}{\beta + 1}, \tag{2.4.34}$$

while as $k \to \infty$,

$$\frac{\beta \tanh(k)}{\beta k + \tanh(k)} \sim \frac{1}{k}. \tag{2.4.35}$$

Similarly, for the left hand side of (2.4.33), as $k \to 0$ we have

$$\frac{\beta \coth(k)}{\beta k + \coth(k)} \sim \beta, \tag{2.4.36}$$

and as $k \to \infty$

$$\frac{\beta \coth(k)}{\beta k + \coth(k)} \sim \frac{1}{k}. \tag{2.4.37}$$

We also note that in this form it is simple to show, by rearrangement, that

$$\frac{\beta \tanh(k)}{\beta k + \tanh(k)} \leq \frac{\beta \coth(k)}{\beta k + \coth(k)}, \tag{2.4.38}$$

since $\tanh(k) \leq \coth(k)$ for any $k > 0$. This formalises the idea found in the previous limiting cases that the symmetric mode has a larger range of instability than the antisymmetric mode as (2.4.38) means that symmetric stability implies antisymmetric stability but not the opposite.

2.4.7 Linear springs-free system

We examine the limiting case when the spring response is negligible when compared to the other parameters, this is equivalent to setting $\gamma = 0$ in the stability conditions.

Antisymmetric Mode

If we set $\gamma = 0$ in (2.4.32), the stability condition becomes

$$\frac{\beta \tanh(k)}{\beta k + \tanh(k)} \leq \alpha k^2 + \tau. \tag{2.4.39}$$

We have already determined the behaviour of the left hand side of (2.4.39) to be $\sim \beta/(\beta + 1)$ as $k \to 0$, and in the same limit the right hand side $\sim \tau$. We obtain the same critical value of τ for stability as the membrane model given by (2.4.17), which we now denote τ_a^c. We therefore consider only the regime in which $\tau < \beta/(\beta + 1)$ to allow for instabilities.

In the limit $k \to \infty$, the right hand side of (2.4.39) behaves like $\sim \alpha k^2$ which dominates the behaviour of the left hand side ($\sim 1/k$ see (2.4.35)) so the system is always stable at short wavelengths.

With stability at short wavelengths and the chance of instability at long wavelengths the qualitative behaviour is the same as that of the membrane model, but it is necessary to determine the effect of α on the system.

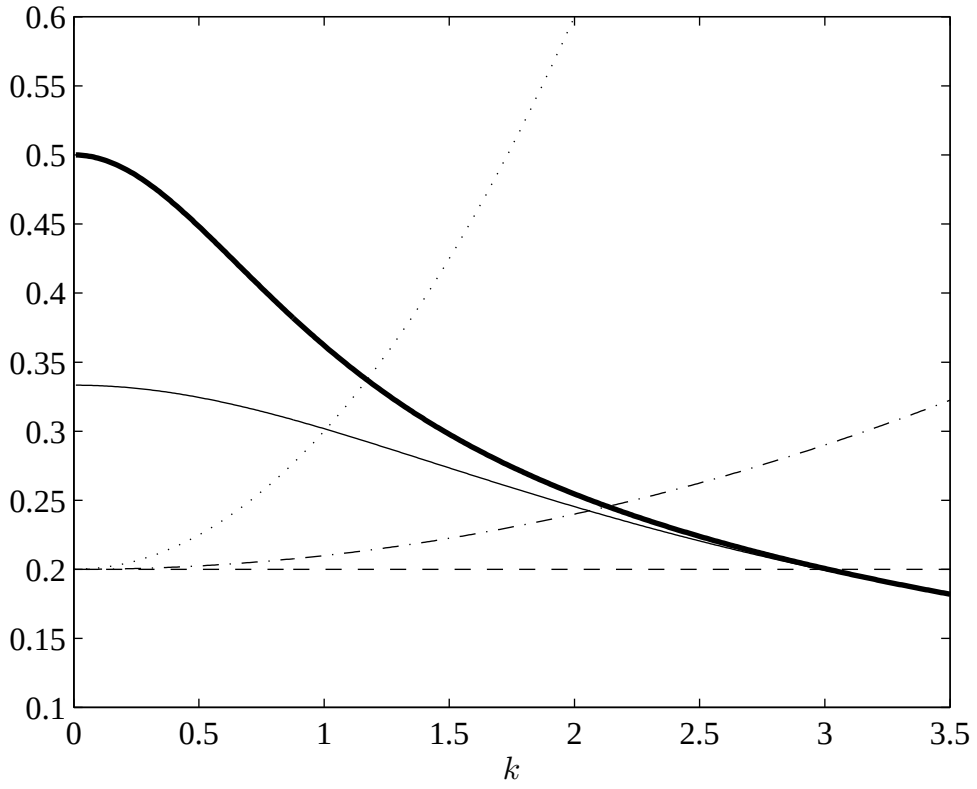

Figure 2.22: The left and right hand sides of (2.4.39) and (2.4.40) to show the effect of changing α on the stability of the linear springs-free system for $\beta = 0.5$, $\tau = 0.2$. The left hand side of (2.4.39) is given by the thin solid line, and the left hand side of (2.4.40) is given by the thick solid line. Above these lines the corresponding mode is stable and below they are unstable. The right hand sides of (2.4.39) and (2.4.40) are shown for varying values of α: $\alpha = 0$ (dashed line, corresponding to the membrane model), $\alpha = 0.01$ (dashed-dot line) and $\alpha = 0.1$ (dotted line).

To this end, the left hand side of (2.4.39) is compared with the right hand side for different values of α in Figure 2.22, while $\beta = 0.5$ and $\tau = 0.2$ are kept fixed, the thin solid line corresponds to the antisymmetric mode. While it is a single example, it captures the general behaviour of the system well. For comparison the case $\alpha = 0$ is plotted, since this is equivalent to the membrane model studied previously, then as we increase α first to 0.01 and then to 0.1 the unstable region decreases rapidly with the change from unstable to stable happening at approximately $k = 3$ for $\alpha = 0$, $k = 2$ for $\alpha = 0.01$ and $k = 1$ for $\alpha = 0.1$. So α is seen to have a stabilising effect on the system.

Symmetric Mode

Under the assumption that spring response is negligible (2.4.33) becomes

$$\frac{\beta \coth(k)}{\beta k + \coth(k)} \leq \alpha k^2 + \tau. \tag{2.4.40}$$

As $k \to 0$ in (2.4.40), the left hand side has already been found to behave like $\sim \beta$, the right hand side is unchanged from the antisymmetric mode and behaves like $\sim \tau$. This gives the same critical value of τ for guaranteed stability as in the symmetric mode of the membrane model given by (2.4.22), now denoted τ_s^c.

The behaviour in the limit $k \to \infty$ is as for the antisymmetric mode and so the system is stable to short wavelength disturbances. The qualitative behaviour is thus the same as the symmetric mode of the membrane model.

The exact behaviour is adjusted by the contribution from α as shown in Figure 2.22, with the thick solid line. The effect of α is seen in a decrease in the size of the unstable region by lowering the critical stability boundary towards $k = 0$. This is in agreement with the antisymmetric mode. As expected, for a given α, the unstable region is also seen to be larger than the unstable region for the antisymmetric mode.

2.4.8 Tension-free system

The penultimate limiting case considered is one where the effects of tension are negligible, obtained by setting $\tau = 0$.

Antisymmetric Mode

With tension negligible, the antisymmetric stability condition, (2.4.32), can be written

$$\frac{\beta \tanh(k)}{\beta k + \tanh(k)} \leq \alpha k^2 + \frac{\gamma}{k^2}. \tag{2.4.41}$$

As previously determined, the behaviour of the left hand side as $k \to 0$ is known to be $\sim \beta/(\beta + 1)$, while the behaviour of the right hand side is now $\sim \gamma/k^2$. Thus for any

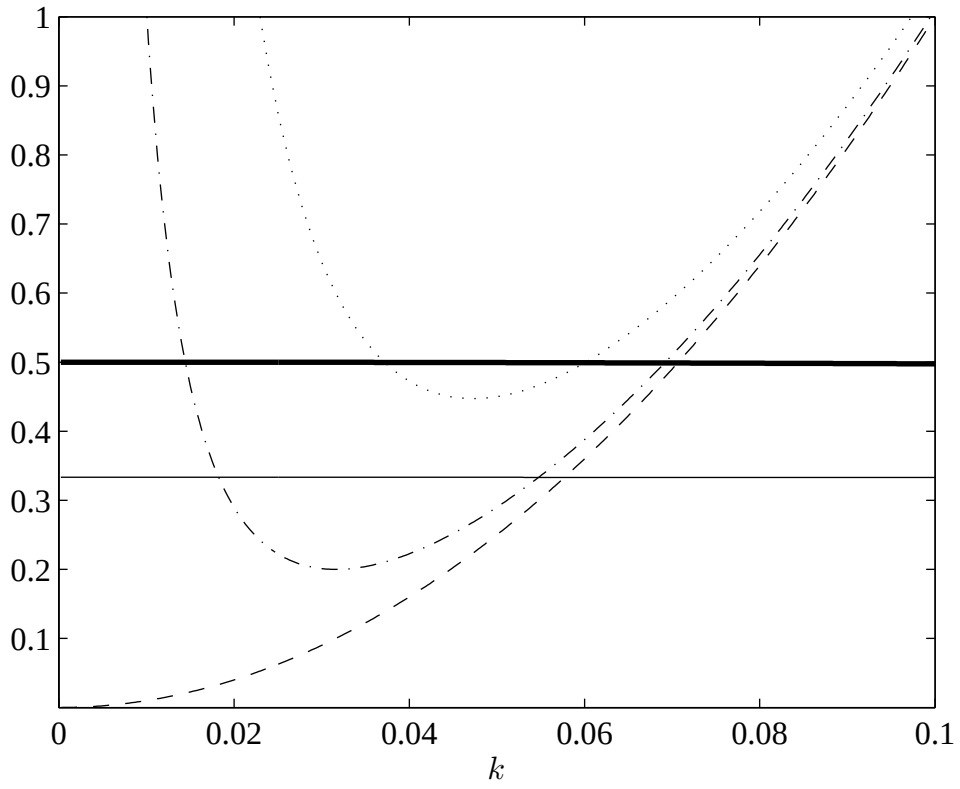

Figure 2.23: The left and right hand sides of (2.4.41) and (2.4.43) to show the effect of changing γ on the stability of the tension-free system for $\beta = 0.5$, $\alpha = 100$. The left hand side of (2.4.41) is given by the thin straight line, and the left hand side of (2.4.43) is given by the thick straight line. Above these lines the corresponding mode is stable and below they are unstable. The right hand sides of (2.4.41) and (2.4.43) are shown for varying values of γ: $\gamma = 0$ (dashed line, corresponding to the linear plate model), $\gamma = 0.0001$ (dashed-dot line) and $\gamma = 0.0005$ (dotted line).

$\gamma > 0$ there is now a stable region near $k = 0$, as found for the elastic solid model.

The behaviour of both sides as $k \to \infty$ is known, as it is the same as the limiting case when $\gamma = 0$, so the system is stable to short wavelength disturbances, this is in contrast to the elastic solid model. At first glance it appears that the system is stable, this turns out not to be the case as the addition of the linear spring term allows an unstable region to develop for a range of k values above the stable region for $k \ll 1$ and below the stable region for $k \gg 1$.

In Figure 2.23 a specific case is used to illustrate the general behaviour of the system. Starting from $\gamma = 0$, equivalent to the linear plate model, which is unstable at long wavelengths and stable at short wavelengths, this is shown using the dashed line. Increasing γ results in a new regime as soon as it is non-zero, in which the system is stable to both short

and long wavelength perturbations but there is a region between these where the system is unstable, in this example this is shown with $\gamma = 0.0001$ shown using the dashed-dot line. As γ increases further the size of the unstable region decreases until $\gamma = \gamma^c_{\alpha a}$ at which point there is only one solution to

$$\frac{\beta \tanh(k)}{\beta k + \tanh(k)} = \alpha k^2 + \frac{\gamma}{k^2}, \tag{2.4.42}$$

in the range $k > 0$. For the illustrated case in Figure 2.23, with $\alpha = 100$ and $\beta = 0.5$, $\gamma^c_{\alpha a} \approx 0.00028$. Finally, as γ is increased beyond $\gamma^c_{\alpha a}$, the antisymmetric mode becomes stable at all wavelengths, this is the dashed line.

Symmetric Mode

For the symmetric mode an assumption of no tension gives a stability condition of

$$\frac{\beta \coth(k)}{\beta k + \coth(k)} \leq \alpha k^2 + \frac{\gamma}{k^2}. \tag{2.4.43}$$

The behaviour of the left hand side as $k \to 0$ is known to be $\sim \beta$, while the right hand side behaves like $\sim \gamma/k^2$. Thus for non-zero γ we obtain the same behaviour as for the antisymmetric mode, namely a stable region for long wavelength perturbations.

As $k \to \infty$ the right hand side looks like $\sim \alpha k^2$ which dominates over the left hand side ($\sim 1/k$), so the system is stable to short wavelength perturbations as well. As antisymmetric mode instabilities imply symmetric mode instabilities, it is realistic to expect a region of instability between the two stable regions already discussed. This turns out to be true and the general behaviour is identical to the behaviour of the antisymmetric mode. The only exception being the critical value of γ is now denoted $\gamma^c_{\alpha s}$. The behaviour is illustrated for a specific pair of values for β and α in Figure 2.23. The qualitative behaviour is the same as the antisymmetric mode, although we note that for the symmetric mode there is no illustration of an entirely stable mode, as the case given by $\gamma = 0.0005$, which is stable to all wavelengths in the antisymmetric mode, still allows a range of instabilities

in the symmetric mode. For the example shown in Figure 2.23, $\gamma_{\alpha s}^{c} \approx 0.00062$, as we would expect, this is greater than the critical value for the antisymmetric mode.

2.4.9 Bending stiffness-free system

The final limiting case to be studied is the one in which the contribution from the bending stiffness is negligible, i.e. we take $\alpha = 0$.

Antisymmetric Mode

Setting $\alpha = 0$ in (2.4.32), the stability condition for the antisymmetric mode is found to be

$$\frac{\beta \tanh(k)}{\beta k + \tanh(k)} \leq \tau + \frac{\gamma}{k^2}. \tag{2.4.44}$$

In this case the behaviour of both the left hand side and the right hand side are both known in the limit $k \to 0$ from previous limiting cases, the left hand side behaves like $\beta/(\beta + 1)$ and the right hand side like γ/k^2. Thus the antisymmetric mode is stable to long wavelength perturbations for any $\gamma > 0$.

Similarly, in the limit $k \to \infty$ the behaviour is known to be dominated by the right hand side ($\sim \tau$) as opposed to the left hand side ($\sim 1/k$), so the antisymmetric mode is stable to short wavelength perturbations. However, as in the previous limiting case, when the effect of tension was negligible, it is possible to obtain a region of instability between the two stable regions at the limiting values of k.

The qualitative behaviour of this region of instability is very similar to the equivalent region in the tension-free system. However, due to the lower order in k of the contribution to the tension in this system, compared with the contribution from the bending in the previous system, the unstable region is present for both higher wavenumbers and over a larger range of k values, as illustrated in Figure 2.24. For the antisymmetric mode, with $\beta = 0.5$ and $\tau = 0.2$ as shown in Figure 2.24, $\gamma_{\tau a}^{c} \approx 0.183$.

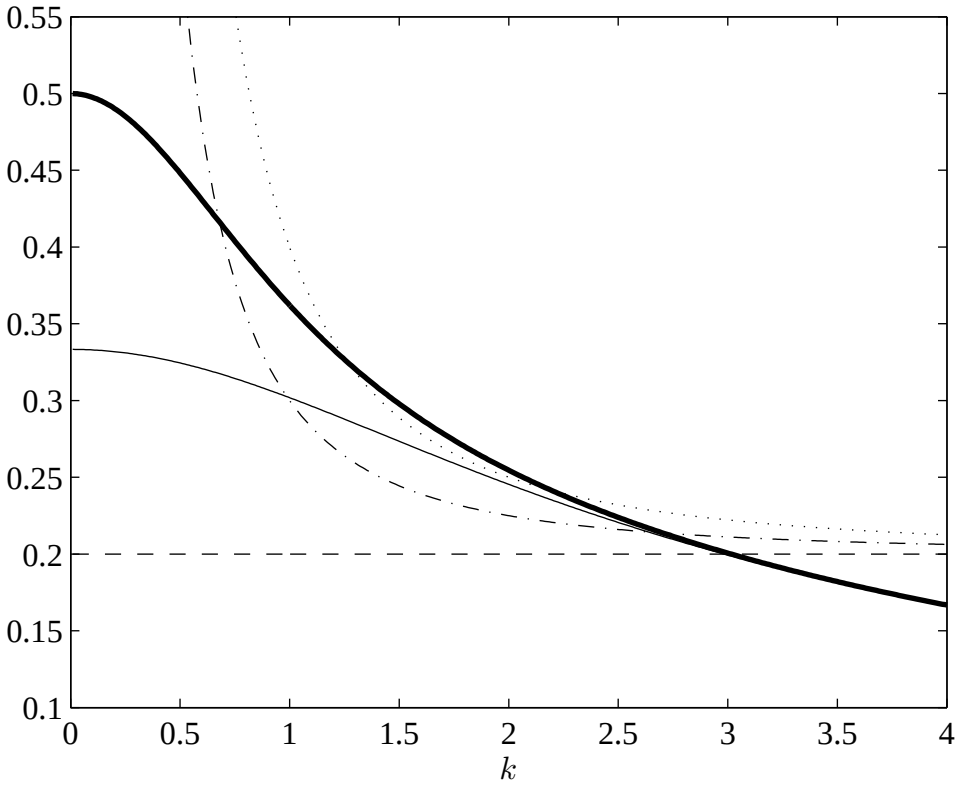

Figure 2.24: The left and right hand sides of (2.4.44) and (2.4.45) to show the effect of changing γ on the stability of the bending stiffness-free system for $\beta = 0.5$, $\tau = 0.2$. The left hand side of (2.4.44) is given by the thin solid line, and the left hand side of (2.4.45) is given by the thick solid line. Above these lines the corresponding mode is stable and below they are unstable. The right hand sides of (2.4.44) and (2.4.45) are shown for varying values of γ: $\gamma = 0$ (dashed line, corresponding to the membrane model), $\gamma = 0.1$ (dashed-dot line) and $\gamma = 0.2$ (dotted line).

Symmetric Mode

The stability condition for the symmetric mode, (2.4.33), can, in the absence of bending be written

$$\frac{\beta \coth(k)}{\beta k + \coth(k)} \leq \tau + \frac{\gamma}{k^2}. \tag{2.4.45}$$

In the limit $k \to 0$, the left hand side of (2.4.45) is known to behave like $\sim \beta$, while the right hand side has the same behaviour as the antisymmetric mode ($\sim \gamma/k^2$), resulting in stability for long wavelength perturbations if $\gamma > 0$.

Similarly, if $k \to \infty$, the right hand side of (2.4.45) ($\sim \tau$) is known to dominate the left hand side ($\sim 1/k$) giving stability to short wavelength perturbations. The same argument that was used to suggest the existence of symmetric mode instabilities for the

tension-free system holds here, namely that instabilities in the antisymmetric mode imply the existence of instabilities in the symmetric mode. This region exists between the two stable regions for similar values of k as in the antisymmetric mode, see Figure 2.24.

There exists a $\gamma^c_{\tau s}$, which corresponds to the critical value of γ above which the mode is stable, and below which the mode has the stable-unstable-stable behaviour evidenced in Figure 2.24, and for the parameters used is given by $\gamma^c_{\tau s} = 0.227$, which is larger than the antisymmetric mode as any critical value of gamma is required to be for the symmetric mode.

2.5 Analysis of the Full System

Having considered numerous limiting cases to the full problem, we now use what we know of the behaviour of the system to extend this analysis to one involving all four parameters α, β, γ and τ.

Antisymmetric Mode

Working with the form of the stability criteria given by (2.4.32)

$$\frac{\beta \tanh(k)}{\beta k + \tanh(k)} \leq \alpha k^2 + \tau + \frac{\gamma}{k^2}. \tag{2.5.1}$$

The behaviour of each side is well known in both the limits $k \to 0$ and $k \to \infty$. In the former the left hand side $\sim \beta/(\beta+1)$ while the right hand side $\sim \gamma/k^2$, so we have stability. While in the limit $k \to \infty$, the right hand ($\sim \alpha k^2$) dominates the left hand side ($\sim 1/k$), again resulting in stability. This suggests that the behaviour exhibited in the tension-free and bending-free limiting cases, where there is an unstable region between two stable regions is possible. This is the case and it is illustrated by the dashed line in Figure 2.25. Another consequence of this behaviour is that there will exist a critical value of γ, denoted γ^c_{fa} such that above this value the system is stable everywhere, this is shown by the dotted line.

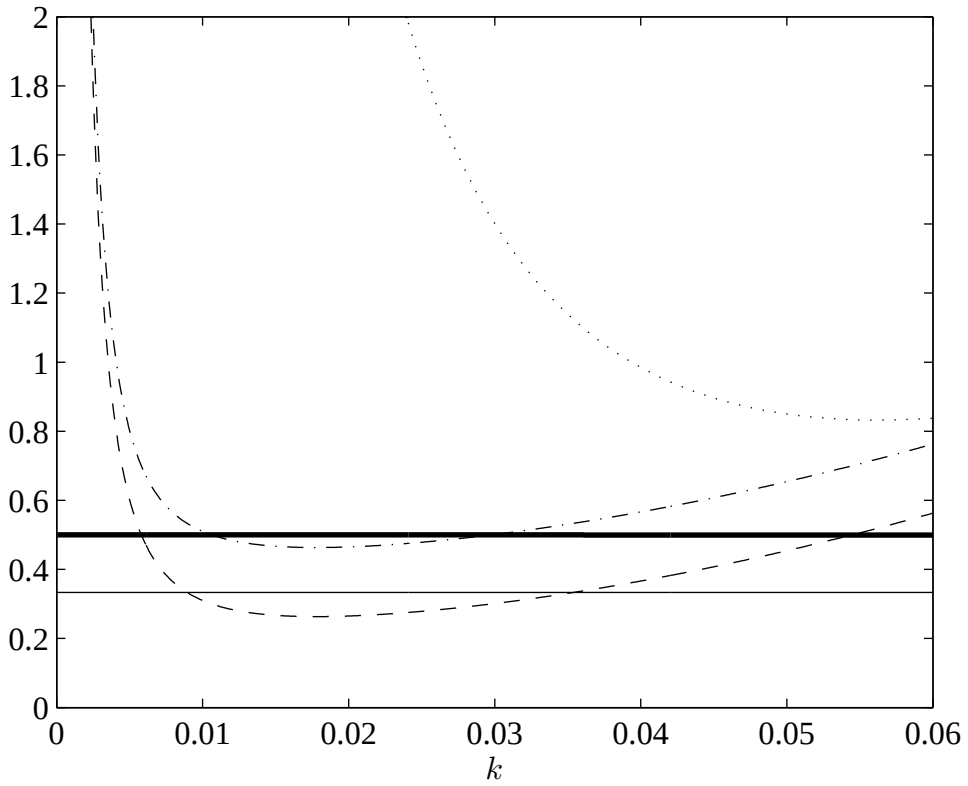

Figure 2.25: The left and right hand sides of (2.5.1) and (2.5.2) to show the different regimes that are possible in the full system for both the antisymmetric and symmetric modes. The left hand sides of (2.5.1) (thin straight line) and (2.5.2) (thick straight line) are given for $\beta = 0.5$. Three cases are illustrated for the right hand sides of (2.5.1) and (2.5.2), all for $\alpha = 100$, the first is given by $\tau = 0.2$ and $\gamma = 0.00001$ (dashed line), the second by $\tau = 0.4$ and $\gamma = 0.00001$ (dashed-dot line) and the final case by $\tau = 0.2$ and $\gamma = 0.001$.

The value of τ chosen for the two cases described was very specifically chosen such that, since $\beta = 0.5$, $\tau < \beta/(\beta + 1)$. It turns out, that the stability condition derived for both the membrane model, and the linear springs-free model holds here as well. Namely, if $\tau \geq \beta/(\beta + 1)$, then the system will be stable for any choice of parameters, this is the final case illustrated by the dashed-dot line in Figure 2.25 where $\tau = 0.4$. The value of γ chosen in this case was done so specifically because it resulted in the stable-unstable-stable regime when $\tau < \tau_{fa}^{c}$ the critical size required for stability.

Symmetric Mode

For the symmetric mode we start from the stability criteria given by (2.4.33)

$$\frac{\beta \coth(k)}{\beta k + \coth(k)} \leq \alpha k^2 + \tau + \frac{\gamma}{k^2}. \tag{2.5.2}$$

As for the antisymmetric mode, the behaviour is well known in both the key limits. As $k \to 0$, the left hand side $\sim \beta$ and the right hand side $\sim \gamma/k^2$, and the system is stable. As $k \to \infty$ the limits are the same as for the antisymmetric mode and so the right hand side dominates leading to stability. The stability condition on τ for the symmetric modes of the membrane and linear springs-free models turns out to hold here as well, and we give the critical value of τ to be $\tau_{fs}^c = \beta$.

Again, we have the existence of the stable-unstable-stable regime, providing $\gamma < \gamma_{fs}^c$, the critical value of γ, this is illustrated by the dashed line in Figure 2.25 and holds for both the antisymmetric and symmetric modes, and by the dashed-dot line only for the symmetric mode while the dotted line shows the case when $\gamma > \gamma_{fs}^c$ and the system is stable everywhere.

2.6 Summary of Results

We have determined the existence of instabilities in a variety of simplifications to the full problem given by the dispersion relations (2.3.33) and (2.3.42). The results are summarised in Table 2.1. The models have not been broken down into their respective modes because in all cases the qualitative behaviour is the same, varying only between the models.

We determined that it is necessary for wall inertia to be present in order for instabilities to arise, and it was shown that in every possible limiting case, as well as the full system, that the symmetric mode has a larger unstable region than the antisymmetric mode. It was also found that if tension is present in the system it will be stable (regardless of mode) if the nondimensional tension is greater than the nondimensional inertia. This

Model	Non-zero parameters	Parameter size	Stability ($k \ll 1$)		Stability ($k \gg 1$)
No Wall Inertia	α, τ, γ		S	—	S
Wall Inertia Only	β		U	—	U
Linear Plate	α, β		U	—	S
Membrane	τ, β	$\tau \geq \tau^c_{ms}$	S	—	S
		$\tau < \tau^c_{ms}$	U	—	S
Elastic Solid	γ, β		S	—	U
No Linear Springs	α, τ, β	$\tau \geq \tau^c_s$	S	—	S
		$\tau < \tau^c_s$	U	—	S
No Tension	α, γ, β	$\gamma \leq \gamma^c_{\alpha s}$	S	U	S
		$\gamma^c_{\alpha s} < \gamma$	S	—	S
No Bending	τ, γ, β	$\gamma \leq \gamma^c_{\tau s}$	S	U	S
		$\gamma^c_{\tau s} < \gamma$	S	—	S
Full Model	$\alpha, \tau, \gamma, \beta$	$\tau < \tau^c_{fs}, \gamma < \gamma^c_{fs}$	S	U	S
		$\tau < \tau^c_{fs}, \gamma \geq \gamma^c_{fs}$	S	—	S
		$\tau \geq \tau^c_{fs}, \gamma < \gamma^c_{fs}$	S	—	S

Table 2.1: A summary of the stability of the varying model simplifications examined. Where parameter sizes have been specified, they are for the corresponding symmetric mode although the qualitative behaviour of the antisymmetric mode is the same. S denotes Stable, U denotes Unstable.

was found to hold in any system in which both tension and inertia were present, including when all parameters are non-zero.

The spring response was found to stabilise the system at long wavelengths, reversing the stability of the system there for any system in which it was included. At short wavelengths, the spring response was found to have no effect, meaning that in the absence of any other parameters the system becomes unstable in this region. However, the inclusion of either bending stiffness or tension immediately dominates at short wavelength to stabilise the system.

The inclusion of a small enough spring response was found to cause an interesting effect when in the presence of at least two other parameters (one of which must be β). Providing γ is small enough it is possible to obtain modes in which the system is stable to both small and large wavenumbers disturbances but unstable for a range of values of k between the two regions of stability. While the critical value of γ, above which this unstable region does not exist and the entire system becomes stable could be calculated numerically, this was omitted due to the difficulty in examining the behaviour of something that depends upon three other quantities.

This has given us different ways in which we can stabilise the full system across all values of $k > 0$, by either making τ or γ large enough, however it emerges there are no cases or modes in which the system is always unstable.

CHAPTER THREE

SPATIAL STABILITY ANALYSIS OF FLOW IN AN ELASTIC CHANNEL

3.1 Introduction

In this chapter we will determine the spatial stability of flow in an infinitely long elastic channel subjected to a oscillatory perturbation at a fixed point. The problem will be formulated for the same channel as used in Chapter 2, but our focus will be on the limiting case of the linear-plate model. We will derive the dispersion relation for the complex wavenumber k in terms of the applied real frequency ω.

If ω were allowed to be complex, we would be studying exactly the same system as de Langre (2002) who determined the velocity at which flow transitions from convective intability to absolute instability without reference to specific roots. Although we restrict ω to be real, we build on this work by calculating the location of roots of the dispersion relation and determining their influence on the stability of the system.

To make this determination a method of classifying both the stability and direction of propagation of these roots for k will be introduced and applied. We begin with the simplest model possible, that is, the inertia β is negligible and the frequency of oscillation ω is zero. We will then make the system more realistic by including a non-zero frequency of oscillation, the roots found previously are tracked and their stability checked as the

frequency changes. Finally, inertia is reintroduced to the system and the roots and their stability are determined for various sizes of the physical parameters. These results are then compared with previous related work in the literature.

3.2 Problem Formulation

The system is identical to the one considered in Chapter 2, therefore the governing equations (2.2.1)–(2.2.2) and boundary conditions (2.2.4)–(2.2.5) still hold. The primary difference arises in the type of perturbation we apply. In this case, we consider a time-dependent oscillation with fixed frequency, ω, applied with a specified amplitude at $x = 0$. This gives us perturbations of the form

$$\begin{aligned} \mathbf{u}' &= e^{i(kx-\omega t)}\hat{\mathbf{u}}(y), \\ p' &= e^{i(kx-\omega t)}\hat{p}(y), \\ \eta'_{\pm} &= e^{i(kx-\omega t)}\hat{\eta}_{\pm}, \end{aligned} \tag{3.2.1}$$

where $\omega \in \mathbb{R}$ and $\hat{\mathbf{u}}(y)$, $\hat{p}(y)$ and $\eta_{\pm}$ are the amplitudes at $x = 0$. Without loss of generality we take $\omega > 0$. We want to find the wavenumbers k, generated by a given forcing frequency ω.

It is possible to perform the stability analysis as in Chapter 2, however, it is more convenient to make a single substitution in the dispersion relation, (2.3.24), found previously. We set

$$s = -i\omega, \tag{3.2.2}$$

where, since $\omega \in \mathbb{R}$, s is purely imaginary. This gives us a new dispersion relation, which we can write in the form

$$\mathcal{D}(\omega, k) = 0, \tag{3.2.3}$$

where

$$\mathcal{D}(\omega, k) = (k - \omega)^2 X(k) - \left(\alpha k^5 - \beta\omega^2 k + \tau k^3 + \gamma k\right). \tag{3.2.4}$$

Here, α, β, τ and γ are dimensionless parameters giving the ratios of various physical effects as in (2.2.10), $X(k) = \tanh(k)$ for the antisymmetric mode, and $X(k) = \coth(k)$ for the symmetric mode. We focus on the linear plate limiting case, where the effects of both tension and spring response are negligible. This is equivalent to setting $\tau = \gamma = 0$ in (3.2.4).

Combining (3.2.3) and (3.2.4), along with our simplifications gives

$$(k - \omega)^2 X(k) = \left(\alpha k^4 - \beta\omega^2\right) k. \tag{3.2.5}$$

In Chapter 2 for temporal stability we sought $\omega \in \mathbb{C}$, in terms of a given $k \in \mathbb{R}$, however, in this case we want to find $k \in \mathbb{C}$ in terms a given $\omega \in \mathbb{R}$. Looking at (3.2.5) it is clear this is not a trivial exercise, as we go from solving an equation quadratic in ω to solving an equation that is quintic in k as well as having a $\tanh$ or $\coth$ component.

3.2.1 Method of determining stability

Once the positions of the roots have been calculated, it is necessary to determine the stability and direction of propagation of the resultant waves. Traditionally this is done by calculating their group velocity. The real part of the group velocity gives the direction of propagation, while the sign of the imaginary part determines the stability (Lighthill, 1960). However, in systems with an infinite amount of fluid that has a background flow, such as we have here with the plug flow, this technique is no longer reliable because it is possible for there to be waves that propagate downstream but have a group velocity pointing upstream (Crighton & Oswell, 1991; Peake, 1997).

To counteract this, an alternative method of determing the stability and propagation of waves when there is a spatial component to the analysis was proposed by Briggs (1964) and then refined by Bers (1983). It was originally developed in the context of plasma physics, but has found extensive use in other areas of mathematics. In its most general form, it is applied to systems in which both the wavenumber and frequency are complex, but it also has applications when the frequency is real (Brazier-Smith & Scott, 1984). For

this reason, we focus on the application as described by Brazier-Smith & Scott (1984), but the formulation by Bers (1983) remains the most detailed introduction to the general method. Illustrated examples of the application of the general technique can also be found in Brambley (2007).

Recall from Chapter 1, that a convectively unstable wave results in a growing disturbance away from the driver, while remaining neutral or decaying at the driver. Similarly, an absolute instability results in a growing disturbance both away from the driver and at the driver. The latter can be thought of as the instability growing more quickly than it is advected away downstream, and thus it contaminates the entire domain.

The Briggs–Bers method we use is as follows. For a root $k = k_0$, $\omega = \omega_0$ of the dispersion relation $\mathcal{D}(k, \omega) = 0$, with $\omega_0 \in \mathbb{R}$, $k_0 \in \mathbb{C}$, locate the equivalent root for k when $\omega = \omega_0 + i\omega_i$ where $\omega_i \in \mathbb{R}$ and $\omega_i > 0$ and suitably large. This choice of ω_i needs to be larger than any naturally occurring growth rate in the system. Then at any point in time the amplitude of the oscillation at the driver will be greater than any growth caused by a natural growing disturbance, and the wave will appear to decay in the direction of propagation.

If, when ω_i is large, the root has $\mathrm{Im}(k) > 0$ then in order to decay it will propagate in the downstream direction, while if $\mathrm{Im}(k) < 0$ it will propagate in the upstream direction. This is fixed by examination of the e^{ikx} term in (3.2.1).

Then, we decrease ω_i continuously until $\omega_i = 0$, relying upon the fact that the direction of propagation does not change as ω_i is decreased (providing no other roots are encountered as ω_i is varied). One of the following three behaviours will be seen

(a) When $\omega_i = 0$ the root is in the same half of the k-plane as it started, thus the wave is evanescent in the direction of propagation.

(b) When $\omega_i = 0$ the root lies on the $\mathrm{Re}(k)$-axis, thus the wave is a neutrally stable travelling wave in the direction of propagation. As ω_i is decreased, the root may cross the $\mathrm{Re}(k)$-axis any number of times.

(c) When $\omega_i = 0$, the root comes to rest in the opposite half of the k-plane as it started,

thus resulting in a convectively unstable wave in the direction of propagation.

It is possible for two roots that originate in opposite halves of the k-plane for large ω_i to come together and form a pinch for $\omega_i \neq 0$. In systems where the frequency ω is allowed to be complex, this results in an absolute instability.

A useful consequence of this, is, if there is to be a convective instability in the system, a root must cross the $\mathrm{Re}(k)$-axis when $\omega_i > 0$, at this point $k \in \mathbb{R}$ and $\omega \in \mathbb{C}$ which are the conditions for a temporally unstable mode. Thus, we must have temporal instability for there to be spatial instability. This is a necessary but not sufficient condition however, since as ω_i decreases further the root may come to lie on the $\mathrm{Re}(k)$-axis, or cross back to the original half-plane.

3.3 Limiting case of $\beta = 0$, $\omega_r = 0$

We consider first a large simplification to the dispersion relation to serve as an introduction to the application of the Briggs–Bers technique. We assume both a lack of inertia in the system and the real part of ω to be zero. Assuming no inertia determines that there should be no instabilities in the system since spatial instabilities require temporal instabilities to be present as discussed above and our work in Chapter 2 found the system had temporal instabilities only when inertia was present. Therefore, we should only be able to find evanescent waves or neutrally stable waves. The assumption that $\omega_r = 0$, where $\omega_r = \mathrm{Re}(\omega)$ is very restrictive, but it gives a simpler system that lends itself well to analysis.

3.3.1 Antisymmetric Mode

Under the assumption of no inertia, $\beta = 0$, the dispersion relation (3.2.5) can be written

$$\alpha k^5 \coth(k) - (k - i\omega_i)^2 = 0. \tag{3.3.1}$$

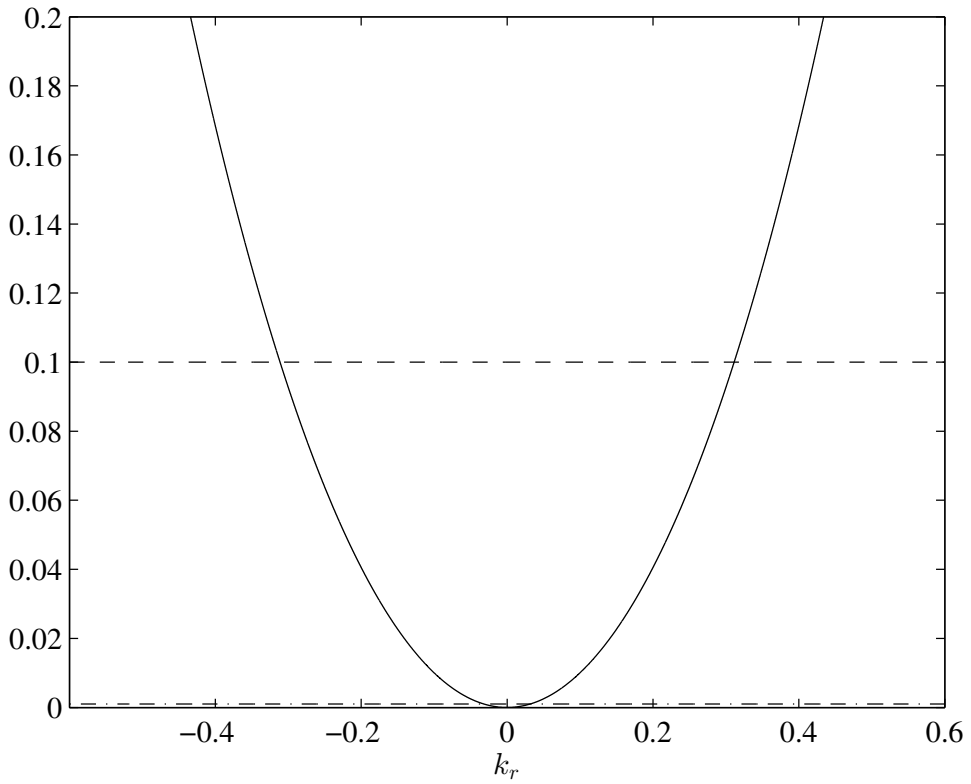

Figure 3.1: Illustrations of the positions of the solutions of (3.3.2) for varying α. The solid line is the left hand side of the equation, while the broken lines are the right hand side. Specifically, the dashed line corresponds to $\alpha = 10$ and the dashed-dot line to $\alpha = 10^3$.

We retain ω in the equation since it is necessary in the application of the Briggs–Bers technique, but it is understood here to be purely imaginary and is ignored when solving for k to find the location of the roots. If $k \in \mathbb{R}$, there exists a double root at $k = 0$ and

$$k_r^3 \coth(k_r) = \frac{1}{\alpha}. \tag{3.3.2}$$

Solving (3.3.2) cannot be done analytically, but there are two roots, which will approach $k = 0$ as $\alpha \to \infty$, and will tend to infinity as $\alpha \to 0$, as illustrated in Figure 3.1. We also consider roots of the form $k = ik_i$, $k_i \in \mathbb{R}$, for which we rewrite (3.3.1) as

$$k_i^5 \cot(k_i) = \frac{(ik_i - \omega)^2}{\alpha}, \tag{3.3.3}$$

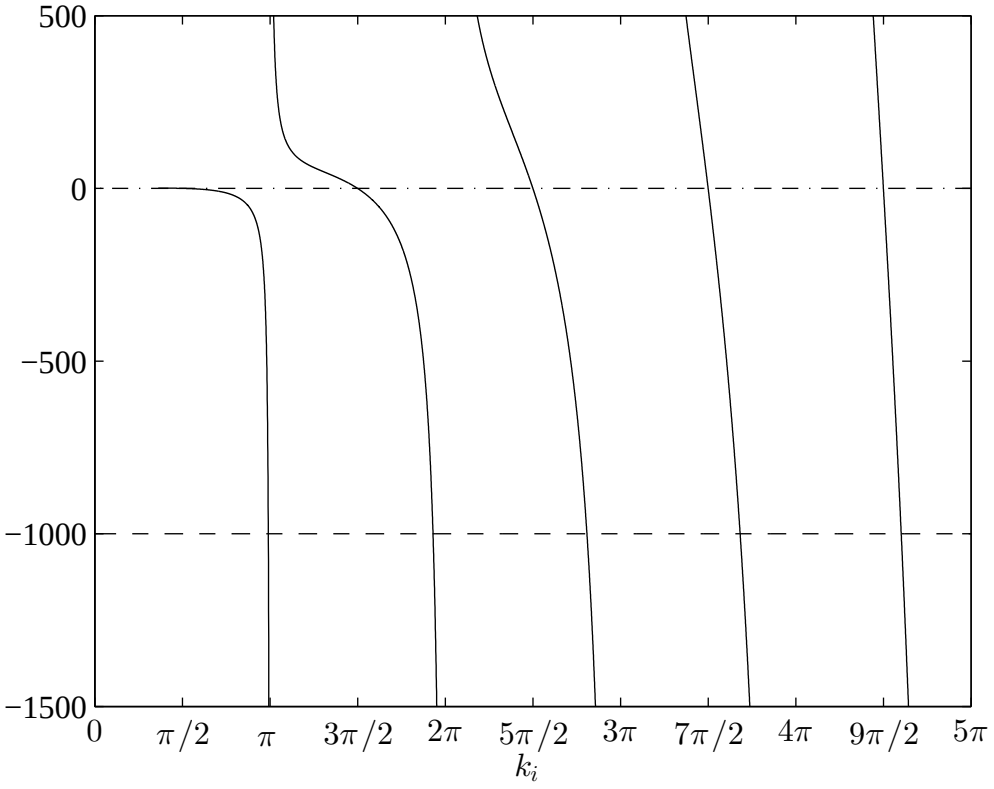

Figure 3.2: Illustrations of the positions of the solutions of (3.3.4) for varying α. The solid line is the left hand side of the equation, while the broken lines are the right hand side. Specifically, the dashed line corresponds to $\alpha = 10^{-3}$ and the dashed-dot line to $\alpha = 10^{3}$. The graph is symmetric about $k_i = 0$.

when $\omega = 0$ this can be written as

$$k_i^3 \cot(k_i) = -\frac{1}{\alpha}, \tag{3.3.4}$$

which has solutions in the range $k_i \in [(n - 1/2)\pi, n\pi]$ for $n \in \mathbb{Z}$. As $\alpha \to \infty$, $k_i \to (n - 1/2)\pi$ and as $\alpha \to 0$, $k_i \to n\pi$. So there is an infinite set of solutions lying on the $\mathrm{Im}(k)$-axis. To illustrate the behaviour of the imaginary roots when α varies, both sides of (3.3.4) have been plotted in Figure 3.2. We could not find any solutions that have both nonzero real and imaginary components of k.

We now apply the Briggs–Bers technique to track these roots and determine the stability of the corresponding waves. The results are illustrated in Figures 3.3 and 3.4 for small and large α respectively, for all the roots with $\mathrm{Im}(k) = 0$. The roots are tracked

by solving the equations numerically using Newton's method for each $\omega_i = \mathrm{Im}(\omega)$. In both cases, we see that both roots that make up the double root at $k = 0$ start in the upper k-plane ($\mathrm{Im}(k) > 0$) for ω_i large and positive, and descend to the $\mathrm{Re}(k)$-axis as ω_i decreases to zero, therefore these are right-travelling neutral waves. Similarly, the two roots that are solutions to (3.3.2) both start in the lower $\mathrm{Im}(k)$ plane and ascend to the $\mathrm{Re}(k)$-axis, suggesting that they are both left-travelling neutral waves. We also see the roots move inwards towards the double root as α increases. One feature of note in Fig 3.3 is that the two branches of the double root at $k = 0$ coalesce before ω_i has been decreased to zero, however since both branches start on the same side of the $\mathrm{Re}(k)$-axis this does not lead to an instability.

For the infinite set of solutions, we provide a non-graphical argument to show the stability of the roots. Consider (3.3.3) with $\omega = i\omega_i$, then

$$k_i^5 \cot(k_i) = -\frac{(k_i - \omega_i)^2}{\alpha}. \tag{3.3.5}$$

For any ω_i the right hand side keeps the same sign as (3.3.4) and thus the root will not cross the $\mathrm{Im}(k)$-axis at any point as ω_i is decreased to zero. These solutions can therefore be divided into two groups, those with $k_i > 0$ and those with $k_i < 0$, the former consist of right-travelling evanescent waves decaying downstream of the driver and the latter are left-travelling evanescent waves decaying upstream of the driver.

We numerically sought solutions for which k had both real and imaginary components but were unable to find any. For this reason it is thought all solutions have been found and so upon the inclusion of the frequency we can track the positions of the roots as they change.

3.3.2 Symmetric Mode

Assuming no inertia, from (3.2.5) the symmetric mode dispersion relation can be written

$$\alpha k^5 \tanh(k) - (k - \omega)^2 = 0, \tag{3.3.6}$$

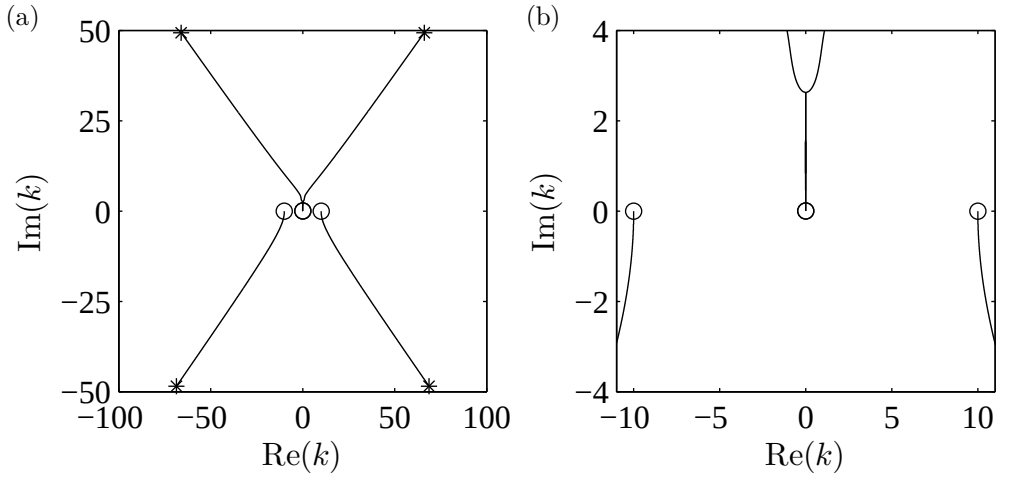

Figure 3.3: (a) Solution paths in k-space for the antisymmetric dispersion relation when $\beta = \mathrm{Re}(\omega) = 0$ for $\mathrm{Im}(\omega) = 2000$ (stars) to $\mathrm{Im}(\omega) = 0$ (circles) when $\alpha = 10^{-3}$. (b) A close up of the origin, to better illustrate the finishing points of the roots.

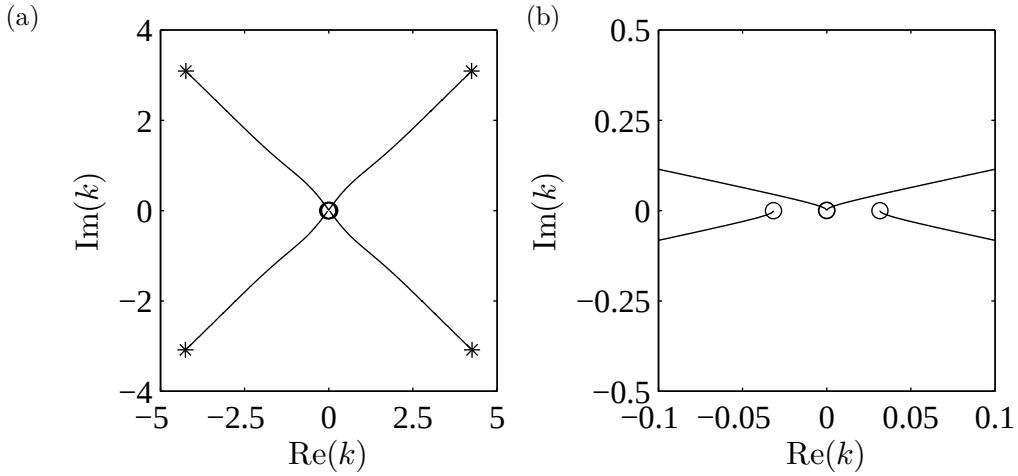

Figure 3.4: (a) Solution paths in k-space for the antisymmetric dispersion relation when $\beta = \mathrm{Re}(\omega) = 0$ for $\mathrm{Im}(\omega) = 2000$ (stars) to $\mathrm{Im}(\omega) = 0$ (circles) when $\alpha = 10^{3}$. (b) A close up of the origin, to better illustrate the finishing points of the roots.

where, again, ω is retained for the application of the Briggs–Bers technique but is ignored when solving for k. As in the antisymmetric mode there still exists the double root at $k = 0$ when $k \in \mathbb{R}$, leaving

$$k^3 \tanh(k) = \frac{1}{\alpha}. \tag{3.3.7}$$

This again has two roots, that behave in the same way as those for the antisymmetric mode, that approach $k = 0$ as $\alpha \to \infty$, and tend to infinity as $\alpha \to 0$. If we consider

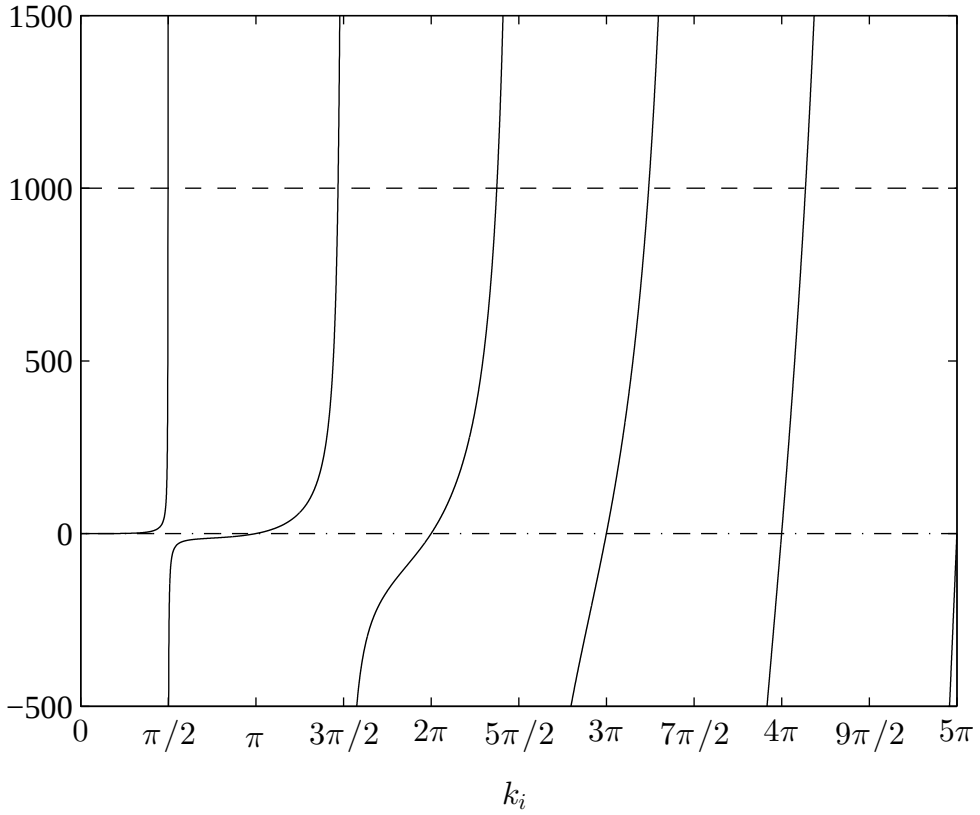

Figure 3.5: Illustrations of the positions of the solutions of (3.3.9) for varying α. The solid line is the left hand side of the equation, while the broken lines to the right hand side. Specifically, the dashed line corresponds to $\alpha = 10^{-3}$ and the dashed-dot line to $\alpha = 10^{3}$. The graph is symmetric about $k_i = 0$.

imaginary roots, then (3.3.6) becomes

$$-k_i^5 \tan(k_i) = \frac{(ik_i - \omega)^2}{\alpha}, \tag{3.3.8}$$

which, when $\omega = 0$ is

$$k_i^3 \tan(k_i) = \frac{1}{\alpha}, \tag{3.3.9}$$

where $k_i \in i\mathbb{R}$. This has solutions in the range $[n\pi, (n + 1/2)\pi]$ where $n \in \mathbb{Z}$. For small α the solution lies closer to $(n + 1/2)\pi$ and for large α it lies closer to $n\pi$. This is shown in Figure 3.5. To avoid unnecessary repetition, we do not give the stability diagrams for the symmetric mode as we obtain the same results as for the antisymmetric mode.

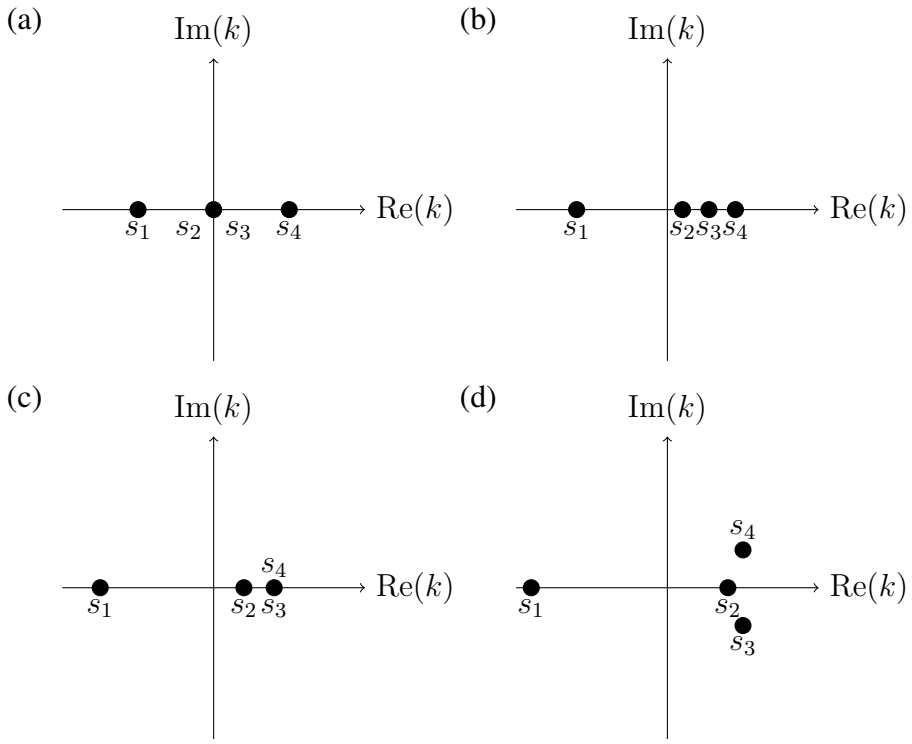

Figure 3.6: Sketch of the movement of solutions to the antisymmetric and symmetric mode dispersion relations as ω_r is varied. (a) $\omega_r = 0$, (b) $0 < \omega_r < \omega_c(\alpha)$, (c) $\omega_r = \omega_c(\alpha)$, (d) $\omega_c(\alpha) < \omega_r$.

3.4 Limiting case of $\beta = 0$

We extend our analysis to include $\omega_r \neq 0$, while continuing to assume a lack of inertia, $\beta = 0$. In the absence of inertia the system should remain stable but with the addition of a real component to the frequency, there will no longer be a double root at $k = 0$ so we will aim to determine how the roots move as ω_r and α are varied.

3.4.1 Antisymmetric Mode

We first consider solutions to the dispersion relation for which $k = k_r \in \mathbb{R}$. Thus, for a real $\omega = \omega_r$, the dispersion relation can be written

$$\alpha k^5 \coth(k) - (k - \omega_r)^2 = 0. \tag{3.4.1}$$

If $\omega_r = 0$ then the previously examined case is recovered, with roots positioned as in Figure 3.6(a). The position of these roots was tracked numerically for ω_r increasing again

using Newton's method, their qualitative behaviour is shown in Figure 3.6(b)–(d). As ω_r is increased to a non-zero value, but is less than a critical value ω_c that depends upon α, the system has four real roots. Two roots, s_1 and s_4, move in the negative $\mathrm{Re}(k)$ direction as ω_r increases, while s_2 and s_3 move in the positive $\mathrm{Re}(k)$ direction, with s_3 moving further than s_2. Once $\omega_r = \omega_c(\alpha)$, roots s_3 and s_4 coalesce and then as ω_r increases further, the system only permits two real roots s_1 and s_2, with s_3 and s_4 leaving the $\mathrm{Re}(k)$-axis to gain an imaginary component.

The stability of the roots as ω_r is varied is determined in Figures 3.8–3.10. As expected from the $\omega_r = 0$ case studied previously, for values of $\omega_r \leq \omega_c(\alpha)$ two neutrally stable waves are obtained travelling in each direction. The meeting of the roots when $\omega_r = \omega_c$ occurs at $\mathrm{Im}(k) = 0$ and therefore does not produce an instability (Brazier-Smith & Scott, 1984). However, once $\omega_r > \omega_c(\alpha)$ the two roots that coalesced separate again with the right-travelling wave gaining a positive $\mathrm{Im}(k)$ component and the left-travelling wave a negative $\mathrm{Im}(k)$ component. These two waves are therefore evanescent, decaying in their direction of travel. The behaviour of the roots was found to be the same across all values of the bending stiffness α, with an inverse correlation between α and ω_c as shown in Figure 3.7.

It is not possible to find solutions to the dispersion relation (3.4.1) of the form $k = ik_i$, $k_i \in \mathbb{R}$ when $\omega_r \neq 0$. However, beginning from the $\omega_r = 0$, case the solutions can be tracked as for the real roots above, the results for this are shown in Figure 3.11.

There is some interesting behaviour exhibited; in all cases there is a pair of solutions equivalent to $\pm n_0$, which move out of the set as ω_r increases. For $\alpha = 10^{-3}$, this occurred for $n_0 = 5$ (not pictured), for $\alpha = 1$, $n_0 = 2$ and for $\alpha = 10^3$, $n_0 = 1$. The behaviour of the roots either side of this root differ. If $|n| < n_0$, the nth root progresses to the next integer multiple of π away from the $\mathrm{Re}(k)$-axis as ω_r increases. However, for $|n| > n_0$, the nth root moves inwards to the next integer multiple of π towards the $\mathrm{Re}(k)$-axis, essentially taking the place of the root that has moved away.

As ω_r increases further and the separated pair of roots move further from the $\mathrm{Re}(k)$-axis, an integer multiple of π near the imaginary axis is always left clear of a root, but

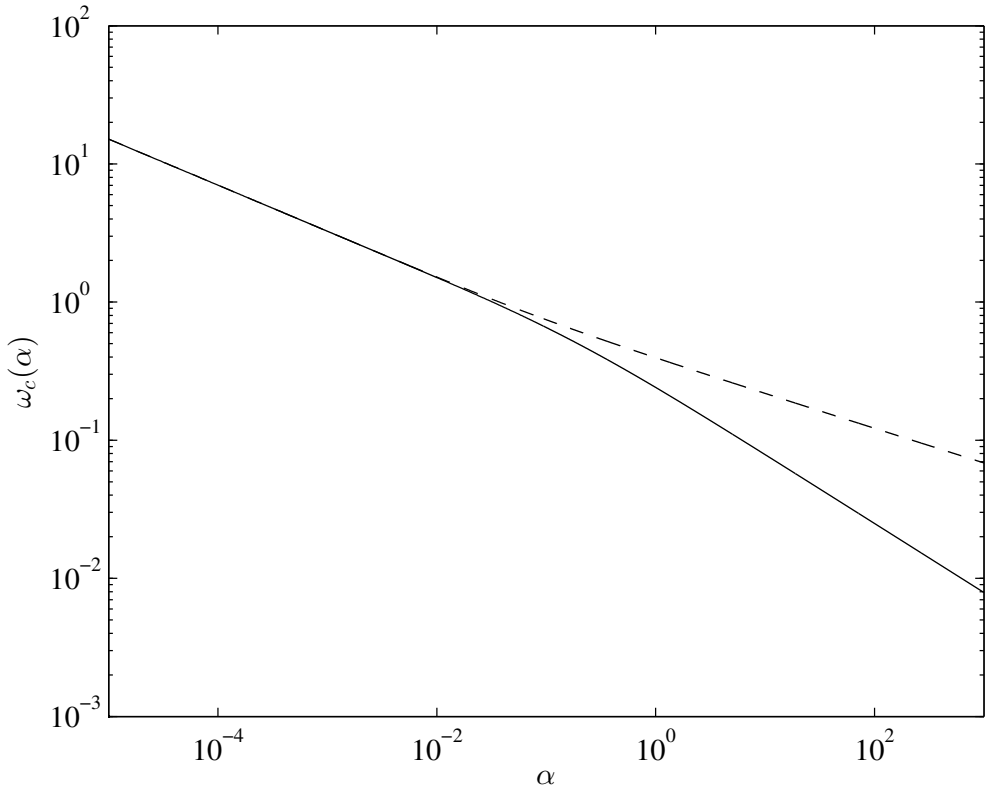

Figure 3.7: The variation of the critical frequency ω_c with respect to the bending stiffness α. The solid line corresponds to the antisymmetric mode, the dashed line to the symmetric mode.

not necessarily the one it started at originally. This effect can be seen in the stability analysis of Figure 3.12(c). The root originally corresponded to $n = 1$ when ω_r was small. However, when ω_r is large, as ω_i decreases (moving towards the circles) the roots move towards the $\mathrm{Im}(k)$-axis but at values near $\pm 2\pi$, equivalent to $n = 2$.

The previously mentioned stability analysis was performed for varying ω_r with the results for $\omega_r = 2000$ shown in Figure 3.12. We can see all roots are evanescent either upstream or downstream. For the roots that lie inside the outlying pair, as ω_i is varied there is only a change in $\mathrm{Re}(k)$ but further out the predominant change is in $\mathrm{Im}(k)$.

The outlying pair of roots from the infinite set have a further significance. When viewed in conjunction with the real roots discussed previously, and the progression of two of the roots away from the $\mathrm{Re}(k)$-axis as ω_r increases, we see a group of six solutions that appear related to each other. The progression and formation of this arrangement of roots is illustrated in Figure 3.13.

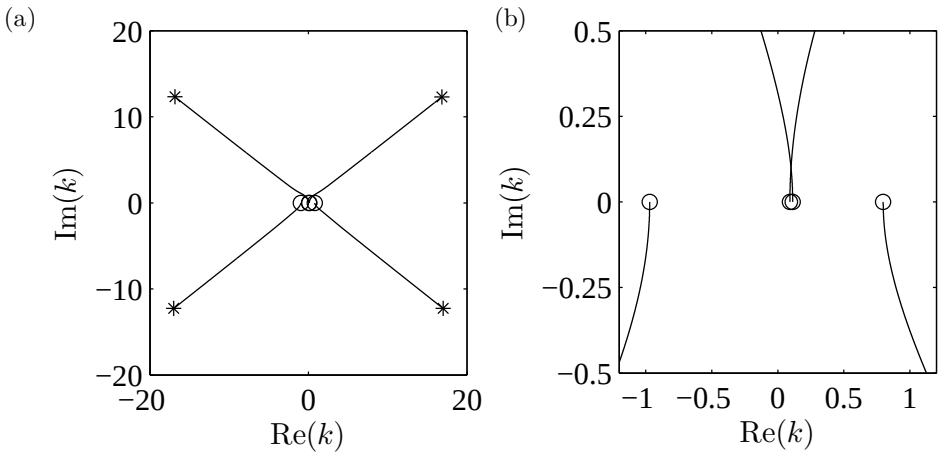

Figure 3.8: (a) Solution paths in k-space for the antisymmetric dispersion relation when $\beta = 0$ and $\omega_r = 0.01 < \omega_c(\alpha)$ for $\mathrm{Im}(\omega) = 2000$ (stars) to $\mathrm{Im}(\omega) = 0$ (circles) when $\alpha = 1$. (b) A close up of the origin, to better illustrate the finishing points of the roots.

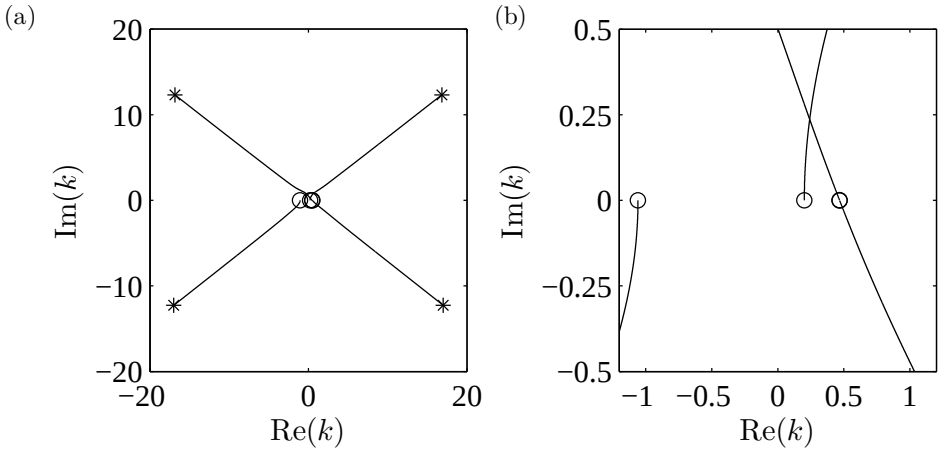

Figure 3.9: (a) Solution paths in k-space for the antisymmetric dispersion relation when $\beta = 0$ and $\omega_r = 0.241235 = \omega_c(\alpha)$ for $\mathrm{Im}(\omega) = 2000$ (stars) to $\mathrm{Im}(\omega) = 0$ (circles) when $\alpha = 1$. (b) A close up of the origin, to better illustrate the finishing points of the roots.

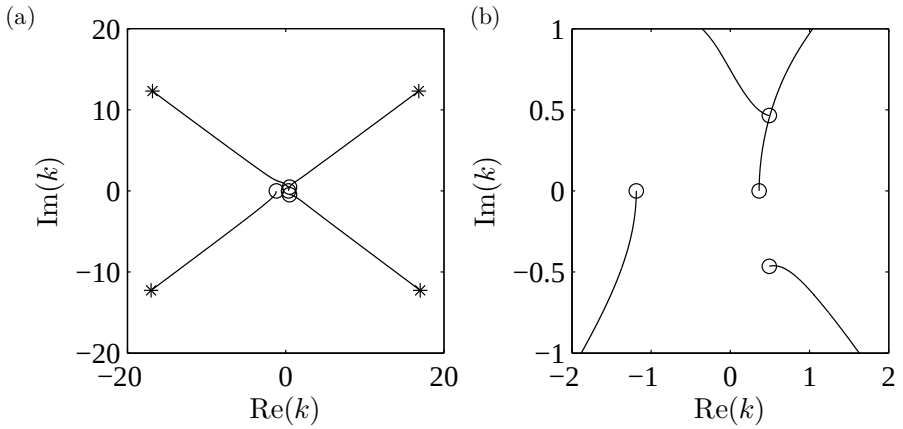

Figure 3.10: (a) Solution paths in k-space for the antisymmetric dispersion relation when $\beta = 0$ and $\omega_r = 0.5 > \omega_c(\alpha)$ for $\mathrm{Im}(\omega) = 2000$ (stars) to $\mathrm{Im}(\omega) = 0$ (circles) when $\alpha = 1$. (b) A close up of the origin, to better illustrate the finishing points of the roots.

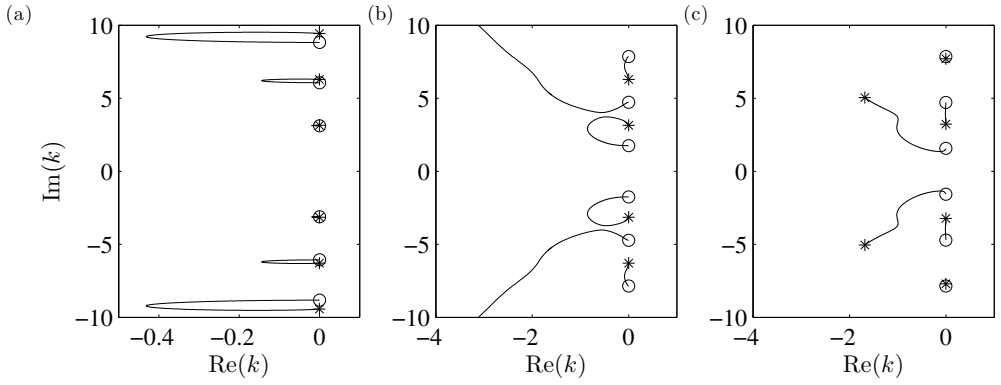

Figure 3.11: Position of the roots of the infinite set of solutions to the dispersion relation up to $|n| = 3$ as ω_r is varied from $\omega_r = 0$ (circles) to $\omega_r = 2000$ (stars). (a) $\alpha = 10^{-3}$, (b) $\alpha = 1$, the $n = \pm 2$ solutions finish at $k = -6.3916 \pm 19.9406i$, (c) $\alpha = 10^{3}$.

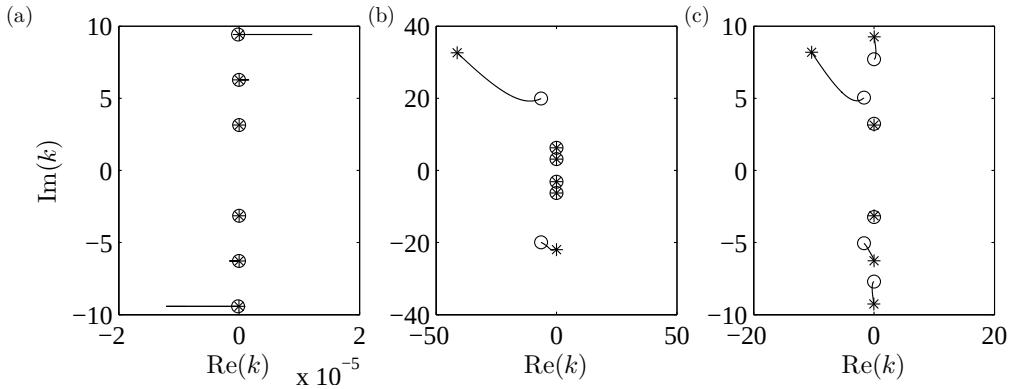

Figure 3.12: Solution paths in k-space for the roots shown in Figure 3.11 when $\omega_r = 2000$ as $\mathrm{Im}(\omega) = 2000$ (stars) to $\mathrm{Im}(\omega) = 0$ (circles). (a) $\alpha = 10^{-3}$, (b) $\alpha = 1$, (c) $\alpha = 10^{3}$.

We can use these numerical solutions as a guide to find analytical expressions for some of the solutions at certain parameter sizes. Looking firstly at Figure 3.13(a), we see four roots with $\omega \ll 1$, and $|k| \ll 1$. Approximating $\tanh(k) \sim k$ for $|k| \ll 1$, (3.4.1), becomes

$$k^4 = \frac{(k-\omega)^2}{\alpha}. \tag{3.4.2}$$

The four solutions to this equation can be written

$$k = \pm\frac{1}{2}\sqrt{\frac{4\omega}{\sqrt{\alpha}} + \frac{1}{\alpha}} - \frac{1}{2\sqrt{\alpha}}, \quad k = \pm\frac{1}{2}\sqrt{\frac{1}{\alpha} - \frac{4\omega}{\sqrt{\alpha}}} + \frac{1}{2\sqrt{\alpha}}. \tag{3.4.3}$$

If $\omega < 1/4\sqrt{\alpha}$ we obtain four real roots. If $\omega > 1/4\sqrt{\alpha}$, we obtain two real roots and

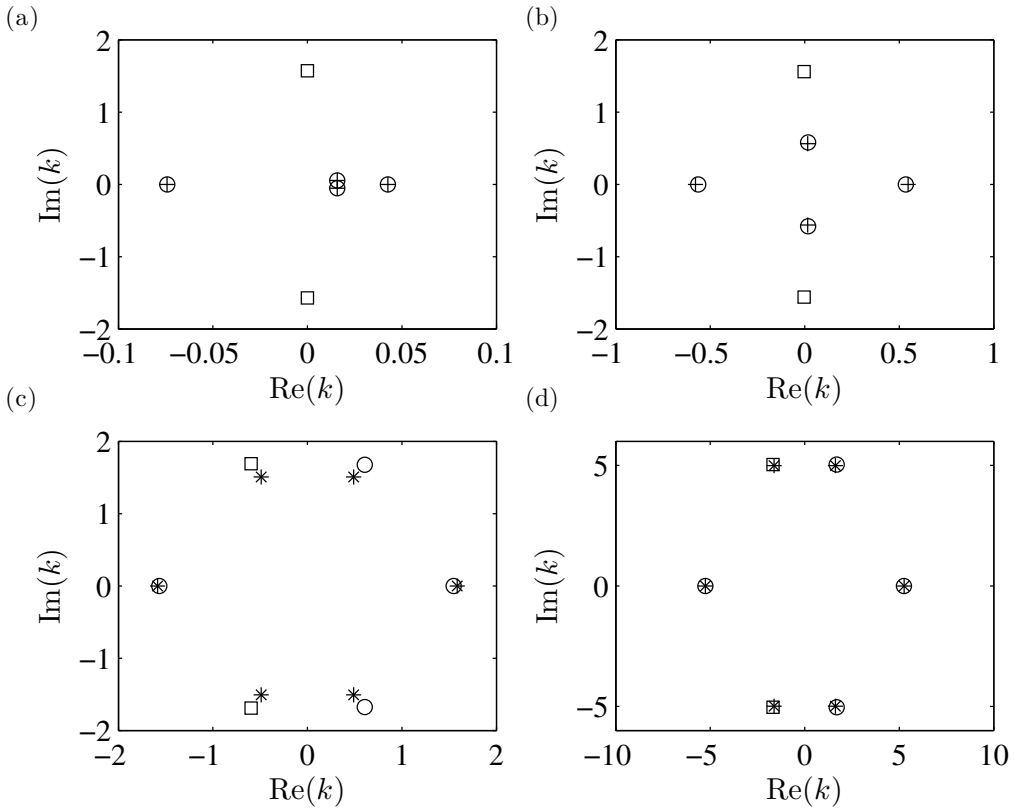

Figure 3.13: The progression of the key roots for $\alpha = 10^3$ as ω_r increases, numerical solutions (circles), numerical solutions for the two roots from the infinite set (squares), approximate solutions given by (3.4.3) (crosses), approximate solutions given by (3.4.6) (stars). (a) $\omega_r = 0.1$, (b) $\omega_r = 10$, (c) $\omega_r = 100$, (d) $\omega_r = 2000$.

two complex roots. Hence an expression for $\omega_c(\alpha)$ is obtained

$$\omega_c(\alpha) = \frac{1}{4\sqrt{\alpha}}, \tag{3.4.4}$$

which, after comparing with Figure 3.7 is found to be valid for $\alpha \approx 1$ and greater. The solutions given by (3.4.3) are shown in Figure 3.13(a)–(b) as a comparison to the numerical solutions. For $\omega_r = 0.1$ the solutions are almost identical, while for $\omega_r = 10$ to solutions are still reasonable but starting to show less agreement as the assumption of $\omega_r \ll 1$ clearly no longer holds.

Similarly, by looking at Figure 3.13(d), we see $\omega_r \gg 1$ and $|\mathrm{Re}(k)|$ is large, we can

approximate $\tanh(k) \sim \mathrm{sgn}(k)$. The dispersion relation, (3.4.1), can be approximated as

$$k^5 = \pm\frac{\omega^2}{\alpha}, \tag{3.4.5}$$

where the plus sign corresponds to $\mathrm{Re}(k) > 0$ and the minus sign to $\mathrm{Re}(k) < 0$. The solution to (3.4.5) can be written

$$k = \pm\left(\frac{\omega^2}{\alpha}\right)^{1/5} \exp\left(\frac{2m\pi i}{5}\right), \tag{3.4.6}$$

where $m = \{-1, 0, 1\}$. We do not pick up all five roots from the exponential term since for roots that would correspond to $m = -2$ and $m = 2$ would lie in the opposite half $\mathrm{Re}(k)$ plane violating the restriction on the sign of k. This gives an approximation of the six roots which are plotted with stars in Figure 3.13(c)–(d). For $\omega_r = 100$ the solutions are accurate for the real roots but not for the complex ones (where $|\mathrm{Re}(k)|$ is not as large). However a much better approximation is found when $\omega_r = 2000$. If ω_r is increased further, these approximations will only become more accurate.

While here it was sufficient to assume that $\omega_r \gg 1$ to find approximate solutions to the roots in practice it must be dependant upon α. As we showed in Figure 3.7, if α is small, the critical value of ω_r above which we develop the complex roots becomes much larger.

3.4.2 Symmetric Mode

As in the previous section when $\omega_r = 0$, the qualitative behaviour of the symmetric mode is the same as the antisymmetric mode. For that reason, discussion of the mode is omitted here, and instead we move on to focus on the full dispersion relation.

3.5 The full dispersion relation

With a good understanding of how the system behaves in the absence of inertia, we now examine the full dispersion relation for flow between two elastic plates as given by (3.2.5).

While the two limiting cases already studied were both predicted and found to be stable to all frequency disturbances independent of the bending stiffness parameter α, the addition of the inertia parameter, β, results in a system that permits temporal instabilities. Thus, while it is unknown which roots, if any, are unstable, their existence is at least permitted by the system. For both the antisymmetric and symmetric modes, $\alpha \ll 1$ and $\alpha \gg 1$ will be considered, for $\beta = 0.1$ and $\beta = 0.8$, with the solutions tracked between the two values of β. These two values of β should be sufficient to capture the relevant behaviours of the system as it is physically unlikely that values of β greater than $\mathcal{O}(1)$ would be found in real systems.

In all cases, there is a root lying on the negative $\mathrm{Re}(k)$-axis, this root is always a left-travelling neutrally stable wave and so has not been illustrated. Similarly, the infinite set of roots lying close to the $\mathrm{Im}(k)$-axis, are always decaying in their direction of travel, and the pair of roots that move away from the axis as ω_r increases behave in the same way as they do in the absence of inertia. For this reason, we consider only the three remaining roots that lie near the positive $\mathrm{Re}(k)$-axis. This is in agreement with Li (1993), who found the same result for plane liquid sheets.

3.5.1 Antisymmetric Mode

Considering first the antisymmetric mode, the dispersion relation (3.2.5) can be written

$$(k-\omega)^2 = \left(\alpha k^4 - \beta\omega^2\right) k \coth(k). \tag{3.5.1}$$

We first consider the case of weak inertia, and take $\beta = 0.1$. When $\alpha \ll 1$, and $\omega_r \ll 1$, we have the behaviour exhibited by the roots in Figure 3.14(a). Using the Briggs–Bers technique, these roots consist of one root that corresponds to a right-travelling evanescent wave, one right-travelling convectively unstable wave, and one root that is a left-travelling neutral wave (not pictured). As ω_r increases, the growth rate of the unstable mode increases (Figure 3.14(b)), until a critical value of ω_r is reached, at which point a pinch occurs in the lower half k plane (Figure 3.14(c)). This pinch is formed from two

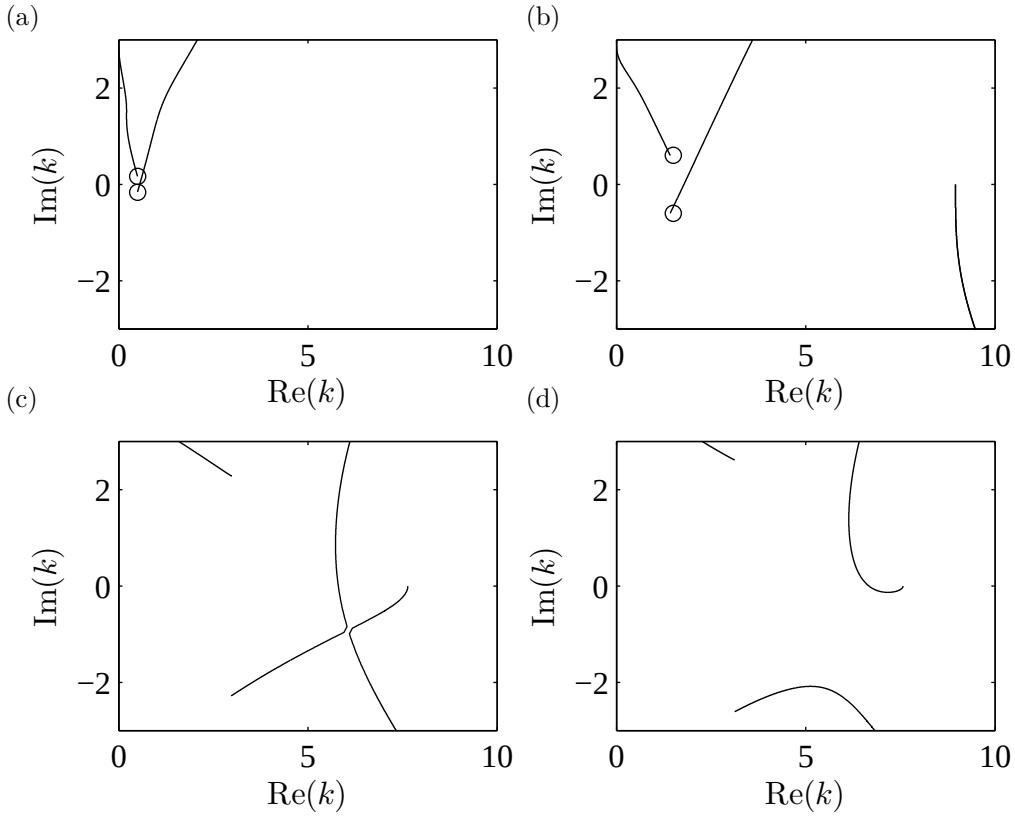

Figure 3.14: Stability of three of the roots to (3.5.1) as the imaginary part of ω is decreased from $\omega_i = 2000$ to $\omega_i = 0$ for varying ω_r, when $\alpha = 10^{-3}$ and $\beta = 0.1$. The end of the curves shown corresponds to $\omega_i = 0$. The circles represent approximate solutions to the roots given by (3.5.6). (a) $\omega_r = 0.5$, (b) $\omega_r = 1.5$, (c) $\omega_r = 3.6725$ (d) $\omega_r = 4$.

roots originating in opposite halves of the k-plane when $\omega_i \gg 1$, satisfying the criteria of an absolute instability. However, as our system requires $\omega \in \mathbb{R}$, and the pinch occurs at $\omega_i > 0$, it does not result in any additional instabilities in the system we consider.

Above this critical value of ω_r the system is stable, consisting now of two evanescent waves, each travelling in the opposite direction and a neutrally stable wave (Figure 3.14(d)).

It is possible to obtain an approximate expression for the position of the unstable root shown in Figure 3.14. By looking at the position of the roots found numerically, we can safely assume that $\mathrm{Re}(k) \ll 1$, suggesting the right hand side of the dispersion relation is much smaller than ω_r^2, thus we require $k \sim \omega$. It is convenient to make the substitution

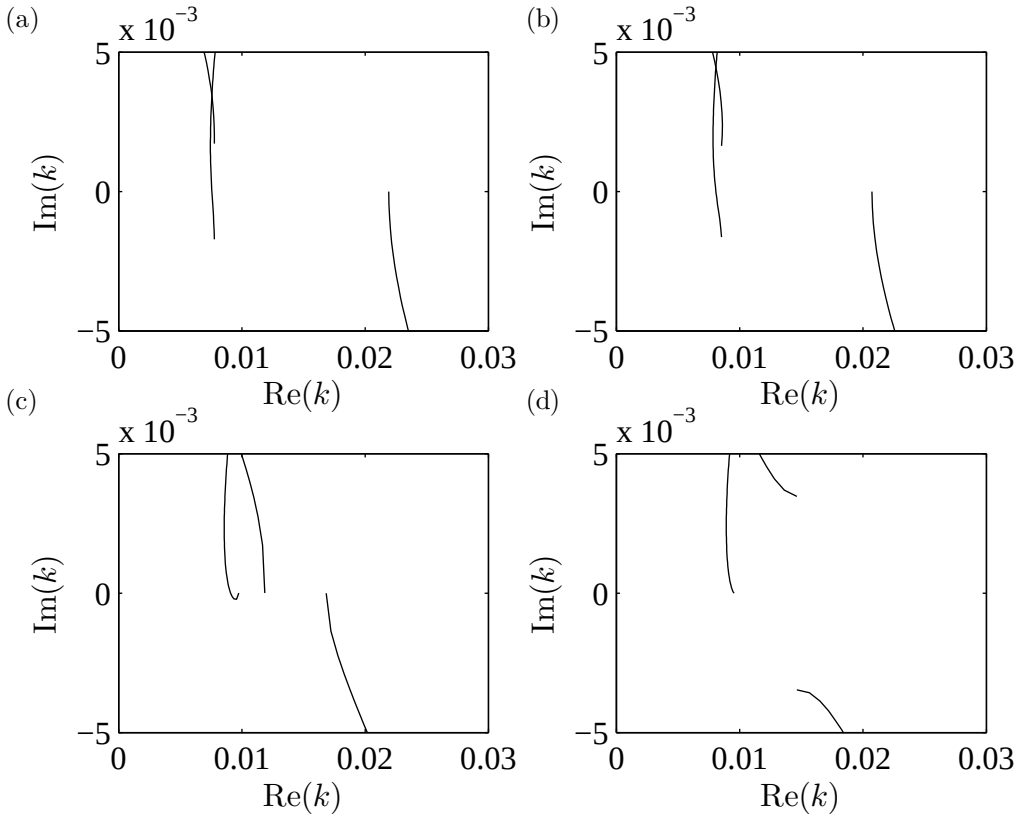

Figure 3.15: Stability of three of the roots to (3.5.1) as the imaginary part of ω is decreased from $\omega_i = 2000$ to $\omega_i = 0$ for varying ω_r, when $\alpha = 10^3$ and $\beta = 0.1$. The end of the curves shown corresponds to $\omega_i = 0$. (a) $\omega_r = 0.00689$, (b) $\omega_r = 0.00734$, (c) $\omega_r = 0.00826$ (d) $\omega_r = 0.00872$.

$\beta = \hat{\beta}\alpha$ in (3.5.1), giving

$$(k-\omega)^2 = \left(k^4 - \hat{\beta}\omega^2\right)\alpha k \coth(k). \tag{3.5.2}$$

Therefore, to obtain a balance in (3.5.2), we require $k-\omega = \mathcal{O}(\alpha^{1/2})$, so a series solution is sought in the form

$$k(\alpha) = \omega + \alpha^{\frac{1}{2}}k_1 + \alpha k_2 + \ldots, \tag{3.5.3}$$

To leading order this is the same as the results found by Li (1993) for a plane liquid sheet, suggesting a qualitative similarity when the effect of the channel walls is small.

Upon substituting (3.5.3) back into (3.5.2), the leading order terms cancel, leaving an equation for the first order correction in α. After substituting and cancelling, the equation

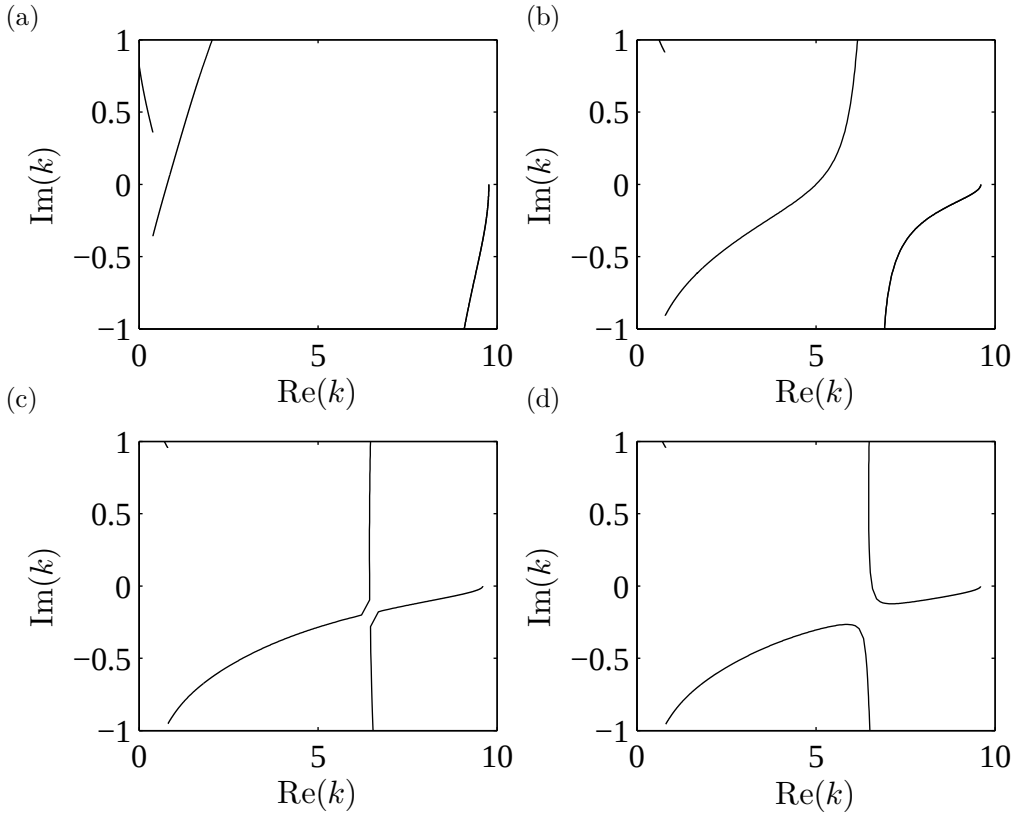

Figure 3.16: Stability of three of the roots to (3.5.1) as the imaginary part of ω is decreased from $\omega_i = 2000$ to $\omega_i = 0$ for varying ω_r, when $\alpha = 10^{-3}$ and $\beta = 0.8$. The end of the curves shown corresponds to $\omega_i = 0$. (a) $\omega_r = 0.4$, (b) $\omega_r = 1$, (c) $\omega_r = 1.0468$ (d) $\omega_r = 1.05$.

can be written

$$k_1^2 = -\left(\hat{\beta} - \omega^2\right)\omega^3 \coth(\omega). \tag{3.5.4}$$

So k_1 is found to be

$$k_1 = \pm i\sqrt{\frac{\omega^3\left(\hat{\beta} - \omega^2\right)}{\tanh(\omega)}}. \tag{3.5.5}$$

and the series solution for antisymmetric perturbations, given $\alpha \ll 1$ can be written

$$k(\alpha) = \omega \pm i\sqrt{\frac{\omega^3\left(\hat{\beta} - \omega^2\right)}{\tanh(\omega)}}\alpha^{\frac{1}{2}} + \mathcal{O}(\alpha) + \ldots. \tag{3.5.6}$$

For $\alpha \ll 1$ this approximate solution remains accurate until $\omega_r \approx 1$, above which it starts to diverge from the numerical solution.

Considering now $\alpha \gg 1$, there is a significant difference in behaviour to that described above for $\alpha \ll 1$. The first difference is there is no longer a pinch associated with a critical value of ω_r, instead there are now two critical values, giving three distinct ranges of ω_r where the behaviour of the system is different. These effects are illustrated in Figure 3.15. In the first region, $0 < \omega_r < \omega_1(\alpha, \beta)$, the behaviour is qualitatively the same as when $\alpha \ll 1$, there are three roots, one evanescent, one neutral and one unstable, the latter of which is right-travelling (Figure 3.15(a)–(b)). At $\omega_r = \omega_1(\alpha, \beta)$, the evanescent and unstable roots coalesce on the $\mathrm{Re}(k)$-axis giving three neutrally stable roots, which exist in the range $\omega_1(\alpha, \beta) < \omega_r \leq \omega_2(\alpha, \beta)$ (Figure 3.15(c)). At $\omega_r = \omega_2(\alpha, \beta)$, the two roots with the largest $\mathrm{Re}(k)$ coalesce, and then split into two complex roots for $\omega_r > \omega_2(\alpha, \beta)$, giving one neutrally stable and two evanescent waves, each travelling in the opposite direction.

We now look at the system when the effect of the inertia is much stronger. The results for $\alpha \ll 1$ can be seen in Figure 3.16. Prior to the pinch occuring, the increase in β has resulted in the unstable root having a larger growth rate (Figure 3.16(a)–(b)). It also becomes clear that the pinch after which the system becomes stable occurs for a much lower value of ω_r when β is larger (Figure 3.16(c)). Above this critical value, the system becomes stable as it did when the effect of the inertia was smaller.

For $\alpha \gg 1$, the results for increased inertia are fundamentally different to those found when β was smaller. In that regime, no pinch occured and instead there were two critical values of ω_r creating three regions in which the behaviour of the system varied. For larger β however, the system retains the behaviour of the equivalent $\alpha \ll 1$ system when β is larger. The key difference between the two is the much smaller size of ω_r at which the system transitions to stable when $\alpha \gg 1$ compared to $\alpha \ll 1$.

There are parallels to be drawn between results from de Langre (2002) and the regimes just discussed. In his paper de Langre found the transition point between convective instability and absolute instability in a fluid channel when both ω and k were allowed to be complex in terms of the nondimensional flow velocity and channel width. For slow flows in a wide channel, the only instability found was convective instability, while for

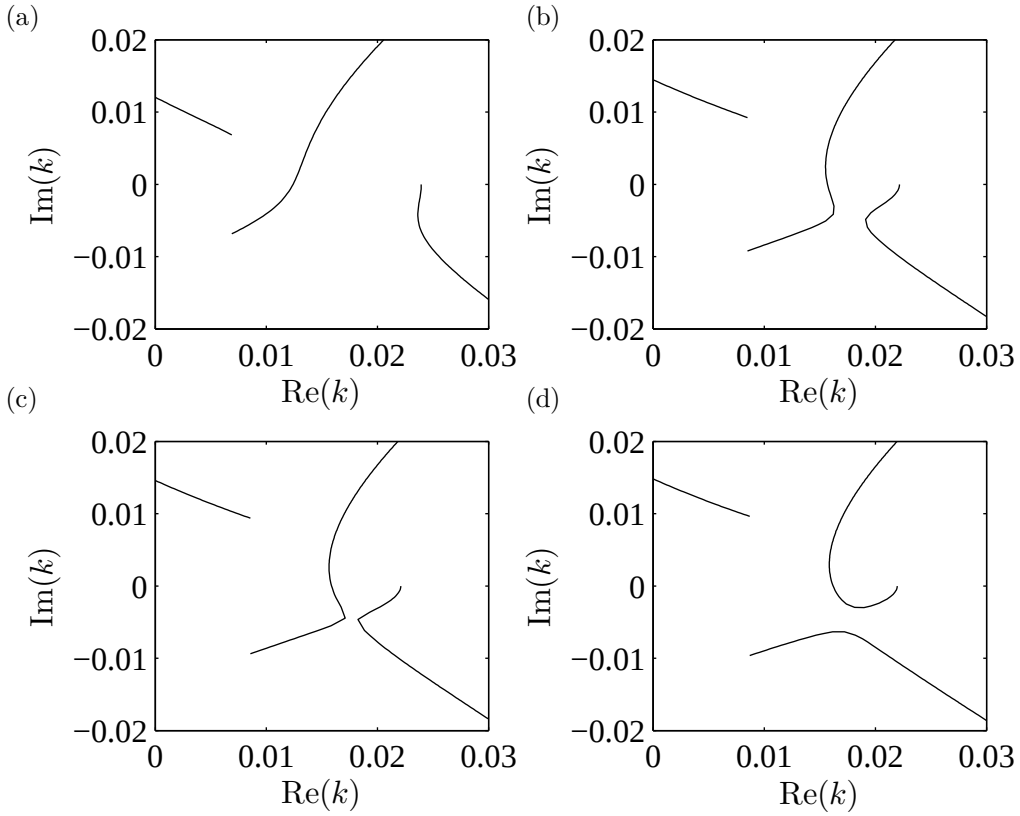

Figure 3.17: Stability of three of the roots to (3.5.1) as the imaginary part of ω is decreased from $\omega_i = 2000$ to $\omega_i = 0$ for varying ω_r, when $\alpha = 10^3$ and $\beta = 0.8$. The end of the curves shown corresponds to $\omega_i = 0$. (a) $\omega_r = 0.00689$, (b) $\omega_r = 0.00872$, (c) $\omega_r = 0.00882$ (d) $\omega_r = 0.009$.

flows above a critical background velocity in any width channel and slow flows in a narrow channel absolute instability was observed. De Langre's nondimensional velocity and channel base-state width are inversely proportional to the parameters we have used for the bending stiffness, α, and inertia, β, respectively. His slow flow in a wide channel therefore corresponds to our large α and small β which is precisely the region in which we did not see a pinch. The three regions where we did see a pinch serve to identify which roots would form the absolute instability if they were admissable to this system.

3.5.2 Symmetric Mode

When considering the symmetric mode, the dispersion relation, (3.2.5) can be written

$$(k-\omega)^2 = \left(\alpha k^4 - \beta\omega^2\right) k \tanh(k). \tag{3.5.7}$$

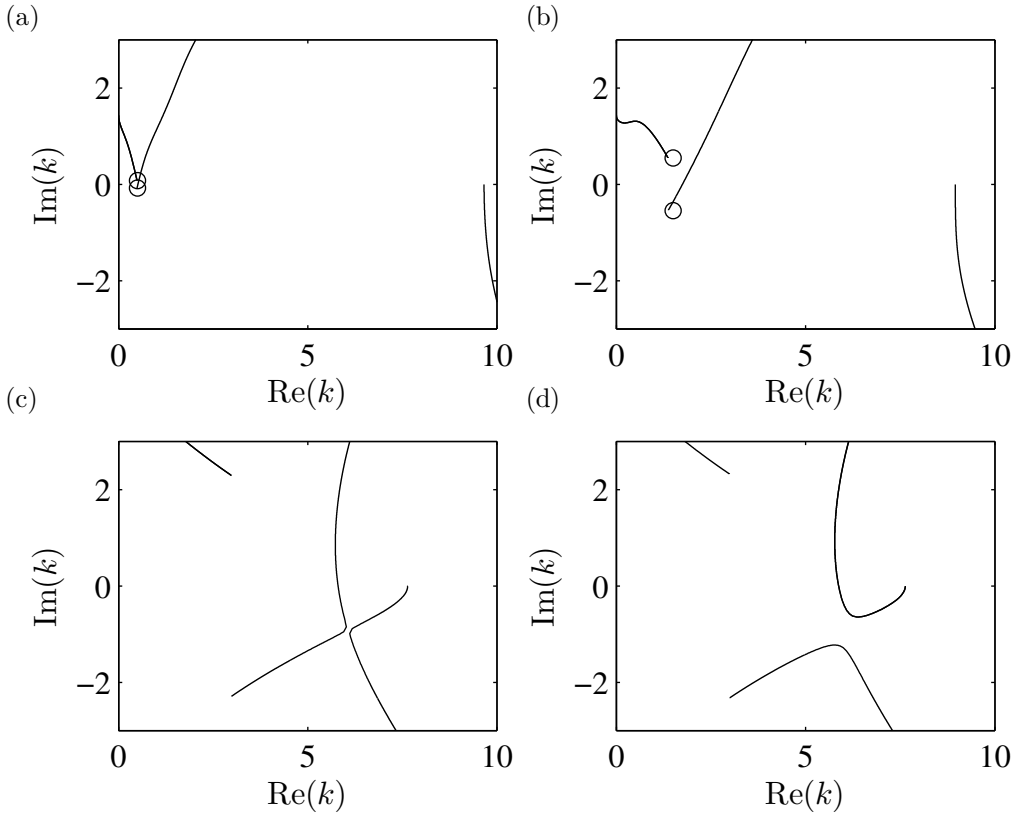

Figure 3.18: Stability of three of the roots to (3.5.7) as the imaginary part of ω is decreased from $\omega_i = 2000$ to $\omega_i = 0$ for varying ω_r, when $\alpha = 10^{-3}$ and $\beta = 0.1$. The end of the curves shown corresponds to $\omega_i = 0$. The circles represent approximate solutions to the roots given by (3.5.6). (a) $\omega_r = 0.5$, (b) $\omega_r = 1.5$, (c) $\omega_r = 3.672$ (d) $\omega_r = 3.7$.

The method of analysis is the same as for the antisymmetric mode, we numerically calculate the roots of the system for $\omega = \omega_r$ and check their stability in the usual way.

Looking first at $\alpha \ll 1$, the results when the effect of inertia is small are shown in Figure 3.18. At this range of α and β the results are almost identical to the results for the antisymmetric mode shown in Figure 3.14 including the frequency of ω_r at which a pinch is seen occuring for $\omega_i > 0$. Until the pinch occurs there is a right-travelling convective instability. This suggests it is possible to find an approximate solution in this parameter range as was done for the antisymmetric mode. By following the same method as outlined for the antisymmetric mode, an expression is readily obtained as

$$k(\alpha) = \omega \pm i\sqrt{\frac{\omega^3\left(\hat{\beta} - \omega^2\right)}{\coth(\omega)}}\alpha^{\frac{1}{2}} + \mathcal{O}(\alpha) + \ldots, \tag{3.5.8}$$

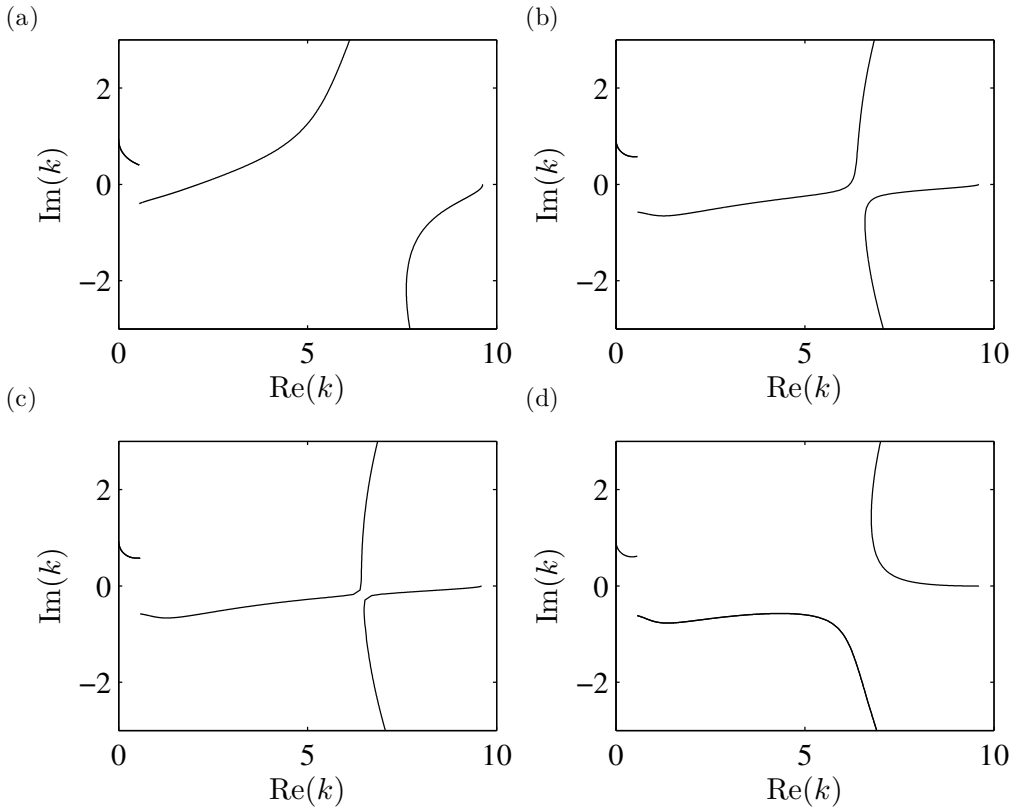

Figure 3.19: Stability of three of the roots to (3.5.7) as the imaginary part of ω is decreased from $\omega_i = 2000$ to $\omega_i = 0$ for varying ω_r, when $\alpha = 10^{-3}$ and $\beta = 0.8$. The end of the curves shown corresponds to $\omega_i = 0$. (a) $\omega_r = 0.8$, (b) $\omega_r = 1.04$, (c) $\omega_r = 1.046$ (d) $\omega_r = 1.1$.

where $\hat{\beta} = \beta/\alpha$ as before. The accuracy of the approximate solutions can be seen in Fig 3.18(a)–(b). The approximation (3.5.8) provides excellent agreement up to $\omega_r \approx 1$, but deteriorates above this value, albeit slowly.

As β is increased, the qualitative behaviour remains the same, but the system transitions through the pinch into stability for a smaller ω_r, which is shown in Figure 3.19. However, below this critical value of ω_r, the growth rate of the convective instability, $|\omega_i|$, will be higher than for an equivalent ω_r with a smaller value of β, so in this sense the system is more unstable when the effect of the inertia is stronger, but over a smaller range of wavelengths.

The behaviour when $\alpha \gg 1$ and the bending stiffness dominates is different again from the behaviour both when $\alpha \ll 1$ and for the equivalent range of α for the anti-symmetric mode. In Figures 3.20–3.21 there is a convectively unstable root with a very small imaginary component and therefore very small growth rate. Due to the size of the

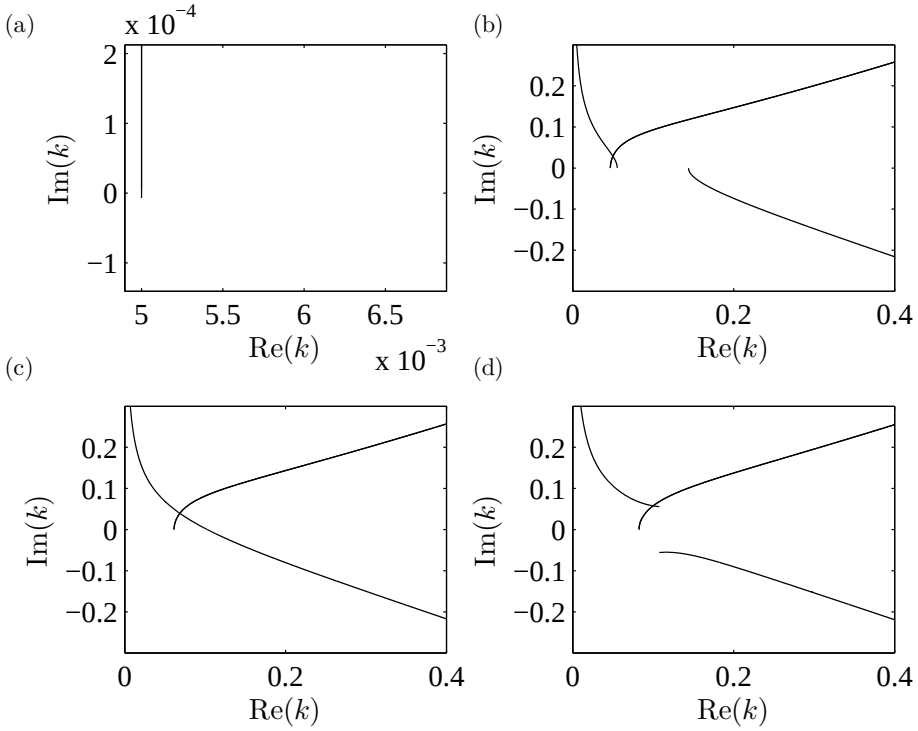

Figure 3.20: Stability of three of the roots to (3.5.7) as the imaginary part of ω is decreased from $\omega_i = 2000$ to $\omega_i = 0$ for varying ω_r, when $\alpha = 10^3$ and $\beta = 0.1$. The end of the curves shown corresponds to $\omega_i = 0$. (a) $\omega_r = 0.005$, (b) $\omega_r = 0.05$, (c) $\omega_r = 0.068579$ (d) $\omega_r = 0.1$.

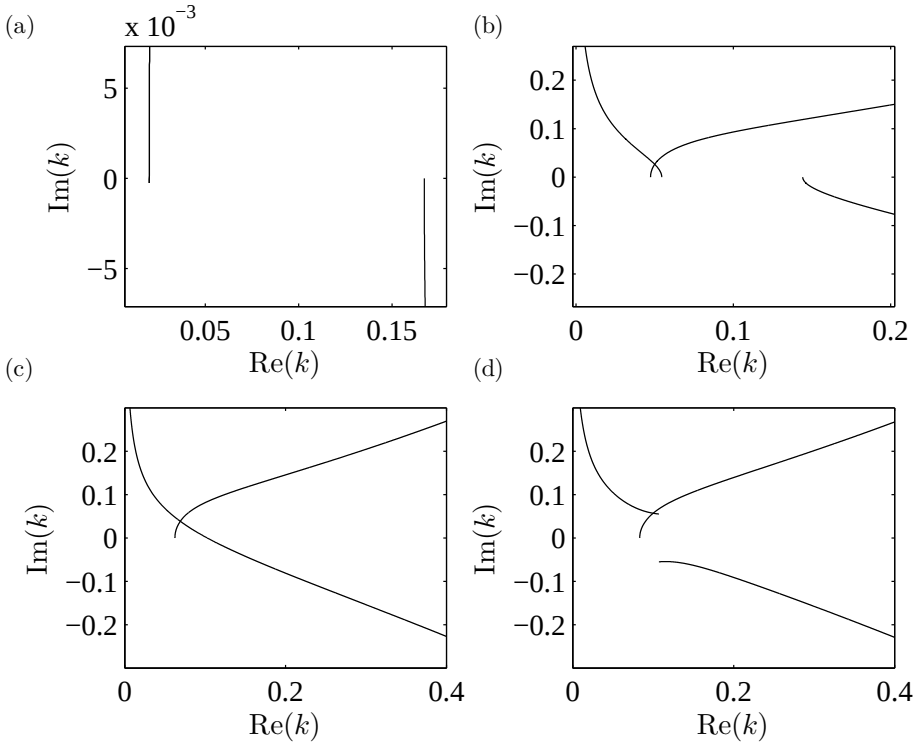

Figure 3.21: Stability of three of the roots to (3.5.7) as the imaginary part of ω is decreased from $\omega_i = 2000$ to $\omega_i = 0$ for varying ω_r, when $\alpha = 10^3$ and $\beta = 0.8$. The end of the curves shown corresponds to $\omega_i = 0$. (a) $\omega_r = 0.02$, (b) $\omega_r = 0.05$, (c) $\omega_r = 0.0691$ (d) $\omega_r = 0.1$.

imaginary component subfigure (a) in each of Figures 3.20–3.21 is more closely zoomed than the others, sometimes to the exclusion of the stable roots. The system then follows the pattern of the antisymmetric mode when α is large and β is small. As ω_r is increased the solutions transition to three neutrally stable roots, and then to one neutrally stable and two evanescent roots travelling in opposite directions. The size of the growth rate of convective instabilities in the $\alpha \gg 1$ regime is much smaller, and α must be reduced by a factor of ten to obtain a growth rate of $\mathcal{O}(10^{-3})$. This too agrees well with de Langre (2002), with both the convective and absolute instability regions of his work caught here.

3.6 Discussion

In this chapter we have extended the linear stability analysis performed in Chapter 2 for the linear plate model by allowing perturbations with a real frequency and seeking solutions in terms of the complex wavenumber. In order to classify the direction and stability of the waves found we introduced the concept of Briggs–Bers analysis. By considering the simplest version of the system possible, we were able to find the location of the roots and successfully classify their direction, and identify that in the absence of inertia all roots are either neutrally stable or evanescent in their direction of propagation. For example, in the absence of inertia or a frequency of oscillation, we found four real roots and an infinite set of roots lying on the imaginary k-axis.

Working with this knowledge of the roots of the simplest system, we gradually increased the complexity and tracked how the behaviour of the roots changed. Interesting behaviour was found for all the roots. When ω_r is increased enough, a pair of solutions from the infinite set move off the $\mathrm{Im}(k)$-axis to gain a negative real component, similarly two of the real roots were shown to gain an imaginary component. The four complex roots and the two remaining real roots were found to be related to each other by their asymptotic approximation when ω_r was large enough.

Upon introducing the effect of inertia, the system could become unstable, and for both the antisymmetric and symmetric modes convective instabilities were observed for

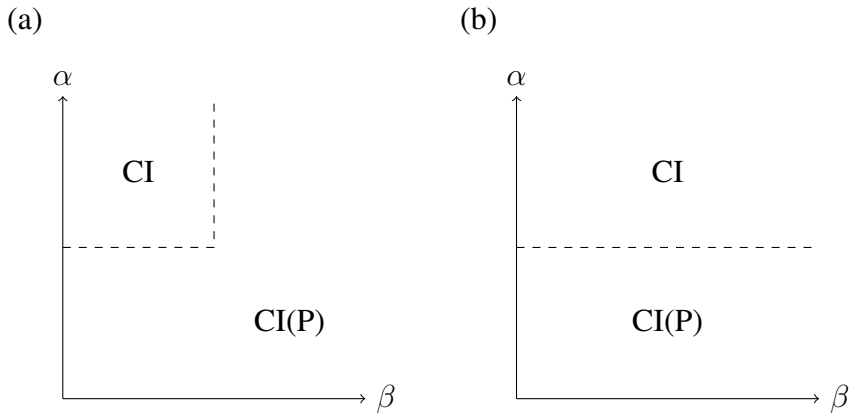

Figure 3.22: Sketch of the qualitative behaviour of (a) the antisymmetric mode, (b) the symmetric mode, as the bending stiffness, α, and the inertia, β, are varied. **CI** denotes the mode is convectively unstable before transitioning to three neutrally stable waves, **CI(P)** denotes the mode is convectively unstable until a pinch forms.

$0 < \omega_r < \omega_c(\alpha, \beta)$ before the system transitioned to being stable. For the majority of parameter sizes a pinch was seen occurring at $\omega_r = \omega_c$ which was dependant upon both the bending stiffness, α, and inertia, β, these regions are denoted by **CI(P)** in Figure 3.22. This pinch occurred between a convectively unstable root and a neutrally stable root, when tracing the stability path according to the Briggs–Bers technique and therefore the pinches occurred when $\omega_i > 0$. After the pinch the two roots consist of right travelling and left travelling evanescent waves. For the other parameter sizes, the system is convectively unstable, before transitioning to three neutrally stable roots and then to one neutrally stable root and two evanescent roots, one travelling upstream and the other downstream. This is denoted by **CI** in Figure 3.22.

If we were considering a system in which both the wavenumber and frequency were complex the pinches that arise would result in the onset of absolute instability, however, in our system absolute instability cannot occur because the amplitude is set in a fixed point for all time so the instability cannot contaminate the entire domain.

CHAPTER FOUR

TRAVELLING WAVES IN THE NONLINEAR SYSTEM

4.1 Introduction

We depart from channels with linear-elastic walls and their stability in favour of examining wave propagation in nonlinear elastic channels. Specifically, in this chapter we extend the work of Mehring & Sirignano (1999), who sought periodic travelling waves for liquid sheets that would lead to breakup of the sheet. We begin by formulating a set of governing equations following the derivation by Mehring & Sirignano (1999), but with the addition of nonlinear elastic walls in place of free surfaces. We also introduce a second length scale, giving a parameter for the aspect ratio. The coupling between the fluid and solid is given by a nonlinear plate equation without inertial effects.

Periodic travelling waves are then sought for two simplified systems, one is a fully linear system, the other linear only in the curvature. In the linear plate system, a nonlinear equation for travelling waves is found which is then solved numerically, to give both the profiles and propagation speed. An asymptotic analysis is performed to give the solution as the channel thickness approaches zero and is compared to the numerical solution. Finally, we derive an equation for travelling waves in the nonlinear system which is solved numerically and the results are discussed.

The work in Chapters 4–5 is currently under review for publication.

4.2 Problem Formulation

Working in Cartesian coordinates (x^*, y^*), we consider an incompressible, inviscid, two-dimensional flow between two flexible walls a mean distance a apart, in a gravity-free regime (see Figure 4.1). The fluid has constant density ρ, and its pressure and velocity fields are denoted p^* and (u^*, v^*) respectively. The upper interface is located at $y^* = \eta^*_+(x^*, t^*)$ and the lower at $y^* = \eta^*_-(x^*, t^*)$. Outside of the channel is assumed to be a vacuum. If the flow and walls are undisturbed, the fluid is assumed to flow at a constant velocity U_r in the x^* direction, with the walls at $y^* = \pm a/2$. We are interested in long wavelength perturbations to this undisturbed state with wavelength L. The equations governing the unsteady fluid flow are the two dimensional Euler equations:

$$\frac{\partial u^*}{\partial x^*} + \frac{\partial v^*}{\partial y^*} = 0, \tag{4.2.1}$$

$$\frac{\partial u^*}{\partial t^*} + u^*\frac{\partial u^*}{\partial x^*} + v^*\frac{\partial u^*}{\partial y^*} = -\frac{1}{\rho}\frac{\partial p^*}{\partial x^*}, \tag{4.2.2}$$

$$\frac{\partial v^*}{\partial t^*} + u^*\frac{\partial v^*}{\partial x^*} + v^*\frac{\partial v^*}{\partial y^*} = -\frac{1}{\rho}\frac{\partial p^*}{\partial y^*}. \tag{4.2.3}$$

At the interface between the fluid and the flexible wall we have the kinematic conditions

$$\frac{\partial \eta^*_\pm}{\partial t^*} + u^*_\pm\frac{\partial \eta^*_\pm}{\partial x^*} = v^*_\pm \tag{4.2.4}$$

where the subscript denotes values at the interface $y^* = \eta^*_\pm$. For the dynamic condition, the wall model is the as in both Plotnikov & Toland (2011) and Blyth *et al.* (2011)

$$p^*_\pm = \pm D^*\left(\frac{\partial^2 \kappa^*_\pm}{\partial {s^*}^2} + \frac{\kappa^{*3}_\pm}{2}\right), \tag{4.2.5}$$

where D^* is the bending stiffness, $\kappa^*_\pm$ is the curvature of the interface and $s^*_\pm$ denotes the arc length. The curvature is related to the interface position by

$$\kappa^*_\pm = \frac{\partial^2 \eta^*_\pm}{\partial {x^*}^2}\left(1 + \left(\frac{\partial \eta^*_\pm}{\partial x^*}\right)^2\right)^{-\frac{3}{2}}. \tag{4.2.6}$$

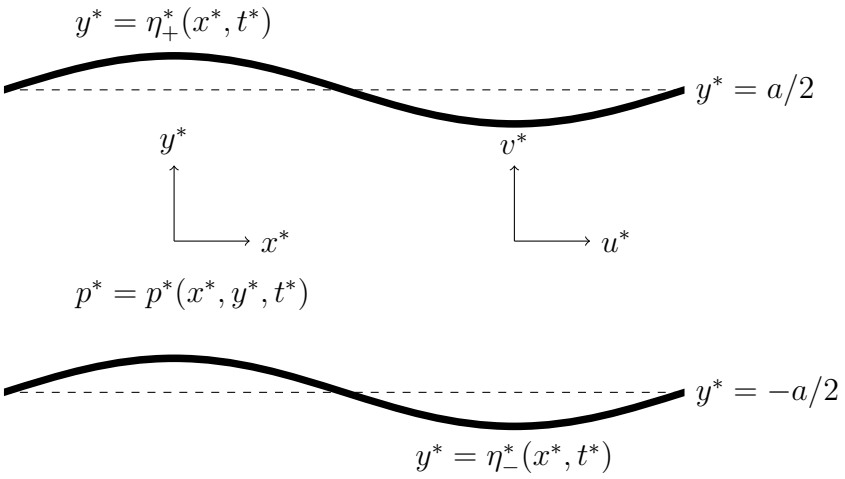

Figure 4.1: Dimensional problem setup.

When the pressure is written in terms of $\eta_\pm^*$ and x^* (4.2.5) becomes

$$p_\pm^* = \pm D^* \left[f_\pm^* \frac{\partial}{\partial x^*} \left(f_\pm^* \frac{\partial}{\partial x^*} \left(f_\pm^{*3} \frac{\partial^2 \eta_\pm^*}{\partial x^{*2}} \right) \right) + \frac{1}{2} \left(f_\pm^{*3} \frac{\partial^2 \eta_\pm^*}{\partial x^{*2}} \right)^3 \right], \tag{4.2.7}$$

with

$$f_\pm^* = \left[1 + \left(\frac{\partial \eta_\pm^*}{\partial x^*} \right)^2 \right]^{-\frac{1}{2}}. \tag{4.2.8}$$

Since there is no wall inertia in our model, the governing equations (4.2.1)–(4.2.7) are invariant under the Galilean transformation $x \mapsto x + U_r t$, $u \mapsto u + U_r$. Without loss of generality, we may therefore take $U_r = 0$, which assumes there is zero mean axial flow. Solutions with a non-zero axial flux can be recovered by applying a suitable Galilean transformation.

Assuming that the fluid layer is thin compared to the wavelength of the disturbance, we follow the derivation of Mehring & Sirignano (1999) who investigated a related problem for liquid sheets. We first define the centreline $\bar{\eta}^*$ and thickness $\tilde{\eta}^*$ by

$$\bar{\eta}^*(x^*, t^*) = \frac{\eta_+^* + \eta_-^*}{2}, \qquad \tilde{\eta}^*(x^*, t^*) = \eta_+^* - \eta_-^*. \tag{4.2.9}$$

The dependant variables are then expanded in powers of $y^* - \bar{\eta}^*$ as

$$u^* = u_0^*(x^*, t^*) + u_1^*(x^*, t^*)[y^* - \bar{\eta}^*] + u_2^*(x^*, t^*)[y^* - \bar{\eta}^*]^2 + \dots, \tag{4.2.10}$$

$$v^* = v_0^*(x^*, t^*) + v_1^*(x^*, t^*)[y^* - \bar{\eta}^*] + v_2^*(x^*, t^*)[y^* - \bar{\eta}^*]^2 + \dots, \tag{4.2.11}$$

$$p^* = p_0^*(x^*, t^*) + p_1^*(x^*, t^*)[y^* - \bar{\eta}^*] + p_2^*(x^*, t^*)[y^* - \bar{\eta}^*]^2 + \dots. \tag{4.2.12}$$

We insert these expansions into the governing equations, and consider only the lowest order in $y^* - \bar{\eta}^*$. This limits us to a long wavelength approximation, or specifically to waves whose initial amplitude is much less than their wavelength.

Upon inserting the dependent variable expansions into $(v_+^* + v_-^*)/2$, using (4.2.4) and (4.2.9), an expression for v_0 is obtained

$$v_0^* = \frac{\partial \bar{\eta}^*}{\partial t^*} + u_0^* \frac{\partial \bar{\eta}^*}{\partial x^*}. \tag{4.2.13}$$

Using the same process, but on $v_+ - v_-$, we can find an expression for v_1^*

$$v_1^* = \frac{\partial \tilde{\eta}^*}{\partial t^*} + u_0^* \frac{\partial \tilde{\eta}^*}{\partial x^*} + u_1^* \tilde{\eta}^* \frac{\partial \bar{\eta}^*}{\partial x^*}. \tag{4.2.14}$$

Inputting the expansions into (4.2.1)–(4.2.3), yields, respectively

$$\frac{\partial u_0^*}{\partial x^*} - u_1^* \frac{\partial \bar{\eta}^*}{\partial x^*} + v_1^* = 0, \tag{4.2.15}$$

$$\frac{\partial u_0^*}{\partial t^*} + u_0^* \frac{\partial u_0^*}{\partial x^*} = -\frac{1}{\rho}\left(\frac{\partial p_0^*}{\partial x^*} - p_1^* \frac{\partial \bar{\eta}^*}{\partial x^*}\right), \tag{4.2.16}$$

$$\frac{\partial v_0^*}{\partial t^*} + u_0^* \frac{\partial v_0^*}{\partial x^*} = -\frac{p_1^*}{\rho}. \tag{4.2.17}$$

We can also combine (4.2.14) and (4.2.15) to eliminate u_1 and v_1

$$\frac{\partial \tilde{\eta}^*}{\partial t^*} + \frac{\partial}{\partial x^*}\left(u_0^* \tilde{\eta}^*\right) = 0. \tag{4.2.18}$$

Looking at the expansion for p, we write $p_0^* = (p_+^* + p_-^*)/2$ and $p_1^* = (p_+^* - p_-^*)/\tilde{\eta}^*$, and

substitute into (4.2.16) and (4.2.17), to be left with

$$\frac{\partial u_0^*}{\partial t^*} + u_0^* \frac{\partial u_0^*}{\partial x^*} = -\frac{1}{\rho}\left(\frac{\partial}{\partial x^*}\left(\frac{p_+^* + p_-^*}{2}\right) - \frac{\partial \bar{\eta}^*}{\partial x^*}\left(\frac{p_+^* - p_-^*}{\tilde{\eta}^*}\right)\right), \tag{4.2.19}$$

$$\frac{\partial v_0^*}{\partial t^*} + u_0^* \frac{\partial v_0^*}{\partial x^*} = -\frac{1}{\rho}\left(\frac{p_+^* - p_-^*}{\tilde{\eta}^*}\right). \tag{4.2.20}$$

This gives us four equations, (4.2.13), (4.2.18), (4.2.19), and (4.2.20) for six variables ($\bar{\eta}^*, \tilde{\eta}^*, u_0^*, v_0^*, p_+^*$ and p_-^*), but we note that we have not yet used the dynamic boundary condition. Therefore, writing (4.2.7) and (4.2.8) in terms of $\bar{\eta}^*$ and $\tilde{\eta}^*$ gives

$$p_\pm^* = \pm D^* \left[f_\pm^* \frac{\partial}{\partial x^*}\left(f_\pm^* \frac{\partial}{\partial x^*}\left(f_\pm^{*3} \frac{\partial^2}{\partial x^{*2}}\left(\bar{\eta}^* \pm \frac{\tilde{\eta}^*}{2}\right)\right)\right) + \frac{1}{2}\left(f_\pm^{*3} \frac{\partial^2}{\partial x^{*2}}\left(\bar{\eta}^* \pm \frac{\tilde{\eta}^*}{2}\right)\right)^3 \right], \tag{4.2.21}$$

where $f_\pm^*$ has been redefined to be

$$f_\pm^* = \left[1 + \left(\frac{\partial}{\partial x^*}\left(\bar{\eta}^* + \frac{\tilde{\eta}^*}{2}\right)\right)^2\right]^{-\frac{1}{2}}. \tag{4.2.22}$$

Therefore, we now have six equations for six variables. We introduce nondimensional quantities, and depart from Mehring & Sirignano (1999) by using two length scales, one each for the axial and transverse lengths. Our axial length scale is the wavelength L, and our transverse length scale is the channel width a. We denote the aspect ratio $\delta = a/L$, and assume $\delta \ll 1$. We use a pressure scale of D^*/L^3 based on the dynamic boundary condition. For the axial velocity scale, we use $U = \sqrt{D^*/2\rho L^3}$ from an inertia–pressure balance in (4.2.2). Natural time and transverse velocity scales then follow as U/L and δU. We therefore introduce the dimensionless variables

$$\begin{aligned} &x = \frac{x^*}{L}, \quad t = \frac{Ut^*}{L}, \quad \eta = \frac{\tilde{\eta}^*}{a}, \quad \hat{\eta} = \frac{\bar{\eta}^*}{a}, \quad u = \frac{u_0^*}{U}, \\ &v = \frac{v_0^*}{\delta U}, \quad p_\pm = \frac{L^3 p_\pm^*}{D^*}, \quad s_\pm = \frac{s_\pm^*}{L}, \quad \kappa_\pm = \frac{L\kappa_\pm^*}{\delta} \end{aligned} \tag{4.2.23}$$

Applying these scales to (4.2.18), (4.2.19), (4.2.13), (4.2.20) and (4.2.21), the final

equations governing the system are found to be, to leading order,

$$\frac{\partial \eta}{\partial t} + \frac{\partial}{\partial x}\left(u\eta\right) = 0, \tag{4.2.24}$$

$$\frac{\partial u}{\partial t} + u\frac{\partial u}{\partial x} = -\left[\frac{\partial}{\partial x}\left(p_+ + p_-\right) - \frac{2}{\eta}\frac{\partial \hat{\eta}}{\partial x}\left(p_+ - p_-\right)\right], \tag{4.2.25}$$

$$\frac{\partial \hat{\eta}}{\partial t} + u\frac{\partial \hat{\eta}}{\partial x} = v, \tag{4.2.26}$$

$$\frac{\partial v}{\partial t} + u\frac{\partial v}{\partial x} = -\frac{2}{\delta^2\eta}\left(p_+ - p_-\right), \tag{4.2.27}$$

where

$$p_\pm = \pm\delta\left(\frac{\partial^2 \kappa_\pm}{\partial s^2} + \frac{\delta^2}{2}\kappa_\pm^3\right) \tag{4.2.28}$$

$$\begin{aligned} &= \pm\delta f_\pm^5 \frac{\partial^4}{\partial x^4}\left(\hat{\eta} \pm \frac{\eta}{2}\right) \\ &\quad \mp \delta^3 f_\pm^7 \left[10\frac{\partial^3}{\partial x^3}\left(\hat{\eta} \pm \frac{\eta}{2}\right)\frac{\partial^2}{\partial x^2}\left(\hat{\eta} \pm \frac{\eta}{2}\right)\frac{\partial}{\partial x}\left(\hat{\eta} \pm \frac{\eta}{2}\right) + 3\left(\frac{\partial^2}{\partial x^2}\left(\hat{\eta} \pm \frac{\eta}{2}\right)\right)^3\right] \\ &\quad \pm \delta^3 f_\pm^9 \left[\frac{1}{2}\left(\frac{\partial^2}{\partial x^2}\left(\hat{\eta} \pm \frac{\eta}{2}\right)\right)^3 + 18\delta^2\left(\frac{\partial^2}{\partial x^2}\left(\hat{\eta} \pm \frac{\eta}{2}\right)\right)^3\left(\frac{\partial}{\partial x}\left(\hat{\eta} \pm \frac{\eta}{2}\right)\right)^2\right], \end{aligned} \tag{4.2.29}$$

and

$$f_\pm = \left[1 + \delta^2\left(\frac{\partial}{\partial x}\left(\hat{\eta} \pm \frac{\eta}{2}\right)\right)^2\right]^{-\frac{1}{2}}. \tag{4.2.30}$$

In (4.2.29) we have expanded the spatial derivatives in (4.2.21). In terms of the centreline and thickness, the curvature can be written, from (4.2.28)

$$\kappa_\pm = f_\pm^3\left(\frac{\partial^2 \hat{\eta}}{\partial x^2} \pm \frac{1}{2}\frac{\partial^2 \eta}{\partial x^2}\right). \tag{4.2.31}$$

Equations (4.2.24)–(4.2.27) are fully coupled, highly nonlinear equations and will be referred to as the 'nonlinear system'. After the nondimensionalisation a factor of δ^{-2} remains in (4.2.27), this is an inevitable consequence of two distinct timescales in the system for symmetric and antisymmetric modes. Whichever mode is being considered, (4.2.24)–(4.2.30) contains all the leading order terms. We will consider the solution to

this system numerically but to make further analytical progress we additionally consider two simplified systems.

Firstly, retaining only the linear terms in η and $\hat{\eta}$ in (4.2.29) and (4.2.30) we obtain the 'linear plate system', which is governed by

$$\frac{\partial \eta}{\partial t} + \frac{\partial}{\partial x}(u\eta) = 0, \tag{4.2.32}$$

$$\frac{\partial u}{\partial t} + u\frac{\partial u}{\partial x} = -\delta\frac{\partial^5 \eta}{\partial x^5}, \tag{4.2.33}$$

$$\frac{\partial \hat{\eta}}{\partial t} + u\frac{\partial \hat{\eta}}{\partial x} = v, \tag{4.2.34}$$

$$\frac{\partial v}{\partial t} + u\frac{\partial v}{\partial x} = -\frac{4}{\delta\eta}\frac{\partial^4 \hat{\eta}}{\partial x^4}. \tag{4.2.35}$$

Note that there is a partial decoupling here, in that neither v or $\hat{\eta}$ appear in (4.2.32) and (4.2.33).

Secondly, we consider a full linearisation of (4.2.24)–(4.2.27) about the undisturbed state. Writing $\eta = 1 + \eta'$, $u = u'$, $\hat{\eta} = \hat{\eta}'$, $v = v'$ and neglecting terms that are quadratic in the primed variables we obtain

$$\frac{\partial \eta'}{\partial t} + \frac{\partial u'}{\partial x} = 0, \tag{4.2.36}$$

$$\frac{\partial u'}{\partial t} = -\delta\frac{\partial^5 \eta'}{\partial x^5} \tag{4.2.37}$$

$$\frac{\partial \hat{\eta}'}{\partial t} = v', \tag{4.2.38}$$

$$\frac{\partial v'}{\partial t} = -\frac{4}{\delta}\frac{\partial^4 \hat{\eta}'}{\partial x^4}. \tag{4.2.39}$$

This will be referred to as the 'fully linear system'. We now have a full decoupling of equations (4.2.36) and (4.2.37) for u' and η' from (4.2.38) and (4.2.39) for v' and $\hat{\eta}'$. The first pair correspond to a symmetric mode, while the second pair correspond to an antisymmetric mode (de Langre, 2002). The symmetric mode is seen physically as the top and bottom interfaces being out of phase with $\eta_+^* = -\eta_-^*$, while the antisymmetric mode is seen as the interfaces being in phase with $\eta_+^* = \eta_-^*$.

4.3 Travelling Waves in the Fully Linear System

We seek the dispersion relations for the two pairs of decoupled equations in the fully linear system (4.2.36)–(4.2.39). From this we will be able to determine any travelling waves and their corresponding velocities.

Looking first at (4.2.36) and (4.2.37), which govern the symmetric mode, we use differentiation to eliminate u' between them to obtain

$$\frac{\partial^2 \eta'}{\partial t^2} - \delta \frac{\partial^6 \eta'}{\partial x^6} = 0. \tag{4.3.1}$$

We now seek solutions of the form $\eta' = \eta'_0 \exp(i(kx - \omega t))$, were k is the wavenumber and ω is the frequency of the wave sought. Any general solution can be expressed as a superposition of these modes. Substituting the ansatz into (4.3.1), we find that the dispersion relation is

$$\omega = \pm k^3 \sqrt{\delta}. \tag{4.3.2}$$

For symmetric travelling waves with wavelength 1, $k = 2\pi$ and the solutions to (4.2.36) and (4.2.37) may be written

$$\eta' = \varepsilon_s \cos(2\pi(x - c_s t)), \tag{4.3.3}$$

$$u' = \varepsilon_s c_s \cos(2\pi(x - c_s t)), \tag{4.3.4}$$

where

$$c_s = \omega/k = \pm 4\pi^2 \sqrt{\delta} \tag{4.3.5}$$

is the wave velocity and ε_s is the amplitude of the travelling wave.

Doing the same for (4.2.38) and (4.2.39), which govern the antisymmetric mode, we eliminate v' to find

$$\frac{\partial^2 \hat{\eta}'}{\partial t^2} + \frac{4}{\delta} \frac{\partial^4 \hat{\eta}'}{\partial x^4} = 0, \tag{4.3.6}$$

and the dispersion relation is found to be

$$\omega = \pm 2k^2\sqrt{\frac{1}{\delta}}. \tag{4.3.7}$$

So, for antisymmetric travelling waves with wavelength 1, the solutions to (4.2.38) and (4.2.39) can be written

$$\hat{\eta}' = \varepsilon_a \cos(2\pi(x - c_a t)), \tag{4.3.8}$$

$$v' = 2\pi\varepsilon_a c_a \sin(2\pi(x - c_a t)), \tag{4.3.9}$$

where

$$c_a = \omega/k = \pm 4\pi\sqrt{\frac{1}{\delta}} \tag{4.3.10}$$

is the wave velocity and ε_a is the amplitude of the travelling wave. From the calculated wavespeeds above we can determine that if $\delta > 1/\pi$ the symmetric mode wave travels faster than the antisymmetric mode, and vice versa if $\delta < 1/\pi$. However, since we have made a long wave approximation, we expect $\delta \ll 1$ and therefore the antisymmetric waves always travel much faster than the symmetric waves.

4.4 Travelling Waves in the Linear Plate System

4.4.1 Symmetric mode travelling waves

Periodic travelling-wave solutions are sought for (4.2.32) and (4.2.33), the linear plate equations that govern the symmetric mode. We seek solutions with wavelength 1 and speed c, giving a temporal period $T = 1/c$. We therefore look for a solution in which u and η depend only upon $Z = x - ct$, and which is periodic in Z with period 1.

Since we have assumed there is no mean axial flow, there must be no net axial flux over one time period, or equivalently

$$\int_0^T u\eta \,\mathrm{d}t = 0 \qquad \Rightarrow \qquad \int_{-1/2}^{1/2} u\eta \,\mathrm{d}Z = 0. \tag{4.4.1}$$

The periodic nature of the waves being sought also means we must have conservation of mass in a spatial period

$$\int_{x_0}^{x_0+1} \eta \, \mathrm{d}x = 1 \qquad \Rightarrow \qquad \int_{-1/2}^{1/2} \eta \, \mathrm{d}Z = 1, \tag{4.4.2}$$

for any x_0.

Writing (4.2.32) and (4.2.33) in terms of Z, we have

$$-c\frac{\mathrm{d}\eta}{\mathrm{d}Z} + \frac{\mathrm{d}}{\mathrm{d}Z}\left(u\eta\right) = 0, \tag{4.4.3}$$

$$-c\frac{\mathrm{d}u}{\mathrm{d}Z} + u\frac{\mathrm{d}u}{\mathrm{d}Z} = -\delta\frac{\mathrm{d}^5\eta}{\mathrm{d}Z^5}. \tag{4.4.4}$$

Integration of (4.4.3) yields

$$-c\eta + u\eta = -c, \tag{4.4.5}$$

where the constant of integration has been fixed to satisfy (4.4.1) using (4.4.2). Using (4.4.5) to eliminate u from (4.4.4) and integrating, we obtain a differential equation for η,

$$\frac{\mathrm{d}^4\eta}{\mathrm{d}Z^4} = -\frac{c^2}{2\delta}\left(\frac{1}{\eta^2} - B^2\right), \tag{4.4.6}$$

where B is a constant of integration. It is convenient to make the change of variables $\eta = Y/B$, to obtain

$$\frac{\mathrm{d}^4 Y}{\mathrm{d}Z^4} = K\left(1 - \frac{1}{Y^2}\right), \tag{4.4.7}$$

where $K = c^2B^3/2\delta$ is to be determined as part of the solution. The value of B is set by the application of (4.4.2) to any solution, from which we obtain

$$B = \int_{-1/2}^{1/2} Y \, \mathrm{d}Z. \tag{4.4.8}$$

Without loss of generality, we assume that the maximum or minimum of Y occurs at $Z = 0$, with $Y\left(0\right) = \varepsilon$. From the symmetry of (4.4.7), Y is an even periodic function on

$[-1/2, 1/2]$. We restrict ourselves to $[0, 1/2]$ and therefore have the boundary conditions

$$Y(0) = \varepsilon, \qquad Y'(0) = Y'''(0) = 0, \qquad Y'(1/2) = Y'''(1/2) = 0. \tag{4.4.9}$$

The first condition fixes the amplitude of the solution while the other four arise from the symmetry of the solution. The unknown parameter K in (4.4.7) is determined as part of the solution. We thus obtain the wave speed c in terms of the maximum or minimum amplitude ε and aspect ratio δ.

The system (4.4.7) and (4.4.9) is solved numerically using the built-in MATLAB function `bvp4c`. As an initial guess for $Y(Z)$ and K we use the solution to the linearised form of (4.4.7) for small perturbations about $Y = 1$:

$$Y = 1 - (1 - \varepsilon)\cos(2\pi Z), \qquad K = 8\pi^4. \tag{4.4.10}$$

Once a numerical solution for $Y(Z)$ is found, the trapezium rule is used to integrate (4.4.8) to find B, and hence η and c can be recovered. Finally, u is found using (4.4.5). Some sample solutions for different values of ε are shown in Figures 4.2–4.4.

In Figure 4.2, we see that the basic sinusoidal shape of the travelling wave profiles found in the fully linear system given by (4.3.3) remains, however we see there is a flattening at the top and a sharpening at the bottom of the solution curves from the nonlinear terms. The equivalent profiles for u are shown in Figure 4.3, where we see a strong nonlinear response as $\varepsilon \to 0$. For a wave moving in the positive x-direction fluid flows in the negative x-direction at the narrowing of the channel, so fluid is forced from in front of the wave to behind it. As $\varepsilon \to 0$ we also see the fluid velocity descending to 0 away from the trough, this arises from the wave velocity c being close to zero.

The relationship between the perturbation amplitude and the velocity of the travelling wave is shown in Figure 4.4. For a given velocity, the same wave will be found twice with two different amplitudes ε corresponding to a translation of half a wavelength. In the limit $\eta(0) = \varepsilon/B \to 1$, we have $c\delta^{-1/2} \to 4\pi^2$, the fixed velocity found for solutions of any amplitude in the fully linear case. In the limit $\varepsilon \to 0$ we have $\eta(0) \to 0$ and $c \to 0$,

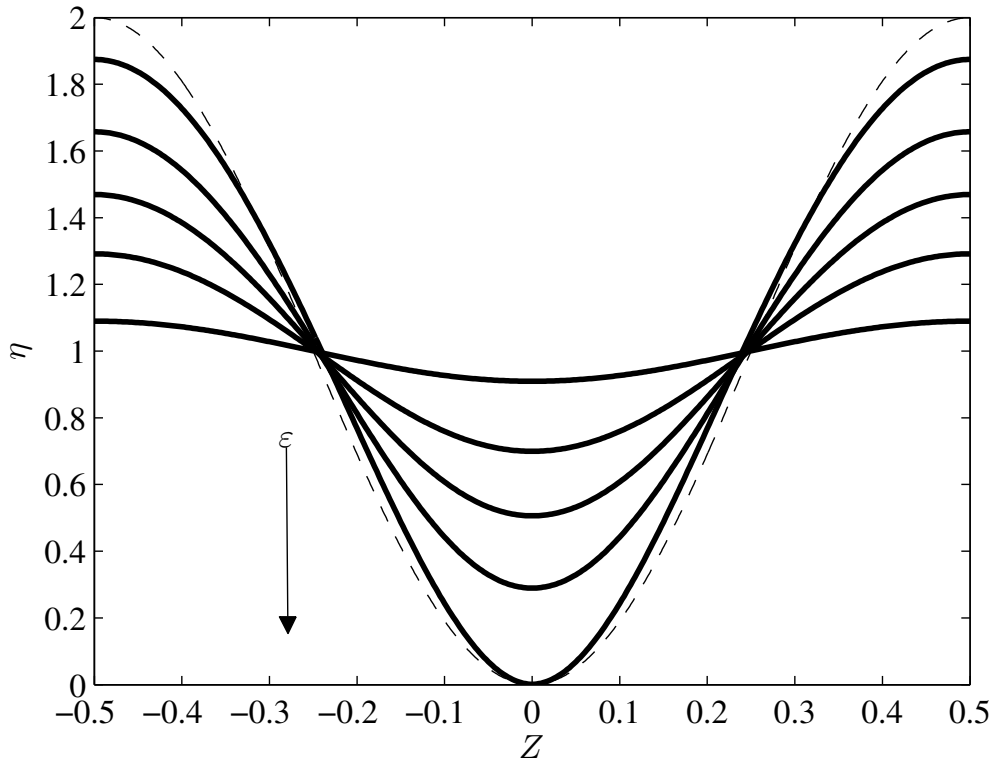

Figure 4.2: A selection of thickness profiles, η, for travelling waves given by (4.4.7) for $\varepsilon = 0.91, 0.75, 0.62, 0.48, 0.03$. The dashed line is $1 - \cos(2\pi Z)$ to illustrate the nonlinear effects.

as the constriction prevents fluid flow back through the minimum gap.

4.4.2 Asymptotic analysis

We perform a matched asymptotic expansion of the solution of equation (4.4.7) subject to the boundary conditions (4.4.9) in the limit $\varepsilon \to 0$. This corresponds to the limit in which the opposite walls are almost touching. We expect to find two asymptotic regions: an inner region close to $Z = 0$, in which $Y = \mathcal{O}(\varepsilon)$ and the right hand side of (4.4.7) is dominated by the Y^{-2} term; and an outer region in which $Z = \mathcal{O}(1)$, where Y is large and the right hand side of (4.4.7) is dominated by the constant term.

The numerical results suggest $Y''(0) \sim \varepsilon^{-3}$, giving the lengthscale for the inner region as $Z = \mathcal{O}(\varepsilon^2)$; and also that $Y \sim \varepsilon^{-3}$ in the outer region, and $K \sim \varepsilon^{-3}$. The symmetries in the problem suggest an expansion in ε^2, and so we write

$$K = \varepsilon^{-3}\left(K_0 + \varepsilon^2 K_1 + \cdots\right), \tag{4.4.11}$$

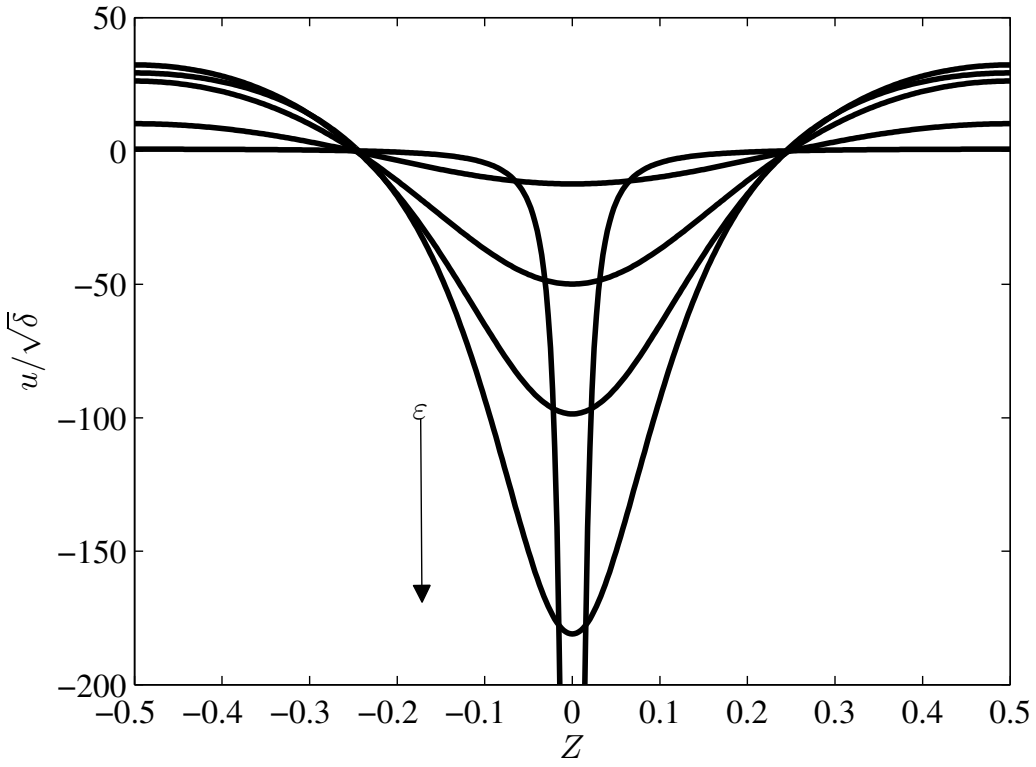

Figure 4.3: A selection of velocity profiles from (4.4.5), corresponding to the thickness profiles shown in figure 4.2. The trough of the largest wave descends to -1196.8 but has been truncated here to better illustrate the shape of the other curves.

where K_0, K_1 are $\mathcal{O}(1)$. Different expansions will be used for Y in the inner and outer regions.

Outer Region $Z = \mathcal{O}(1)$

In the outer region Y scales like ε^{-3}, so a solution is sought of the form

$$Y = \varepsilon^{-3}\left[W_0(Z) + \varepsilon^2 W_1(Z) + \cdots\right], \tag{4.4.12}$$

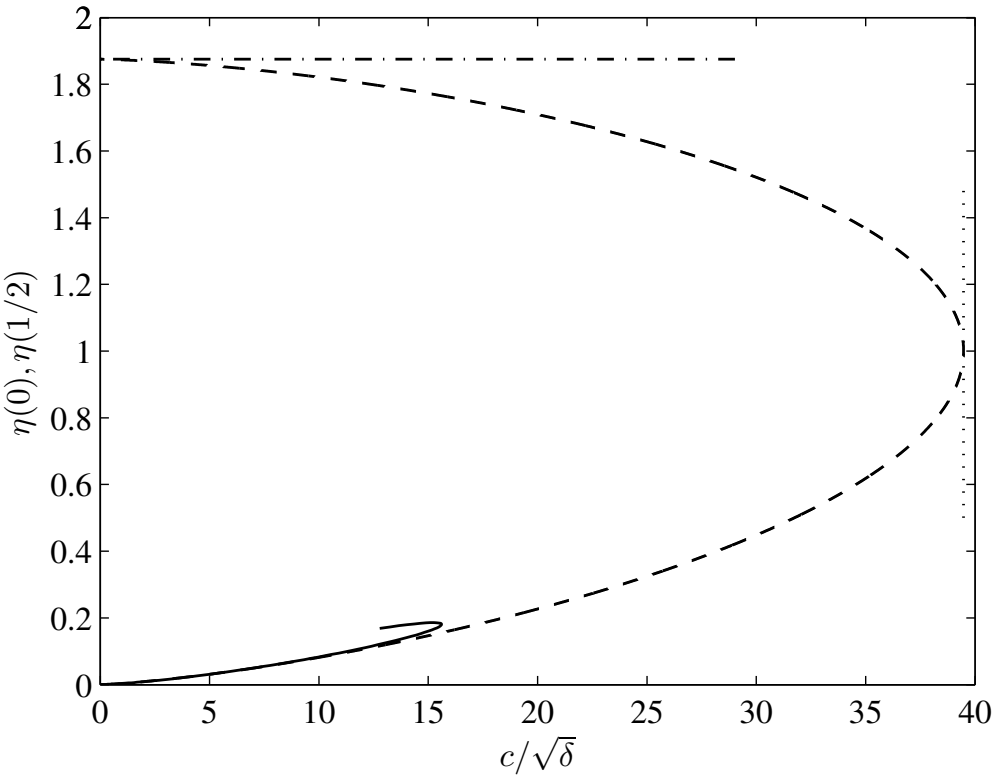

Figure 4.4: The velocity c of the travelling wave as a function of the maximum or minimum displacements $\eta(0)$ and $\eta(1/2)$. The dashed line is the numerical results, the dotted line is the linear wavespeed (4.3.5), then the asymptotic results are given by the solid line which is $\eta(0)$ against c from (4.4.47) and (4.4.46) and the dot-dashed line which is $\eta(1/2)$ against c from (4.4.48) and (4.4.46).

Substituting (4.4.11) and (4.4.12) into (4.4.7), we obtain

$$\varepsilon^{-3}\left[\frac{\mathrm{d}^4 W_0}{\mathrm{d}Z^4} + \varepsilon^2 \frac{\mathrm{d}^4 W_1}{\mathrm{d}Z^4} + \cdots\right] = \varepsilon^{-3}\left(K_0 + \varepsilon^2 K_1 + \cdots\right)\left[1 - \frac{1}{\left(\varepsilon^{-3}\left[W_0(Z) + \varepsilon^2 W_1(Z) + \cdots\right]\right)^2}\right], \tag{4.4.13}$$

or alternatively,

$$\frac{\mathrm{d}^4 W_0}{\mathrm{d}Z^4} + \varepsilon^2 \frac{\mathrm{d}^4 W_1}{\mathrm{d}Z^4} + \ldots = \left(K_0 + \varepsilon^2 K_1 + \cdots\right)\left(1 + \mathcal{O}\left(\varepsilon^6\right)\right) \tag{4.4.14}$$

The boundary conditions are

$$W_0'(1/2) + \varepsilon^2 W_1'(1/2) + \ldots = 0, \qquad W_0'''(1/2) + \varepsilon^2 W_1'''(1/2) + \ldots = 0. \quad (4.4.15)$$

Writing down the leading-order terms of (4.4.14) and (4.4.15), we have

$$\frac{\mathrm{d}^4 W_0}{\mathrm{d}Z^4} = K_0 \quad \text{subject to} \quad W_0'(1/2) = W_0'''(1/2) = 0. \quad (4.4.16)$$

The solution to (4.4.16) can be written as

$$W_0(Z) = \frac{K_0}{24}\left(Z - \frac{1}{2}\right)^4 + \frac{B_0}{2}\left(Z - \frac{1}{2}\right)^2 + E_0, \quad (4.4.17)$$

where B_0 and E_0 are constants of integration. The constants will be determined later through matching.

Evaluating the terms at the next order we have

$$\frac{\mathrm{d}^4 W_1}{\mathrm{d}Z^4} = K_1 \quad \text{subject to} \quad W_1'(1/2) = W_1'''(1/2) = 0. \quad (4.4.18)$$

The form of the solution to (4.4.18) is the same as (4.4.17) and after application of the boundary conditions is

$$W_1(Z) = \frac{K_1}{24}\left(Z - \frac{1}{2}\right)^4 + \frac{B_1}{2}\left(Z - \frac{1}{2}\right)^2 + E_1, \quad (4.4.19)$$

with K_1, B_1 and E_1 to be determined through matching.

The outer solution with first-order correction is therefore

$$Y = \varepsilon^{-3}\left[\frac{K_0}{24}\left(Z - \frac{1}{2}\right)^4 + \frac{B_0}{2}\left(Z - \frac{1}{2}\right)^2 + E_0 + \varepsilon^2\left(\frac{K_1}{24}\left(Z - \frac{1}{2}\right)^4 + \frac{B_1}{2}\left(Z - \frac{1}{2}\right)^2 + E_1\right) + \cdots\right]. \quad (4.4.20)$$

Inner Region $Z = \mathcal{O}(\varepsilon^2)$

For the inner solution we use the scaled coordinate $\zeta = Z/\varepsilon^2$. In this inner region, Y scales like ε, so a solution is sought in the form

$$Y = \varepsilon \left(F_0(\zeta) + \varepsilon^2 F_1(\zeta) + \varepsilon^4 F_2(\zeta) + \cdots \right). \tag{4.4.21}$$

We substitute (4.4.21) into (4.4.7) and obtain

$$\begin{aligned} &\varepsilon^{-7}\frac{\mathrm{d}^4 F_0}{\mathrm{d}\zeta^4} + \varepsilon^{-5}\frac{\mathrm{d}^4 F_1}{\mathrm{d}\zeta^4} + \varepsilon^{-3}\frac{\mathrm{d}^4 F_2}{\mathrm{d}\zeta^4} + \cdots \\ &\qquad = \varepsilon^{-3}\left(K_0 + \varepsilon^2 K_1 + \cdots\right)\left(1 - \varepsilon^{-2}F_0^{-2}\left(1 + 2\varepsilon^2\frac{F_1}{F_0} + \cdots\right)\right). \end{aligned} \tag{4.4.22}$$

or alternatively,

$$\begin{aligned} &\frac{\mathrm{d}^4 F_0}{\mathrm{d}\zeta^4} + \varepsilon^2\frac{\mathrm{d}^4 F_1}{\mathrm{d}\zeta^4} + \varepsilon^4\frac{\mathrm{d}^4 F_2}{\mathrm{d}\zeta^4} + \cdots \\ &\qquad = \varepsilon^2\Big(K_0 + \varepsilon^2 K_1 + \mathcal{O}\left(\varepsilon^4\right)\Big)\left(-F_0^{-2} + \varepsilon^2\left(1 + 2\frac{F_1}{F_0^3}\right) + \mathcal{O}\left(\varepsilon^4\right)\right). \end{aligned} \tag{4.4.23}$$

subject to

$$F_0(0) + \varepsilon^2 F_1(0) + \ldots = 1, \quad F_0'(0) + \varepsilon^2 F_1'(0) + \ldots = 0, \quad F_0'''(0) + \varepsilon^2 F_1'''(0) + \ldots = 0. \tag{4.4.24}$$

At leading order (4.4.23) and (4.4.24) imply

$$\frac{\mathrm{d}^4 F_0}{\mathrm{d}\zeta^4} = 0, \qquad \text{subject to} \qquad F_0(0) = 1, \quad F_0'(0) = F_0'''(0) = 0. \tag{4.4.25}$$

The solution to (4.4.25) is

$$F_0 = 1 + a_0^2\zeta^2, \tag{4.4.26}$$

where the constant a_0 will be determined later by matching.

At $\mathcal{O}(\varepsilon^2)$, (4.4.23) and (4.4.24) imply

$$\frac{\mathrm{d}^4 F_1}{\mathrm{d}\zeta^4} = -\frac{K_0}{F_0^2} \qquad \text{subject to} \qquad F_1(0) = F_1'(0) = F_1'''(0) = 0. \tag{4.4.27}$$

By repeated integration, the solution of (4.4.27) is

$$F_1 = -\frac{K_0}{4a_0}\left[\left(\frac{\zeta^3}{3} + \frac{\zeta}{a_0^2}\right)\arctan\left(a_0^2\zeta\right) - \frac{1}{3a_0^3}\ln\left(1 + a_0^2\zeta^2\right) + \hat{\beta}_1\zeta^2\right], \tag{4.4.28}$$

where $\hat{\beta}_1$ is another constant, which can only be determined by matching.

To achieve a full matching it becomes necessary to determine some behaviour of the second- and third-order corrections, F_2 and F_3, to the inner solution. At $\mathcal{O}(\varepsilon^4)$, (4.4.23) implies

$$\frac{\mathrm{d}^4 F_2}{\mathrm{d}\zeta^4} = -\frac{K_1}{F_0^2} + K_0\left(1 + 2\frac{F_1}{F_0^3}\right) \qquad \text{subject to} \qquad F_2(0) = F_2'(0) = F_2'''(0) = 0. \tag{4.4.29}$$

Writing

$$F_2 = \frac{K_0\zeta^4}{24} + \tilde{F}_2\left(\zeta\right), \tag{4.4.30}$$

we see that

$$\frac{\mathrm{d}^4 \tilde{F}_2}{\mathrm{d}\zeta^4} = -\frac{K_1}{F_0^2} + 2K_0\frac{F_1}{F_0^3} \qquad \text{subject to} \qquad \tilde{F}_2(0) = \tilde{F}_2'(0) = \tilde{F}_2'''(0) = 0. \tag{4.4.31}$$

In the limit $\zeta \to \infty$, $\tilde{F}_2'''' \to 0$ which implies $\tilde{F}''' \to \alpha_2$, a constant. We then have

$$\alpha_2 = \left[\tilde{F}_2'''\right]_0^\infty = \int_0^\infty \frac{\mathrm{d}^4\tilde{F}_2}{\mathrm{d}\zeta^4}\,\mathrm{d}\zeta = \left(-\frac{K_1\pi}{4a_0} - \frac{K_0^2}{6a_0^5}\left[\frac{\pi}{16}\left(7 - 3\ln(4)\right) + \frac{3\hat{\beta}_1 a_0\pi}{16}\right]\right). \tag{4.4.32}$$

The large-ζ behaviour of F_2 is thus given by $F_2 \sim K_0\zeta^4/24 + \alpha_2\zeta^3/6 + \cdots$. Similarly, it can be shown that $F_3 \sim K_1\zeta^4/24$ as $\zeta \to \infty$. We now have all the terms necessary to provide a complete matching.

The inner solution, is then given by

$$Y = \varepsilon \left(1 + a_0^2 \zeta^2 - \varepsilon^2 \frac{K_0}{4a_0} \left[\left(\frac{\zeta^3}{3} + \frac{\zeta}{a_0^2} \right) \arctan(\zeta) - \frac{1}{3a_0^3} \ln\left(1 + a_0^2 \zeta^2\right) + \hat{\beta}_1 \zeta^2 \right] + \varepsilon^4 \left[\frac{K_0}{24} \zeta^4 + \frac{1}{6} \alpha_2 \zeta^3 + \cdots \right] + \varepsilon^6 \left[\frac{K_1}{24} \zeta^4 + \cdots \right] + \cdots \right), \tag{4.4.33}$$

or, when rewritten in terms of Z,

$$Y = \varepsilon \left(1 + a_0^2 \frac{Z^2}{\varepsilon^4} - \varepsilon^2 \frac{K_0}{4a_0} \left[\left(\frac{Z^3}{3\varepsilon^6} + \frac{Z}{a_0^2 \varepsilon^2} \right) \arctan\left(a_0 \frac{Z}{\varepsilon^2} \right) - \frac{1}{3a_0^3} \ln\left(1 + a_0^2 \frac{Z^2}{\varepsilon^4} \right) + \hat{\beta}_1 \frac{Z^2}{\varepsilon^4} \right] + \varepsilon^4 \left[\frac{K_0}{24} \frac{Z^4}{\varepsilon^8} + \frac{1}{6} \alpha_2 \frac{Z^3}{\varepsilon^6} + \cdots \right] + \varepsilon^6 \left[\frac{K_0}{24} \frac{Z^4}{\varepsilon^8} + \cdots \right] + \cdots \right). \tag{4.4.34}$$

Matching

To perform an accurate matching it is traditional to introduce an intermediate variable, however, in this case it was possible to perform the matching in terms of the outer variable Z. Beginning with the outer solution (4.4.20), we write it in terms of ascending powers of ε

$$Y = \varepsilon^{-3} \Gamma_{-3} + \varepsilon^{-1} \Gamma_{-1} + \mathcal{O}(\varepsilon), \tag{4.4.35}$$

where

$$\Gamma_{-3} = \left(\frac{K_0}{384} + \frac{B_0}{8} + E_0 \right) - Z \left(\frac{K_0}{48} + \frac{B_0}{2} \right) + Z^2 \left(\frac{K_0}{16} + \frac{B_0}{2} \right) - Z^3 \frac{K_0}{12} + Z^4 \frac{K_0}{24} \tag{4.4.36}$$

$$\Gamma_{-1} = \left(\frac{K_1}{384} + \frac{B_1}{8} + E_1 \right) - Z \left(\frac{K_1}{48} + \frac{B_1}{2} \right) + Z^2 \left(\frac{K_1}{16} + \frac{B_1}{2} \right) - Z^3 \frac{K_1}{12} + Z^4 \frac{K_1}{24}. \tag{4.4.37}$$

For the inner solution (4.4.34), in the limit $\varepsilon \to 0$ the natural log term is negligible relative to the other terms and we replace the arctan term with the first two terms of an expansion

around $Z = \infty$. Written in ascending powers of ε it becomes

$$Y = \varepsilon^{-3}\gamma_{-3} + \varepsilon^{-1}\gamma_{-1} + \mathcal{O}(\varepsilon), \tag{4.4.38}$$

where

$$\gamma_{-3} = Z^2 a_0^2 - Z^3 \frac{K_0 \pi}{24 a_0} + Z^4 \frac{K_0}{24} \tag{4.4.39}$$

$$\gamma_{-1} = Z^2 \left(\frac{K_0}{12 a_0^2} - \frac{K_0 \hat{\beta}_1}{4 a_0} \right) - Z^3 \frac{1}{6} \left(\frac{K_1 \pi}{4 a_0} + \frac{K_0^2}{6 a_0^5} \left[\frac{\pi}{16} \left(7 - 3\ln(4) \right) + \frac{3 \hat{\beta}_1 a_0 \pi}{16} \right] \right) + Z^4 \frac{K_1}{24}. \tag{4.4.40}$$

Comparing coefficients of varying powers of Z in the ε^{-3} terms in (4.4.35) and (4.4.38) we obtain a set of equations for a_0, K_0, B_0 and E_0. These can be solved to find

$$a_0 = \frac{\pi}{2}, \quad K_0 = 6\pi^2, \quad B_0 = -\frac{\pi^2}{4}, \quad E_0 = \frac{\pi^2}{64}. \tag{4.4.41}$$

Comparing the coefficients in the ε^{-1} terms gives us a set of equations for $\hat{\beta}_1$, K_1, B_1 and E_1, which when solved yield

$$\hat{\beta}_1 = -\frac{2}{3\pi} \left(7 - 6\ln(2) \right), \quad K_1 = 96(4 - 3\ln(2)),$$
$$B_1 = 4(3\ln(2) - 4), \qquad E_1 = \frac{1}{4} \left(4 - 3\ln(2) \right). \tag{4.4.42}$$

In both cases, there are five equations for only four unknowns, but the coefficients of Z^4 are already identical, reducing the number of equations by one.

Composite Solution

To calculate a composite solution, which is valid across the entire domain, we add together the inner and outer solutions and subtract off the overlapping terms. The overlapping terms are the limit of the outer solution as $Z \to 0$, or equivalently the limit of the inner solution as $\zeta \to \infty$. Substitution of (4.4.41) and (4.4.42) removes the parameters

from the solution, and the composite solution is then

$$
\begin{aligned}
Y = \varepsilon^{-3} \Bigg\{ & \frac{\pi^2}{4}\left(Z-\frac{1}{2}\right)^4 - \frac{\pi^2}{8}\left(Z-\frac{1}{2}\right)^2 + \frac{\pi^2}{64} \\
& + \varepsilon^2 \left(4\left(4-3\ln(2)\right)\left(Z-\frac{1}{2}\right)^4 + 2\left(3\ln(2)-4\right)\left(Z-\frac{1}{2}\right)^2 + \frac{1}{4}\left(4-3\ln(2)\right)\right) \Bigg\} \\
& + \varepsilon \Bigg\{ 1 + \frac{\pi^2 Z^2}{4\varepsilon^4} - \varepsilon^2 3\pi \Bigg[\left(\frac{Z^3}{3\varepsilon^6} + \frac{4Z}{\pi^2\varepsilon^2}\right)\arctan\left(\frac{\pi Z}{2\varepsilon^2}\right) - \frac{8}{3\pi^3}\ln\left(1+\frac{\pi^2 Z^2}{4\varepsilon^4}\right) \\
& - \frac{2}{3\pi}\left(7-3\ln(4)\right)\frac{Z^2}{\varepsilon^4} \Bigg] \Bigg\} - \left\{ \frac{\pi^2 Z^2}{4\varepsilon^3} - \frac{\pi^2 Z^3}{2\varepsilon^3} + \left(16-6\ln(4)\right)\frac{Z^2}{\varepsilon} \right\}. \qquad (4.4.43)
\end{aligned}
$$

The term in the first set of curly brackets is the outer solution, the second set contains the inner solution and the third set are the overlap terms. The second-order correction terms to the inner are omitted from the composite solution as they were not fully calculated, and only used to provide a complete matching.

Recovery of η and c

To express this solution in terms of the scaled variable η we need to compute B using (4.4.8). Taking into account the symmetries of the solution we have

$$B = 2\int_0^{1/2} Y \,\mathrm{d}Z. \qquad (4.4.44)$$

Looking again at (4.4.43) we can see that the contributions from the inner solution at the two leading orders $\mathcal{O}(\varepsilon^{-3})$ and $\mathcal{O}(\varepsilon^{-1})$ are cancelled out by the terms in the overlap, so the greatest contribution from the inner solution will be $\mathcal{O}(\varepsilon)$, this takes place over the inner region of $\mathcal{O}(\varepsilon^2)$ so we would expect the contribution from the integral to be $\mathcal{O}(\varepsilon^3)$. This is negligible compared with the contribution from the outer solution. So we can rewrite (4.4.44) as

$$B = 2\varepsilon^{-3}\int_0^{1/2} W_0 + \varepsilon^2 W_1 \,\mathrm{d}Z + \mathcal{O}(\varepsilon) = \varepsilon^{-3}\left(\frac{\pi^2}{120} + 2\varepsilon^2\left(\frac{4-3\ln(2)}{15}\right) + \mathcal{O}\left(\varepsilon^4\right)\right). \qquad (4.4.45)$$

Using (4.4.11) and (4.4.45) the wavespeed c can then be expanded as

$$c = \sqrt{\frac{2K\delta D}{B^3}} = \frac{1440}{\pi^2}\sqrt{10\delta}\varepsilon^3\left(1 - \frac{16}{\pi^2}\varepsilon^2\left(4 - 3\ln(2)\right) + \mathcal{O}\left(\varepsilon^4\right)\right), \tag{4.4.46}$$

while using (4.4.45) the minimum value of η can be expanded as

$$\eta(0) = \frac{\varepsilon}{B} = \frac{120}{\pi^2}\varepsilon^4\left(1 - \frac{16}{\pi^2}\varepsilon^2\left(4 - 3\ln(2)\right) + \mathcal{O}\left(\varepsilon^4\right)\right). \tag{4.4.47}$$

Finally, using (4.4.20) and (4.4.45), the maximum value of η can be expanded as

$$\eta\left(1/2\right) = \frac{Y\left(1/2\right)}{B} = \frac{15}{8}\Big(1 + \mathcal{O}\left(\varepsilon^4\right)\Big). \tag{4.4.48}$$

Comparison with numerical solutions

The numerical and asymptotic results are compared in Figure 4.5. Figure 4.5(a) shows the point of largest deflection, which occurs at $Z = 1/2$. The asymptotic solution remains accurate up to initial amplitudes of $\varepsilon \approx 0.1$. Similarly, Figure 4.5(b) shows that the asymptotic solution for the unscaled velocity, K of the travelling waves remains accurate up to a similar value of ε. For an initial amplitude of $\varepsilon = 0.03$ the numerical solution is indistinguishable from the asymptotic solution (as shown in Figure 4.5(c)), while when $\varepsilon = 0.2$ the asymptotic solution is still reasonable but it is starting to diverge from the numerical solution (see Figure 4.5(d)). The asymptotic results from (4.4.46)–(4.4.48) for the speed–amplitude relationship are also shown in Figure 4.4. The lower curve fits the numerical data much better because the asymptotic solution has greater accuracy there; the error in the lower line is $\mathcal{O}(\varepsilon^8)$ while in the upper line it is $\mathcal{O}(\varepsilon^4)$.

4.4.3 Antisymmetric mode travelling waves

To look for antisymmetric travelling-wave solutions of the linear plate system (4.2.32)–(4.2.35), we take $\eta = 1$ and $u = 0$ in the governing equations. On making this substitution, (4.2.32) and (4.2.33) are identically satisfied, while (4.2.34) and (4.2.35) become

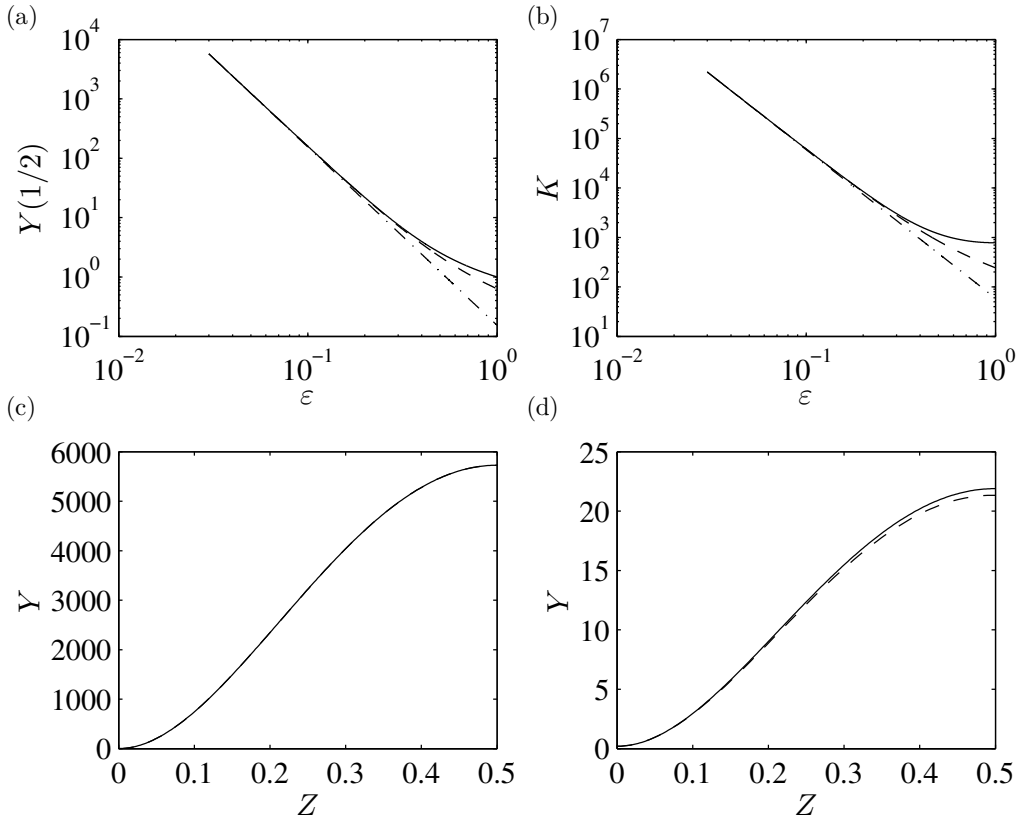

Figure 4.5: A comparison of the numerical results for symmetric travelling-wave solutions of the linear plate system (4.4.7)–(4.4.9), with the asymptotic analysis of section 4.4.2 for $\varepsilon \ll 1$. (a) The maximum thickness perturbation $Y(1/2)$ against ε. (b) The scaled wave speed K against ε. (c) and (d) The thickness perturbation for $\varepsilon = 0.03$ and $\varepsilon = 0.2$ respectively. In all cases, the numerical results are shown with solid lines, leading-order asymptotic results with dot-dashed lines and the first order corrections with dashed lines.

linear equations equivalent to (4.2.38) and (4.2.39). The travelling wave solutions are therefore the same as the antisymmetric solutions found for the fully linearised system, as given by (4.3.8) and (4.3.9). With no nonlinear effects contributing, antisymmetric travelling waves of any amplitude have a sinusoidal profile $\tilde{\eta} = \varepsilon \sin(2\pi(x - ct))$ and move with speed $c = 4\pi/\sqrt{\delta}$.

4.4.4 Mixed-mode travelling waves

We consider whether there exist any travelling wave solutions to (4.2.32)–(4.2.35) in which both the symmetric and antisymmetric components are non-zero. The partial decoupling means that the symmetric component of any such solution must satisfy (4.2.32)

and (4.2.33) and so be a symmetric travelling-wave solution in its own right. We therefore look for travelling-waves solutions to (4.2.34) and (4.2.35) with η and u given by the previous solution with speed c.

We can eliminate u from these equations using (4.4.5). Equation (4.2.35) can then be integrated once, and v eliminated using (4.2.34). The resulting equation for $\hat{\eta}$ is

$$\frac{\mathrm{d}^3\hat{\eta}}{\mathrm{d}Z^3} + \frac{\delta c^2}{4\eta}\frac{\mathrm{d}\hat{\eta}}{\mathrm{d}Z} = F, \tag{4.4.49}$$

where F is a constant of integration. This equation is linear in $\hat{\eta}$ but contains a non-constant coefficient involving η, where η and $c/\sqrt{\delta}$ are known from the symmetric solution. For a given symmetric-mode amplitude ε we thus have a third-order equation with two unknown parameters: δ and F. The required five boundary conditions are

$$\hat{\eta}'(0) = \varepsilon_a, \qquad \hat{\eta}(0) = \hat{\eta}''(0) = 0, \qquad \hat{\eta}(1/2) = \hat{\eta}''(1/2) = 0. \tag{4.4.50}$$

These conditions specify an odd solution with wavelength 1, and the arbitrary amplitude is set by ε_a. The system (4.4.49) and (4.4.50) are then solved using `bvp4c`.

For symmetric travelling wave components with $\varepsilon \approx 1$ we found $\delta \approx 1/\pi$, which is the value at which the symmetric and antisymmetric waves in the fully linear system have the same speed. As $\varepsilon \to 0$ the required aspect ratio δ increased. Since we assumed $\delta \ll 1$ in the problem formulation, these solutions are not valid in our model. It follows that there are no long-wavelength mixed-mode travelling waves in the linear plate system.

We can interpret this result in terms of interactions between symmetric and antisymmetric travelling-wave components. For such interactions to arise, the components need to have comparable velocities at the same wavelength. However, in the fully linear system, we saw that at long wavelengths ($\delta \ll 1$) the velocity of the antisymmetric mode was much greater than that of the symmetric mode. Therefore no interactions are possible when the system is close to being linear. Nonlinear effects only serve to slow down the symmetric modes still further, and hence make the velocity difference even greater.

4.5 Travelling Waves in Nonlinear System

4.5.1 Symmetric mode travelling waves

To seek travelling-wave solutions to the symmetric mode of the nonlinear system; we have to use a different formulation to the one used for the linear plate system as we are unable to make the change of variables $\eta = Y/B$ to eliminate the constant of integration B.

Since we are considering the symmetric mode, we must have $\hat{\eta} = v = 0$, and from (4.2.31) the curvature can be simplified to

$$\kappa_{\pm} = \pm\frac{\kappa}{2}, \tag{4.5.1}$$

where

$$\kappa = \frac{\eta_{ZZ}}{\left(1 + \frac{1}{4}\delta^2\eta_Z^2\right)^{3/2}}. \tag{4.5.2}$$

From (4.2.28), the pressure can be written

$$p_{\pm} = \frac{p}{2}, \tag{4.5.3}$$

where

$$p = \delta\left(\frac{\partial^2\kappa}{\partial s^2} + \frac{\delta^2\kappa^3}{8}\right). \tag{4.5.4}$$

Thus we have, from (4.2.24) and (4.2.25),

$$\frac{\partial\eta}{\partial t} + \frac{\partial}{\partial x}(u\eta) = 0, \tag{4.5.5}$$

$$\frac{\partial u}{\partial t} + u\frac{\partial u}{\partial x} = -\frac{\partial p}{\partial x}. \tag{4.5.6}$$

Note, (4.2.34) and (4.2.35) are identically satisfied. The formulation proceeds in the same way as for the linear plate system until (4.4.6), which is replaced with

$$-\frac{c^2}{2\delta}\left(1 - \frac{1}{\eta^2}\right) + \kappa_{ss} + \frac{\delta^2\kappa^3}{8} - B = 0. \tag{4.5.7}$$

To provide a way to ensure the conservation of mass constraint (4.4.2) can be satisfied, we introduce the incremental volume

$$V(Z) = \int_0^Z \eta(Z')\,\mathrm{d}Z'. \tag{4.5.8}$$

The fifth-order system (4.5.2)–(4.5.8) is then recast as a system of first order equations in η, η_Z, κ, κ_s and V

$$\frac{\partial \eta}{\partial Z} = \eta_Z, \tag{4.5.9}$$

$$\frac{\partial \eta_Z}{\partial Z} = \left(1 + \frac{1}{4}\delta^2\eta_Z^2\right)^{3/2}\kappa, \tag{4.5.10}$$

$$\frac{\partial \kappa}{\partial Z} = \left(1 + \frac{1}{4}\delta^2\eta_Z^2\right)^{1/2}\kappa_s, \tag{4.5.11}$$

$$\frac{\partial \kappa_s}{\partial Z} = \left(1 + \frac{1}{4}\delta^2\eta_Z^2\right)^{1/2}\left(B + \frac{c^2}{2\delta}\left(1 - \frac{1}{\eta^2}\right) - \frac{\delta^2\kappa^3}{8}\right), \tag{4.5.12}$$

$$\frac{\partial V}{\partial Z} = \eta. \tag{4.5.13}$$

With five equations and two unknown parameters B and c we require seven boundary conditions. With an imposed amplitude, the symmetry conditions used before, and required volume constraint, we set

$$\begin{aligned} &\eta(0) = 1 + a, \qquad \eta_Z(0) = 0, \qquad \kappa_s(0) = 0, \qquad V(0) = 0, \\ &\qquad\qquad\quad \eta_Z(1/2) = 0, \qquad \kappa_s(1/2) = 0, \qquad V(1/2) = 1/2. \end{aligned} \tag{4.5.14}$$

This system is then solved using `bvp4c` as previously.

The wave profiles were found to be almost identical to the profiles found for the linear plate system. The primary consequence of the extra nonlinearity is a lowering of the speed for a travelling wave when compared to the linear plate system. This is illustrated in figure 4.6(a) for varying values of δ, while in figure 4.6(b) we can see how little the wave profiles vary with δ. For the velocity, the difference between the nonlinear system and the linear plate system is very small for $\delta = 0.1$ but becomes greater as δ increases

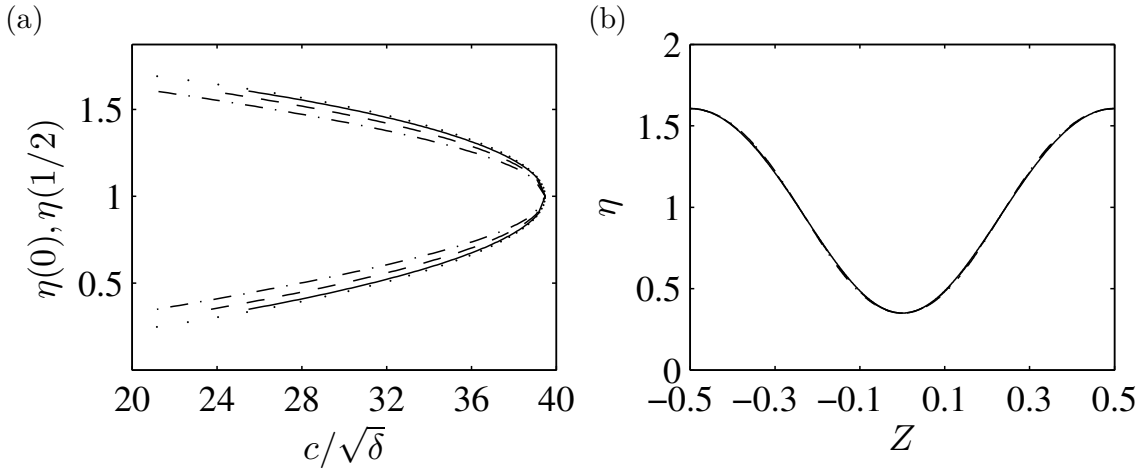

Figure 4.6: (a) The velocity c of the nonlinear system symmetric mode travelling waves as a function of the maximum or minimum displacements, $\eta(0)$ and $\eta(1/2)$ respectively, for varying values of δ. (b) A selection of thickness profiles for travelling solutions of the nonlinear system with $\varepsilon = 0.35$. In both cases the thin solid line is $\delta = 0.1$, the dashed line is $\delta = 0.2$ and the dot-dashed line is $\delta = 0.3$. The dotted line is the velocity in the linear plate system, equivalent to the limit $\delta \to 0$.

from there.

4.6 Discussion

We have formulated a nonlinear set of equations to describe the propagation of waves at the interface of fluid and solid in a channel with elastic sides. We also derived simplified models in the form of a linear plate system and a fully linearised system. Analytic solutions were found for both the symmetric and antisymmetric modes in the case of the fully linearised system.

For the linear plate system, an equation for symmetric mode travelling waves was found and solved numerically for both the wave profile and propagation speed. An asymptotic analysis was performed for the symmetric mode as the channel thickness approached zero and this was found to have a strong agreement with the numerical solution. The antisymmetric mode was shown to be identical to the fully linear system. When travelling waves were sought that involved both a symmetric and antisymmetric component, it was found that due to the size of the difference in propagation speed they were unlikely to be observed in the aspect ratio regime we considered.

In the nonlinear system, we again found an equation governing symmetric mode travelling waves, which was solved numerically in the same way as the linear plate system. The profiles were found to be almost identical to those in the linear plate system, just propagating at a lower velocity. Further to this, the profiles were also shown to be almost independent of δ, which as it was increased, had the primary effect of decreasing propagation velocity futher still.

CHAPTER FIVE

TEMPORAL EVOLUTION OF LINEAR DISTURBANCES IN THE NONLINEAR SYSTEM

5.1 Introduction

In this chapter, we build on the work done in Chapter 4 to determine numerically the temporal evolution of linear disturbances in the nonlinear system. The governing equations of the previous chapter are transformed into finite difference analogues. A numerical scheme is then constructed to solve the equations in both space and time for a given set of initial conditions. This scheme is then validated before being used to investigate the effects of the nonlinear terms in the curvature have upon the temporal evolution of linear travelling wave solutions from Chapter 4. As the amplitude of the initial profiles is increased, the effects of the nonlinearities become move prevalent and some interesting results are observed and discussed.

5.2 Numerical Method

Our starting point is the equations derived in the previous chapter to describe inviscid flow in an elastic-walled channel. For reference, they consist of the full curvature system,

the linear plate system and the fully linear system. The full curvature system is given by

$$\frac{\partial \eta}{\partial t} + \frac{\partial}{\partial x}(u\eta) = 0, \tag{5.2.1}$$

$$\frac{\partial u}{\partial t} + u\frac{\partial u}{\partial x} = -\left[\frac{\partial}{\partial x}(p_+ + p_-) - \frac{2}{\eta}\frac{\partial \hat{\eta}}{\partial x}(p_+ - p_-)\right], \tag{5.2.2}$$

$$\frac{\partial \hat{\eta}}{\partial t} + u\frac{\partial \hat{\eta}}{\partial x} = v, \tag{5.2.3}$$

$$\frac{\partial v}{\partial t} + u\frac{\partial v}{\partial x} = -\frac{2}{\delta^2 \eta}(p_+ - p_-), \tag{5.2.4}$$

where

$$p_\pm = \pm\delta\left(\frac{\partial^2 \kappa_\pm}{\partial s^2} + \frac{\delta^2}{2}\kappa_\pm^3\right) \tag{5.2.5}$$

$$\begin{aligned} &= \pm\delta f_\pm^5 \frac{\partial^4}{\partial x^4}\left(\hat{\eta} \pm \frac{\eta}{2}\right) \\ &\quad \mp \delta^3 f_\pm^7 \left[10\frac{\partial^3}{\partial x^3}\left(\hat{\eta} \pm \frac{\eta}{2}\right)\frac{\partial^2}{\partial x^2}\left(\hat{\eta} \pm \frac{\eta}{2}\right)\frac{\partial}{\partial x}\left(\hat{\eta} \pm \frac{\eta}{2}\right) + 3\left(\frac{\partial^2}{\partial x^2}\left(\hat{\eta} \pm \frac{\eta}{2}\right)\right)^3\right] \\ &\quad \pm \delta^3 f_\pm^9 \left[\frac{1}{2}\left(\frac{\partial^2}{\partial x^2}\left(\hat{\eta} \pm \frac{\eta}{2}\right)\right)^3 + 18\delta^2\left(\frac{\partial^2}{\partial x^2}\left(\hat{\eta} \pm \frac{\eta}{2}\right)\right)^3\left(\frac{\partial}{\partial x}\left(\hat{\eta} \pm \frac{\eta}{2}\right)\right)^2\right], \end{aligned} \tag{5.2.6}$$

and

$$f_\pm = \left[1 + \delta^2\left(\frac{\partial}{\partial x}\left(\hat{\eta} \pm \frac{\eta}{2}\right)\right)^2\right]^{-\frac{1}{2}}. \tag{5.2.7}$$

The linear plate system is given by

$$\frac{\partial \eta}{\partial t} + \frac{\partial}{\partial x}(u\eta) = 0, \tag{5.2.8}$$

$$\frac{\partial u}{\partial t} + u\frac{\partial u}{\partial x} = -\delta\frac{\partial^5 \eta}{\partial x^5}, \tag{5.2.9}$$

$$\frac{\partial \hat{\eta}}{\partial t} + u\frac{\partial \hat{\eta}}{\partial x} = v, \tag{5.2.10}$$

$$\frac{\partial v}{\partial t} + u\frac{\partial v}{\partial x} = -\frac{4}{\delta\eta}\frac{\partial^4 \hat{\eta}}{\partial x^4}. \tag{5.2.11}$$

Finally, the fully linear system is given by

$$\frac{\partial \eta'}{\partial t} + \frac{\partial u'}{\partial x} = 0, \tag{5.2.12}$$

$$\frac{\partial u'}{\partial t} = -\delta \frac{\partial^5 \eta'}{\partial x^5} \tag{5.2.13}$$

$$\frac{\partial \hat{\eta}'}{\partial t} = v', \tag{5.2.14}$$

$$\frac{\partial v'}{\partial t} = -\frac{4}{\delta} \frac{\partial^4 \hat{\eta}'}{\partial x^4}. \tag{5.2.15}$$

We wish to solve for the temporal evolution of u, v, η and $\hat{\eta}$ given periodic boundary conditions in x and initial conditions at $t = 0$. To solve (5.2.1)–(5.2.4) or (5.2.8)–(5.2.11) numerically we use a Crank–Nicolson scheme (e.g. Smith, 1985). This involves discretising the domain into a grid before rewriting the governing equations as finite difference analogues. For the grid we divide the spatial domain $x \in [0, 1]$ up into n equally spaced nodes, with the spacing denoted Δx. We split the grid for the temporal domain into m points with a spacing of Δt. Each point is defined by $()_i^j$, with i denoting the spatial grid point and j the temporal grid point, this can be seen in Figure 5.1.

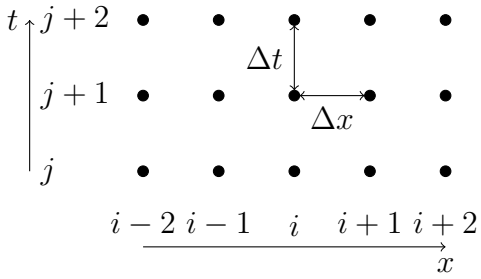

Figure 5.1: Diagram of the numerical grid.

The functions u, v, η and $\hat{\eta}$ are all calculated in a time-weighted manner, in the form

$$g_i = g_i^j + \theta \left(g_i^{j+1} - g_i^j \right), \tag{5.2.16}$$

where θ is the weighting term produced by time averaging (e.g. Eggers & Dupont, 1994; Cheong & Howes, 2004). For the Crank–Nicolson scheme, $\theta = 0.5$, while $\theta = 0$ corresponds to a fully explicit scheme in time, and $\theta = 1$ is a fully implicit scheme. The Crank–Nicolson scheme is advantageous over an explicit scheme such as Lax–Wendroff

which requires prohibitively small timesteps for convergence due to the high order of the spatial derivatives. Central finite differences replace the spatial derivatives as follows (e.g. Abramowitz & Stegun, 2012)

$$\left.\frac{\partial g}{\partial x}\right|_{x=x_i} \rightarrow \; g_i^{\mathrm{I}} = \frac{-g_{i-1}+g_{i+1}}{2\Delta x}, \tag{5.2.17}$$

$$\left.\frac{\partial^2 g}{\partial x^2}\right|_{x=x_i} \rightarrow g_i^{\mathrm{II}} = \frac{g_{i-1}-2g_i+g_{i+1}}{(\Delta x)^2}, \tag{5.2.18}$$

$$\left.\frac{\partial^3 g}{\partial x^3}\right|_{x=x_i} \rightarrow g_i^{\mathrm{III}} = \frac{-2g_{i-2}+4g_{i-1}-4g_{i+1}+2g_{i+2}}{4(\Delta x)^3}, \tag{5.2.19}$$

$$\left.\frac{\partial^4 g}{\partial x^4}\right|_{x=x_i} \rightarrow g_i^{\mathrm{IV}} = \frac{g_{i-2}-4g_{i-1}+6g_i-4g_{i+1}+g_{i+2}}{(\Delta x)^4}. \tag{5.2.20}$$

The maximum error in these spatial derivatives is $-(\Delta x)^3 f^{(3)}/6$, and is the error for the first derivative approximation. For the temporal derivative, forward differencing is used and can thus be written as

$$\left.\frac{\partial g}{\partial t}\right|_{t=t_j,x=x_i} \rightarrow \frac{g_i^{j+1}-g_i^j}{\Delta t}, \tag{5.2.21}$$

with error $\mathcal{O}(\Delta t)$, which decreases to $\mathcal{O}((\Delta t)^2)$ when $\theta = 0.5$ (Cheong & Howes, 2004). Finally, we note that it is convenient to use a staggered spatial grid, with η and $\hat{\eta}$ evaluated at the grid points, and u and v evaluated halfway between grid points. Thus, equations involving a time derivative of η or $\hat{\eta}$, are solved at the grid points x_i, and equations involving time derivatives of u and v, references to the thickness and centerline are solved at the half grid points $x_{i+1/2}$, for example

$$\left.\frac{\partial g}{\partial x}\right|_{x=x_{i+\frac{1}{2}}} \rightarrow \frac{-g_i+g_{i+1}}{\Delta x}. \tag{5.2.22}$$

At this point, we can rewrite the governing equations as finite difference analogues,

and in so doing the fully nonlinear system, (5.2.1)–(5.2.4), can be written as

$$\eta_i^{j+1} - \eta_i^j + \frac{\Delta t}{\Delta x}\left[\frac{(u_i + u_{i-1})(\eta_{i+1} - \eta_{i-1})}{4} + (u_i - u_{i-1})\eta_i\right] = 0, \tag{5.2.23}$$

$$\begin{aligned} &u_i^{j+1} - u_i^j + \frac{\Delta t}{\Delta x}\left[\frac{u_i(u_{i+1} - u_{i-1})}{2}\right] \\ &+\frac{\Delta t}{\Delta x}\left[p_{i+1}^+ - p_i^+ + p_{i+1}^- - p_i^- - 2\left(\frac{\hat{\eta}_{i+1} - \hat{\eta}_i}{\eta_{i+1} + \eta_i}\right)\left(p_{i+1}^+ + p_i^+ - p_{i+1}^- - p_i^-\right)\right] = 0 \end{aligned} \tag{5.2.24}$$

$$\hat{\eta}_i^{j+1} - \hat{\eta}_i^j + \frac{\Delta t}{\Delta x}\left[\frac{(u_i + u_{i-1})(\hat{\eta}_{i+1} - \hat{\eta}_{i-1})}{4}\right] - \Delta t\left[\frac{v_i + v_{i-1}}{2}\right] = 0, \tag{5.2.25}$$

$$v_i^{j+1} - v_i^j + \frac{\Delta t}{\Delta x}\left[\frac{u_i(v_{i+1} - v_{i-1})}{2}\right] + \frac{2\Delta t}{\delta^2(\eta_{i+1} + \eta_i)}\left(p_{i+1}^+ + p_i^+ - p_{i+1}^- - p_i^-\right) = 0, \tag{5.2.26}$$

where

$$\begin{aligned} p_i^{\pm} = &\pm\delta f_{i\pm}^5\left(\hat{\eta}_i^{\mathrm{IV}} \pm \frac{\eta_i^{\mathrm{IV}}}{2}\right) \\ &\pm \delta^3 f_{i\pm}^7\left[10\left(\hat{\eta}_i^{\mathrm{III}} \pm \frac{\eta_i^{\mathrm{III}}}{2}\right)\left(\hat{\eta}_i^{\mathrm{II}} \pm \frac{\eta_i^{\mathrm{II}}}{2}\right)\left(\hat{\eta}_i^{\mathrm{I}} \pm \frac{\eta_i^{\mathrm{I}}}{2}\right) + 3\left(\hat{\eta}_i^{\mathrm{II}} \pm \frac{\eta_i^{\mathrm{II}}}{2}\right)^3\right] \\ &\pm \delta^3 f_{i\pm}^9\left[\frac{1}{2}\left(\hat{\eta}_i^{\mathrm{II}} \pm \frac{\eta_i^{\mathrm{II}}}{2}\right)^3 + 18\delta^2\left(\hat{\eta}_i^{\mathrm{II}} \pm \frac{\eta_i^{\mathrm{II}}}{2}\right)^3\left(\hat{\eta}_i^{\mathrm{I}} \pm \frac{\eta_i^{\mathrm{I}}}{2}\right)^2\right], \end{aligned} \tag{5.2.27}$$

and

$$f_{i\pm} = \left[1 + \delta^2\left(\hat{\eta}_i^{\mathrm{I}} \pm \frac{\eta_i^{\mathrm{I}}}{2}\right)^2\right]^{-\frac{1}{2}}. \tag{5.2.28}$$

Note, p_i and f_i are evaluated on the grid points x_i. The finite difference analogue equations for the linearplate system, (5.2.8)–(5.2.11), are given by

$$\eta_i^{j+1} - \eta_i^j + \frac{\Delta t}{\Delta x}\left[\frac{(u_i + u_{i-1})(\eta_{i+1} - \eta_{i-1})}{4} + (u_i - u_{i-1})\eta_i\right] = 0, \quad (5.2.29)$$

$$u_i^{j+1} - u_i^j + \frac{\Delta t}{\Delta x}\left[\frac{u_i(u_{i+1} - u_{i-1})}{2}\right] + \frac{\delta \Delta t}{\Delta x}\left(\eta_{i+1}^{\mathrm{IV}} - \eta_i^{\mathrm{IV}}\right) = 0, \quad (5.2.30)$$

$$\hat{\eta}_i^{j+1} - \hat{\eta}_i^j + \frac{\Delta t}{\Delta x}\left[\frac{(u_i + u_{i-1})(\hat{\eta}_{i+1} - \hat{\eta}_{i-1})}{4}\right] - \Delta t\left[\frac{v_i + v_{i-1}}{2}\right] = 0, \quad (5.2.31)$$

$$v_i^{j+1} - v_i^j + \frac{\Delta t}{\Delta x}\left[\frac{u_i(v_{i+1} - v_{i-1})}{2}\right] + \frac{4\Delta t}{\delta(\eta_{i+1} + \eta_i)}\left(\hat{\eta}_{i+1}^{\mathrm{IV}} + \hat{\eta}_i^{\mathrm{IV}}\right) = 0, \quad (5.2.32)$$

There is no need for finite difference analogues to the fully linear system, (5.2.12)–(5.2.15) since we have found analytic solutions. At each timestep a matrix system of equations is formed from the finite difference analogues that is then solved by LU decomposition and back substitution. To ensure periodicity of solutions, we insist that in a spatial domain with n grid points we must have $f_1 = f_n$ for the four variables. We use linear travelling wave solutions from Chapter 4 as initial conditions, specifically, for the symmetric mode we use (4.3.3)–(4.3.4), and the antisymmetric mode uses (4.3.8)–(4.3.9).

It was found that in some cases, particularly when solving the equations for large amplitude symmetric disturbances, spurious numerical oscillations occured. To suppress this numerical noise we follow Eggers & Dupont (1994), and include an additional term in the left-hand side of (5.2.24) and (5.2.30). This takes the form of a numerical viscosity, and in derivative form it looks like

$$-\frac{\vartheta \Delta x}{\eta^2}\left(\eta^2 u u_x\right)_x, \quad (5.2.33)$$

where the subscripts denote differentiation and ϑ is an upwinding parameter. It turns out the effect of the numerical viscosity is not significantly dependent on the magnitude of ϑ, therefore $\vartheta = 0.05$ was chosen following Eggers & Dupont (1994).

As a final note, the numerical model breaks down as $\eta \to 0$, so we terminate our calculations if $\eta = 0.01$ or less at any point in the domain at any timestep.

5.3 Validation

It is necessary to test the numerical scheme to ensure the results are sufficiently accurate. To do this, we test the effects of varying both the spatial and temporal resolutions, before considering the principle of energy conservation.

5.3.1 Spatial and temporal resolutions

We first test the effect of varying both the spatial and temporal resolutions. This is done by considering the evolution in time of a travelling wave solution to the fully nonlinear system as given by solutions to (4.5.7). If the code is accurate, the profile of η should be preserved. We calculate solutions over one period of the travelling wave for four spatial resolutions: $\Delta x = 0.01$, $\Delta x = 0.005$, $\Delta x = 0.0025$ and $\Delta x = 0.00125$, and three temporal resolutions: $\Delta t = 0.001$, $\Delta t = 0.0001$ and $\Delta t = 0.00005$. At the end of the period each solution is compared to the original profile by calculating the root mean square error (RMSE), for two vectors x and y of length n, the RMSE is given by

$$\mathrm{RMSE} = \sqrt{\frac{1}{n}\sum_{i=1}^{n}(x_i - y_i)^2}. \tag{5.3.1}$$

The RMSE is a suitable choice of error measure for this system since it provides a good balance between both local and global error, as well as being efficient to calculate from the natural output of the code at each time step. The results are illustrated in Figure 5.2.

In Figure 5.2(a) we see that for all temporal resolutions, as the spatial resolution increase (Δx decreases) the error in the solution profile decreases. We chose $\Delta x = 0.0025$ as our working resoution as the large increase in time required to calculate the solution at the finest resolution was not worth the reduction in error offered.

Figure 5.2(b) shows that the coarsest temporal resolution ($\Delta t = 0.001$) gives a significantly larger error than the two finer resolutions. However the difference between the two finer resolutions is negligible at any spatial resolution. Again, we do not take the finest temporal resolution to work with, instead we take $\Delta t = 0.0001$ as the reduced

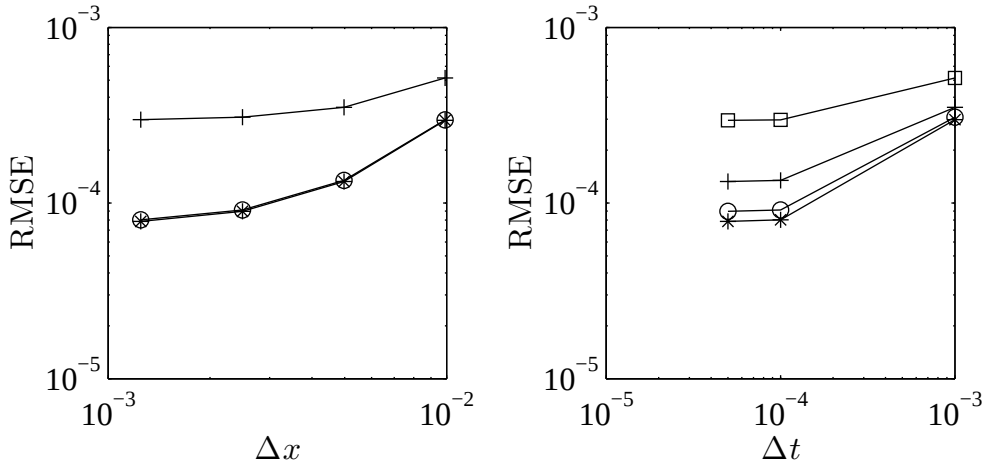

Figure 5.2: Root mean square errors after one period of a travelling wave solution of the symmetric mode of the nonlinear system. (a) Spatial error for $\Delta t = 0.001$ (plus signs), $\Delta t = 0.0001$ (circles), $\Delta t = 0.00005$ (asterisks). (b) Temporal error for $\Delta x = 0.01$ (squares), $\Delta x = 0.005$ (plus signs), $\Delta x = 0.0025$ (circles), $\Delta x = 0.00125$ (asterisks)

computation time results in such a small increase in error.

These results are specific for the symmetric mode, as we do not have nonlinear travelling wave solutions for the antisymmetric mode. To test the effect of varying the spatial and temporal resolutions on the antisymmetric mode we are limited to examining the behaviour of a fixed point in the domain ($x = 0$) over time as we vary both the spatial and temporal resolutions. In Figure 5.3 we illustrate the results for varying spatial resolutions at $t = 0.1$ for a fixed $\Delta t = 0.0001$, similarly in Figure 5.4 the results are shown for varying temporal resolutions at $t = 0.1$ for a fixed $\Delta x = 0.0025$. We find the same behaviour as in the symmetric mode.

We also note the same tests were performed for the linear plate systems and the results were consistent with what has been presented here so they have not been included.

5.3.2 Energy conservation

The formulation of the system and governing equations is such that there is no method of energy dissipation built in, for that reason it should be possible to construct energy conservation equations for both the nonlinear and linear plate systems.

To construct our energy equation for the nonlinear system we first note that work done

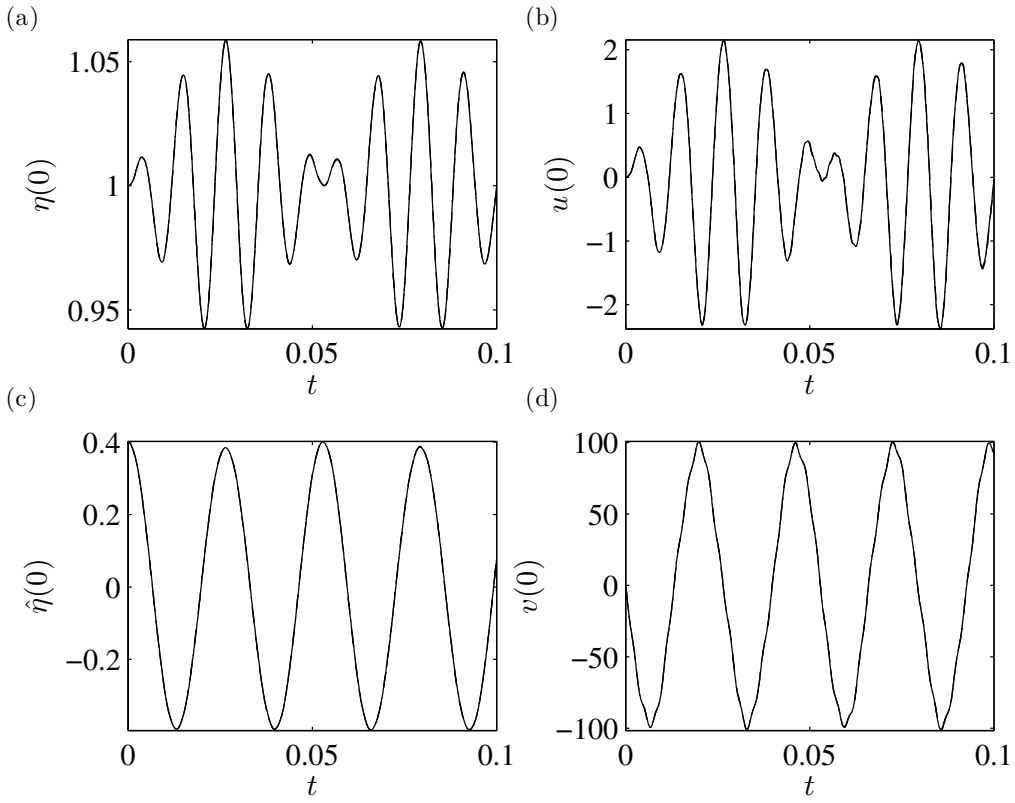

Figure 5.3: The effect of varying the spatial resolution on the fully nonlinear antisymmetric mode at a fixed point in the domain. The dashed line corresponds to $\Delta x = 0.005$, the solid line to $\Delta x = 0.0025$ and the dashed-dot line to $\Delta x = 0.00125$.

on either wall can be expressed as the rate of change of bending energy, and is then given by

$$W = \frac{\mathrm{d}}{\mathrm{d}t}\left(\frac{1}{2}\int_0^1 \kappa^2 \,\mathrm{d}s\right) = \frac{\mathrm{d}}{\mathrm{d}t}\left(\frac{1}{2}\int_0^1 \frac{(\eta_\pm'')^2}{(1+(\eta_\pm')^2)^{5/2}}\,\mathrm{d}x\right). \tag{5.3.2}$$

We take ηu times (5.2.2) and $u^2/2$ times (5.2.1), and add them together to obtain

$$\frac{\partial}{\partial t}\left(\frac{\eta u^2}{2}\right) + \frac{\partial}{\partial x}\left(\frac{\eta u^3}{2} + 2u\eta\bar{p}\right) = -2\frac{\partial}{\partial x}(\eta u)\,\bar{p} + 2u\frac{\partial \hat{\eta}}{\partial x}\hat{p}, \tag{5.3.3}$$

where $\bar{p} = (p_+ + p_-)/2$, $\hat{p} = p_+ - p_-$. We also take ηv times (5.2.4) and $v^2/2$ times (5.2.1)

$$\frac{\partial}{\partial t}\left(\frac{\eta v^2}{2}\right) + \frac{\partial}{\partial x}\left(\frac{\eta u v^2}{2}\right) = -\frac{2v}{\delta^2}\hat{p}, \tag{5.3.4}$$

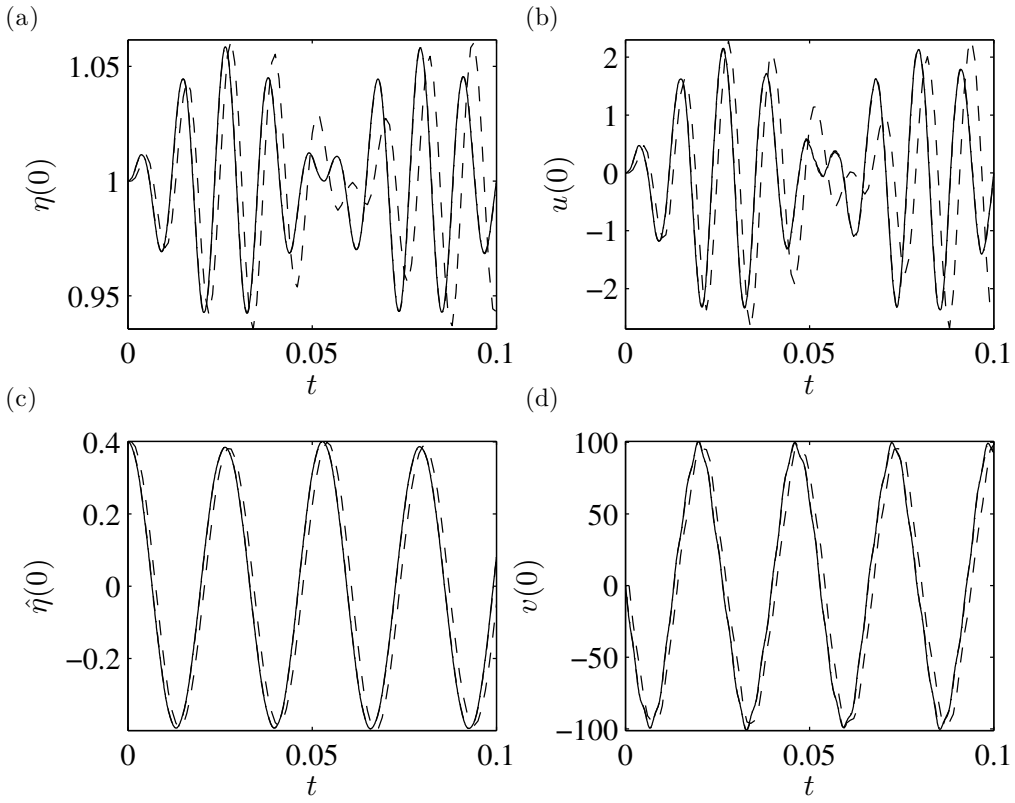

Figure 5.4: The effect of varying the temporal resolution on the fully nonlinear antisymmetric mode at a fixed point in the domain. The dashed line corresponds to $\Delta t = 0.001$, the solid line to $\Delta t = 0.0001$ and the dashed-dot line to $\Delta t = 0.00005$.

we now combine (5.3.3) and δ^2 times (5.3.4) and rearrange to get

$$\frac{\partial}{\partial t}\left(\frac{\eta}{2}\left(u^2+\delta^2 v^2\right)\right)+\frac{\partial}{\partial x}\left(\frac{\eta u}{2}\left(u^2+\delta^2 v^2\right)+2u\eta\bar{p}\right)+2\left(\frac{\partial \eta}{\partial t}\bar{p}+\frac{\partial \hat{\eta}}{\partial t}\hat{p}\right)=0, \quad (5.3.5)$$

where we have used (5.2.1) and (5.2.3) to replace

$$\frac{\partial}{\partial x}(u\eta)=-\frac{\partial \eta}{\partial t}, \quad u\frac{\partial \hat{\eta}}{\partial x}=v-\frac{\partial \hat{\eta}}{\partial t}, \quad (5.3.6)$$

respectively. Integrating over one wavelength, the middle term is periodic and so vanishes, leaving

$$\frac{\partial}{\partial t}\frac{1}{2}\int_0^1 \eta\left(u^2+\delta^2 v^2\right)\,\mathrm{d}x+2\int_0^1\left(\frac{\partial \eta_+}{\partial t}p_+-\frac{\partial \eta_-}{\partial t}p_-\right)\,\mathrm{d}x=0. \quad (5.3.7)$$

The last term is seen to be equivalent to the work done and we so our energy equation for

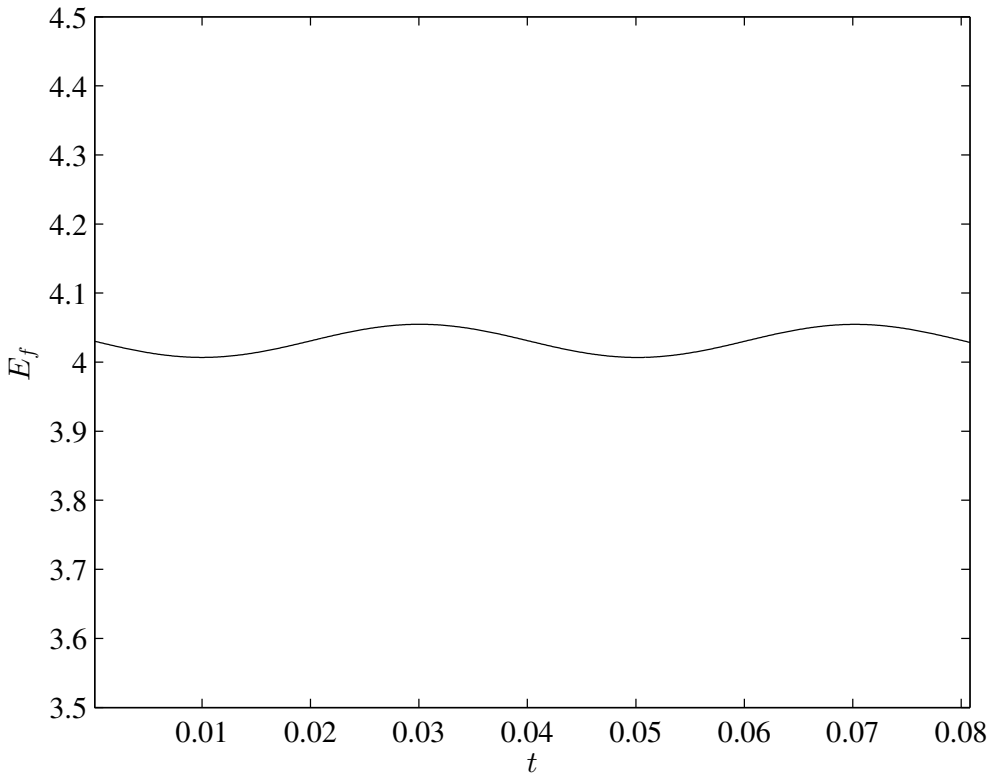

Figure 5.5: The variation in the energy in the nonlinear system over time, as given by (5.3.8). ($\varepsilon_s = 0.1$, $\delta = 0.1$)

the nonlinear curvature system is

$$\frac{1}{2}\int_0^1 \eta\left(u^2 + \delta^2 v^2\right)\,\mathrm{d}x + \int_0^1 \frac{\eta_+''^2}{\left(1+\eta_+'^2\right)^{5/2}} + \frac{\eta_-''^2}{\left(1+\eta_-'^2\right)^{5/2}}\,\mathrm{d}x = E_f, \tag{5.3.8}$$

where E_f is the constant energy in the system. At each timestep these integrals are evaluated numerically using the trapezium rule, for a travelling wave solution to the nonlinear system with amplitude $\varepsilon_s = 0.1$, and the results are shown in Figure 5.5. We see a small smooth fluctuation of less than 1.2% but the energy remains fairly constant around $E_f = 4.03$, suggesting the code is accurate.

For the linear plate system, due to the decoupling we only derive the energy equation to the symmetric mode. If we multiply (4.2.33) by $u\eta$, rearrange the derivatives and

integrate over one wavelength, then we find

$$\frac{\mathrm{d}}{\mathrm{d}t}\int_0^1 \left\{\frac{\eta u^2}{2}+\frac{\delta}{2}\left(\frac{\partial^2\eta}{\partial x^2}\right)^2\right\}\mathrm{d}x+\left[\frac{\eta u^3}{2}+\delta\left(u\eta\frac{\partial^4\eta}{\partial x^4}+\frac{\partial\eta}{\partial t}\frac{\partial^3\eta}{\partial x^3}-\frac{\partial^2\eta}{\partial t\partial x}\frac{\partial^2\eta}{\partial x^2}\right)\right]_0^1=0, \tag{5.3.9}$$

The two terms in the integrand in (5.3.9) represent kinetic energy in the fluid and bending energy in the wall respectively. The terms contained within the square brackets represent energy fluxes with the first being the flux of kinetic energy, while the final three represent flux of bending energy. All the terms in the square brackets in (5.3.9) are periodic in space and so this equation simplifies to

$$\int_0^1 \frac{\eta u^2}{2}+\frac{\delta}{2}\left(\frac{\partial^2\eta}{\partial x^2}\right)^2\mathrm{d}x=E_l, \tag{5.3.10}$$

where E_l is the constant energy in the system. This integral is evaluated numerically at every time step using the trapezium rule. We found that the energy varied on a scale of $\mathcal{O}\left(10^{-5}\right)$ implying the energy is conserved and verifying that the wave is neutrally stable, as we would expect an unstable wave to have an energy increase associated with it, and a decaying wave to have an energy decrease.

5.4 Results

5.4.1 Symmetric waves

The effect of nonlinearity upon the propagation of waves in a symmetrically disturbed channel is investigated by comparing a linear solution, a solution of the linear plate system and a solution of the full curvature system. In all cases, we start with the linear travelling-wave solution (4.3.3) and (4.3.4) as the initial conditions for η and u at $t=0$, with $\hat{\eta}=v=0$. We then compare the analytical evolution of the linear solution with the numerical solutions to (5.2.1)–(5.2.4), and also (5.2.8)–(5.2.11).

Figure 5.6 shows the propagation of a wave with initial amplitude $\varepsilon_s=0.7$ and $\delta=0.1$ for one nondimensional time period $T=0.0801$ determined by (4.3.6). It is worth

noting in light of (4.2.23) the transverse and axial length scales are different. We see that the nonlinear terms in the linear plate system and nonlinear system solutions reduce the velocity at which the wave propagates, as in the time taken for the linear solution to advance one wavelength, the linearised- and full-curvature solutions travel much less. This also agrees with the results from the travelling waves for the fully nonlinear system found previously, that the waves in that system travel slower than those in the linear plate system. In the nonlinear solutions, the fluid tends to group into bulges with a clear steepening and slackening of the gradient of the wall shape.

Figure 5.7 shows the resultant axial velocity profiles for the perturbations. Comparing Figures 5.6 and 5.7 directly we can see that the narrowing channel results in an increase in the magnitude of the velocity driving the flow backwards through the channel into the bulges.

At this amplitude it is necessary to use the full solution as the linear and leading-order solutions do not capture the full nonlinear behaviour. We note that for amplitudes of $\varepsilon_s \approx 0.3$ and below, the three solutions are virtually indistinguishable as the effect of nonlinear terms becomes negligible. For amplitudes of $\varepsilon_s \approx 0.8$ and larger, it was found that in finite time η will become small enough to halt our calculations. An example of the wall profiles and the axial velocity at the moment we stop the calculations is illustrated in Figure 5.8.

5.4.2 Anti-symmetric waves

We can perform the same investigation for antisymmetric waves as we did for symmetric waves. Our three solutions are again a linear solution, a linear plate solution and a full curvature solution. For antisymmetric solutions the linear solution corresponds to (4.3.8), the leading-order solution to (4.2.26) and (4.2.35) with initial conditions (4.3.8), (4.3.9) and a constant thickness $\eta = 1$, and the full-curvature solution corresponds to (4.2.24)–(4.2.27) with initial conditions (4.3.8), (4.3.9), $\eta = 1$ and $u = 0$.

The propagation of the three waves for an initial amplitude $\varepsilon_a = 0.8$ is illustrated in Figure 5.9, with $\delta = 0.1$. The linear and leading-order solutions are identical because

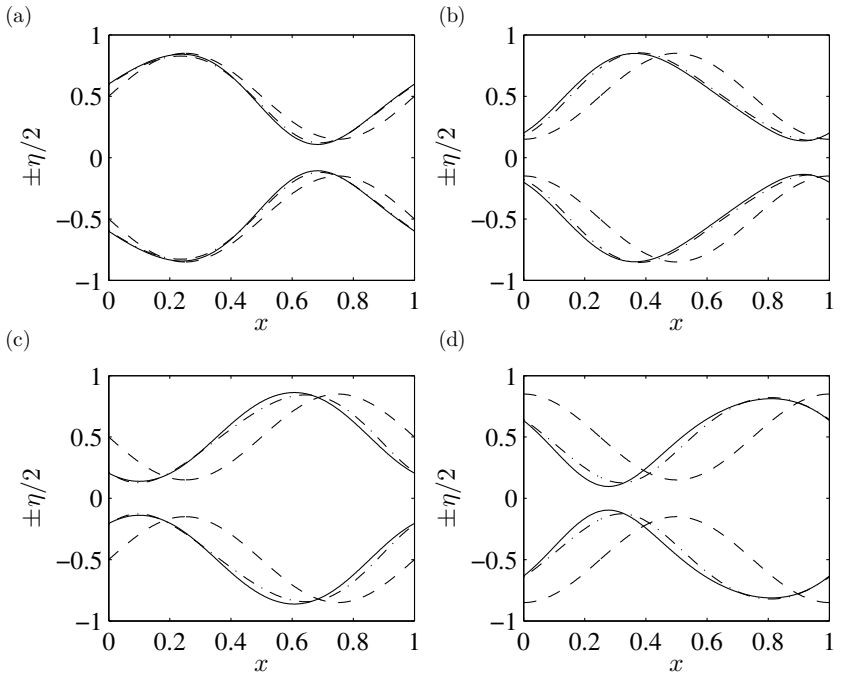

Figure 5.6: Propagation of waves with initial profiles given by (4.3.3) and (4.3.4) with $\varepsilon_s = 0.7$ and $\delta = 0.1$. In all cases the dashed line is the fully linearised profile, the dot-dashed line is the linear plate profile and the solid line is the full curvature profile. (a) $t = T/4$, (b) $t = T/2$, (c) $t = 3T/4$ and (d) $t = T$.

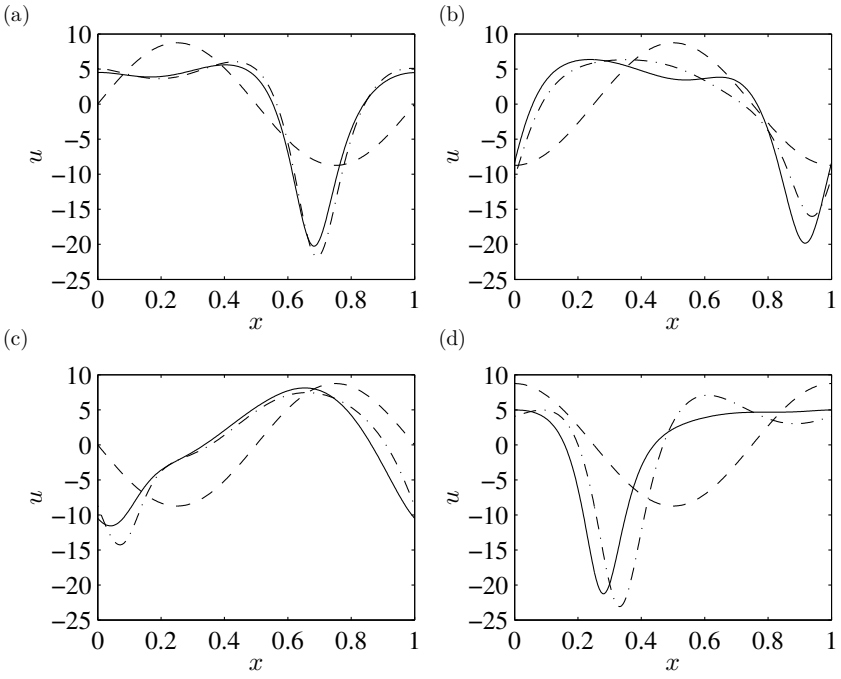

Figure 5.7: The axial velocity profiles associated with the wall profiles in Figure 5.6 with $\varepsilon_s = 0.7$ and $\delta = 0.1$. In all cases the dashed line is the fully linearised profile, the dot-dashed line is the linear plate profile and the solid line is the full curvature profile. (a) $t = T/4$, (b) $t = T/2$, (c) $t = 3T/4$ and (d) $t = T$.

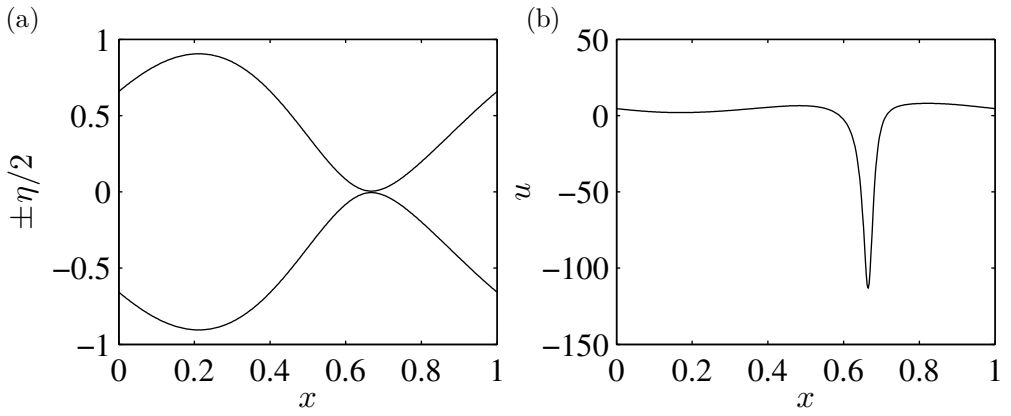

Figure 5.8: (a) The wall profiles as η approaches 0 for the symmetric mode. (b) The corresponding axial velocity profile. In both cases $\varepsilon_s = 0.8$, $\delta = 0.1$ and $t = 0.0241$

(4.3.8) and (4.3.9) satisfy (4.2.26) and (4.2.35) directly. The magnitude of the variation between the full-curvature and the other two solutions even at this amplitude is caused by the coupling in the governing equations that is not present in the linear or leading order solutions. We also see the same reduction in the wave velocity for the full-curvature solution that was present in the symmetric waves. The channel thins on the slopes and gathers in bulges at the bends. The antisymmetric mode can handle much larger perturbations than the symmetric mode, as a consequence the thickness is not small enough to halt the calculations until $\varepsilon_a \approx 1.25$, as illustrated in Figure 5.10, along with the axial velocity profile. It is possible to see two spikes in the magnitude of the axial velocity profile corresponding to the two points the channel is narrowing at. It is worth noting that while both the symmetric and antisymmetric profiles illustrating the moment the calculations halt occur at the same time, this is coincidental as the calculations are stopped at different times for different initial amplitudes of the perturbations.

The difference in velocity of the waves in the symmetric mode and the antisymmetric mode has been discussed for the fully linear system and linear plate system. This difference is accounted for physically by the difference in magnitude of the axial and transverse velocities required to move the fluid in the channel. It is illustrated for the fully nonlinear system in Figure 5.11. To show the differing wave speeds, the symmetric and antisymmetric modes were calculated separately for the same amplitude of disturbance and parameter values, and then the deviation of the thickness and centerline from

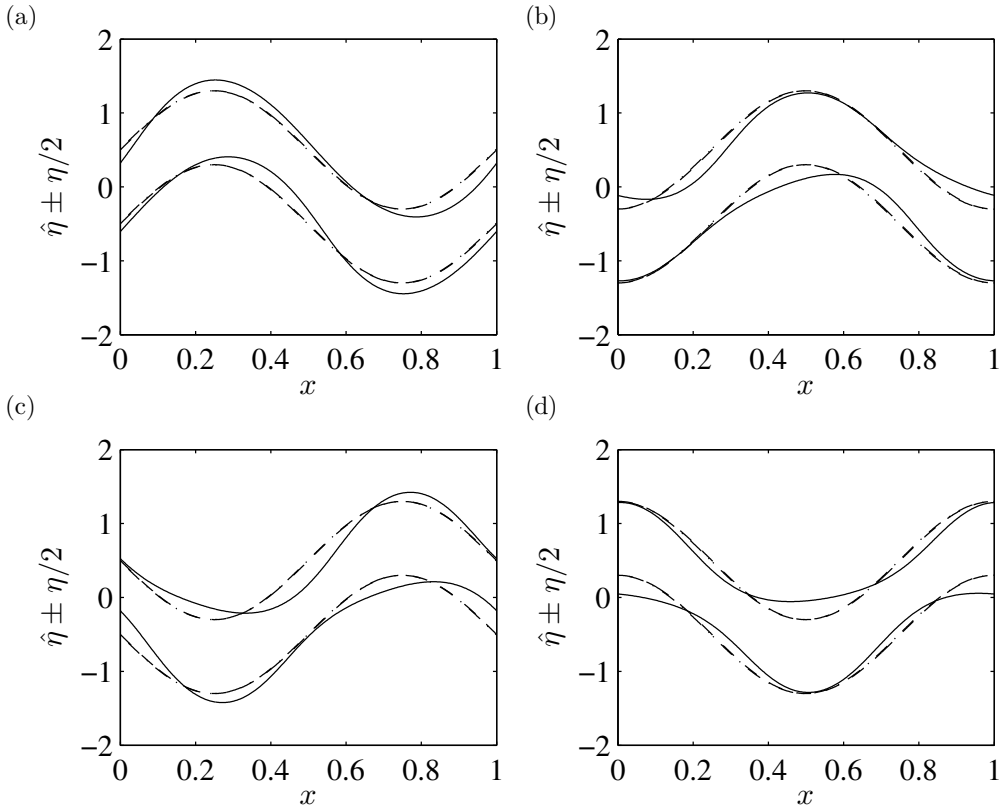

Figure 5.9: Propagation of waves with initial profiles given by (4.3.8) and (4.3.9) with $\varepsilon_a = 0.8$ and $\delta = 0.1$. In all cases the dashed line is the fully linearised profile, the dot-dashed line is the linear plate profile and the solid line is the full curvature profile. (a) is $T/4$, (b) is $T/2$, (c) is $3T/4$ and (d) is T.

their base values were plotted for a specific point over time. In the symmetric mode we can see a higher order temporal oscillation stemming from the nonlinear terms, this is in agreement with Mehring & Sirignano (1999) who found the same oscillations arose for liquid sheets.

Figure 5.12 shows the evolution over one period of the thickness of disturbances to all four variables, rather than just two as illustrated previously. Even for such small perturbations, we can see that there is quite a large response when both the centreline and thickness are disturbed.

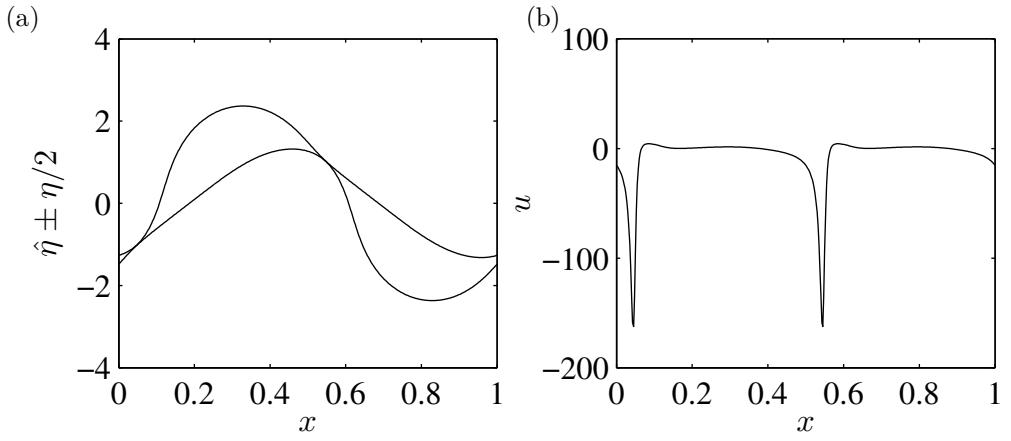

Figure 5.10: (a) The wall profiles as η approaches 0 for the antisymmetric mode. (b) The corresponding axial velocity profile. In both cases $\varepsilon_a = 1.25$, $\delta = 0.1$ and $t = 0.0241$

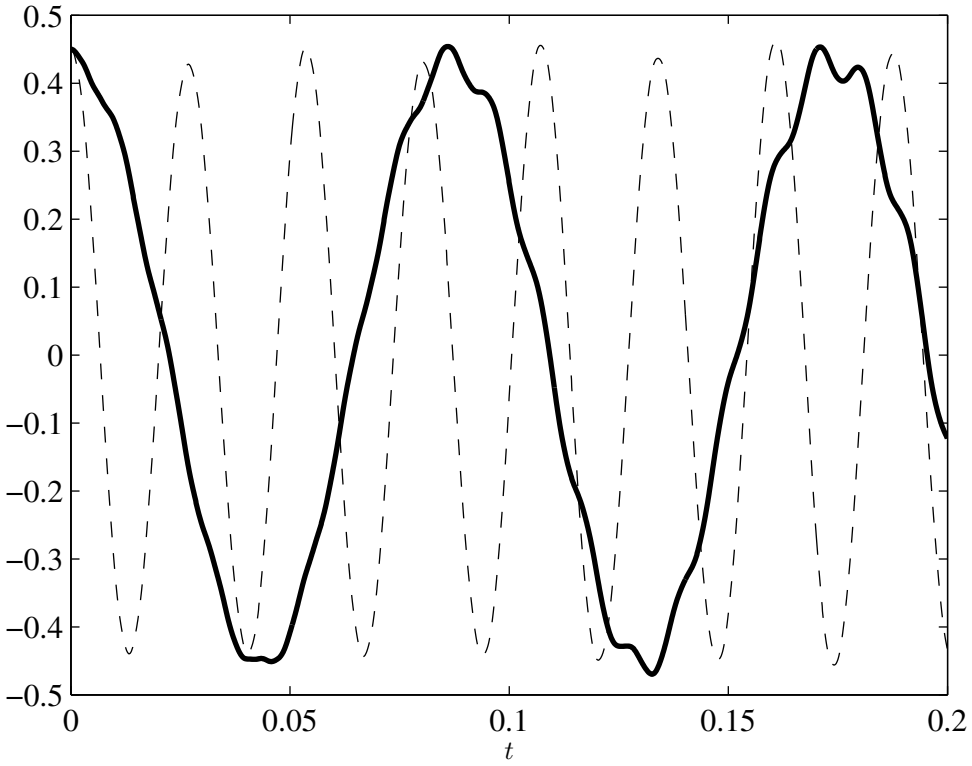

Figure 5.11: The deviation from the undisturbed values of the thickness, $\eta(0,t)$, with $\varepsilon_s = 0.45$ and $\delta = 1$ given by the solid line, and the centreline, $\hat{\eta}(0,t)$, with $\varepsilon_a = 0.45$ and $\delta = 0.1$ given by the dashed line.

5.5 Discussion

We have discretised the equations derived in Chapter 4, to formulate a numerical scheme to describe the propagation of waves at the the interface of fluid and solid in a channel with elastic sides. The numerical scheme was then validated to ensure the spatial

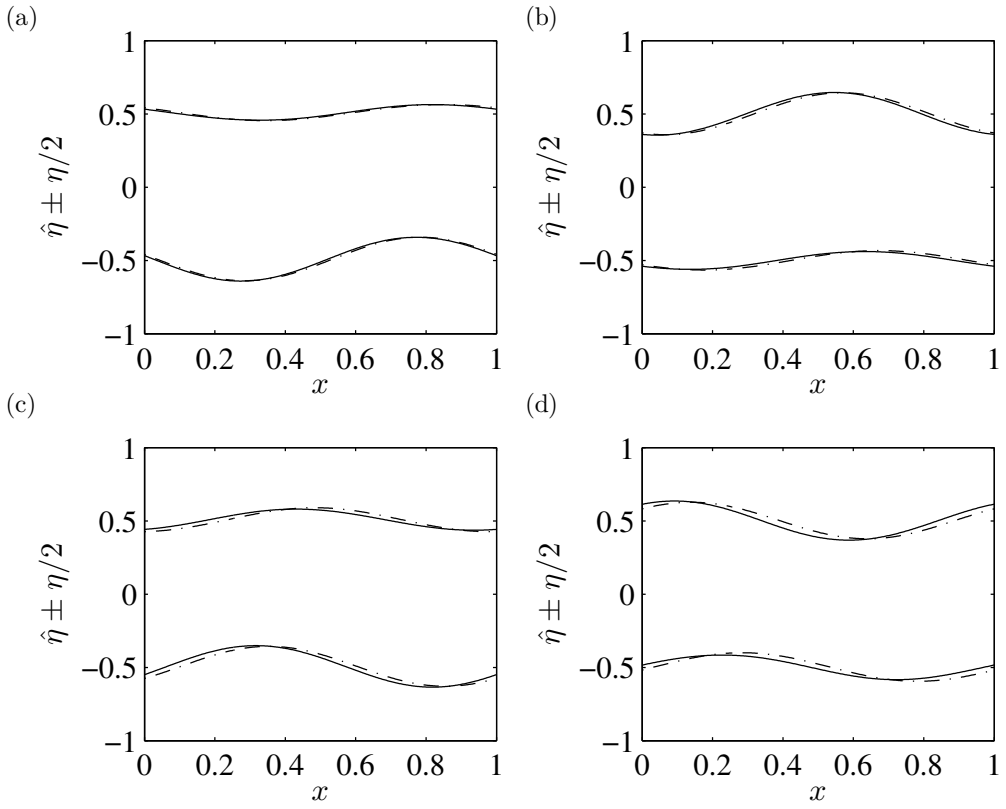

Figure 5.12: Propagation of waves with initial profiles given by (4.3.3), (4.3.4), (4.3.8) and (4.3.9) with $\varepsilon_a = \varepsilon_s = 0.1$ and $\delta = 0.1$. In both cases the linear plate profile is given by the dot-dashed line and the full curvature profile is given by the solid line. (a) is $T/4$, (b) is $T/2$, (c) is $3T/4$ and (d) is T.

and temporal resolution were sufficiently accurate. We also derived energy conservation equations for both the nonlinear and linear plate systems and checked the numerical scheme satisfied this condition.

Qualitatively the results found are similar to work done on liquid sheets. We showed that for large-amplitude disturbances the curvature causes strongly nonlinear behaviour and introduces a higher-order temporal oscillation on top of the main wave. Similar higher-order oscillations have been observed in analogous problems for liquid sheets. In both the symmetric and antisymmetric modes the accumulation of fluid in bulges in the channel is similar to the formation of droplets when the elastic plates are replaced by free surfaces (Mehring & Sirignano, 1999).

CHAPTER SIX

CHANNEL FLOW WITH DIFFERING WALL ELASTICITIES

6.1 Introduction

As a natural extension to the work done previously in Chapters 4 and 5 we now seek to determine how the behaviour of the system changes when the bending stiffnesses of the two channel walls are independent of each other. Recent work by Vance *et al.* (2014) suggests that Jupiter's moon Ganymede may have an internal structure consisting of alternating ice and ocean layers, with the ice layers having different physical properties which may lead to a situation such as the one dealt with in this chapter.

We will first formulate the governing equations in the same manner as in Chapter 4 before seeking linear travelling wave solutions. In contrast to the work in Chapter 4 however, travelling wave solutions are not sought for the nonlinear system. Instead, the focus is upon numerical results such as were found in Chapter 5, where the evolution of the nonlinear system is determined for varying values of the bending stiffness ratio. We will also investigate the interesting limiting cases of the ratio tending to zero and infinity, corresponding to flow between one rigid wall and one elastic wall.

6.2 Problem Formulation

As in Chapters 4–5, working in Cartesian coordinates (x^*, y^*), we consider an incompressible, inviscid, two-dimensional flow between two flexible walls a mean distance a apart, in a gravity-free regime. The fluid has constant density ρ, and its pressure and velocity fields are denoted p^* and (u^*, v^*) respectively. The upper interface is located at $y^* = \eta_+^*(x^*, t^*)$ and the lower at $y^* = \eta_-^*(x^*, t^*)$. Outside of the channel is assumed to be a vacuum. If the flow and walls are undisturbed, the fluid is assumed to flow at a constant velocity U_r in the x^* direction, with the walls at $y^* = \pm a/2$. We are interested in long wavelength perturbations to this undisturbed state with wavelength L. In contrast with Chapters 4 and 5 we allow the elasticities of the interfaces to be independent of each other.

The governing equations are established in a similar way to Chapter 4; we will just highlight the key differences here. The first difference is in the dynamic condition at the channel walls, in place of (4.2.7) we now have

$$p_\pm^* = \pm D_\pm^* \left[f_\pm^* \frac{\partial}{\partial x^*} \left(f_\pm^* \frac{\partial}{\partial x^*} \left(f_\pm^{*3} \frac{\partial^2 \eta_\pm^*}{\partial x^{*2}} \right) \right) + \frac{1}{2} \left(f_\pm^{*3} \frac{\partial^2 \eta_\pm^*}{\partial x^{*2}} \right)^3 \right], \tag{6.2.1}$$

where

$$f_\pm^* = \left[1 + \left(\frac{\partial \eta_\pm^*}{\partial x^*} \right)^2 \right]^{-\frac{1}{2}}, \tag{6.2.2}$$

and $D_\pm^*$ is the bending stiffness of the walls, with the subscript specifying the top $(+)$ or bottom $(-)$ wall. For simplicity, we choose to scale the axial velocity based on the bottom wall parameter, namely

$$U = \sqrt{\frac{D_-^*}{2\rho L^3}}. \tag{6.2.3}$$

This introduces a new nondimensional quantity

$$D = \frac{D_+^*}{D_-^*}, \tag{6.2.4}$$

the ratio of the elasticities of the walls. We consider only $D_+ \geq 0$ and $D_- \geq 0$, ensuring

$D \geq 0$. If $D = 0$ this corresponds to an entirely passive top wall, or to a rigid bottom wall, similarly as $D \to \infty$, this corresponds to a passive bottom wall or to a rigid top wall.

The nondimensional governing equations are given by

$$\frac{\partial \eta}{\partial t} + \frac{\partial}{\partial x}(u\eta) = 0, \tag{6.2.5}$$

$$\frac{\partial u}{\partial t} + u\frac{\partial u}{\partial x} = -\left[\frac{\partial}{\partial x}(Dp_+ + p_-) - \frac{2}{\eta}\frac{\partial \hat{\eta}}{\partial x}(Dp_+ - p_-)\right], \tag{6.2.6}$$

$$\frac{\partial \hat{\eta}}{\partial t} + u\frac{\partial \hat{\eta}}{\partial x} = v, \tag{6.2.7}$$

$$\frac{\partial v}{\partial t} + u\frac{\partial v}{\partial x} = -\frac{2}{\delta^2 \eta}(Dp_+ - p_-), \tag{6.2.8}$$

where

$$\begin{aligned} p_\pm = {} & \pm\delta f_\pm^5 \frac{\partial^4}{\partial x^4}\left(\hat{\eta} \pm \frac{\eta}{2}\right) \\ & \mp \delta^3 f_\pm^7 \left[10\frac{\partial^3}{\partial x^3}\left(\hat{\eta} \pm \frac{\eta}{2}\right)\frac{\partial^2}{\partial x^2}\left(\hat{\eta} \pm \frac{\eta}{2}\right)\frac{\partial}{\partial x}\left(\hat{\eta} \pm \frac{\eta}{2}\right) + 3\left(\frac{\partial^2}{\partial x^2}\left(\hat{\eta} \pm \frac{\eta}{2}\right)\right)^3\right] \\ & \pm \delta^3 f_\pm^9 \left[\frac{1}{2}\left(\frac{\partial^2}{\partial x^2}\left(\hat{\eta} \pm \frac{\eta}{2}\right)\right)^3 + 18\delta^2\left(\frac{\partial^2}{\partial x^2}\left(\hat{\eta} \pm \frac{\eta}{2}\right)\right)^3\left(\frac{\partial}{\partial x}\left(\hat{\eta} \pm \frac{\eta}{2}\right)\right)^2\right], \end{aligned} \tag{6.2.9}$$

and

$$f_\pm = \left[1 + \delta^2\left(\frac{\partial}{\partial x}\left(\hat{\eta} \pm \frac{\eta}{2}\right)\right)^2\right]^{-\frac{1}{2}}. \tag{6.2.10}$$

The above set of equations is referred to as the nonlinear system. If $D = 1$ these reduce to equations (4.2.24)–(4.2.30) of Chapter 4.

We introduce a fully linear system based on a linearisation about the undisturbed state by writing $\eta = 1 + \eta'$, $u = u'$, $\hat{\eta} = \hat{\eta}'$, $v = v'$ and neglecting terms that are quadratic in

the primed variables. The resulting system of equations can be written

$$\frac{\partial \eta'}{\partial t} + \frac{\partial u'}{\partial x} = 0, \tag{6.2.11}$$

$$\frac{\partial u'}{\partial t} = -\delta \left[D \frac{\partial^5}{\partial x^5} \left(\hat{\eta}' + \frac{\eta'}{2} \right) - \frac{\partial^5}{\partial x^5} \left(\hat{\eta}' - \frac{\eta'}{2} \right) \right], \tag{6.2.12}$$

$$\frac{\partial \hat{\eta}'}{\partial t} = v', \tag{6.2.13}$$

$$\frac{\partial v'}{\partial t} = -\frac{2}{\delta} \left[D \frac{\partial^4}{\partial x^4} \left(\hat{\eta}' + \frac{\eta'}{2} \right) + \frac{\partial^4}{\partial x^4} \left(\hat{\eta}' - \frac{\eta'}{2} \right) \right]. \tag{6.2.14}$$

6.3 Linear Analysis

We look first at the linear system given by (6.2.11)–(6.2.14), to seek a dispersion relation, observing that if $D \neq 1$ then the decoupling of the system that exists when $D = 1$ is no longer present. Eliminating u' and v' from (6.2.11)–(6.2.14) we insert an ansatz for η' and $\hat{\eta}'$ given by

$$\eta' = \eta'_0 \exp(i(kx - \omega t)), \tag{6.3.1}$$

$$\hat{\eta}' = \hat{\eta}'_0 \exp(i(kx - \omega t)). \tag{6.3.2}$$

In order to avoid $\eta'_0 = \hat{\eta}'_0 = 0$, we must satisfy the following quadratic in ω^2

$$\omega^4 - \left(\frac{2k^4}{\delta} + \frac{\delta k^6}{2} \right) (D+1)\, \omega^2 + 4k^{10} D = 0. \tag{6.3.3}$$

The solution for ω can be written as

$$\omega = \pm k^3 \sqrt{\left(\frac{\delta}{4} + \frac{1}{\delta k^2} \right) (D+1) \pm \sqrt{\left(\frac{\delta}{4} + \frac{1}{\delta k^2} \right)^2 (D+1)^2 - \frac{4D}{k^2}}}. \tag{6.3.4}$$

From (6.3.4) we can obtain an expression for the phase velocity

$$c = \frac{\omega}{k} = \pm k^2 \sqrt{\left(\frac{\delta}{4} + \frac{1}{\delta k^2} \right) (D+1) \pm \sqrt{\left(\frac{\delta}{4} + \frac{1}{\delta k^2} \right)^2 (D+1)^2 - \frac{4D}{k^2}}}. \tag{6.3.5}$$

The choice of either a plus or a minus before the second square root suggests the existence of two different modes; these can be considered continuations of the antisymmetric and symmetric modes that exist when $D = 1$. The positive root is analagous to the antisymmetric phase velocity and the negative root is analagous to the symmetric phase velocity when the roots are calculated numerically. The two differing phase velocities are denoted

$$c_a = \pm k^2 \sqrt{\left(\frac{\delta}{4} + \frac{1}{\delta k^2}\right)(D+1) + \sqrt{\left(\frac{\delta}{4} + \frac{1}{\delta k^2}\right)^2 (D+1)^2 - \frac{4D}{k^2}}}, \tag{6.3.6}$$

$$c_s = \pm k^2 \sqrt{\left(\frac{\delta}{4} + \frac{1}{\delta k^2}\right)(D+1) - \sqrt{\left(\frac{\delta}{4} + \frac{1}{\delta k^2}\right)^2 (D+1)^2 - \frac{4D}{k^2}}}, \tag{6.3.7}$$

where the subscripts denote which mode the velocity approaches as $D \to 1$. For simplicity, the two modes will be referred to throughout as the antisymmetric mode and the symmetric mode, but it is understood that this is a simplified description as the lack of decoupling means these terms no longer hold any real meaning. We instead use them to refer to the continuation that collapses to the traditional mode when $D = 1$. Having now determined the dispersion relations and phase velocities we seek travelling wave solutions to the linear system of equations for each mode.

Antisymmetric Mode

We seek periodic travelling wave solutions so we look for solutions of the form $\eta' = A\cos(2\pi(x - c_a t)$, where A is the amplitude and c_a is the phase velocity. Using a bit of foresight, we rescale the amplitude as $A \to A'(D-1)$ since we require the amplitude of η' to be zero when $D = 1$. Upon substituting this into the linear system of equations

(6.2.11)–(6.2.14) and following through the algebra, we obtain a system of solutions

$$\eta' = A'(D-1)\cos(2\pi(x - c_a t)), \tag{6.3.8}$$

$$u' = A'(D-1)c_a\cos(2\pi(x - c_a t)), \tag{6.3.9}$$

$$\hat{\eta}' = A'\left[\frac{c_a^2}{\delta(2\pi)^4} - \frac{(D+1)}{2}\right]\cos(2\pi(x - c_a t)), \tag{6.3.10}$$

$$v' = A'\left[\frac{c_a^2}{\delta(2\pi)^4} - \frac{(D+1)}{2}\right]2\pi c_a\sin(2\pi(x - c_a t)). \tag{6.3.11}$$

Symmetric Mode

We perform the same operation, again seeking periodic travelling wave solutions, this time starting with a solution of the form $\hat{\eta}' = B\cos(2\pi(x - c_s t)$, where B is the amplitude and c_s is the phase velocity. We make the same rescaling of $B \to B'(D-1)$, and from this we obtain a new system of solutions

$$\eta' = B'\left[\frac{\delta c_s^2}{(2\pi)^2} - 2(D+1)\right]\cos(2\pi(x - c_s t)), \tag{6.3.12}$$

$$u' = B'\left[\frac{\delta c_s^2}{(2\pi)^2} - 2(D+1)\right]c_s\cos(2\pi(x - c_s t)), \tag{6.3.13}$$

$$\hat{\eta}' = B'(D-1)\cos(2\pi(x - c_s t)), \tag{6.3.14}$$

$$v' = B'(D-1)2\pi c_s\sin(2\pi(x - c_s t)). \tag{6.3.15}$$

6.4 Numerical Method

To determine the temporal evolution of waves in the nonlinear system, we use the same scheme as we did previously in Chapter 5, adjusted for this problem. For this reason we omit the details of the scheme, but we will still validate our choice of spatial and temporal resolution.

To obtain the numerical solution and allow us to perform the tests listed above we need to specify initial conditions for the system. We use the travelling wave solutions to the fully linear system given above by (6.3.8)–(6.3.11) for the antisymmetric mode

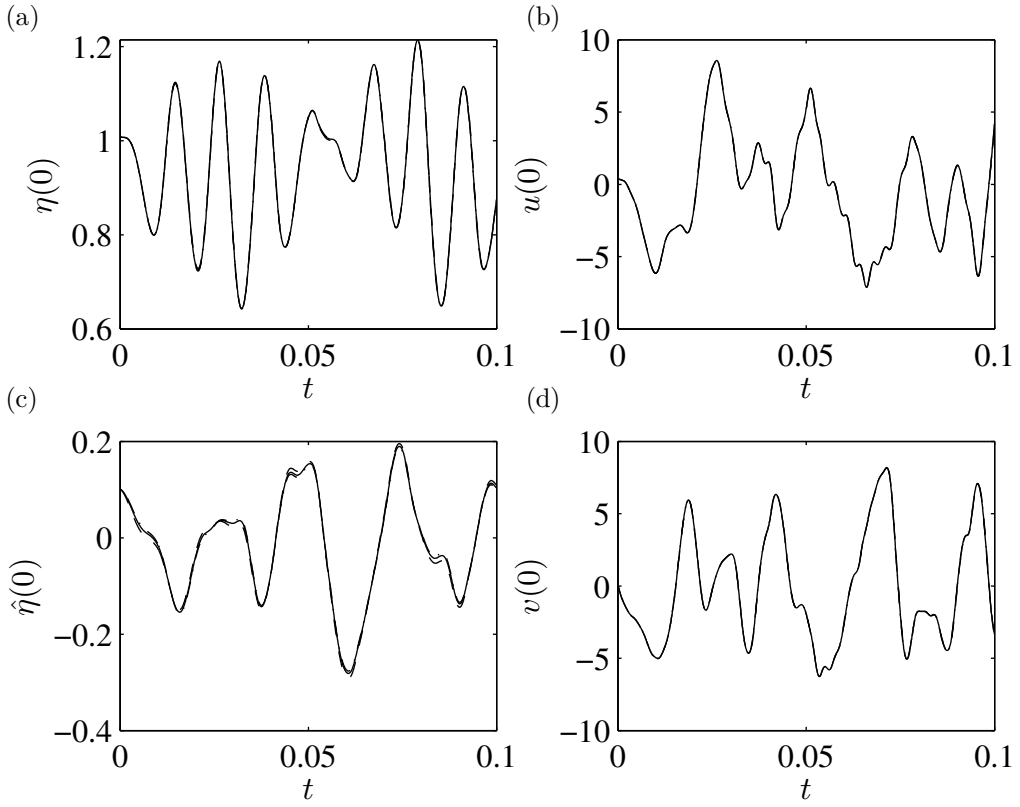

Figure 6.1: The effect of varying the spatial resolution on the continuation of the fully nonlinear antisymmetric mode at a fixed point in the domain. The dashed line corresponds to $\Delta x = 0.005$, the solid line to $\Delta x = 0.0025$ and the dashed-dot line to $\Delta x = 0.00125$. In all cases $\Delta t = 0.0001$, $D = 2$, $\delta = 0.1$, $\varepsilon_a = 0.1$.

and (6.3.12)–(6.3.15) for the symmetric mode as with one change in each case. We do a second scaling of the amplitude for each mode to ensure that the amplitude of $\hat{\eta}$ for the antisymmetric mode and η for the symmetric mode can be explicitly set, this helps when comparing numerical solutions. These rescalings are

$$A' \to \frac{\varepsilon_a}{\left[\frac{c_a^2}{\delta(2\pi)^4} - \frac{(D+1)}{2}\right]}, \tag{6.4.1}$$

$$B' \to \frac{\varepsilon_s}{\left[\frac{\delta c_s^2}{(2\pi)^2} - 2(D+1)\right]}, \tag{6.4.2}$$

with ε_a representing the amplitude of the antisymmetric mode and ε_s the amplitude of the symmetric mode.

The spatial resolution test for the numerical scheme consists of running the code until

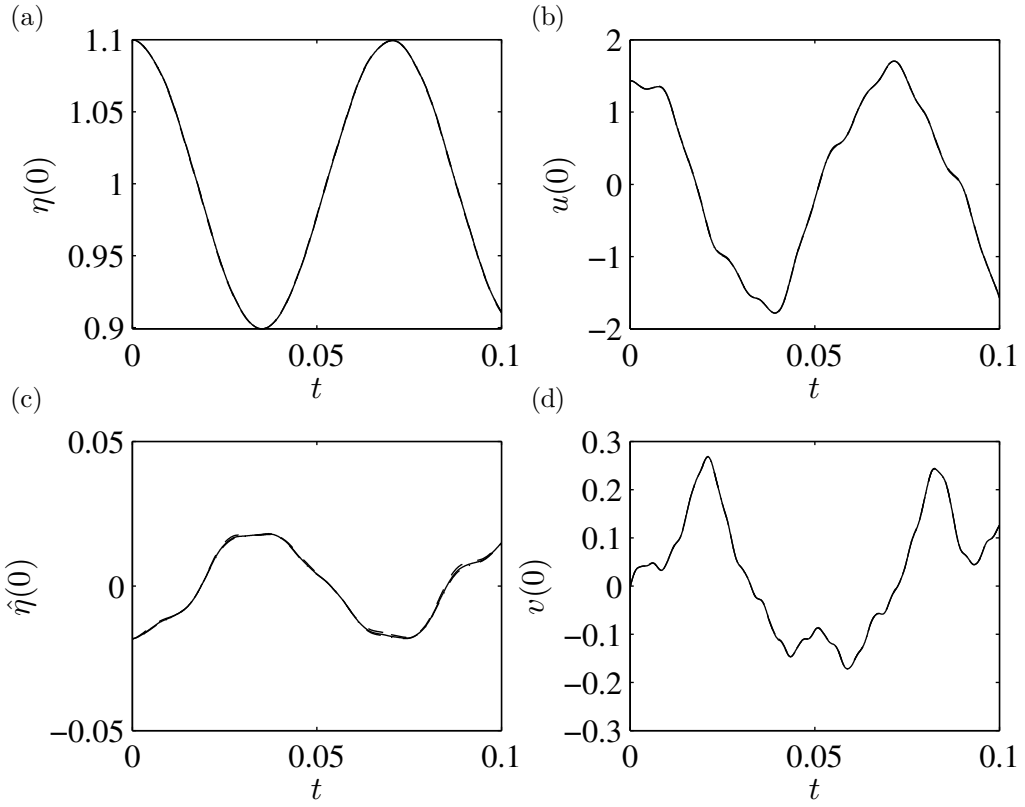

Figure 6.2: The effect of varying the spatial resolution on the continuation of the fully nonlinear symmetric mode at a fixed point in the domain. The dashed line corresponds to $\Delta x = 0.005$, the solid line to $\Delta x = 0.0025$ and the dashed-dot line to $\Delta x = 0.00125$. In all cases $\Delta t = 0.0001$, $D = 2$, $\delta = 0.1$, $\varepsilon_s = 0.1$.

$t = 0.1$ with a fixed temporal resolution of $\Delta t = 0.0001$ and a fixed bending stiffness ratio of $D = 2$. We track a single point in the domain ($x = 0$) for the duration of the run and then plot the results to compare three spatial resolutions, $\Delta x = 0.005$, $\Delta x = 0.0025$ and $\Delta x = 0.00125$. The results for the antisymmetric mode are shown in Figure 6.1 and for the symmetric mode in Figure 6.2. For both modes, the two finer resolutions are of similar accuracy, while $\Delta x = 0.005$ is of similar accuracy for η, u and v but with some variation in $\hat{\eta}$, we take $\Delta x = 0.0025$ in what follows.

The temporal resolution test consists of running the code until $t = 0.1$ with $D = 2$ and a fixed spatial resolution of $\Delta x = 0.0025$, while varying Δt. The three temporal resolutions tested are $\Delta t = 0.001$, $\Delta t = 0.0001$ and $\Delta t = 0.00005$. The value of the four variables at the tracked point is plotted for the antisymmetric mode in Figure 6.3 and for the symmetric mode in Figure 6.4. For all four variables in both modes,

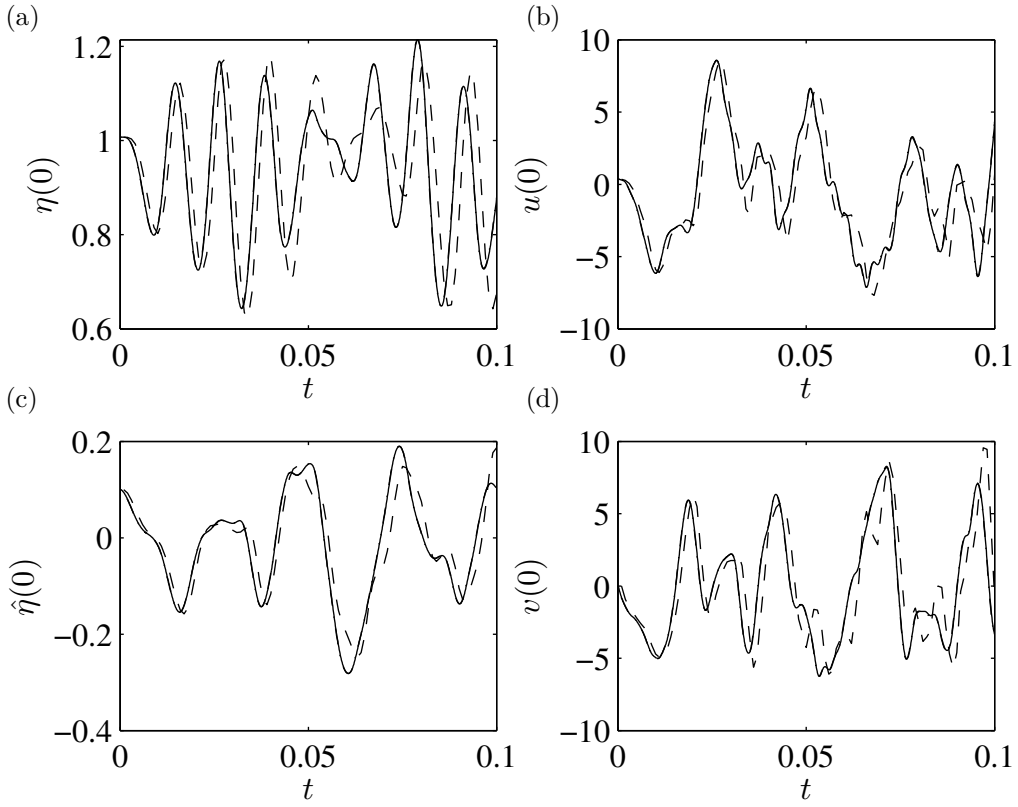

Figure 6.3: The effect of varying the temporal resolution on the continuation of the fully nonlinear antisymmetric mode at a fixed point in the domain. The dashed line corresponds to $\Delta t = 0.001$, the solid line to $\Delta t = 0.0001$ and the dashed-dot line to $\Delta t = 0.00005$. In all cases $\Delta x = 0.0025$, $D = 2$, $\delta = 0.1$, $\varepsilon_a = 0.1$.

a temporal resolution of $\Delta t = 0.001$ was found to be insufficiently accurate and clearly different to the two finer resolutions which show no visible difference. In order to save on computation time, we fixed $\Delta t = 0.0001$ rather than using $\Delta t = 0.00005$ as we maintain a sufficient level of accuracy.

6.5 Equivalence of $D = 1/n$ and $D = n$

We remark first upon the equivalence of examining both $D = 1/n$ and $D = n$ for any $n \in \mathbb{R}_+$. Physically, this is simply a switching of the bending stiffness of each wall, and is solving the same system under a reflection. In the nondimensional system the transformation also involves a temporal element, as the velocity scaling is based on one wall and this in turn has an effect upon the temporal scaling. The transformation, to

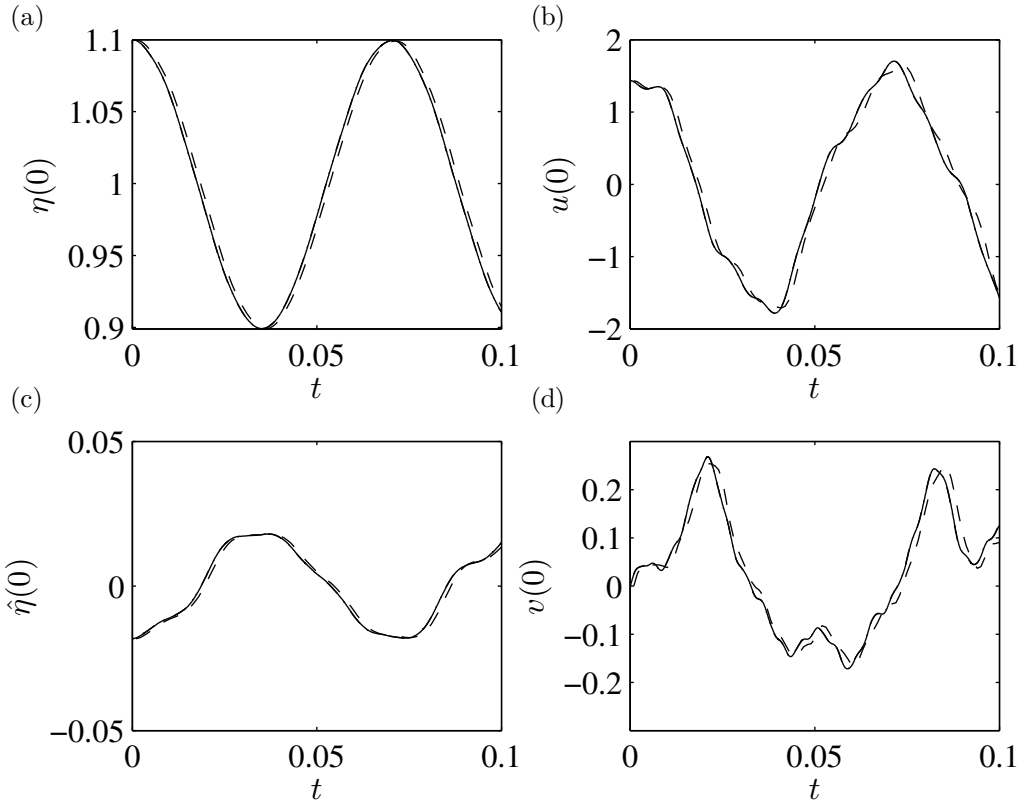

Figure 6.4: The effect of varying the temporal resolution on the continuation of the fully nonlinear symmetric mode at a fixed point in the domain. The dashed line corresponds to $\Delta t = 0.001$, the solid line to $\Delta t = 0.0001$ and the dashed-dot line to $\Delta t = 0.00005$. In all cases $\Delta x = 0.0025$, $D = 2$, $\delta = 0.1$, $\varepsilon_s = 0.1$.

change a solution for $D = 1/n$ into a solution for $D = n$ is as follows,

$$t \to \frac{t}{\sqrt{n}}, \tag{6.5.1}$$

$$\eta \to \eta, \tag{6.5.2}$$

$$u \to \sqrt{n}u, \tag{6.5.3}$$

$$\hat{\eta} \to -\hat{\eta}, \tag{6.5.4}$$

$$v \to -\sqrt{n}v. \tag{6.5.5}$$

For the travelling wave initial conditions the wavenumbers stays the same but because the temporal scale changes we also need

$$c_a \to \frac{c_a}{\sqrt{n}}, \quad c_s \to \frac{c_s}{\sqrt{n}}. \tag{6.5.6}$$

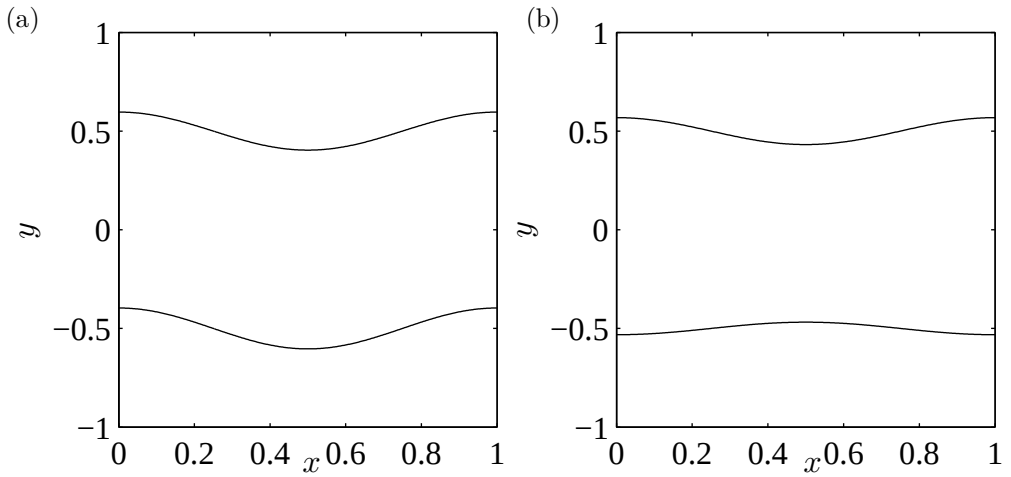

Figure 6.5: The initial positions of the channel walls when $D = 1/2$, (a) Antisymmetric mode ($\varepsilon_a = 0.1$), (b) Symmetric mode ($\varepsilon_s = 0.1$). In both cases $\delta = 0.1$.

For the antisymmetric mode there is another transformation needed, that is

$$x \to x + \frac{\lambda}{2}, \tag{6.5.7}$$

where λ is the wavelength of the initial disturbance applied to the system, at all times in this chapter $\lambda = 1$. The need for this half wavelength shift is due to the symmetry of the mode under a reflection in y. It is best described through the use of an illustration, see Figure 6.5, which shows a pair of example initial conditions when $D = 1/2$. We consider a transformation of the vertical axis $y \to -y$, which captures both (6.5.2) and (6.5.4). We can clearly see, looking at the symmetric mode in Figure 6.5(b), that the walls both bend in towards $y = 0$, and so after the transformation both walls with still point in. Conversely, both walls bend down for the antisymmetric mode (Figure 6.5(a)), one towards $y = 0$ and one away, after the transformation both walls bend up hence we need the half wavelength shift.

6.6 Phase velocity

The dependence of the phase velocity on the bending stiffness is seen in the expressions for c_a and c_s, (6.3.6) and (6.3.7) respectively, and hinted at by the necessity of the transformation (6.5.6). Figure 6.6 illustrates this dependence explicitly when other variables are held constant.

The phase velocity of the antisymmetric mode is shown in Figure 6.6(a), and tends to infinity as D does. However, at $D = 0$, the phase velocity can be calculated from (6.3.6) to be

$$c_a = k^2\sqrt{2\left(\frac{\delta}{4} + \frac{1}{\delta k^2}\right)}, \tag{6.6.1}$$

which is shown by the dashed-dot line in Figure 6.6(a) for $k = 2\pi$.

Similarly, the phase velocity of the symmetric mode is illustrated in Figure 6.6(b). This mode has zero velocity when $D = 0$, so there is only one mode of travelling wave to be found at this point. However, in contrast to the antisymmetric mode, the symmetric mode has a finite phase velocity as $D \to \infty$. Specifically, from (6.3.7), we obtain

$$c_s \to k\sqrt{\frac{8\delta}{\delta^2 + 4k^{-2}}}, \tag{6.6.2}$$

which is shown by the dashed-dot line in Figure 6.6(b) for $k = 2\pi$.

A key result to take away from the dependence of the phase velocities on the bending stiffness ratio is the breakdown of the transformations when $D = 0$ as can be seen in Figure 6.6. This will be discussed further in section 6.8. As a consequence of this equivalence, in the rest of this chapter we only consider bending stiffnesses in the range $0 \leq D \leq 1$.

6.7 Temporal Evolution

With a spatial and temporal resolution shown to be sufficiently accurate, we now investigate the effect of varying the ratio of bending stiffnesses, D, on the nonlinear temporal

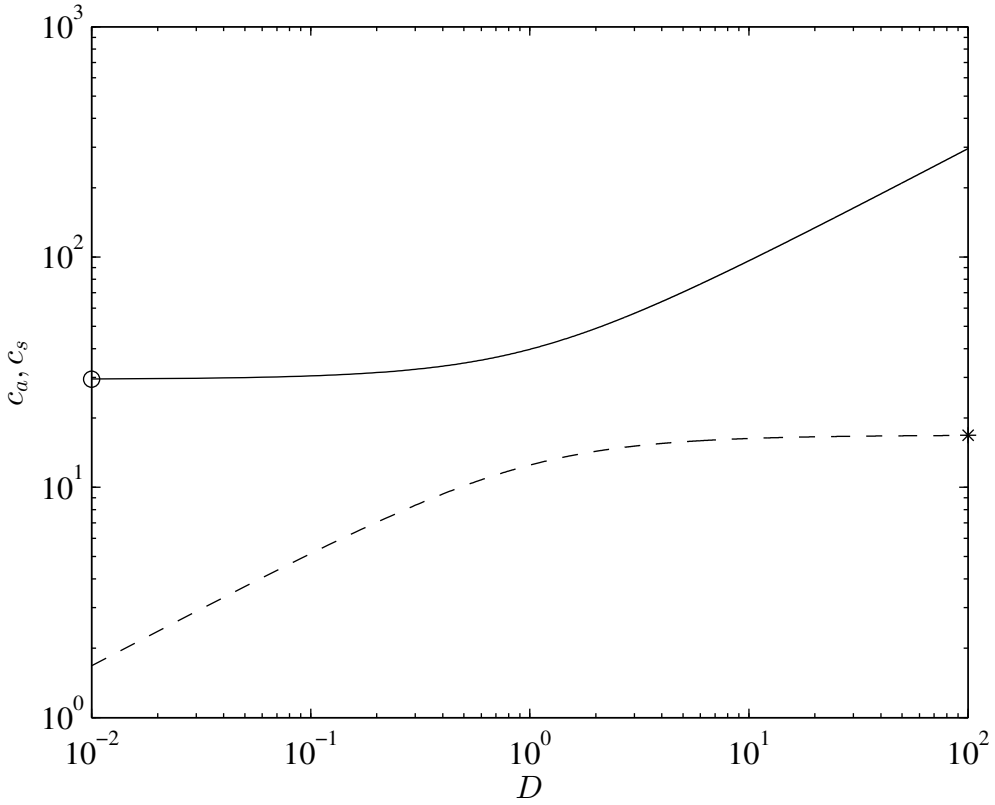

Figure 6.6: The change in phase velocity with respect to the ratio of bending stiffnesses for the antisymmetric mode (solid line) and symmetric mode (dashed line). The antisymmetric phase velocity at $D = 0$ (circle) and the symmetric phase velocity in the limit $D \to \infty$ (star) are also shown. In both cases $\delta = 0.1$.

evolution of travelling wave solutions to the linearised system. As a reminder, the numerical model breaks down as $\eta \to 0$, so we cease calculations when the thickness of the channel drops below $\eta = 0.01$.

6.7.1 Antisymmetric Mode

Using the numerical scheme and initial conditions outlined in section 6.4 for the antisymmetric mode, we investigated four values of the bending stiffness ratio, $D = 1/2$, $D = 1/4$, $D = 1/8$ and $D = 1/10$, for a fixed amplitude initial disturbance of $\varepsilon_a = 0.1$. We ran the codes for the duration of a single period of the equivalent linear travelling wave for $\hat{\eta}$. We found that at amplitudes this small, the effect of the nonlinear terms was negligible upon the antisymmetric mode even for $D = 1/10$ which was the smallest value we tested. This is shown in Figure 6.7(a), where the linear and nonlinear solutions are

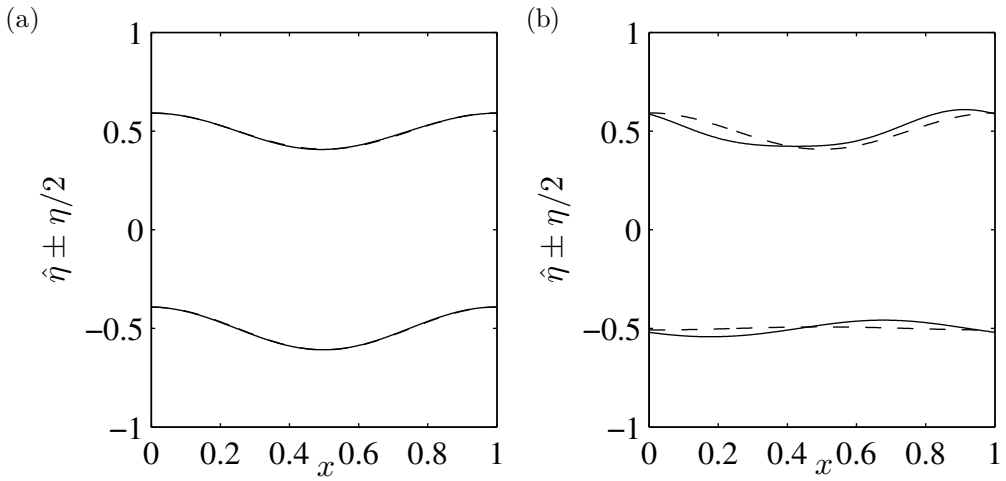

Figure 6.7: The position of the channel walls at the end of one period of the linear travelling wave solution when $D = 1/2$, (a) Antisymmetric mode ($\varepsilon_a = 0.1$), (b) Symmetric mode ($\varepsilon_s = 0.1$). In both cases the solid line is the nonlinear system, the dashed line is the linear system and $\delta = 0.1$.

plotted over each other due to their similarity. This is backed up by results from Chapter 5 where it was found that nonlinear effects are negligible at small amplitudes. Since the nonlinear effects are negligible, the leading order behaviour (which would be affected by variations in D) clearly does not change enough to become significant.

At larger amplitudes the effect of the bending stiffness ratio, D, becomes much more obvious. Figure 6.8 shows the position of the channel walls for varying D after one period of the equivalent linear travelling wave. The results indicate that as the ratio decreases from $D = 1/2$ (Figure 6.8(a)) to $D = 1/10$ (Figure 6.8(d)), the difference in velocity between the nonlinear and linear systems actually reduces. We also see that the channels exhibit the same thickening at the bends and thinning on the straights that is evident when $D = 1$ (e.g. Figure 5.9), however this effect is more pronounced at ratios closer to $D = 1$ and weakens as $D \to 0$. This is due to the top wall having less resistance to motion from the bending stiffness and so it starts becoming slaved to the bottom wall, matching its motion.

We were able to obtain numerical solutions for amplitudes up to $\varepsilon_a = 1$ before the codes broke down, however, even at this large amplitude we were unable to obtain results for the antisymmetric mode that had a sufficient narrowing of the channel to cease calculations within one time period.

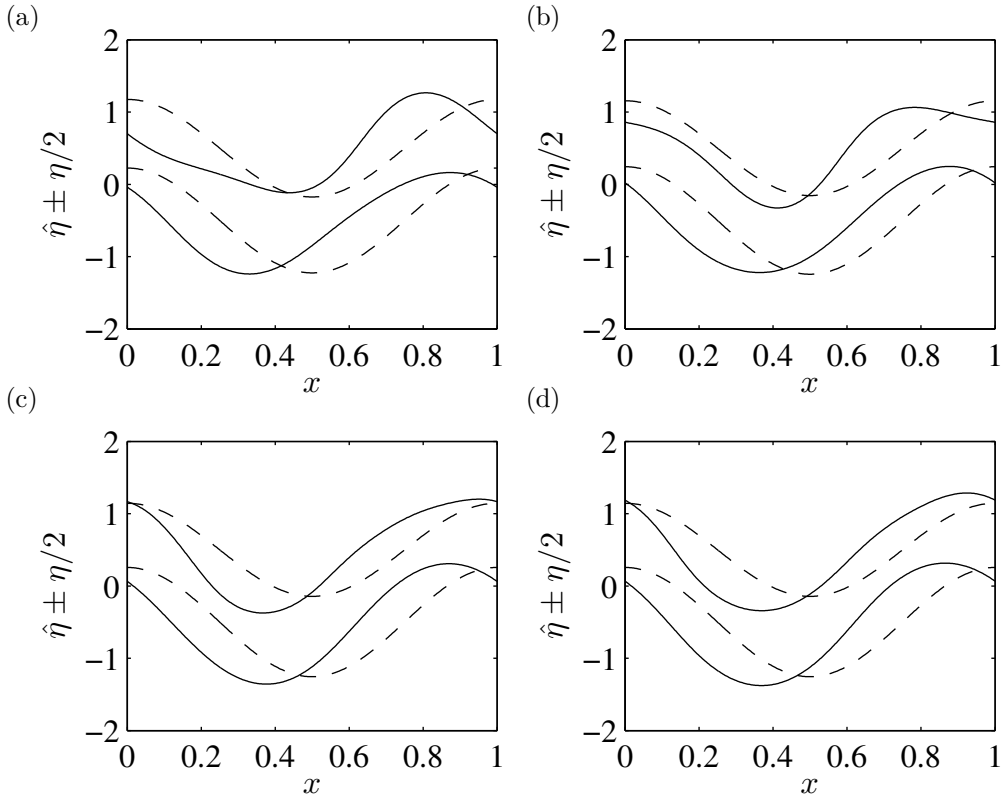

Figure 6.8: The position of the channel walls at the end of one period of the linear travelling wave solution for the antisymmetric mode, (a) $D = 1/2$, (b) $D = 1/4$, (c) $D = 1/8$ and (d) $D = 1/10$. In all cases the solid line is the nonlinear system, the dashed line is the linear system, $\varepsilon_a = 0.7$ and $\delta = 0.1$.

6.7.2 Symmetric Mode

We now investigate the effect of the bending stiffness ratio on the symmetric mode. Following the same procedure used for the antisymmetric mode we run the numerical code for varying D for the duration of one period of the linear travelling wave solution (for the symmetric mode, the duration is set by the period of η).

In contrast to the antisymmetric mode we see that even for small amplitudes, at smaller ratios of D, the effect of the bending stiffness can be seen to be reducing the velocity of the travelling waves, as shown in Figure 6.9 for $D = 1/10$.

As the amplitude increases the nonlinear effects become stronger and the wall profiles begin to deviate from those of the linear travelling wave profiles. The nonlinear effects can be seen to decrease the phase velocity of the waves. As the bending stiffness ratio, D, decreases, the nonlinear effects become even stronger and results in the majority of

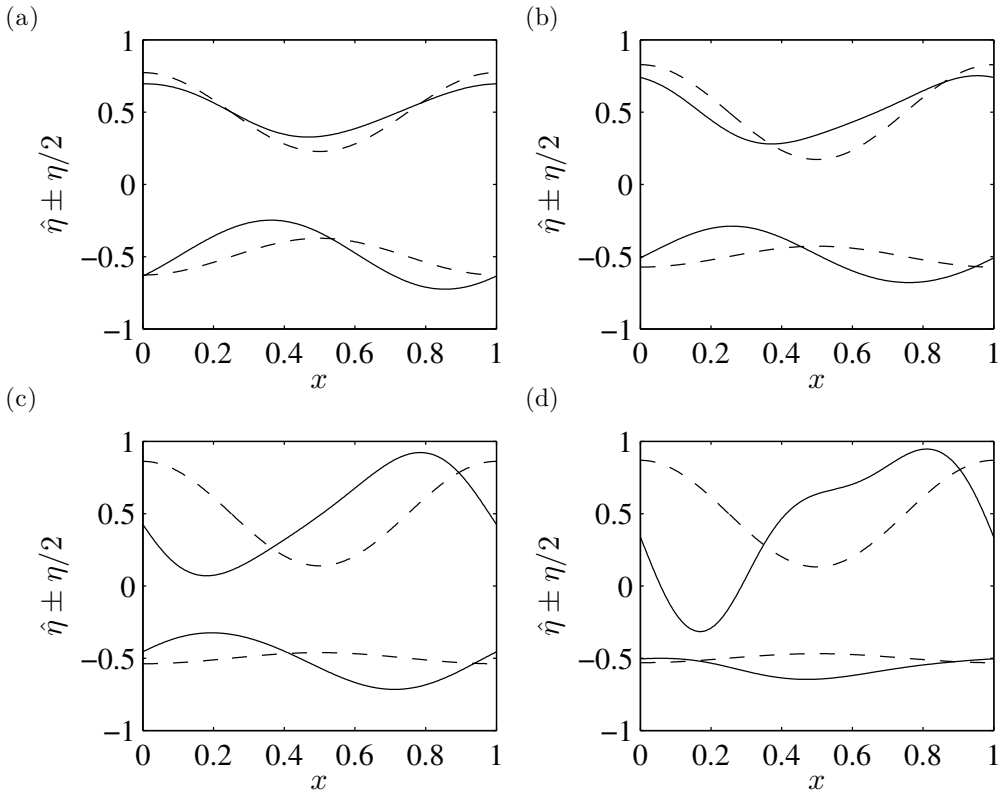

Figure 6.9: The position of the channel walls for the symmetric mode at the end of a single period of the linear travelling wave, (a) $D = 1/2$, (b) $D = 1/4$, (c) $D = 1/8$ and (d) $D = 1/10$. In all cases the solid line is the nonlinear system, the dashed line is the linear system, $\varepsilon_s = 0.4$ and $\delta = 0.1$.

the fluid gathering in a single bulge.

At larger amplitudes the symmetric mode exhibits strong nonlinear effects leading to η decreasing below the threshold required for the calculations to cease. We found that the thickness passing this threshold occured for smaller amplitudes of disturbance than were required previously when $D = 1$ (see Figure 5.8), occuring here for amplitudes of $\varepsilon_s = 0.7$ while for $D = 1$ ampitudes of $\varepsilon_s = 0.8$ or higher were required. The timestep that calculations were ceased for the varying values of D tested are shown in Figure 6.10, where we immediately notice the similarity of the profiles in subfigures (b)–(d). The difference between the shape of the channel walls in subfigure (a) and subfigures (b)–(d) is explained by the size of D, as D gets larger and approaches $D = 1$ it would be expected that the required amplitude for the thickness η to break the threshold should increase towards $\varepsilon_s = 0.8$ and so the wall profiles illustrated can be put down to the same

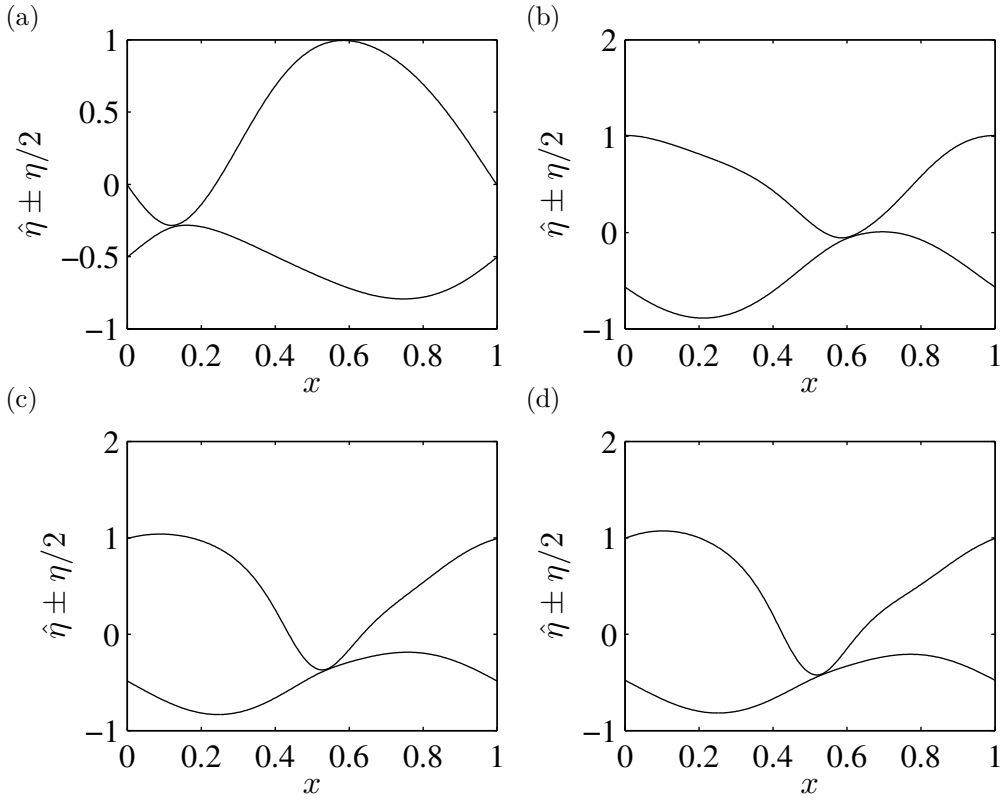

Figure 6.10: The position of the channel walls at the point the channel walls touch for the symmetric mode (a) $D = 1/2$ at $t = 0.0901$, (b) $D = 1/4$ at $t = 0.0222$, (c) $D = 1/8$ at $t = 0.0243$ and (d) $D = 1/10$ at $t = 0.0256$. In all cases the solid line is the nonlinear system, the dashed line is the linear system, $\varepsilon_s = 0.7$ and $\delta = 0.1$.

nonlinear effects that caused wall touches in Chapter 5.

Equivalently, as D gets smaller, the top surface becomes freer and the touch can occur earlier than for $D = 1/2$, with the difference in bending stiffness between the two walls having a greater effect. As the bending stiffness ratio decreases further towards $D = 0$ the wall profiles become more similar in shape but steepening on the back end of the fluid bulge and shallowing at the front end. As D decreases, we find the nonlinear time for the walls to touch starts increasing again, this is due to the decreased phase velocity of the waves as $D \to 0$ as shown in Figure 6.6, so although the profiles are relatively similar in shape, they travel slower and take longer to experience the same point as higher values of D.

6.8 Limiting cases of $D = 0$ and $D \to \infty$

As briefly touched upon in section 6.6, the limiting cases of $D \to 0$ and $D \to \infty$ are not trivial and we see some interesting results arise. From a physical point of view, these modes are equivalent but mathematically they appear at first glance to exhibit different behaviour.

Physically, in the limits $D \to 0$ and $D \to \infty$, one wall is much stiffer than the other, and thus has a much higher natural oscillation frequency. At lower frequencies this wall apears rigid, so we get one slow travelling wave solution in which the stiff wall has negligible motion. The motion of the wave is governed by a balance between the elasticity of the weaker wall and the fluid inertia.

At higher frequencies the weaker wall appears to offer no resistance to motion, and acts as a stress free boundary. The second travelling wave solution is therefore a fast wave in which the stiffer boundary oscillates. In this case the wave motion is governed by a balance between the elasticity of the stiffer wall and the fluid inertia. The weaker wall becomes slaved to the motion of the stiffer wall.

Looking at the case when $D \to 0$, we refer back to Figure 6.6 and we see that in that limit, the phase velocity of the antisymmetric mode tends to a non-zero value but the phase velocity of the symmetric mode tends to zero. This implies that there are therefore no linear travelling-wave solutions to the symmetric mode when $D = 0$ with a non-zero phase velocity. This was tested numerically using the standard initial conditions given by (6.3.12)–(6.3.15) and (6.4.2), and we found that the inital profiles were conserved without moving for all time.

For the equivalent ratio of bending stiffnesses, the antisymmetric mode does have travelling wave solutions to the linear system with a phase velocity given by (6.6.1). This system can be thought of physically in two different ways, firstly it can be obtained by the top wall of the channel having no bending stiffness whatsoever, or secondly by the bottom wall becoming rigid. This mode was tracked over one period of the equivalent linear travelling wave and is illustrated in Figure 6.11, where we can see that there is a

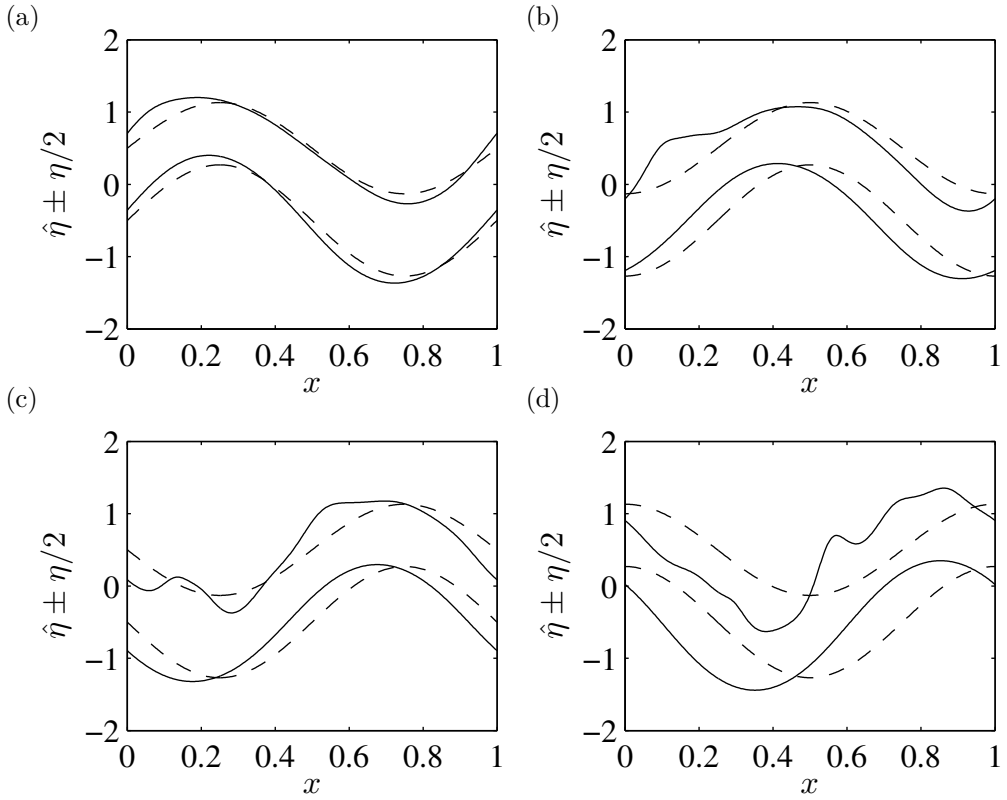

Figure 6.11: Propagation of waves in the nonlinear antisymmetric mode when $D = 0$ and $\varepsilon_a = 0.7$ for the duration of one period of the equivalent linear travelling wave solution. In all cases the dashed line is the fully linearised profile and the solid line is the nonlinear profile. (a) is $T/4$, (b) is $T/2$, (c) is $3T/4$ and (d) is T.

distinct difference in the behaviour of the two walls. The bottom wall appears to behave normally, maintaining a steady profile shape while moving to the right albeit at a slower pace than the linear travelling wave profile, this decrease in velocity is expected due to the nonlinear terms, while the smooth shape is maintained as the timescale of the system is nondimensionalised on the bending stiffness of the bottom wall. However, the top wall starts out smooth but begins to exhibit strong deformations from the smooth profile at $t = T/2$ (subfigure (b)) which progressively gets worse. Due to the form this deformation takes we remain unsure as to whether it is a physical response or an indicator that the numerical model cannot cope with a completely free boundary with no restoring force.

Looking now at the limiting case of $D \to \infty$, examination of relation between phase velocity and the bending stiffness shows that waves in the antisymmetric mode move have

$c_s \to \infty$ as $D \to \infty$. This is unphysical and suggests that the problem is ill-posed in its current form. This could be counteracted by rescaling U based on the bending stiffness of the top wall before taking the limit $D \to \infty$. However, this in turn would lead to one of the modes having an unbounded phase velocity as $D \to 0$ so it is not beneficial to do so.

Conversely, in the symmetric mode as $D \to \infty$, the phase velocity tends to the finite limit given in (6.6.2), suggesting the existence of travelling waves in the symmetric mode. Physically, these would be the equivalent of the two cases mentioned previously, but flipped. So it could occur through the bottom wall of the channel having no bending stiffness, or by the top wall becoming rigid. It was not possible to examine this mode numerically, although we would expect the results to be the equivalent of those presented in Figure 6.11 under some suitable transformation to switch the bending stiffnesses of the wall whilst retaining the requisite features of the rest of the system.

6.9 Discussion

In this chapter, we have formulated a nonlinear system of equations for a channel with elastic boundaries, with each boundary having an independent bending stiffness. By taking a suitable linearisation of this system we were able to find linear travelling wave profiles for the two modes that are analagous to the antisymmetric and symmetric modes we had previously in Chapters 4 and 5, which are obtained in this system when the ratio of the bending stiffnesses is equal, i.e. $D = 1$.

The symmetry of the bending stiffness ratio meant a transformation could be found to show the equivalence of two bending-stiffness ratios $D = 1/n$ and $D = n$ for $n \in \mathbb{R}_+$, allowing us to limit our investigation to $0 \leq D < 1$. The numerical scheme used in Chapter 5 was modified to allow its use with the new system of equations, and we were then able to start determing the temporal behaviour of waves within the system. The effect of the bending stiffness ratio was found to be negligible when the nonlinear effects of the curvature were negligible, and significant when the nonlinear effects were present. We

were able to make the walls touch for the symmetric mode (insofar as the code considers a touch, i.e. $\eta < 0.01$ at some point in the domain) and at amplitudes smaller than when $D = 1$, but not for the antisymmetric mode before the code broke down. Finally we discussed the limiting case of either wall losing any bending stiffness and observed that the two-mode system collapses to a single mode by examining the effect of D upon the phase velocity of travelling waves in the linear system.

CHAPTER SEVEN

CONCLUSIONS

7.1 Summary of Results

In this thesis we have considered the hydroelastic stability and propagation of waves in fluid-filled channels. Throughout, we have discussed the results at relevant points, but here we summarise what was done in each chapter and the key results.

In Chapter 2 we performed a temporal linear stability analysis for plug flow between two elastic plates. We incorporated the physical effects of bending stiffness, inertia, axial tension in the channel walls, and a spring backing to the channel walls. The dispersion relation for the full problem was derived and analysed for various limiting values of the physical parameters. It was found that the only physical effect that destabilised the system was the wall inertia, β. At long wavelengths the spring response, γ, was found to be stabilising, while the bending stiffness, α, was stabilising for short wavelength disturbances. The effect of the axial tension, τ, is to stabilise the system at long wavelengths above a critical value that is dependent upon the other parameters present. In the presence of inertia and a small spring response, and at least one other parameter, the system exhibited the interesting behaviour of being stable at both short and long wavelengths but unstable for a range of wavelengths in-between. To the best of this author's knowledge this behaviour was previously unknown and so the results presented here provide a good

starting point for further research to be carried out into the likelihood of these behaviours to show up in real world systems.

In Chapter 3 we reconsidered the stability analysis from a spatial perspective, and formulated the required dispersion relation for the system considered in Chapter 2. We then focused on the linear plate model which included the bending stiffness and the wall inertia. The Briggs–Bers technique was introduced to determine the stability and direction of propagation of the roots to the dispersion relation. Unstable roots were discovered for a range of parameter values and frequencies of the driver. The results in this chapter were compared with those of de Langre (2002) and in each of the key regions he outlined, we were able to determine the root that would result in convective instability. Furthermore, although the setup of our system precluded the formation of absolute instabilities, we were still able to determine which roots would correspond to the formation of this instability type when the frequency, ω was allowed to be complex.

At this point, our focus switched from performing stability analyses on potentially unstable systems, to focusing on the propagation of waves in systems that are stable. In Chapter 4 we extended the work of Mehring & Sirignano (1999) on the nonlinear breakup of liquid sheets to elastic channels. We formulated the governing equations as in Mehring & Sirignano (1999), although with the addition of a nondimensional parameter of an aspect ratio, and with the behaviour of the elastic plate governed by a nonlinear plate equation in the absence of inertia. Two simplified systems were also considered, one with a linearised curvature, and the other with a ful linearisation of the flow and curvature. For the fully linear system, analytic travelling wave solutions were found, while for the linearised curvature system, an equation was derived for travelling waves that was solved numerically due to its nonlinearity. An asymptotic analysis of these equations was performed in the limit of the channel thickness tending to zero. The asymptotic solution showed good agreement with the numerical simulations. A similar numerical approach was used on the full system. The travelling wave profiles were found to be nearly identical to the linearised-curvature system, but propagating at a much lower velocity.

This work was built upon in Chapter 5 where we determined numerically how the nonlinear terms affected the propagation of linear travelling-wave profiles. We constructed central finite difference analogues for the governing equations of Chapter 4, and used a Crank–Nicolson scheme to advance the system forward in time. This scheme was validated using the nonlinear travelling wave profiles of the previous chapter, as well as verifying that a derived energy conservation equation was satisfied at each timestep. The primary effect of the nonlinear terms in the curvature was to reduce the velocity at which waves propagated through the system. At higher amplitude disturbances the nonlinearities were also responsible for a higher order temporal oscillation forming. Despite the system being stable, this oscillation could lead to the channel walls touching in finite time. The work in Chapters 4 and 5 had not been applied to the study of elastic-walled channels before, and so resulted in the observation of new periodic travelling waves, as well as the higher order oscillation giving rise to a mechanism to force the closure of a stable channel.

Finally, we considered in Chapter 6 an extension of the system in Chapters 4 and 5, whereby we considered the equivalent system without the assumption of the flexural rigidity of each wall being the same. The governing equations were formed in the same way, with the introduction of a second nondimensional parameter, D, the ratio the bending stiffness of the top wall to the bottom wall. By performing a linear analysis we showed that there were two modes in the system, analogous to the traditional antisymmetric and symmetric modes, which were recovered when $D = 1$. It was shown that there was an equivalence between studying $D = n$ and $D = 1/n$ for n real and positive, so we were able to limit our study to $0 \leq D < 1$. We also discussed the physical and mathematical relevance of $D = 0$ and $D \to \infty$.

Aside from the already discussed new instabilities found when performing the temporal stability analysis, it is worth reinforcing what new work this thesis has introduced. In our spatial stability analysis, we determined the particular roots that cause unstable waves for a range of frequencies and physical parameter values. By adopting the Plotnikov & Toland (2011) model of nonlinear curvature we have extended the work of Mehring &

Sirignano (1999) to include the effect of elastic channel walls. This resulted in new travelling wave solutions that have not been considered before. We also managed to determine what effects are caused by the nonlinear terms in the curvature. The work in the final chapter was all new as the flow through an elastic channel with differing bending stiffnesses has not been considered before.

7.2 Further work

The work contained in this thesis can be extended in several ways which will be discussed in this section to serve as a possible motivator for future work.

This thesis has considered only inviscid plug flows in channels between two elastic walls, this was done to allow us to focus on the fluid-structure interaction. A natural next step would therefore be to include the effect of viscosity in the fluid. This would introduce another physical parameter to the system and also result in the introduction of boundary layers at the interfaces between the fluid and solid. While viscosity is known to act like an energy sink and thus is likely to have a stabilising effect upon the system, it is not known for sure if that will be the case in this regime.

Another physical effect that has been ignored in this thesis is the effect of gravity. While it is not believed that it will have much effect on the horizontal configurations we have considered here, it would be likely to have an effect when considering vertical flows. For the equivalent problem of liquid sheets falling under gravity, a thinning of the sheet is found to occur (Lin, 2003). For a channel equivalent, this may lead to a detachment of the fluid from the elastic walls, but it is currently unknown if this will be the case.

In Chapters 4–6, we considered stable systems for which wall inertia was negligible, this was in order to make the problem easier to work with. These systems can be thought of as ones where the channel walls are particularly light or thin, or the fluid is particularly heavy. Our work in Chapters 2–3 showed that inertia is required for instabilities to occur. Therefore, the next logical step in considering these systems would be to introduce this effect, and investigate how this alters the behaviours currently exhibited. This

would involve adding a term to the right hand side of (4.2.7), which would take the form $\pm\rho_b h_b \partial^2 \eta_\pm / \partial t^2$, where ρ_b and h_b are the density and thickness of channel wall. Care must be taken when dealing with this term numerically, as currently time derivatives are calculated using forward differences. A preliminary numerical calculation suggests that instabilities do arise, and also result in a significant decrease in the propagation speed.

A final extension of this work would be to consider the same system as in Chapter 6 but with the top elastic wall replaced by a free surface. A system like this would be useful in modelling very large floating objects, such as floating runways and ice sheets. Some work has been done on this system already, Mohapatra & Sahoo (2011) have considered the interaction of surface gravity waves in the presence of an elastic bottom. The difference in order between the boundary conditions at the free surface and elastic plate, although making the system harder to work with, could lead to some interesting results.

References

ABRAMOWITZ, M. & STEGUN, I. A. (2012) *Handbook of Mathematical Functions*. Courier Dover Publications.

ACHESON, D. J. (1990) *Elementary Fluid Dynamics*. Oxford University Press.

BERS, A. (1983) Space-time evolution of plasma instabilities – absolute and convective. In *Handbook of Plasma Physics*, vol. 1, pp. 451–517, North-Holland.

BLYTH, M., PĂRĂU, E. & VANDEN-BROECK, J. (2011) Hydroelastic waves on fluid sheets. *J. Fluid Mech.* **689** (1), 541–551.

BRAMBLEY, E. (2007) *The Acoustics of Curved and Lined Cylindrical Ducts with Mean Flow*. Ph.D. thesis, University of Cambridge.

BRAZIER-SMITH, P. & SCOTT, J. (1984) Stability of fluid flow in the presence of a compliant surface. *Wave Motion* **6** (6), 547–560.

BRIGGS, R. J. (1964) *Electron-Stream Interaction with Plasmas*. MIT Press.

CHEONG, B. & HOWES, T. (2004) Capillary jet instability under the influence of gravity. *Chem. Eng. Sci.* **59** (11), 2145–2157.

CRIGHTON, D. G. & OSWELL, J. E. (1991) Fluid loading with mean flow. I. Response of an elastic plate to localized excitation. *Phil. Trans. Roy. Soc. London Ser. A* **335** (1639), 557–592.

EGGERS, J. & DUPONT, T. F. (1994) Drop formation in a one-dimensional approximation of the Navier–Stokes equation. *J. Fluid Mech.* **262**, 205–221.

GAVER, D. P., HALPERN, D., JENSEN, O. E. & GROTBERG, J. B. (1996) The steady motion of a semi-infinite bubble through a flexible-walled channel. *J. Fluid Mech.* **319**, 25–65.

GROTBERG, J. (1994) Pulmonary flow and transport phenomena. *Annu. Rev. Fluid Mech.* **26** (1), 529–571.

HEIL, M. & HAZEL, A. L. (2011) Fluid–structure interaction in internal physiological flows. *Annu. Rev. Fluid Mech.* **43**, 141–162.

KELLER, J. B., RUBINOW, S. & TU, Y. (1973) Spatial instability of a jet. *Phys. Fluids* **16**, 2052–2055.

KIM, G. & DAVIS, D. (1995) Hydrodynamic instabilities in flat-plate-type fuel assemblies. *Nucl. Eng. Des.* **158** (1), 1–17.

KOROBKIN, A., PĂRĂU, E. I. & VANDEN-BROECK, J.-M. (2011) The mathematical challenges and modelling of hydroelasticity. *Phil. Trans. Roy. Soc. London Ser. A* **369** (1947), 2803–2812.

DE LANGRE, E. (2000) Ondes variqueuses absolument instables dans un canal élastique. *C. R. Acad. Sci. II. B* **328** (1), 61–65.

DE LANGRE, E. (2002) Absolutely unstable waves in inviscid hydroelastic systems. *J. Sound Vib.* **256** (2), 299–317.

DE LANGRE, E. & OUVRARD, A. E. (1999) Absolute and convective bending instabilities in fluid-conveying pipes. *J. Fluid Struct.* **13**, 663–680.

LI, X. (1993) Spatial instability of plane liquid sheets. *Chem. Eng. Sci.* **48**, 2973–2981.

LIGHTHILL, M. (1960) Studies on magneto-hydrodynamic waves and other anisotropic wave motions. *Phil. Trans. Roy. Soc. London Ser. A* **252**, 397–430.

LIN, S. P. (2003) *Breakup of Liquid Sheets and Jets*. Cambridge University Press, Cambridge.

MEHRING, C. & SIRIGNANO, W. A. (1999) Nonlinear capillary wave distortion and disintegration of thin planar liquid sheets. *J. Fluid Mech.* **388**, 69–113.

MICHELIN, S. & LLEWELLYN SMITH, S. (2009) Linear stability of coupled parallel flexible plates in an axial flow. *J. Fluid Struct.* **25**, 1136–1157.

MOHAPATRA, S. & SAHOO, T. (2011) Surface gravity wave interaction with elastic bottom. *Appl. Ocean Res.* **33** (1), 31–40.

PEAKE, N. (1997) On the behaviour of a fluid-loaded cylindrical shell with mean flow. *J. Fluid Mech.* **338**, 387–410.

PEAKE, N. (2001) Nonlinear stability of a fluid-loaded elastic plate with mean flow. *J. Fluid Mech.* **434**, 101–118.

PEAKE, N. & SOROKIN, S. (2001) On the behaviour of fluid-loaded sandwich panels with mean flow. *J. Sound Vib.* **242** (4), 597–617.

PLOTNIKOV, P. & TOLAND, J. F. (2011) Modelling nonlinear hydroelastic waves. *Phil. Trans. Roy. Soc. London Ser. A* **369** (1947), 2942–2956.

RAO, V. N. & RAMAMURTHI, K. (2009) Internal instability of thin liquid sheets. *Phys. Fluids* **21** (9), 092106.

SCHOUVEILER, L. & ELOY, C. (2009) Coupled flutter of parallel plates. *Phys. Fluids* **21**, 081703.

SMITH, G. D. (1985) *Numerical Solution of Partial Differential Equations: Finite Difference Methods*. Oxford University Press.

SQUIRE, H. (1953) Investigation of the instability of a moving liquid film. *Brit. J. Appl. Phys.* **4**, 167–169.

TANG, L. & PAÏDOUSSIS, M. (2009) The coupled dynamics of two cantilevered flexible plates in axial flow. *J. Sound Vib.* **323**, 790–801.

TRIANTAFYLLOU, G. S. (1992) Physical condition for absolute instability in inviscid hydroelastic coupling. *Phys. Fluids A-Fluid* **4** (3), 544–552.

VANCE, S., BOUFFARD, M., CHOUKROUN, M. & SOTIN, C. (2014) Ganymedes internal structure including thermodynamics of magnesium sulfate oceans in contact with ice. *Planet. Space Sci.* **96**, 62–70.

WALSH, C. (1995) Flutter in one-dimensional collapsible tubes. *J. Fluid Struct.* **9**, 393–408.